Fabrication and Qualification of Arbitrarily Patterned Seamless Tooling for Continuous Roll-to-Roll Microcontact Printing

by

Peter A. Ascoli

B.Eng. Mechanical Engineering, The Cooper Union for the Advancement of Science and Art (2015)

Submitted to the Department of Mechanical Engineering
in partial fulfillment of the requirements for the degree of

Master of Science in Mechanical Engineering

at the

MASSACHUSETTS INSTITUTE OF TECHNOLOGY

June 2017

© Massachusetts Institute of Technology 2017. All rights reserved.

Author .... Signature redacted
Department of Mechanical Engineering
May 12, 2017

Certified by .... Signature redacted
David E. Hardt
Ralph E. Cross and Eloise F. Cross Professor of Mechanical Engineering
Thesis Supervisor

Accepted by .... Signature redacted
Rohan Abeyaratne
Chairman, Committee on Graduate Students

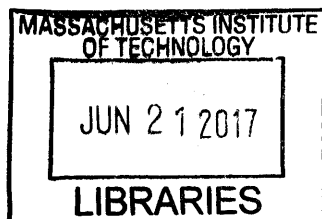
MASSACHUSETTS INSTITUTE OF TECHNOLOGY
JUN 21 2017
LIBRARIES
ARCHIVES

Fabrication and Qualification of Arbitrarily Patterned Seamless Tooling for Continuous Roll-to-Roll Microcontact Printing

by

Peter A. Ascoli

Submitted to the Department of Mechanical Engineering
on May 12, 2017, in partial fulfillment of the
requirements for the degree of
Master of Science in Mechanical Engineering

Abstract

Microcontact printing is form of soft lithography utilizing an elastomeric stamp with a molded relief pattern to print features on substrates through ink transfer at micron and nanometer scales. This is a low-cost technique when compared with other printing and patterning processes. Traditional microcontact printing using flat stamps and planar, rigid substrates, which limit production output, manufacturing scale, and capital efficiency. However, a precise, scalable, roll-to-roll process could lower production costs, increase output, and enable the creation new technologies. Specifically, flexible displays, photovoltaic systems and accessories, and other large area electronics could be fabricated using a continuous roll-to-roll microcontact printing process.

This work builds on existing research in fabricating seamless cylindrical PDMS stamps (tools) for microcontact printing using laser direct-write lithography for micro-patterning. Specifically, the scale-up requirement for microcontact printing to have arbitrarily patterned tools with diverse feature sets was addressed. The manufacturing process window of AZ 9260 photoresist was examined through numerical simulation and experimentation to determine an input set for the most robust performance and ideal tool feature geometry. A raster-scan protocol was developed to arbitrarily pattern the photoresist in a cylindrical setting. Additionally, non-destructive metrology equipment for analyzing the patterned photoresist and tool contact region were developed.

Tools with multiple feature patterns were fabricated, and the evolution of critical feature dimensions were measured from simulation, to the photoresist mold, to the PDMS stamp, to the stamp in contact, and finally to the printed features. Manufacturing tools with diverse patterns was demonstrated, and the contribution of tool fabrication steps to ultimate print geometries was studied. The presented findings further the development of a scaled-up microcontact printing process in a continuous roll-to-roll setup.

Thesis Supervisor: David E. Hardt
Title: Ralph E. Cross and Eloise F. Cross Professor of Mechanical Engineering

Acknowledgments

First, I would like to thank my family. Simply put, I would not be where I am today without the unconditional support I have received along the way. I similarly want to extend gratitude to the friends, faculty, advisors, and mentors from my undergraduate experience. Without them, I doubt that I would have ended up at MIT.

I would like to thank my advisor, David Hardt, for his guidance in research, navigating graduate school, career advice, and otherwise. His advice, support, and anecdotal engineering stories continuously made for a smooth and enjoyable time at MIT. I would also like to acknowledge current and former Hardt Lab members and collaborators: Maia Bageant, Peter Chamberlain, Christopher Merian, Shaswat Anand, Xian Du, Larissa Nietner, and Scott Nill. I am very grateful for their advice and assistance in research, as well as for making the otherwise dreary and rundown 35 a fun place to work.

Most of the magic of MIT lies in the community. I am forever grateful for all of the friends I have made in my time here. The academic support, and the fun adventures in, around, and outside of Boston/Cambridge were undoubtably key to a succesful MIT experience, and made for great memories. I hope that the relationships I have built in the past two years only grow with time.

Finally, I must acknowledge my funding sources. I would like to thank the MIT School of Engineering for the KUT fellowship. Additionally, I want to thank the Center for Clean Water and Clean Energy, the MIT partnership with King Fahd Universty of Petroleum and Minerals (KFUPM), for supporting this research.

THIS PAGE INTENTIONALLY LEFT BLANK

Contents

1 Introduction **29**

1.1 Overview of Microcontact Printing 29

1.2 Potential Applications 31

1.3 Scale-Up of Microcontact Printing 32

1.4 Focus of Thesis 32

2 Prior Work **35**

2.1 Fundamentals of Soft Lithography 35

2.2 Inking 36

2.3 Tooling 37

2.3.1 PDMS Stamps 37

2.3.2 Petrzelka's Centrifugal Casting Machine 39

2.3.3 SPR 220 and AZ 9260 Patterning Layer Investigation 40

2.4 Printing 44

2.4.1 The Petrzelka Machine 44

2.4.2 The MIT Machine 44

2.4.3 Insights into Tool Quality from Printing 45

3 Machine Design for Tools of Arbitrary Patterns **49**

3.1 Overview of the Centrifugal Caster 49

3.1.1 Centrifuge System 51

3.1.2 Linear Stage and Laser Optics System 53

3.1.3 Thermal System 54

3.1.4 Direct Write Lithography Software 54
3.2 Design of a Raster-Scan Writing Protocol 55
3.3 Design for Imaging Arbitrary Patterned Tools 60
3.3.1 Episcopic Microscopy of the Patterning Layer 60
3.3.2 Episcopic Microscopy of Tool Contact 64

4 Process Window for Tool Fabrication **67**
4.1 Lithography Simulation 68
4.1.1 Governing Physics for an Analytical Model 68
4.1.2 Single Exposure Features 72
4.1.3 Multi-Exposure Features 88
4.2 Characterization of Machine Errors 91
4.2.1 Linear Stage Error Motions 91
4.2.2 Planarizing Layer Flatness 92
4.2.3 Thermal Processing Uniformity and Repeatability 93
4.3 Photoresist Processing 96
4.3.1 Defects and Processing Optimization 96
4.3.2 AZ 9260 Photoresist Processing Literature Review 102
4.4 Minimization of Laser Focusing Errors 107
4.4.1 Experiment 1: 400 Micron Focus Shift 107
4.4.2 Experiment 2: 200 Micron Focus Shift 109
4.4.3 Summary of Focus Experiments 110

5 Experimentation **111**
5.1 Goals 111
5.2 Methods 112
5.2.1 Experimental Parameters and Feature Types 112
5.2.2 Procedure 117
5.3 Tool Measurement Processes 121
5.3.1 Optical Microscopy of PDMS Tools 121
5.3.2 Episcopic Microscopy of the Patterning Layer 123

5.3.3 Episcopic Microscopy of Tool Contact 125
5.3.4 Optical Microscopy of Prints 127
5.3.5 Measurement Order 129
5.4 Single Exposure Feature Results 130
5.4.1 Patterning Layer Repeatability 130
5.4.2 Pattern Replication and PDMS Stamp Repeatability 148
5.4.3 Contact Visualization and Analysis 158
5.4.4 Print Visualization and Analysis 162
5.4.5 Summary 164
5.5 Multiple Exposure Feature Results 165
5.5.1 Patterning Layer Repeatability 165
5.5.2 Pattern Replication and PDMS Stamp Repeatability 183
5.5.3 Contact Visualization 198
5.5.4 Print Visualization 200
5.5.5 Overlapping Exposure Failure 203
5.5.6 Summary 204

6 Discussion **205**

6.1 Towards Manufacturing Arbitrarily Patterned Tools 205
6.2 Contributions of the Tool 206
6.2.1 Pattern Similarity to Simulation 206
6.2.2 Pattern Replication by PDMS Stamp 207
6.2.3 Patterning Layer Repeatability 207
6.2.4 PDMS Stamp Repeatability 208
6.2.5 Contact Replication of Pattern Geometry 208
6.2.6 Printing Replicaiton of Contact Geometry 209
6.3 Future Work 209

7 Conclusion **211**

7.1 Thesis Contributions 211
7.2 Next Steps 212

A Planarizing Layer Casting Procedure 215

B Patterning Layer Procedure 219

C Single Layer PDMS Stamp Casting Procedure 225

D Dual Layer PDMS Stamp Casting Procedure 229

E MATLAB Code Photoresist Pattern 235

F MATLAB Code for Analyzing Print and Contact Images 243

G MATLAB Code for Contact Image Binarization 255

H MATLAB Code for Print Image Binarization 263

I MATLAB Code for Line Width Analysis 267

J MATLAB Code for Plotting Contact and Print Data 273

K MATLAB Code for Lithography Simulation 281

L MATLAB Code for Creating Stamp Feature Shape 295

M MATLAB Code for Single Exposure Simulation Trends 303

N MATLAB Code for Overlapping Exposure Lithography Simulation 309

List of Figures

1-1 An overview of the μCP process [6]. 1) A master pattern is created using lithography techniques. 2) PDMS elastomeric resin is poured over the mold. 3) The cured PDMS is removed from the master, yielding the patterned stamp. 4,5) The stamp is inked and dried. 6) The stamp contacts the substrate. 7). The SAM ink is transfered to the substrate. 8) Etching processes remove uncovered portions of the substrate, thereby replicating the stamp pattern. 30

2-1 A generalized schematic of an SAM on a substrate [6]. The head group (red) bonds to the substrate (orange). The molecular chains neatly align such that the surface properties reflect those of the tail group (blue). 36

2-2 A microcontact print of liquid ink onto a polymer substrate by Hale [20]. The hexagonal lines of silver nanoparticle ink are approximately 5 μm in width. 37

2-3 A schematic of conformal PDMS stamp contact in the presence of substrate surface roughness [6]. 38

2-4 Four failure modes of PDMS stamp features determined by Petrzelka [10]. (a) sidewall collapse, (b) roof collapse, (c) buckling of features, and (d) lateral collapse. 38

2-5 A process schematic for creating cylindrical PDMS tools [23]. A machined centrifuge drum (a) is coated in a SU8 photoresist and cross-linked to planarize the rough machined surface (b). A second photoresist coats the planarizing layer. The patterning layer is exposed and developed using maskless lithography, creating a microscopic 3D topology (c). PDMS is cast inside the centrifuge drum to form the stamp (d). The cured PDMS is removed from the centrifuge, creating a cylindrical stamp with outside surface features replicating the patterning layer (e). Finally, the PDMS stamp is mounted to a shaft for roll-to-roll printing. 40
2-6 The centrifugal casting machine by Petrzelka and Hardt [23]. 41
2-7 An SEM image of PDMS tool features created by Petrzelka and Hardt [23]. 42
2-8 An air bearing designed by Petrzelka for mounting cylindircal tools to metal shafts [10]. A cushion of air prevents adhesion of PDMS to the roll allowing the stamp to be smoothly transferred from one end of the roll (a) to the ideal mounting position (b). Once the stamp is properly located, the air bearing is disabled, and adhesion holds the PDMS tool in place. 42
2-9 Photographs of PDMS stamps and features created by Nietner [16]. 43
2-10 Stamp feature variation at a fixed centrifuge speed of 2 rev/s [16]. 43
2-11 Petrzelka's roll-to-plate printing apparatus [10]. 44
2-12 The MIT printing machine by Libert, Nill, Merian, and Bageant [14] [12] [13] [6]. The web handling system can be viewed on the left side of the image. The web stretches over the impression rool, where the print head system brings the stamp into contact with the web substrate. The two unlabled idler rollers currently measure reaction forces, subsequently leading to closed-loop web tension control. 45
2-13 A schematic of the stamp-substrate interface [12]. 46

2-14 Photographs of the printhead assembly. In Figure 2-14a, the stamp (b) is mounted to a steel shaft, supported in rotary air bearings (a). Voice coils (c) translate each arm of the assembly, which are supported on linear air bearings (d). This configuration permits a displacement and angle for contact to be set. Structural compliances in the form of flexural elements eliminate overconstraint (blue rotation), and serve as stiff force sensors (blue translation). In Figure 2-14b, nozzles (a) blow air over the stamp (b) to dry it. The stamp continuously rolls through an ink bath in the ink tank (c), which can be actuated (d) vertically to provide clearance for the stamp-mounting process. 47

3-1 A photograph of the current centrifugal casting system. The laser (a), optics (b), linear stage (c), centrifuge drum (d), temperature sensor (e), heat gun (f), and cooling fan (g), are labeled. The machine is mounted to an optical breadbord. Wired connections are bundled and brought through 3D printed brackets, which are secured to the back of the board. 50

3-2 CAD schematics of the safey enclosure for the centrifugal caster. 50

3-3 A labeled diagram of key centrifuge subassembly components. 52

3-4 Steady state centrifuge velocity performance of the Teknic ClearPath AC servo motor at a standard write speed of 9.42 rad/s (1.5 rev/s). The measured velocity response is oscillatory but comparable to the previous brushless DC motor. 52

3-5 The coordinate system and DOFs of the centrifugal casting machine. The axial position of the linear stage is denoted by x, while θ represents the rotational, or circumferential, position of the centrifuge. The two labeled x locations represent the axial boundaries of the photoresist casting area in the centrifuge drum. 55

3-6 A flowchart of the raster-scan direct-write protocol in LabVIEW. Blue blocks denote operations beformed on the host PC. Red blocks are operations executed on the FPGA, which require fast and precise timing. 59

3-7 A CAD schematic of the episcopic microscope for photoresist imaging with key components labeled. 62
3-8 A labeled optical schematic from CAD of the episcopic microscope for photoresist imaging. The image path is traced out in blue, the coaxial light path is yellow. 62
3-9 A photograph of the episcopic microscopy system imaging the photoresist mold. The illumination spot on the patterning layer is clearly visible. 64
3-10 A labeled CAD model the bechtop contact visualization setup. The print head is installed on the setup in this image. 66
3-11 A photograph of the benchtop contact system. Kinematic couplings (not shown in Figure 3-10) locate the printhead assembly with high repeatability. 66

4-1 A schematic of the lithography simulation. A numerical integration of $M(x, y, t)$ and $I(x, y, t)$ is performed to track the exposure of the photoresist and conversion of the PAC. The model allows for the laser focus and angle of incidence to be adjusted from the previously fixed $x = y = \theta = 0$ scenario. 71
4-2 Interpolated exposure dose [31] and centrifuge speed requirements for AZ 9260 at varying photoresist thicknesses. Curves for 50%, 100%, and 200% of the recommended dose at the given thickness are plotted in blue. The corresponding centrifuge speeds to apply 50%, 100%, and 200% of the recommended dose at full laser power are shown in orange. The maximum limit represents the maximum centrifuge speed at which the LabVIEW software can enable/disable the laser without missing a tick of the 8000 counts/rev centrifuge rotary encoder. Therefore, the centrifugal caster machine cannot achieve centrifuge speeds higher than this value, and the corresponding dose values are unachievable with the current hardware and software setup. 74

4-3 Interpolated exposure dose [31] and exposure time requirements for AZ 9260 at varying photoresist thicknesses. Curves for 50%, 100%, and 200% of the recommended dose at the given thickness are plotted in blue. The corresponding exposure time to apply 50%, 100%, and 200% of the recommended dose at full laser power are shown in orange. The minium limit represents the fastest exposure time, which is determined by how quickly the LabVIEW software can enable/disable the laser without missing a tick of the 8000 counts/rev centrifuge rotary encoder. Therefore, the centrifugal caster machine cannot achieve exposure times smaller than this value, and the corresponding dose values are unachievable with the current hardware and software setup. 75

4-4 A single exposure simulation for a focus of 0 microns and 26 ms exposure time. The ideal focus position of f=0 yields vertical feature sidewalls. 78

4-5 A single exposure simulation for a focus of 20 microns and 26 ms exposure time. Rounded features are characteristic of of an above focus scenario. . . 79

4-6 A single exposure simulation for a focus of -35 microns and 26 ms exposure time. Straight, tapered sidewalls are indicitive of a below focus feature. . . . 80

4-7 A single exposure simulation for a focus of -35 microns, beam tilt of 10 degrees, and 26 ms exposure time. The deviation from perpendicularity of the beam axis relative to the photoresist top surface yields an asymmetric feature . . . 81

4-8 Feature root width for a single exposure in 5 micron thick photoresist. Root width appears virtually invariant with changes to exposure time (dose) and focus. 83

4-9 Feature root width for a single exposure in 10 micron thick photoresist. Root width appears virtually invariant with changes to exposure time (dose) and focus. 83

4-10 Feature root width for a single exposure in 15 micron thick photoresist. Root width appears virtually invariant with changes to exposure time (dose) and focus. 84

4-11 Feature top width for a single exposure in 5 micron thick photoresist. Top width decreases significantly with focusing errors, though is slightly less sensitive to below focus. Focusing errors can be compensated for by increasing exposure time (dose), which minimizes dimensional sensitivity to focus. . . . 84

4-12 Feature top width for a single exposure in 10 micron thick photoresist. Top width decreases significantly with focusing errors, though is slightly less sensitive to below focus. Focusing errors can be compensated for by increasing exposure time (dose), which minimizes dimensional sensitivity to focus . . . 85

4-13 Feature top width for a single exposure in 15 micron thick photoresist. Top width decreases significantly with focusing errors, though is slightly less sensitive to below focus. Focusing errors can be compensated for by increasing exposure time (dose), which minimizes dimensional sensitivity to focus . . . 85

4-14 Feature height for a single exposure in 5 micron thick photoresist. Height decreases with deviations in focus, but is less sensitive than the top width dimension. Longer exposure times (higher doses) promote bottoming out the exposure against the SU8 substrate, and exhibit a favorable asymmetry towards below focus. 86

4-15 Feature height for a single exposure in 10 micron thick photoresist. Height decreases with deviations in focus, but is less sensitive than the top width dimension. Longer exposure times (higher doses) promote bottoming out the exposure against the SU8 substrate, and exhibit a favorable asymmetry towards below focus. 86

4-16 Feature height for a single exposure in 15 micron thick photoresist. Height decreases with deviations in focus, but is less sensitive than the top width dimension. Longer exposure times (higher doses) promote bottoming out the exposure against the SU8 substrate, and exhibit a favorable asymmetry towards below focus. 87

4-17 An overlapping exposure simulation for a focus of -35 microns and an exposure offset of 6 microns. The 26 ms exposure refers to each individual exposure, indicating that this feature require a net 52 ms exposure time. 89

4-18 Feature top width for two exposures of 39 ms each, in 15 micron thick photoresist. Top width linearly grows with increase axial offset at a rate of 1 micron per micron. Null width indicates that the exposure did not permeate full resist thickness. 90

4-19 Displacement of the linear stage (change in focus) over the axial positions corresponding to tool length. The data presented are mean values recorded from ten trials. Error bars represent one standard deviation above and below the mean value. The data exceed the flatness tolerance of the polished surface used for optical measurement, clearly showing the presence of error motions impacting laser focus. 92

4-20 Atomic force microscopy (AFM) of a PDMS mold of the SU8 surface. Only a few nanometers of roughness suggest that the planarizing layer is indeed flat after casting. 93

4-21 Axial temperature distribution of the centrifuge drum at thermal equilibrium. Temperature varies over 5°C. The open end of the drum (near an axial position of 80 mm) is substantially warmer than the mounted end of the drum (near an axial position of 140 mm). 94

4-22 Two thermal transisent trajectories to the softbake set point of 110°C. The two trials both take minutes to rise, though the second extends about three minutes longer. The variation shows that the patterning layer cast in the second trial received about 25% more energy input due to the transient process. 95

4-23 Defects in the AZ 9260 photoresist using Nietner's tool fabrication process [11]. Bubbles emerged during the PDMS casting step. Removal of the tool introduced additional resist peel-off defects in the exposed (white) and unexposed regions (amber). 98

4-24 Photoresist peel-off and bubble defects in the PDMS tool cast in Figure 4-23. The photograph shows one-half of the clear, PDMS tool against a white background. 99

4-25 Microscopic images of bubbles and peel-off defects replicated by the PDMS tool. 99

4-26 A schematic demonstrating the setup for imparting a focus shift. A change in focus, f over the axial length of the drum, specifically over the patterned area of the stamp between $x = 90$ mm and $x = 130$ mm, was created by tilting the drum an angle ψ through shimming the kinematic couplings for vertical displacements δ_1 and δ_2. The fixed laser focus should result in $f = 0$ at the axial center of the drum, and $\pm f/2$ at opposite ends. 108
4-27 Cross sections of above and below focus feature in a PDMS tool. 108
4-28 Cross sections of two features in a PDMS tool, from the same axial traverse that should have experienced a 150 μm difference in laser focal point position. However, the features are very similar in size and shape. 110

5-1 A general schematic of the photoresist pattern, and subsequent stamp pattern. Four feature sets, A, B, C, and D are each repeated four times over the circumference of the centrifuge and subsequent tool. Each set (such as A1, A2, A3, and A4) should theoretcally be identical and thus allows any physical circumferntial variation to be noted should it arise. Note that 0 and 8000 centrifuge counts correspond to 0° and 360° respectively, giving rise to the centrifuge rotation direction ω. 113
5-2 A generalized schematic of section A, consisting of 100 circumferential (θ-oriented) lines of 100 μm axial (x-oriented) pitch. The features, shown as the expected shape from simulation in an advantageous below-focus configuration, are created in the photoresist mold through single exposures and yield the resulting PDMS tool shape. 114
5-3 A generalized schematic of section B, consisting of 50 circumferential (θ-oriented) lines of 200 μm axial (x-oriented) pitch. The features, shown as the simulated shape in an advantageous below-focus configuration, are created in the photoresist mold through single exposures and yield the resulting PDMS tool shape. 114

5-4 A generalized schematic of section C, consisting of 50 circumferential (θ-oriented) lines of 200 μm axial (x-oriented) pitch. The features, shown as the simulated shape in an advantageous below-focus configuration, are created in the photoresist mold through two partially overlapping exposures and yield the resulting PDMS tool shape. Exposure offsets of 5, 10, 15, 20, and 25 μm, were tested 10 times each and were expected to form wider features than A and B. 115

5-5 A generalized schematic of section D, consisting of 10 circumferential (θ-oriented) line segments of varying length of 200 μm axial (x-oriented) pitch. The features, shown as the simulated shape in an advantageous below-focus configuration, are created in the photoresist mold through eleven partially overlapping exposures and yield the resulting PDMS tool shape. Exposure offsets of 5, 10, 15, 20, and 25 μm (fixed value for each 11-exposure feature), were tested twice each and were expected to form features with a significant axial dimension, some even appearing as axially-oriented lines.. 116

5-6 The measured centrifuge drum temperature for baking steps during photoresist casting of the experimental patterning layer. The casting procedure calls for a 30 minute post apply bake (PAB) at 60°C followed by a soft bake for 3 minutes and 20 seconds at 110°C. In addition to displaying these bakes, the plot also shows the rise trajectory to each bake and the cool down trajectory to ambient temperature. All baking steps, except cool down, are performed using closed loop temperature control. 118

5-7 Photographs of the centrifuge interior during the patterning layer casting process for the experimentation tools. 119

5-8 Photographs of the S1 and S2 PDMS tools, single layer and dual layer respectively, created for experimentation. Note how easily dust particles adhere to the PDMS. 120

5-9 Sample photographs of features in a PDMS tool with labeled dimensions (top width, root width, and height). Two extreme feature geometries are shown in cross section to demonstrate the measurement ordinates. Note that root width is always measured from the widest locations, ignoring an undercut if present. 122

5-10 Photographs of the AZ 9260 photoresist patterning layer with labeled dimensions for measuring features. The damaged patterning layer compares the aesthetic of AZ 9260 and SU8 in the same image, showing that a bottomed-out feature should have clear top width with a well defined border. Cross section interpretations suggest two types of features through the extend of dark grey portions of the image (the sidewall). Note the dashed red lines indicating other sidewall geometries, since the 2D image makes it impossible to exactly infer the slope shape. 124

5-11 An example original and the subsequently processed (binarized) contact image at 6.30 N of measured open loop force. Corresponding lines are labeled and the processing algorithm clearly identifies and maintains defects in line continuity. 125

5-12 Contact data corresponding to the image(s) in Figure 5-11. Note that CL 1 representents Contact Line 1, and so on. For this image, line widths are extremely tight, $< 1\ \mu$m, suggesting that features dimensions vary minimally over the area of the image. 126

5-13 An example original and subsequently processed (binarized) print image at a mean closed loop print force of 7.41 N. Corresponding lines are labeled and Merian's processing algorithm clearly identifies and maintains defects in line continuity [6]. 127

5-14 Print data corresponding to the image(s) in Figure 5-13. Note that PL 1 representents Print Line 1, and so on. For this image, line widths data encompass a large range, $\approx 5\ \mu$m. 128

5-15 Photographs of the photoresist at location A1 throughout the tool-making process. Note the obvious change between Figures 5-15a and 5-15b as if the PDMS casting slanted a previously vertical sidwall. There is no obvious alteration to the photoresist between casting tool S1 (Figure 5-15b) and tool S3 (Figure 5-15c), minor root width edge roughness and defects are consistent between the two. Both S1 and S3 molds also exhibit bottomed out features, where the exposure propogated all the way through to the SU8 planarizing layer. 132

5-16 Photographs of the photoresist at location A2 throughout the tool-making process. There are no apparent changes between development (Figure 5-16a) and subsequent tool castings (Figure 5-16b and Figure 5-16c). Features obviously bottom out and mild edge defects are visible and consistent between images. 134

5-17 Photographs of the photoresist at location A3 throughout the tool-making process. There are no apparent changes between development (Figure 5-17a) and subsequent tool castings (Figure 5-17b and Figure 5-17c). Features obviously bottom out and mild edge defects are visible and consistent between images. 136

5-18 Photographs of the photoresist at location A4 throughout the tool-making process. There are no apparent changes between development (Figure 5-18a) and subsequent tool castings (Figure 5-18b and Figure 5-18c). Features obviously bottom out and mild edge defects are visible and consistent between images. Most notable, the roughly vertical *scar* in the middle of this resist section is still visisble after each process step. 138

5-19 Photographs of the photoresist at location B1 throughout the tool-making process. Note the obvious change between Figures 5-19a and 5-19b as if the PDMS casting slanted a previously vertical sidewall. There is no obvious alteration to the photoresist between casting tool S1 (Figure 5-19b) and tool S3 (Figure 5-19c), and minor root width edge roughness and defects are consistent between the two. Both S1 and S3 molds also exhibit bottomed out features, where the exposure propogated all the way through to the SU8 planarizing layer. 140

5-20 Photographs of the photoresist at location B2 throughout the tool-making process. There are no apparent changes between development (Figure 5-20a) and subsequent tool castings (Figure 5-20b and Figure 5-20c). Features obviously bottom out and mild edge defects are visible and consistent between images. 142

5-21 Photographs of the photoresist at location B3 throughout the tool-making process. There are no apparent changes between development (Figure 5-21a) and subsequent tool castings (Figure 5-21b and Figure 5-21c). Features obviously bottom out and mild edge defects are visible and consistent between images. 144

5-22 Photographs of the photoresist at location B4 throughout the tool-making process. There are no apparent changes between development (Figure 5-22a) and subsequent tool castings (Figure 5-22b and Figure 5-22c). Features obviously bottom out and mild edge defects are visible and consistent between images. 146

5-23 Photographs of PDMS tool S1 at location A*. Note the near-trapezoidal cross section feature geoemtry with approximately flat tops. Crisp lines and edges are evident in the top view. 149

5-24 Photographs of PDMS tool S3 at location A*. Again, note the near-trapezoidal cross section feature geoemtry with approximately flat tops, and crisp liines in the top view. 150

5-25 Photographs of PDMS tool S1 at location B*. Note the near-trapezoidal cross section feature geoemtry with approximately flat tops, as seen in A*. Crisp lines and edges are evident in the top view as well. 151
5-26 Photographs of PDMS tool S3 at location B*. Again, note the near-trapezoidal cross section feature geoemtry with approximately flat tops. and crisp liines in the top view. 152
5-27 Photographs of the photoresist at location A* throughout the tool-making process. There are no apparent changes between casting tool S1 (Figure 5-27a) and tool S3 (Figure 5-27a). Although the features in the A* PDMS looked most ideal, the corresponding photoresist location may not look the best. Note the lack of colorlessness of the bottomed out region compared to A1 (Figure 5-15b). 153
5-28 Photographs of the photoresist at location B* throughout the tool-making process. There are no apparent changes between casting tool S1 (Figure 5-28a) and tool S3 (Figure 5-28a). 154
5-29 Measured A* and B* feature top widths in PDMS tools and in the photoresist patterning layer. Data presented are mean values. Error bars span one standard deviation above and below. 155
5-30 Measured A* and B* feature root widths in PDMS tools and in the photoresist patterning layer. Data presented are mean values. Error bars span one standard deviation above and below. 156
5-31 Measured A* and B* feature heights in PDMS tools. Data presented are mean values. Error bars span one standard deviation above and below. 156
5-32 Unprocessed images of A* and B* contact regions at measured open loop forces was 4.91 N and 4.84 N respectively. The spots and discontinuities are dust particles. 158
5-33 A schematic showing the theoretical compressed tool cross section corresponding to contact. 159

5-34 Mean contact line width as function of the measured applied force for single exposure lines of differerent axial pitches (features A and B). The contact response of A* is fit with $y = 0.97x + 17.55$ with $R^2 = 0.98$. B* is fit with $y = 1.52x + 18.52$ with $R^2 = 0.96$. 160
5-35 Measured A* and B* feature top widths in PDMS tools and in the photoresist patterning layer, and top width estimations from contact imaging. Data presented are mean values. Error bars span one standard deviation above and below. Note that all data belong to the same continuous distribution and therefore represent the same measurement. 161
5-36 Sample print and contact images of A* features using tool S4. 163
5-37 A histogram of print and contact line widths for A* features. The two data sets exhibit a ≈ 5 μm mean shift. 163
5-38 Photographs of the photoresist at location C1 throughout the tool-making process. Note the obvious change between Figures 5-38a and 5-38b as if the PDMS casting slanted a previously vertical sidwall. This same phenomenon was observed for A1 and B1 in Figures 5-15 and 5-19. There is no obvious alteration to the photoresist between casting tool S1 (Figure 5-38b) and tool S3 (Figure 5-38c), minor root width edge roughness and defects are consistent between the two. Both S1 and S3 molds also exhibit bottomed out features, where the exposure propogated all the way through to the SU8 planarizing layer. 167
5-39 Photographs of the photoresist at location C2 throughout the tool-making process. There are no apparent changes between development (Figure 5-39a) and subsequent tool castings (Figure 5-39b and Figure 5-39c). Features obviously bottom out and mild edge defects are visible and consistent between images. 169

5-40 Photographs of the photoresist at location C3 throughout the tool-making process. There are no apparent changes between development (Figure 5-40a) and subsequent tool castings (Figure 5-40b and Figure 5-40c). Features obviously bottom out and mild edge defects are visible and consistent between images. 171
5-41 Photographs of the photoresist at location C4 throughout the tool-making process. There are no apparent changes between development (Figure 5-41a) and subsequent tool castings (Figure 5-41b and Figure 5-41c). Features obviously bottom out and mild edge defects are visible and consistent between images. Most notably, the near-vertical scratches are present in all three images. . . 173
5-42 Photographs of the photoresist at location D1 throughout the tool-making process. There are no apparent changes between development (Figure 5-42a) and subsequent tool castings (Figure 5-42b and Figure 5-42c). Features obviously bottom out, exhibit steep (near-vertical) sidewalls, have mild edge defects, and are surrounded by small bubble defects. These properties are present in all three images. 175
5-43 Photographs of the photoresist at location D2 throughout the tool-making process. There are no apparent changes between development (Figure 5-43a) and subsequent tool castings (Figure 5-43b and Figure 5-43c). Features obviously bottom out, exhibit steep (near-vertical) sidewalls, have mild edge defects, and are surrounded by small bubble defects. These properties are present in all three images. 177
5-44 Photographs of the photoresist at location D3 throughout the tool-making process. There are no apparent changes between development (Figure 5-44a) and subsequent tool castings (Figure 5-44b and Figure 5-44c). Features obviously bottom out, exhibit steep (near-vertical) sidewalls, have mild edge defects, and are surrounded by small bubble defects. These properties are present in all three images. 179

5-45 Photographs of the photoresist at location D4 throughout the tool-making process. There are no obvious changes between development (Figure 5-45a) and subsequent tool castings (Figure 5-45b and Figure 5-45c). Features obviously bottom out, exhibit steep (near-vertical) sidewalls, have mild edge defects, and are surrounded by small bubble defects. These properties are present in all three images, though the bubbling does appear to grow slightly in size between removing tool S1 and removing tool S3. 181

5-46 Photographs of PDMS tool S3 at location C*. Note the more rounded cross section feature geometry with than A and B features. 185

5-47 Photographs of PDMS tool S3 at location C*. Note the more rounded cross section feature geometry with than A and B features. 186

5-48 Photographs of PDMS tool S1 at location D*. Note the trapezoidal-rectangular cross section feature geoemtry with extremely flat tops. Crisp lines and edges are evident in the top view. Only the features constructed with 25 μm exposure offset exhibit axially-oriented characteristics, in the form of partially formed line segments. In all cases, only the first exposed area of the photoresist developed into a full feature, of notably different geometry than A, B, or C features. 189

5-49 Photographs of PDMS tool S3 at location D*. Note the trapezoidal-rectangular cross section feature geoemtry with extremely flat tops. Crisp lines and edges are evident in the top view. Only the features constructed with 25 μm exposure offset exhibit axially-oriented characteristics, in the form of partially formed line segments. In all cases, only the first exposed area of the photoresist developed into a full feature, of notably different geometry than A, B, or C features. 192

5-50 Photographs of the photoresist at location C* throughout the tool-making process There are no apparent changes between casting removing tool S1 and tool S3. While the C* PDMS looked most ideal, the corresponding photoresist location may not look the best. NOte the lack of colorlessness of the bottom out region compared to C3 (Figure 5-40b). 194

5-51 Photographs of the photoresist at D* locations throughout the tool-making process. In all cases, the feature clearly bottoms out against the SU8 has a steep sidewall and some minor edge defects. These properties are present both after casting and removing tool S1 and S3. However, the nearby bubbles do appear to grow in size and in the case of features constructed with 25 μm offsets, the only partially formed line segments appear to smooth out over multiple castings. 197
5-52 Unprocessed images of B* and C* contact regions at a measured force of 4.9 N. C* contact widths are noticeably larger. 199
5-53 Unprocessed images of D*15 and D*25 contact regions at a measured force of 4.9 N. 199
5-54 Unprocessed images of B3 and C3 prints at a measured print force of 4.9 N. C3 print widths are noticeably larger. Present roof collapse indicates that this was not the optimal print load, but a difference in widths is still noticeable. As with contact in Figure 5-52, C* print widths are much larger than B* at the same loading conditions. 201
5-55 A schematic for interpretting prints with roof collapse. Sparse features on a tool loaded with relatively high force will exhibit roof collapse. In this failure mode, PDMS material between features bulges towards the print/contact interface. 201
5-56 An unprocessed print image of D features at 4.9 N measured force. The printed shape agrees qualitatively with the contact geometry at the same applied load. 202
5-57 A schematic demonstrating how D features fromed in the photoresist (left) versus the intended photoresist geometry (right). 203

6-1 Expected feature geometry from contact analysis. Left: For a perfectly flat top feature, initially only the top width comes into conctact (blue, W(0)) at 0 N of force. As F increases, PDMS is displaced into the surface and the feature effectively widens to W(F) as it compresses (red). Right: For an approximately flat top feature, only a small portion of the approximate top width is in contact at F = 0 (blue). After applying a small force dF, or through adhesion, the PDMS conforms and the top width is achieved (green, W(0)). As F is increased again, the feature widens to W(F) (red). 209

List of Tables

3.1 A list of exposure inputs. 57

3.2 Part name, number, and supplier info for the optics shown in Figure 3-8. . . 63

3.3 Manufacturer reported specifications of the Mitutoyo 5x objective lens. The depth of focus defines an arbitrary distnace of moderate focus at which the image information is still discernible. This lens allowed for sufficiently viewing nominally 15 μm tall photoresist features. The optical resolution and field of view were adequate for extracting dimensional data over a large number of features. 63

4.1 Values of fixed parameters in the numerical simulation. A spatial step size of 0.25 μm is so small that the resist fully bleaches once exposed, signifying no PAC gradient across the element [37]. A resist width of 30 μm was selected such that M remained unity at the x-boundaries for all tested exposure scenarios, allowing for Equation 4.9 to be applied over the entire photoresist area experiencing changes in PAC concentration. 76

4.2 Value ranges (minimum, maximum, and step size) of the adjustable simulation input parameters. Focus is adjusted between -50 μm and 50 μm at 5 μm steps. Resist thickness of 5 μm, 10μm, and 15 μm. Values of f greater than 0 are hereon refered to as above focus, while values of f less than 0 are called below focus. Ideal focus is achieved when f is equal to 0. 76

4.3 Simulation times of interest, the associated centrifuge speed during writing, and the corresponding exposure dose. Each dose was studied for each focus position and resist thickness tested. 77

4.4 procedure 102

5.1 Exposure and general feature information for each tool section. Axial Pitch and Features Written denote the number of each feature and its linear axial density written per each section (1 cm in length). Laser Power and Centrifuge Speed control the exposure dose supplied to the photoresist. The reported dose denotes the theoretical dose per single exposure (not cumulative in the case of an overlap) at the given settings. 112

5.2 An outline of the experimentation procedure. 129

5.3 Axial and circumferential positions of the patterning layer that were imaged for photoresist repeatability tests of features created using single exposures. 130

5.4 Axial and circumferential locations of ideal features A* and B*. 149

5.5 Axial and circumferential positions of the patterning layer that were imaged for photoresist repeatability tests of features created using overlapping exposures. 165

5.6 Axial and circumferential locations of ideal features C* and D*. D features varied greatly in cross section shape with the amount of overlap. D*5 is a feature constructed with 5 μm offset in exposures. D*15 uses a 15 μm offset in exposures. D*25 has a 25 μm offset. Finally D*x is an additional feature constructed with 25 μm offset in exposures but viewed in a different location to provide extra insight into overlapping exposures. The dashed nature of D features required multiple imaging locations, each best catered to the specific microscopy type. Circumferential positions labeled (a) were used for imaging the photoresist, positions (b) represent PDMS tool cross sections, while (c) locations were used for creating top views of the PDMS tools. 183

Chapter 1

Introduction

1.1 Overview of Microcontact Printing

Microcontact printing (μCP) is type of soft lithography developed by Xia and Whitesides of Harvard University [1]. The process creates sub-micron scale patterns on a substrate through contact-based ink transfer using an elastomeric printing stamp. Specifically, the patterned stamp deposits a self-assembling molecular monolayer to the substrate in regions of contact. Figure 1-1 presents an overview of the process. Stamps are typcially cast using polydimethysiloxane (PDMS) and have been shown to replicate features down to 30 nm [2]. Alkanethiols are common SAM inks for forming patterns on gold films through subsequent etching of the substrate.

This soft lithography process has demonstrated great potential as a top candidate for creating nano-patterned surfaces [3]. However, μCP is most frequently performed in a plate-to-plate process at small scales [4]. Roll-to-roll systems for large area, high rate printing of flexible films has been successfully demonstrated. Newspaper printing presses, for example, represent a high throughput roll based printing process. It has also recently been shown that successful microcontact printing can be performed at speeds as high as 2 m/s [5]. Implementing microcontact printing in a roll-to-roll setup is therefore a promising path towards converting μCP to a high throughput manufacturing method. Consequently, roll-to-roll microcontact printing, the stamps, and the associated inspection processes at laboratory scale are the focus of this research.

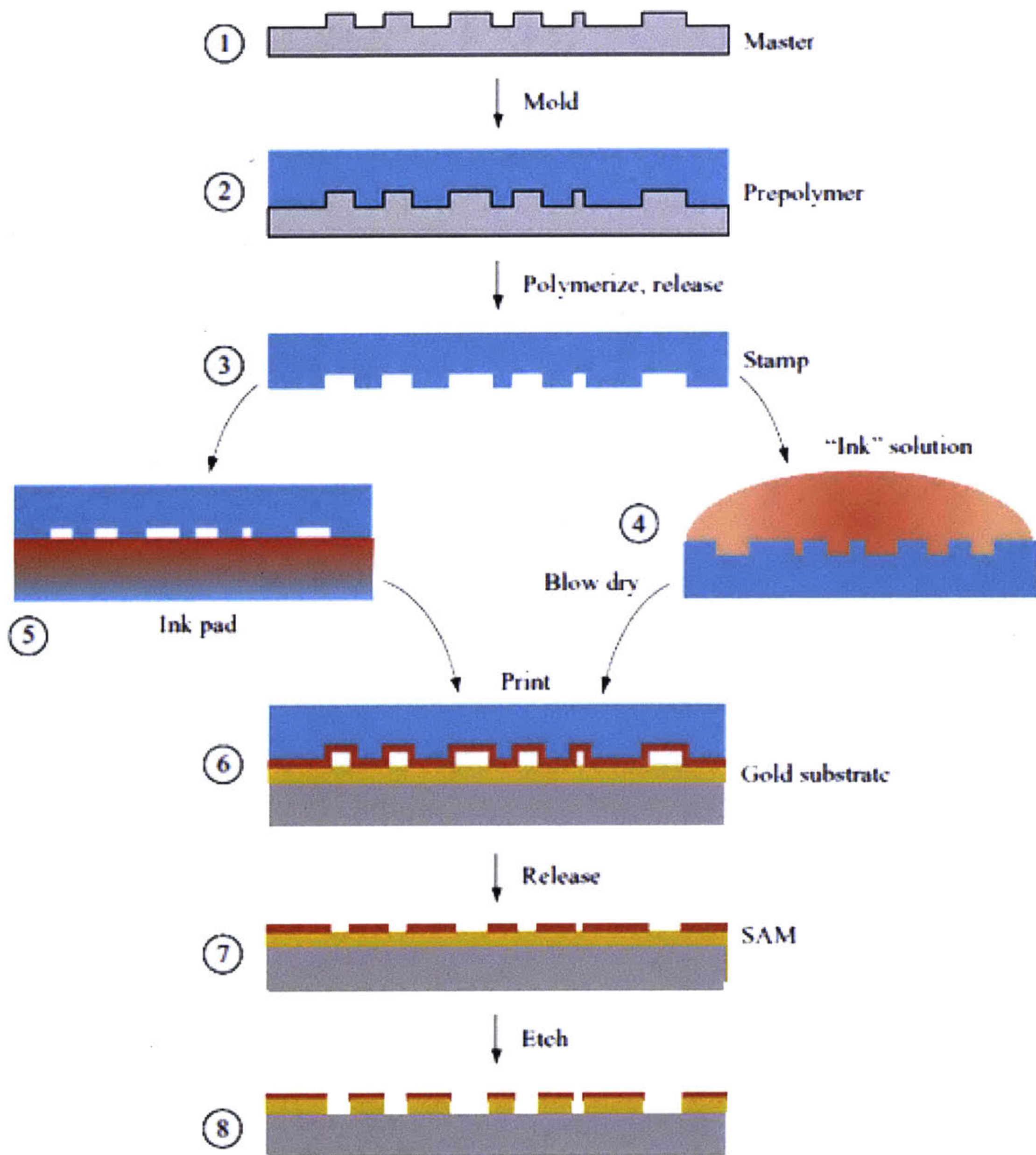

Figure 1-1: An overview of the μCP process [6]. 1) A master pattern is created using lithography techniques. 2) PDMS elastomeric resin is poured over the mold. 3) The cured PDMS is removed from the master, yielding the patterned stamp. 4,5) The stamp is inked and dried. 6) The stamp contacts the substrate. 7). The SAM ink is transfered to the substrate. 8) Etching processes remove uncovered portions of the substrate, thereby replicating the stamp pattern.

1.2 Potential Applications

Khan et al. [7] present a thorough review and comparison of various contact and non-contact processes for printing electronics. The feasbilitiy, drawbacks, and benefits of operating each in a roll-to-roll system for high production rates is also addressed. Of the analyzed printing processes, microcontact printing offers significant capital savings for patterning small features over large areas. Furthermore, the printing process is not limited to rigid or planar substrates [3]. As such, μCP has the potential to become a standardized manufacturing process. Suitable applications of μCP, as well as the pros and cons of competeting manufacturing processes are discussed below [8] [9].

Gravure and inkjet printing are perhaps the two most direct competitors to continuous roll-to-roll μCP. Inkjet is a non-contact form of printing in which droplets of ink are sequentially deposited on to a substrate. The advantageous location selectivity is mirrored in μCP by the rapid manufacturing of PDMS stamps using photoresist molds created from maskless, direct-write lithography. In this way, the image pattern is unrestricted with little to no start up costs for each new desired print geometry. As a serial process, inkjet is signifanctly more limited in production rate than μCP.

Gravure printing uses a cylindrical, metal tool with high start up costs to contact a substrate and transfer ink from tool groove through capillary action. Each new pattern involves signifacant lead time and tooling costs, but roll-to-roll printing at high rates is the manufacturing standard for this process. The elastomeric stamps of μCP could overcome the lead time and cost downsides of gravure, but registration difficulties of PDMS compared to metal are a severe drawback [7]. As the research in μCP develops the technology, applications may emerge requiring the benefits of high-rate elastomeric contact priting over other existing printing processes.

Flexible electronics and large area sensors are two key windows where μCP could claim a share of the printed electronics market. Solar panels in particular, could significantly benefit from such technologies. In desert environments in particular, dust build-up is a common source of energy loss [8]. Efficiencies can decrease up to 30% (the oberserved power output decrease is used to detect the dust build-up), and water, a limited desert resource, is

frequently used to remove the disruptive particulate [9]. Large area μCP printed electrodes could address both the dust detection and dust rejection challenges. Mazumder et al. [9] propose a rejection solution using electrodynamic screens. Indium tin oxide electrodes on a PET substrate, when supplied with three phase power, were shown to transport dust and inhibit deposition. The proposed electrode structure had 100 μm wide features spaced 1000 μm apart. The use of ink and substrate materials common to μCP, geometric scales easily achievable by μCP, and demanding such a large area of small coarsly spaced patterns, makes this application a prime candidate.

1.3 Scale-Up of Microcontact Printing

Little outside research has been conducted to solve challenges associated with manufacturing scale-up. The most prevalent barriers to scale up currently being addressed include in-process measurements of prints, precision control of the contact region for printing stamps of different patterns, and the creation of uniform quality, arbitrarily patterned tools. Petrzelka and Hardt [10], and Nietner and Hardt [11] demonstrated the fabrication of continuous cylindrical tooling through a novel centrifugal casting machine using direct-write lithography to create the master mold. Libert developed a precision printhead assembly for a laboratory-scale roll-to-roll setup designed by Libert [12] and Nill [13]. Bageant and Hardt [14] proposed a method for implementing force control for precision manipulation of contact using Libert's setup. Merian [6] developed a continuous inking system, and successfully demonstrated printing on the roll-to-roll setup. Finally Merian et al. [15] demonstrated a proof-of-concept controlled condensation method for inspecting pre-etched prints.

1.4 Focus of Thesis

The focus of this work addresses the tooling challenges of moving towards high-rate, large area, microcontact printing on a flexiblle substrate in a roll-to-roll system. At the time of start of this thesis, cylindrical tooling could be manufactured with simple patterns, continuous inking and open-loop printing were demonstrated, precision feedback contract control

was in progress, and in-situ measurement techniques were under investigation. However, tool features were limited to complete circumferential lines of about 20 μm width. Furthermore, significant variation in tool quality was observed [6] [16]. Scaled-up, large area microcontact printing would require uniform tool geometry and tools with diverse feature patterns and shapes spread across the tool surface.

Therefore, the fabrication of arbitarily patterned seamless cylindrical tooling and the development of new measurement instruments and techniques for qualifying PDMS stamps were the interests of this thesis. The manufacturing process window for laser scribing more complicated lithography patterns in a cylindrical setting was investigated. Upgrades to the centrifugal casting machine were performed to permit spatially-arbitrary exposure of the photoresist mold. Non-destructive measurement techniques for analyzing the photoresist mold and resulting stamps were developed. Finally, experiments were conducted to test the feasibility of manufacturing and measuring tools of diverse feature patterns.

THIS PAGE INTENTIONALLY LEFT BLANK

Chapter 2

Prior Work

2.1 Fundamentals of Soft Lithography

Microcontact printing is a form of soft lithography developed by the Whitesides group at Harvard University [1]. Soft lithography techniques emerged from the limitations of conventional photolithography for creating micro and nano-scale patterns (30 nm - 100μm). μCP specifically utilizes a relief-patterned elastomer stamp to transfer ink onto a substrate. This method has many advantages, most direclty related to many material choices for inks and substrates. Inks can be specifically engineered to created desirable surface properties on the susbtrate. In some cases even used to seed 3D topologies. Substrates are also not required to be planar. All in all, the development of μCP and soft lithography techniques in general expanded micro and nano patterning capabilities.

The original μCP process cast a PDMS stamp on a master patter, photolithographically patterend SU8 photoresist on a silicon wafer. Alkanethiol ink subsequently coated the PDMS tool, which was then brought into contact with a gold coated susbstrate. Thus, the patterned substrate reflected the PDMS stamp geometry. Liquid etching of the print removed gold not covered (protected) by the printed pattern, resulting in the final print. Biebyuck et al. [17] improved the process to reliabily print geometries smaller than 100 nm in size.

Reviews of numerous μCP applications and current field technologies are avaible [3]. Other forms of soft lithography are also well documented [1].

2.2 Inking

Microcontact printing is commonly performed with molecular inks of self assembling monolayers (SAMs). The inks are chains of organic molecules with functional groups at the head and tail of the chain. The head group is designed to form a covalent bond with a target substrate upon contact, but does not have an affinity to other molecules or to the tail of the chain. Consequently, the SAMs bond to the substrate and self-align into a single molecular monolayer. Figure 2-1 depicts this arrangement. The tail functional groups can be engineered for specific monolayer properties.

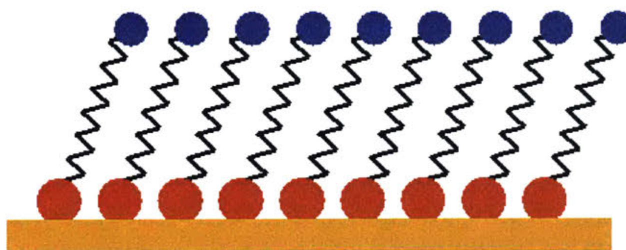

Figure 2-1: A generalized schematic of an SAM on a substrate [6]. The head group (red) bonds to the substrate (orange). The molecular chains neatly align such that the surface properties reflect those of the tail group (blue).

Alkanethiols are one type of SAMs with advantageous properties for μCP. When a PDMS stamp coated in dried alkanethiol ink is brought into contact with a gold substrate, the ink is absorbed by the gold surface and self assembles. Contact time can be as short as 1 ms [18]. Because only the contacted substrate regions should have absorbed ink, pattern replication of the tool in prints is very accurate. Lastly, dried alkanethiols diffuse into PDMS, making for simple re-inking of stamps [19]. Therefore, printing of alkanethiols on gold substrates have become a common μCP method. Merian [6] successfully used one such alkanethiol, hexadecanethiol (HDT), to continuously ink and print on a gold-coated polythylene terephthalate (PET) substrate.

The ink selection for μCP is not limited to alkanethiols. Liquid inks are common in printed electronics applications, for ease of creating conductive traces by printing with conductive inks on a variety of insulated substrates. The fluid dynamics of microcontact printing with liquid inks adds a great deal of process complexity. Hale [20] studied liquid ink transfer at the micron scale, creating a process model for printing conductive inks patterns on

polymer substrates that could be used to scale-up the manufacturing process. Her work demonstrated the need for thin ink films ($\approx$ 100 nm) and continuous inking. Figure 2-2 presents an example print.

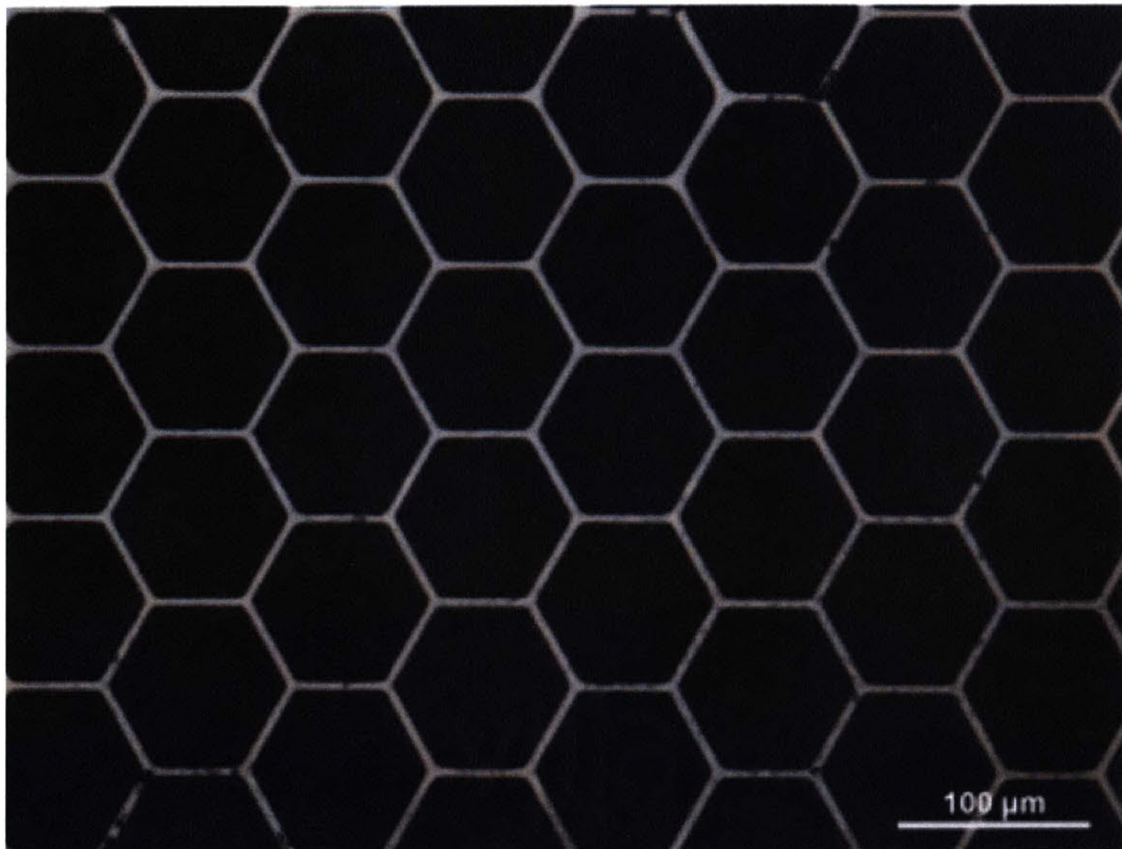

Figure 2-2: A microcontact print of liquid ink onto a polymer substrate by Hale [20]. The hexagonal lines of silver nanoparticle ink are approximately 5 μm in width.

2.3 Tooling

2.3.1 PDMS Stamps

Tools for μCP are commonly PDMS stamps. PDMS is a thermoset silicone-based elastomer that easily converts from a fluid to a solid through crosslinking. A wide variety of PDMS base-elastomers and curing agents are commericially available. For this thesis and many other works in μCP, Sylgard 184 by Dow Corning was used. The PDMS stamp is created by casting a mixture of degassed base elastomer and curing agent into a master mold.

The advantages and disadvantages of PDMS as a stamp material are discused by Xia and Whiteside [1] and Lee et al. [21]. Most significantly, PDMS easily converts to a solid with high replication accuracy, is optically transparent above thickness of 300 nm, is chemically stable, and flexible enough to conform to surface roughness without exhibiting irreversible adhesion (Figure 2-3). However, PDMS can absorb many solvents, causing swelling of the tool and stamp features. Additionally, the high elasticity and low coefficient of thermal expansion properties make the repeatable registration of PDMS features very challenging. Finally, high surface energy and low elastic modulus make the stamp features prone to collapse and problematic deformations under printing loads (Figure 2-4). Considering the spatial density of features in stamp design can overcome collapse to a certain extent. Proven methods for stiffening stamp features include casting features with h-pdms [2], and vapor desposition of surface stiffening chemicals on feature sidewalls [3].

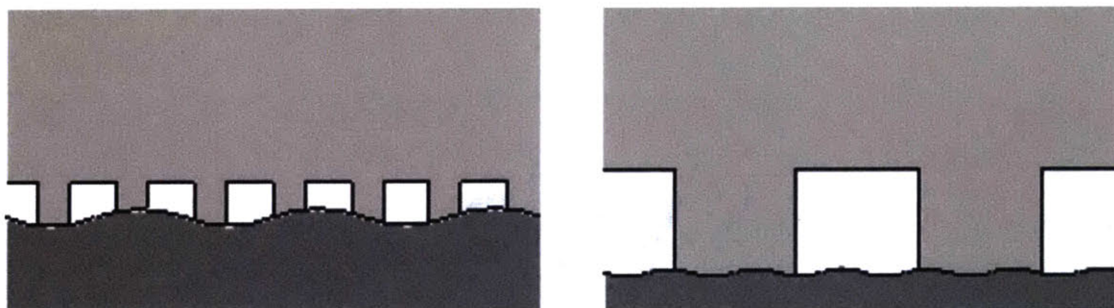

Figure 2-3: A schematic of conformal PDMS stamp contact in the presence of substrate surface roughness [6].

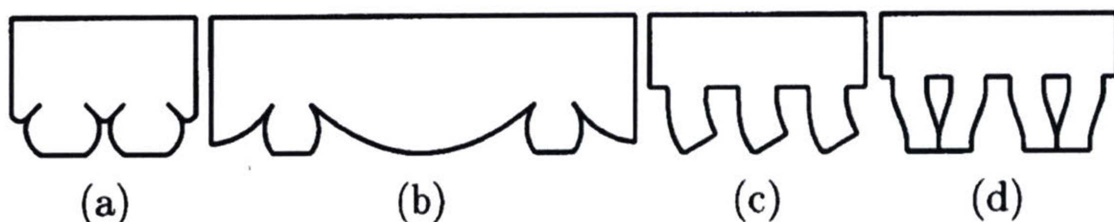

Figure 2-4: Four failure modes of PDMS stamp features determined by Petrzelka [10]. (a) sidewall collapse, (b) roof collapse, (c) buckling of features, and (d) lateral collapse.

PDMS tools for μCP can be flat or cylindrical to accomodate plate-to-plate, roll-to-plate, and roll-to-roll processes. Flat stamps are PDMS tools cast on wafer substrates patterned by conventional lithography. The resulting stamps remain planar and are used in plate-to-

plate or roll-to-plate (substrate would be rolled) printing processes. Cylindrical PDMS tools are used for roll-to-plate (planar substrate) or roll-to-roll applications. Cylindical tools can be made by wrapping flat stamp along a shaft (with an intended gap or gapless but with an unavoidable seam), or by casting a cylindrical tool. μCP began with planar stamps [1]. Planar tools have been wrapped on rollers [22]. However, wrapping results in an inevitable tool discontinuity, leading to some sort of print discrepancy every one revolution. Perzelka and Hardt [23] fabricated seamless cylindrical PDMS stamps using a completely cylindrical master mold. A seamless tool for roll based system has the potential for truly continuous large area printing. Park takes an approach similar to Petrzelka and Hardt, but uses two fused semicylindrical PDMS stamps [24]. Park's method creates a solid cylindrical tool and avoids the challenges of processing photoresist molds in a centrifugal setting. However, again the discontinuities associated with multi-part or wrapped tools prevent the formation of a continuous circumferential stamp feature.

Whitesides and many other researchers in the field cast PDMS stamps onto photoresist molds [1] [23] [25]. SU8 is a particularly common thick film resist. However, PDMS stamps can also be cast against micromachined surfaces, or even complex microcontact printed relief patterns [1] [26]. CNC milling of the master mold out of polymethyl methacrylate (PMMA) or glass are the most common alternatives to constructing the master mold from conventional photolithography techniques [7].

2.3.2 Petrzelka's Centrifugal Casting Machine

Petrzelka and Hardt [23] designed a centrifugal casting machine for fabricating seamless cyldindrical PDMS stamps. A photoresist pattern is created on the inside of a centrifuge drum with a horizontal spin axis. A PDMS tool is cast over the pattern, removed, and mounted to a steel print roller. A schematic in Figure 2-5 demonstrates this process.

The centrifugal casting machine is presented in Figure 2-6a. Direct-write, maskless lithography is performed by focusing a UV laser on the photoresist patterning layer. The spinning centrifuge and linear stage create two relative motions between the laser and photoresist (Figure 2-6b). SEMs of resulting stamp features exhibit flat tops (Figure 2-7), ideal for microcontact printing. Flat tops occured when the exposed photoresist feature bottoms out

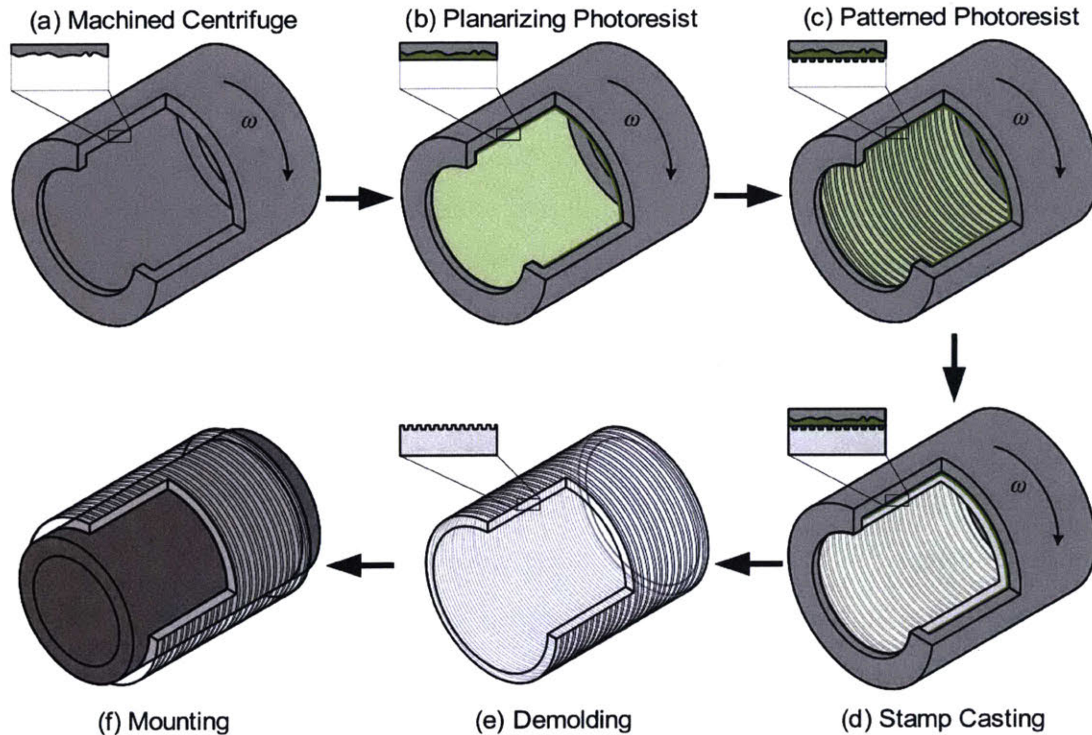

Figure 2-5: A process schematic for creating cylindrical PDMS tools [23]. A machined centrifuge drum (a) is coated in a SU8 photoresist and cross-linked to planarize the rough machined surface (b). A second photoresist coats the planarizing layer. The patterning layer is exposed and developed using maskless lithography, creating a microscopic 3D topology (c). PDMS is cast inside the centrifuge drum to form the stamp (d). The cured PDMS is removed from the centrifuge, creating a cylindrical stamp with outside surface features replicating the patterning layer (e). Finally, the PDMS stamp is mounted to a shaft for roll-to-roll printing.

against the planarizing layer.

PDMS is highly adhesive, posing challenges for placing a cylindrical PDMS tool on a roller mandrel. A custom air bearing (Figure 2-8) creates an air cushion to prevent adhesion while mounting to metal shafts. Unfortunately, the tool is susceptible to elastic straining and stamp features may become distorted.

2.3.3 SPR 220 and AZ 9260 Patterning Layer Investigation

Nietner and Hardt [16] continued the work of Petrzelka and Hardt by investigating the lithograpy process. Two positive-tone photoresists, SPR 220 and AZ 9260, were explored as better candidates for the patterning layer. Numerical simulations and experimentation

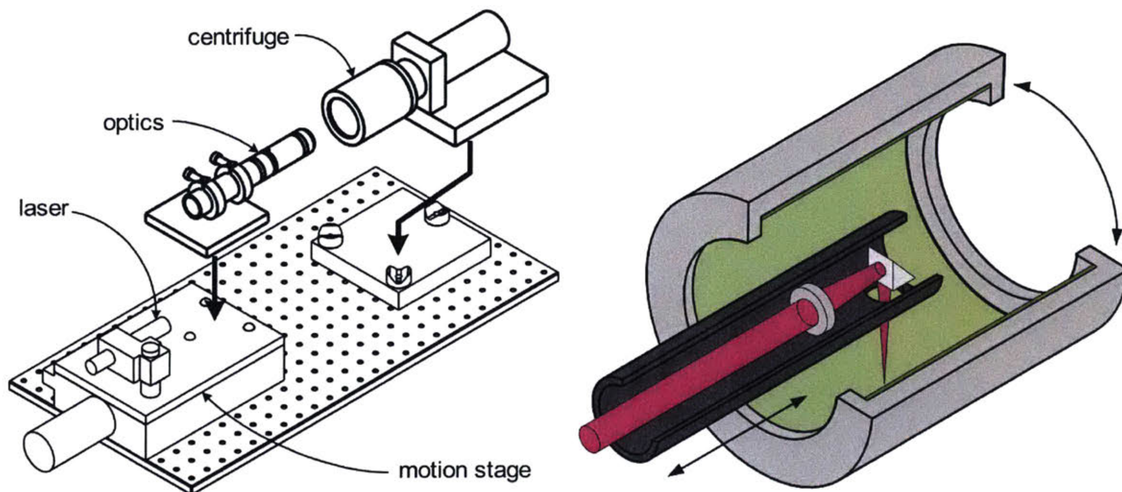

(a) An general schematic of the centrifugal casting machine. The optics and the centrifuge are mounted via kinematic couplings.

(b) A diagram of the UV laser optics exposing the photoresist patterning layer.

Figure 2-6: The centrifugal casting machine by Petrzelka and Hardt [23].

demonstrated process sensitivities impacting feature shape. AZ 9260 was selected for creating ideal feature geometries of trapezoidal shape, for which Petrzelka demonstrated high stiffness in printing [27] [28]. Nietner also proposed a fluorescent method of contact imaging using composite stamps. Figure 2-9 show microscopic and macroscopic images of the PDMS tools created using AZ 9260 of the photoresist mold. Figure 2-10 presents observed variation in geometry, hypothesized to be caused by focus variation.

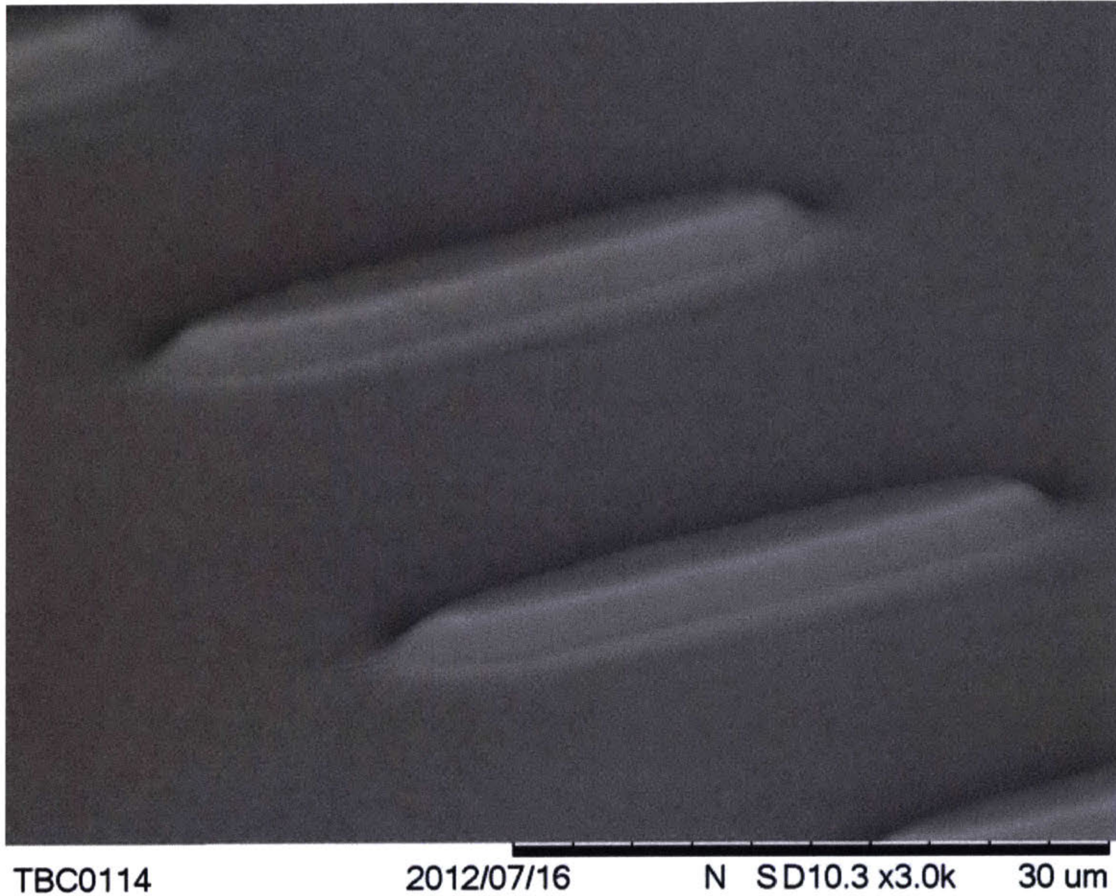

Figure 2-7: An SEM image of PDMS tool features created by Petrzelka and Hardt [23].

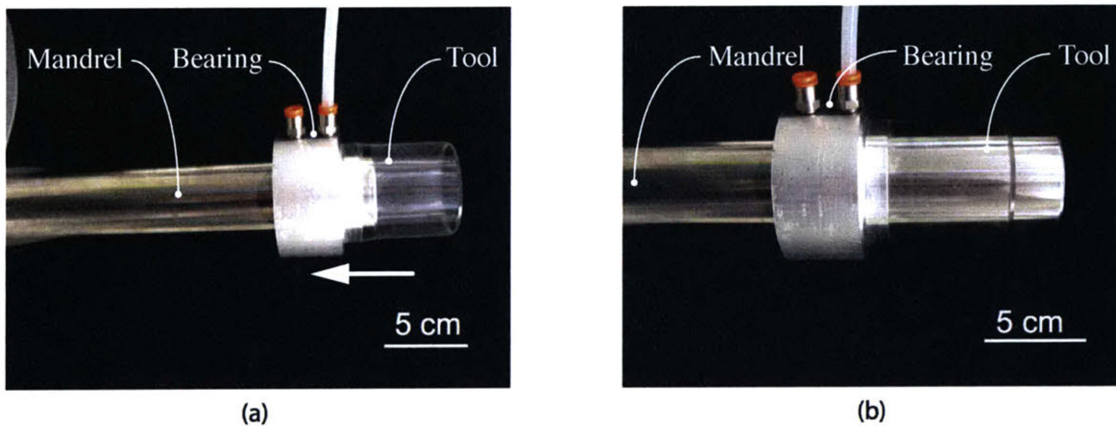

Figure 2-8: An air bearing designed by Petrzelka for mounting cylindircal tools to metal shafts [10]. A cushion of air prevents adhesion of PDMS to the roll allowing the stamp to be smoothly transferred from one end of the roll (a) to the ideal mounting position (b). Once the stamp is properly located, the air bearing is disabled, and adhesion holds the PDMS tool in place.

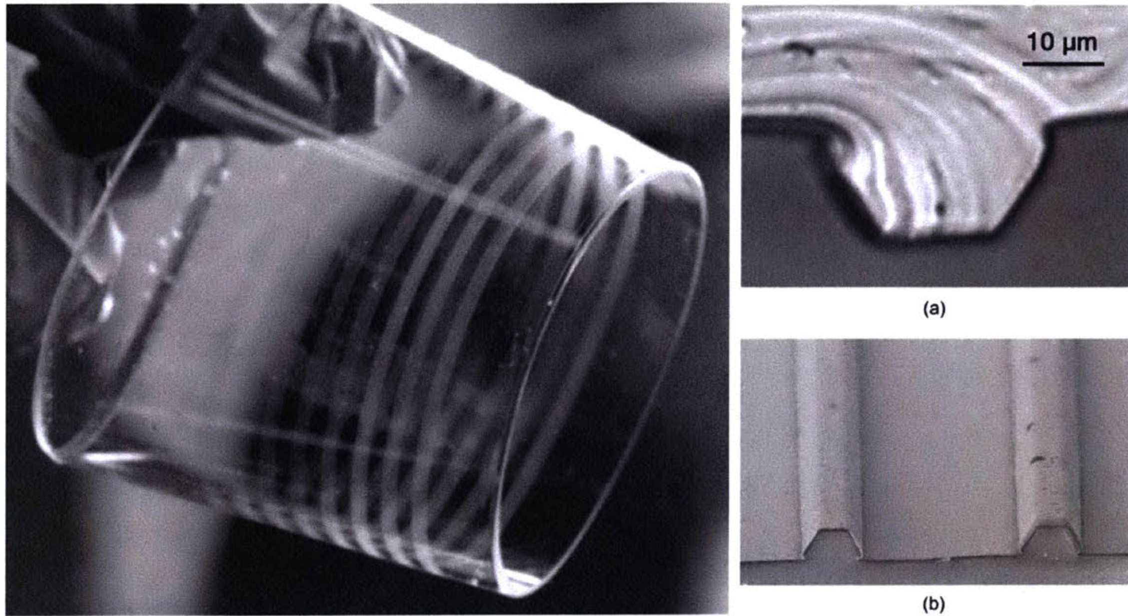

(a) A PDMS stamp with 1mm bands of features.

(b) A cross section of a feature in PDMS (a). An SEM image of features in PDMS (b).

Figure 2-9: Photographs of PDMS stamps and features created by Nietner [16].

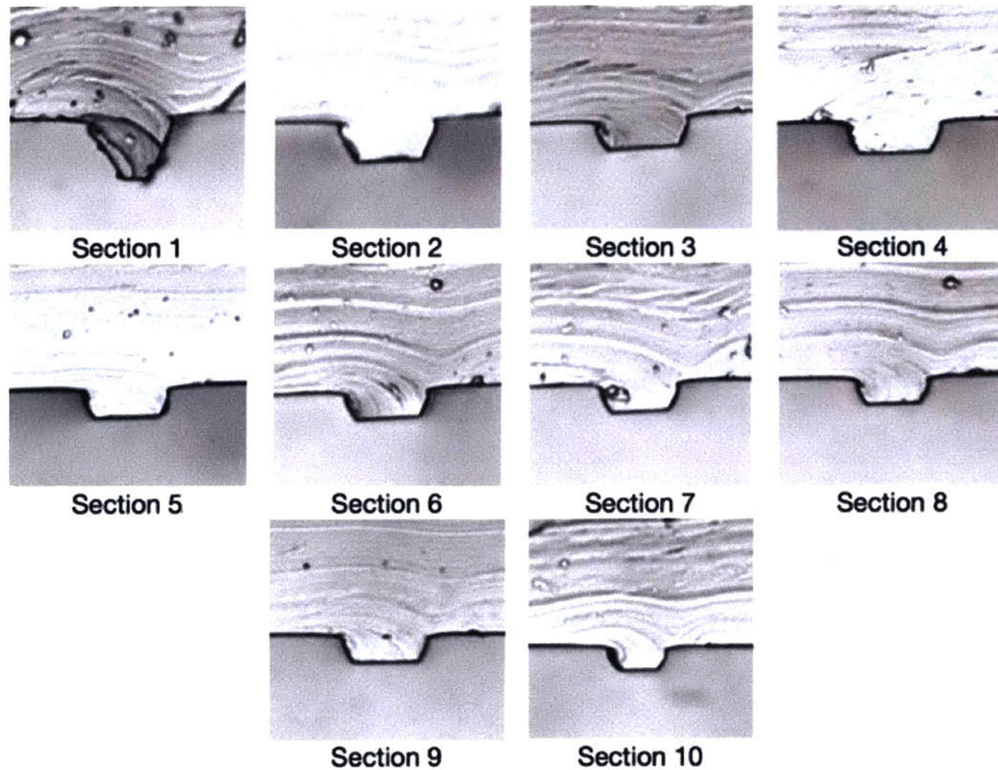

Figure 2-10: Stamp feature variation at a fixed centrifuge speed of 2 rev/s [16].

2.4 Printing

2.4.1 The Petrzelka Machine

Petrzelka investigated roll-based printing of the novel, seamless, cylindrical stamps using a custom roll-to-plate microcontact printing machine (Figure 2-11) [10]. The substrate, applied to a linear stage, was translated beneath the stamp, which was free to rotate. Unlike plate-to-plate μCP, this process continuously varied the contact region between the tool and substrate. Petrzelka's in-process contact inspection during experimentation with displacement and impedence control demonstrated the need for precision control to manipulate the contact region.

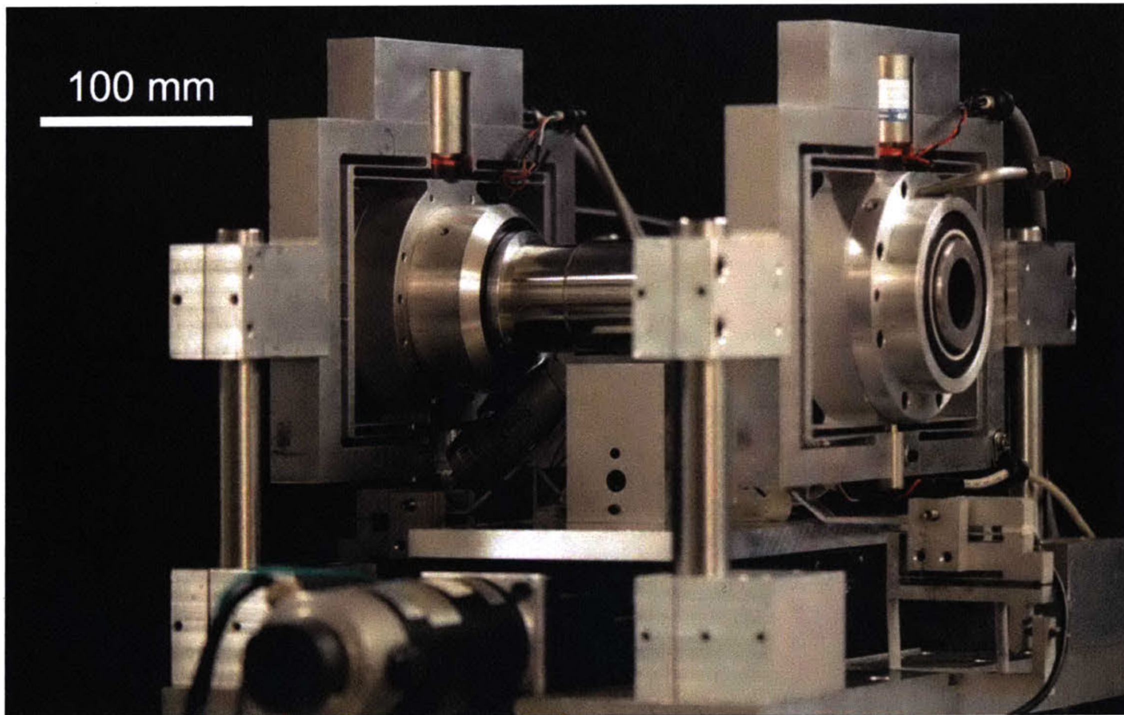

Figure 2-11: Petrzelka's roll-to-plate printing apparatus [10].

2.4.2 The MIT Machine

Building on the work of Petrzelka, Libert and Nill built a laboratory-scale roll-to-roll setup with web handling and precision print head systems (Figure 2-12) [12] [13]. The machine uses predomintly commerical components for web handling and has a custom built precision print

head. Figure 2-13 shows a cross section schematic of the roll-to-roll setup at the printing interface. Figure 2-14 presents the precision print head assembly, and the custom built setup for continuous inking. Web speed and tension can be controlled. Bageant and Hardt [14] are working towards implementing a working closed-loop force control on the print head. In the meantime, the printhead position can be measured with 100 nm resolution, and force with about 0.1 N resolution.

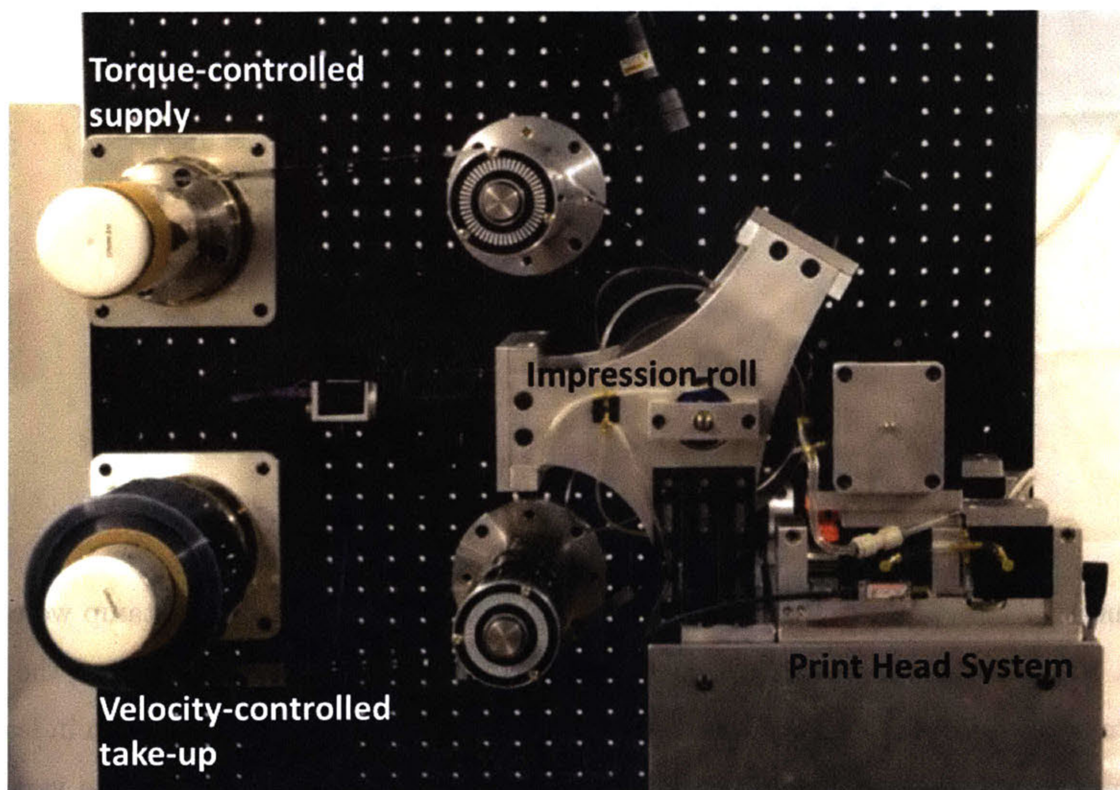

Figure 2-12: The MIT printing machine by Libert, Nill, Merian, and Bageant [14] [12] [13] [6]. The web handling system can be viewed on the left side of the image. The web stretches over the impression rool, where the print head system brings the stamp into contact with the web substrate. The two unlabled idler rollers currently measure reaction forces, subsequently leading to closed-loop web tension control.

2.4.3 Insights into Tool Quality from Printing

Merian printed HDT on gold using the MIT printing machine under open loop force control using Nietner's PDMS stamps [6]. He observed roof collapse as the dominant failure mode

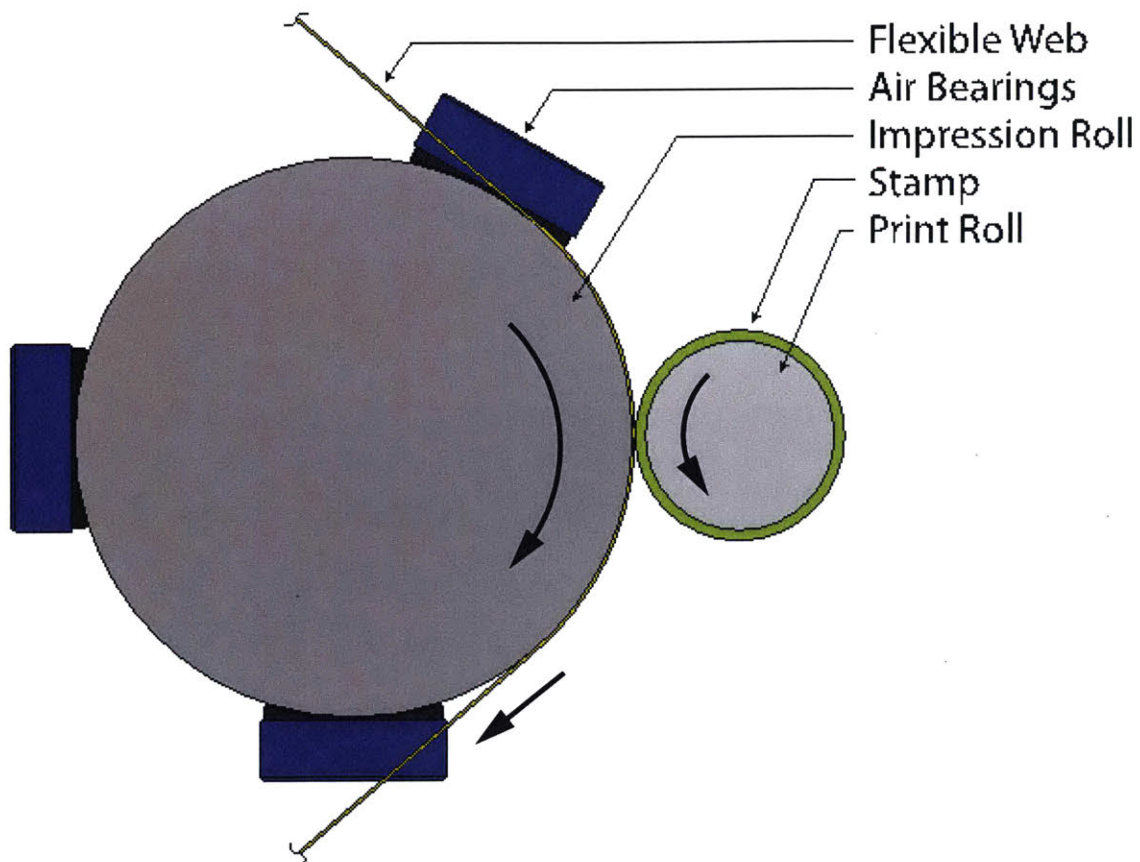

Figure 2-13: A schematic of the stamp-substrate interface [12].

in printing. Observations of inconsistent print widths over the area of the stamp were also noted. While variations can occur from printing dynamics and force control errors, the non-uniformity of tools was a likely contributor. Nietner recorded significant variation in feature geoemtry over one axial traverse of the stamp, and Merian's results suggest the variation may be a much greater spatial concern [16].

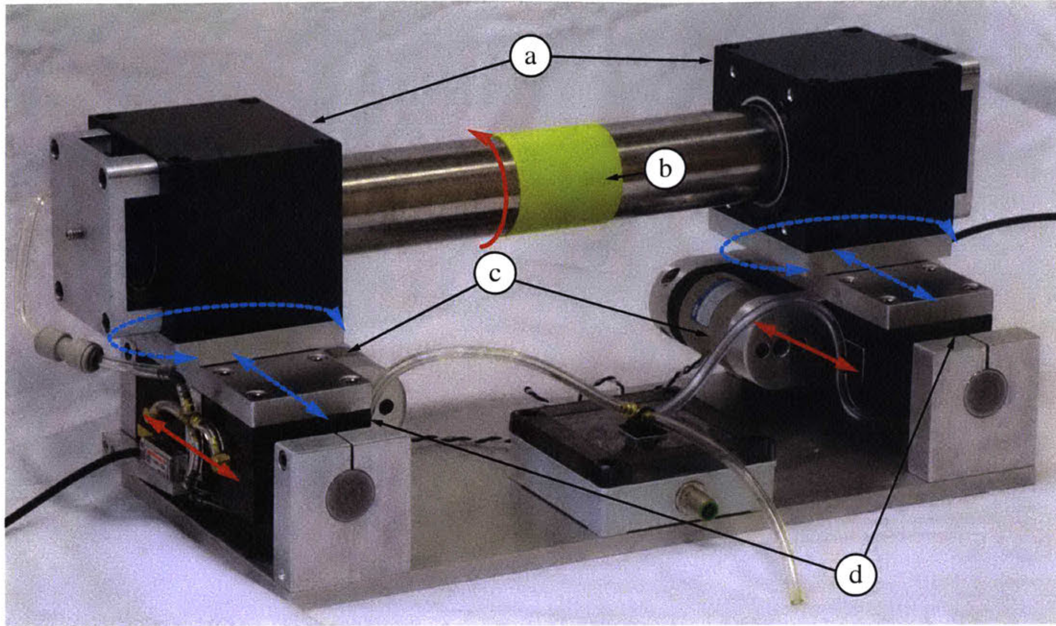

(a) The precision print head assembly with annotated controllable motions (red), and structural compliances (blue) [14] [12].

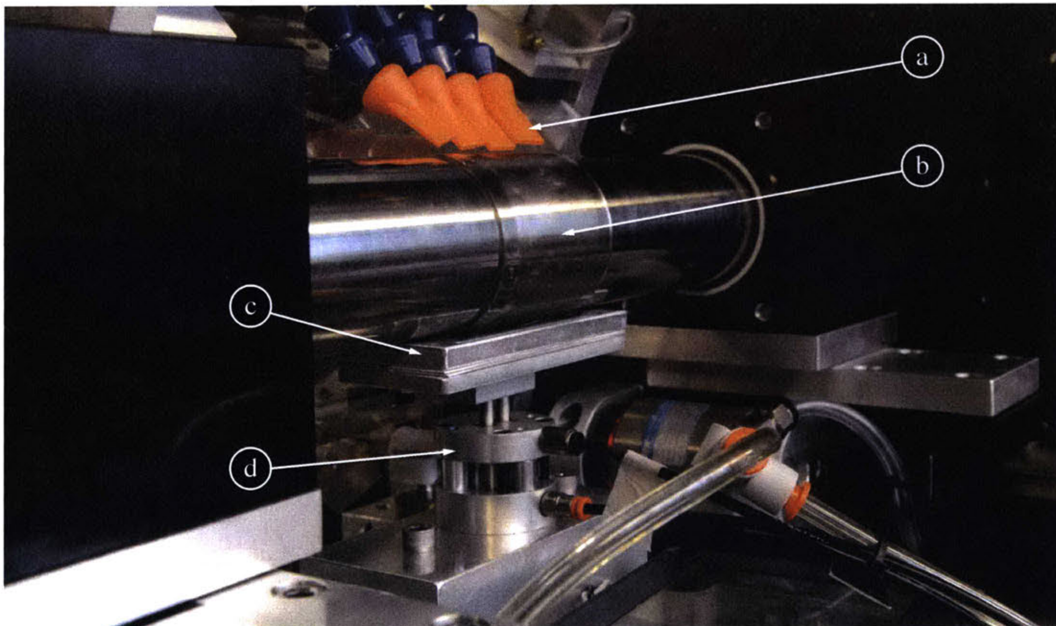

(b) Merian's continuous inking system in the print head assembly [6].

Figure 2-14: Photographs of the printhead assembly. In Figure 2-14a, the stamp (b) is mounted to a steel shaft, supported in rotary air bearings (a). Voice coils (c) translate each arm of the assembly, which are supported on linear air bearings (d). This configuration permits a displacement and angle for contact to be set. Structural compliances in the form of flexural elements eliminate overconstraint (blue rotation), and serve as stiff force sensors (blue translation). In Figure 2-14b, nozzles (a) blow air over the stamp (b) to dry it. The stamp continuously rolls through an ink bath in the ink tank (c), which can be actuated (d) vertically to provide clearance for the stamp-mounting process.

THIS PAGE INTENTIONALLY LEFT BLANK

Chapter 3

Machine Design for Tools of Arbitrary Patterns

This thesis builds on the work of the Petrzelka and Hardt [23], and Nietner and Hardt [16], in the manufacturing of seamless tooling for roll-to-roll μCP. As such, the centrifugal casting machine designed and built by Petrelka was utilized [23]. However, machine upgrades were required to fabricate arbitrarily patternd PDMS stamps, and to qualify the new tools. This chapter provides descriptions of the current machine and subsystems, as well as details the design of new microscopy accessories and software advancing machine utility towards making μCP tools with diverse feature sets.

3.1 Overview of the Centrifugal Caster

The centrifugal casting machine designed by Petrzelka was used for fabricating PDMS stamps [23]. The setup remains similar to the original design and implementation, though with some hardware and software adjustments having been made over the years. A labeled photograph of the current machine is presented in Figure 3-1. A centrifuge drum (d) is spun relative to laser optics (a,b). A linear stage (c) also provides relative motion between the laser and centrifuge. The machine's thermal system comprises an infrared temperature sensor (e), a heat gun (f), and a cooling fan (g). Control of the machine is implemented through National Instrumens LabVIEW software. A National Instruments PCIe-7852R FPGA card reads and

writes all inputs and outputs to the machine. The FPGA has a 10 MHz hardware clock. The precision timing is used to control system actuators. General protocols are written in a LabVIEW VI on the host PC, which communicates with the FPGA, but does not direclty utilize its limited resources.

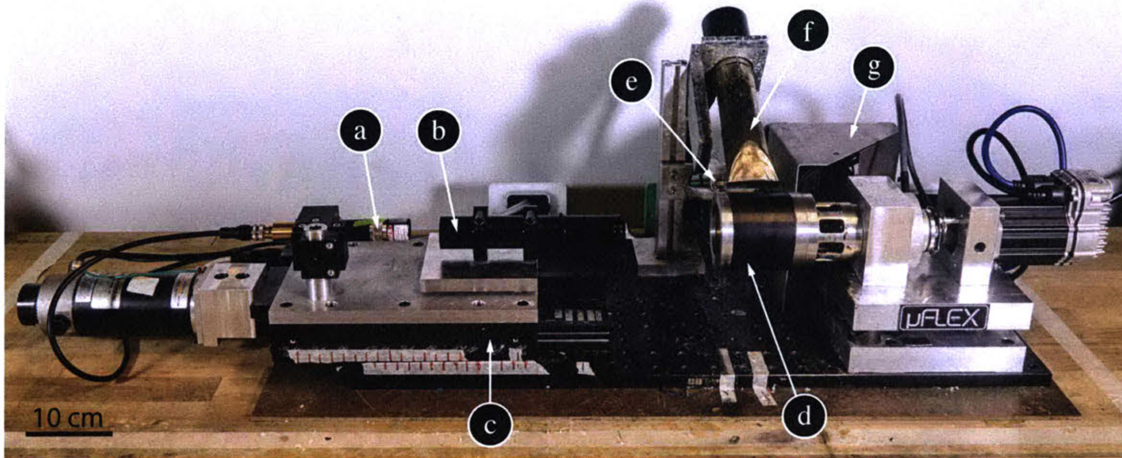

Figure 3-1: A photograph of the current centrifugal casting system. The laser (a), optics (b), linear stage (c), centrifuge drum (d), temperature sensor (e), heat gun (f), and cooling fan (g), are labeled. The machine is mounted to an optical breadbord. Wired connections are bundled and brought through 3D printed brackets, which are secured to the back of the board.

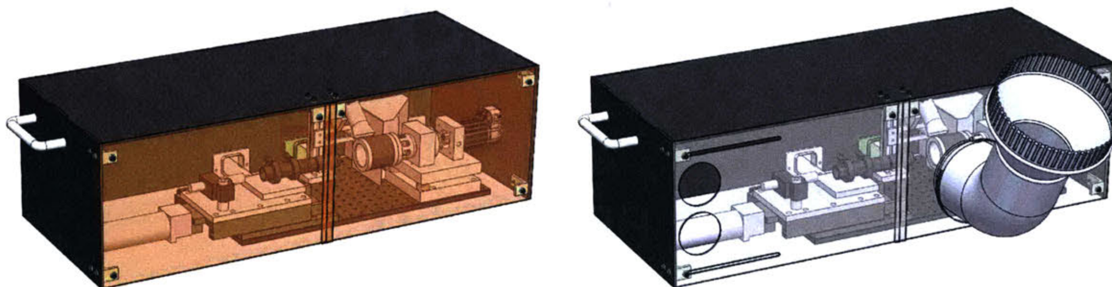

(a) In the configuration for laser safety. (b) In the configuration for chemical safety.

Figure 3-2: CAD schematics of the safey enclosure for the centrifugal caster.

The centrifugal caster operates inside an acrylic enclosure for laser and chemical safety. Pictures from CAD of the enclosure are presented in Figure 3-2. Figure 3-2a the laser safety acrylic front windows, of OD 5 at the operating wavelength of 405 nm. The laser configuration is used during photoresist exposure only. For all other processes, clear ventilation

front panels, in Figure 3-2b connect the enclouse to a lab snorkel via aluminum sheet metal tubing. The enclosure in this form contains two air intakes on the left for continuous air flow, and the left panel can be slid to create a small opening for chemcial dispensing.

3.1.1 Centrifuge System

The centrifuge subassembly is shown in Figure 3-3. A hollow aluminum cylinder serves as the centrifuge drum. The drum is mounted to a steel spacer with low thermall mass and a fin-like structure for convective cooling to minimize heat transfer to the bearings during baking. A thin steel plate covers the back opening of the drum, again to limit heat and mass transfer. A composite, steel and aluminum shaft drives the drum. Angular contact ball bearings in a back-to-back configuration have high stiffness, life, occupy minimal space, and constrain the shaft in the axial and radial directions. The aluminum portion of the shaft extends beyond the steel section mated to the bearings. A rotary encoder (15T-02SF- 2000NV1ROC-F03 by Encoder Products Company) tracks the rotational position of the aluminum shaft. In software, the encoder provides 8000 counts, 2000 counts expanded in quadrature, per revolution (about 20 μm of internal circumferential resolution at the photoresist surface), directional control, and an indexing line for establishing a repeatable zero position. The shaft is coupled to a commercial AC servo motor (Teknic ClearPath CPM-MCVC-2321-RLN), which ultimately drives the centrifuge, actuating the caster's rotational degree of freedom. The centrifuge subassembly mounts the machine's base through three ball and groove kinematic couplings.

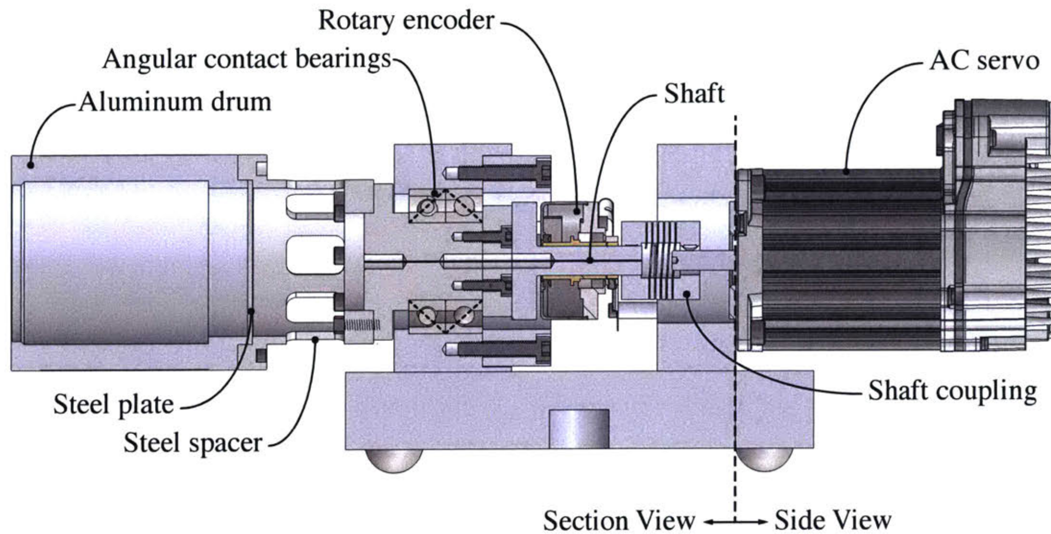

Figure 3-3: A labeled diagram of key centrifuge subassembly components.

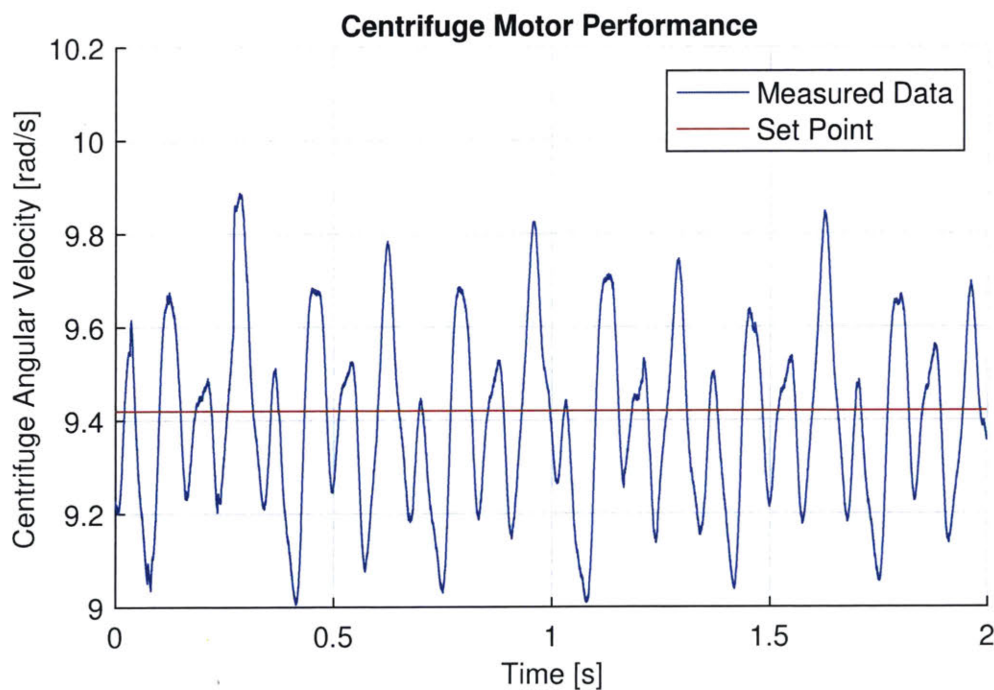

Figure 3-4: Steady state centrifuge velocity performance of the Teknic ClearPath AC servo motor at a standard write speed of 9.42 rad/s (1.5 rev/s). The measured velocity response is oscillatory but comparable to the previous brushless DC motor.

A standard brushed DC motor, and a brushless DC motor were both previously used to actuate the centrifuge using controllers programmed into LabVIEW. The motor running the centrifuge must be able to actuate the drum at low and high speeds (1 rev/s to 48 rev/s) for

writing and casting respectively. Low variation at low speed is required to maintain a near-constant exposure dose. The brushless DC motor inherited at the start of this thesis failed, and required replacement. A commercial AC servo motor was selected as a replacement for its low price, easy integration, and internal velocity control to eliminate cogging at low writing speeds. The AC servo motor's minimum and maximum speeds, acceleration profile, and input method were set up in the accompanying MSP software provided by the manufacturer. The controller was also tuned by the software on the full centrifuge assembly.

Figure 3-4 shows a plot of closed-loop centrifuge at the average ideal write speed of 1.5 rev/s (9.42 rad/s) [11]. The velocity output shown was commanded in LabVIEW using a PWM input of 20 Hz. Duty cycle linearly sets the speed between the minimum (0% duty cycle) and maximum (100% duty cycle) programmed values. These parameters were chosen for the smallest steady stsate error and most tightly controlled velocity about the mean. No circuferentially periodic changes in photoresist feature dimensions were observed, indicating that velocity variation was not signifantly impacting the lithography performance of the centrifugal caster.

3.1.2 Linear Stage and Laser Optics System

The laser and optics for the centrifugal caster are mounted to a linear stage (4945 ball bearing stage with a 1 μm resolution linear encoder by Parker). A brushed DC motor (RX130HR1017 by Gec Alsthom) actuates the stage to provide relative motion between the photoresist surface and laser, accounting for the machine's axial degree of freedom. Petrzelka outlines the benefits for this configuration, and discusses the implemented control system [10]. Most advantageous is the simplicity of translating laser-optics of low mass compared to the substantial mass of the centrifuge subsystem. The linear stage is zeroed against the back hardstop for repeatable positioning since this system lacks an encoder index. The optical stack for focusing the laser on the photoresist was also designed by Petrzelka [23]. An 80 mW, 405 nm laser (Z80M18H-F-404-pe by Z-LASER Germany), used by Nietner, was also used for the work presented in this thesis [16]. While the laser is fixed to the stage, the optical stack can be removed since it mounts with three ball and groove kinematic couplings.

3.1.3 Thermal System

A thermal system is included in the machine for heating the centrifuge in photoresist baking processes. Figure 3-1 shows temperature sensor (e), heat gun (f), and cooling fan (g) that make up the thermal system. An infrared temperature sensors (Omega OS801-MT) continuously reads the temperature of the centrifuge outer diameter. The centrifuge drum is coated in a black spray paint (Krylon Black Flat, emissivity of 0.95), so that the fixed emmisivity (0.95) infrared sensor accurately measures the drum temperature. The sensor is positioned 3.9 inches outward of the drum outer diameter to minimize the sensor's viewing spot size, mitigating errors from a curved measurement surface. The heat gun (handheld heat gun of approximately 1500 W) provides energy to the centrifuge drum during baking steps while the large computer cooling fan blows air over the steel spacer to minimize heat flow to the centrifuge bearings. An on/off controller actuates the heat input to the centrifuge.

3.1.4 Direct Write Lithography Software

The software used by Nietner only permited the exposure of complete circumferential lines in the photoresist. The linear stage traveled between set axial positions, and exposed the resist for one revolution at each location. The software was written such that multiple centrifuge speeds could be applied during exposure, effectively allowing for testing multiple exposure doses on a single photoresist patterning layer. All writing parameters were set by controls in LabVIEW, restricting the flexibility to alter the system for different patterns in the future.

3.2 Design of a Raster-Scan Writing Protocol

Creating μCP tools of useful manufacturing patterns via direct-write lithography requires the ability to traverse complex write paths. Interchangable optics sets could also prove to be beneficial for exposing a diverse set of photoresist (and subsequently PDMS stamp) feature geometries. The centrifugal caster's setup permits control over two degrees of relative motion, axial translation x and rotation θ about x in (see Figure 3-5). Nietner only varied features over the axial length of the drum [16]. Raster-scan or vector writing approaches could be taken to control exposure parameters and vary feature shape over both degrees of freedom (DOFs).

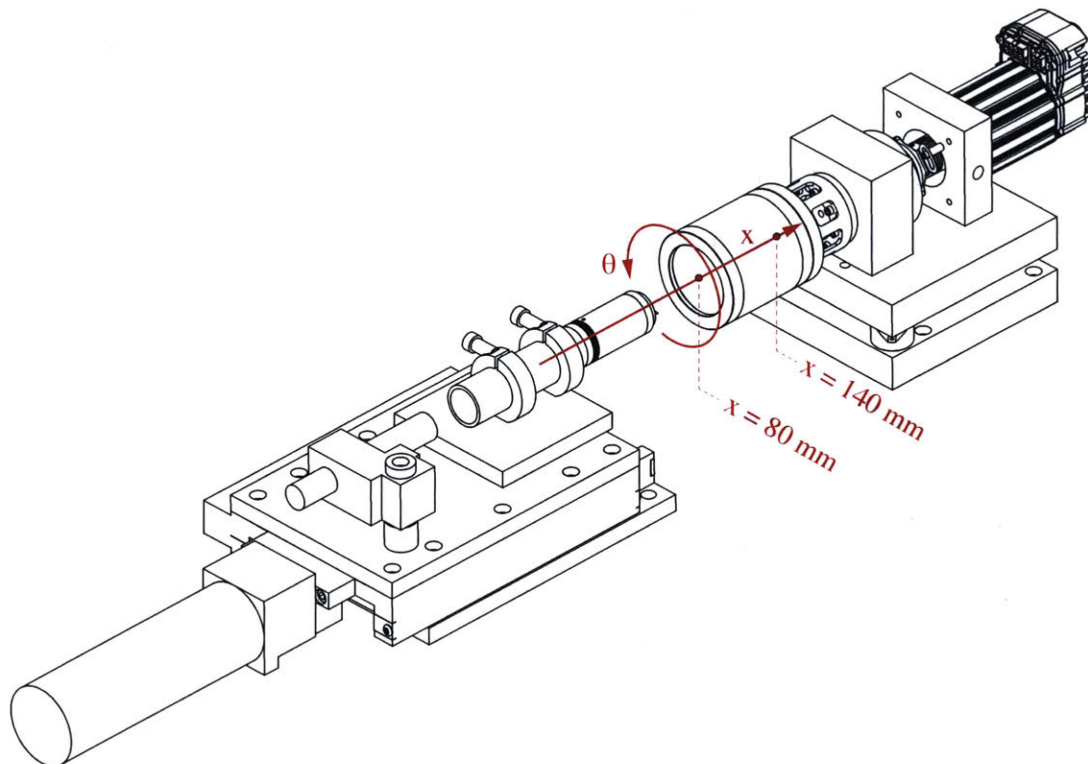

Figure 3-5: The coordinate system and DOFs of the centrifugal casting machine. The axial position of the linear stage is denoted by x, while θ represents the rotational, or circumferential, position of the centrifuge. The two labeled x locations represent the axial boundaries of the photoresist casting area in the centrifuge drum.

With a single laser-optics set, a raster-scan approach was chosen to demonstrate the feasability of manufacturing cylindrical, seamless, PDMS stamps with arbitrary patterns. A

raster method could alter exposure parameters as a function of θ while still sweeping through the desired x locations. For instance, dots could be written, by turning the laser on for only one count of the rotary encoder. Adjacent axial positions could even be only a few microns apart to write features with partially overlapping exposures. This approach would still only require velocity control on the centrifuge, and position control on the stage. Therefore, software adjustments would be purely logistical. A vector-based writing approach could also have been taken. However, additional complexitity would have been added, caused by the coupling of the write speed to both stage and centrifuge actuator motions. Consequently, a vector approach requires more advanced control systems and places stringent acceleration requirements on the actuators to maintain a constant write speed. A fixed write speed is needed to maintain a constant exposure dose. Therefore, the raster-scan direct-write system was selected for simpler implementation.

A flow chart of the raster-scan writing protocol implemented in LabVIEW is presented in Figure 3-6. To start, MATLAB code nested inside of a MathScript node generates the exposure pattern for the μCP stamp mold, and the associated arrays required by LabVIEW for actuation of the centrifugal caster machine. Appendix E provides an example MATLAB script for reference.

The first step, in Figure 3-6, *initialize inputs*, runs the MATLAB code, generating the required machine inputs. The inputs include n, $[LP]$, $[P]$, $[\omega]$, and $[x]$. The scaler input n is the total number of rows of the stamp, or the number of axial positions at which the laser will expose the photoresist. The tool pattern $[LP]$ is an n x 8000 matrix containing the laser power at every rotary encoder position (8000 counts) for every every row. Power is specified on a U8 scale, 0 representing 0 mW and 255 representing 80 mW. A 0V to 1V voltage command to the laser linearly scales power between null and full. In theory, laser power in $[LP]$ can vary by row and column. For simplicity in execution, laser power is either 0 or P_i in each row. P_i represents a constant laser power over an entire revolution at row i (i is a strictly positive integer). The n x 1 vector $[P]$ contains the row-constant power (P_u) from each row of $[LP]$. Similarly, centrifuge speed is not varied over the period of one drum revolution. As such, the n x 1 vector $[\omega]$ is populated by the write speed (drum angular velocity) for each row i. Finally, the n x 1 vector $[x]$ lists the axial position of the linear

stage for each row i. Elements of $[x]$ do not have to be unique. Table 3.1 summaries these inputs.

Input Name	Description
n	number of rows (scalar)
$[LP]$	laser power as a function of tool position (x,θ) (2D matrix)
$[P]$	row-wise power (vector)
$[\omega]$	row-wise centrifuge speed (vector)
$[x]$	axial position of each row (vector)

Table 3.1: A list of exposure inputs.

The machine then proceeds to write one full revolution at each row, starting at row $i = 1$, and ending at row $i = n$. Once the final row is exposed, the machine stops the writing process ($i > n$? and]textitstop blocks). For all other i in the range $[1, n-1]$ the centrifugal caster will actuate the ith entries of the inputs (*actuate system at* i^{th} *entries*). The centrifuge speed is set to $\omega(i)$, the stage moves to axial position $x(i)$, and laser power is set to $P(i)$. For safety the laser is disabled and is not enabled until exposure is exactly required. However, Laser power can be set indpendently.

After actuation, the software extracts row i of $[LP]$ $(LP(i, 1 : 8000))$. Edge detection is performed to determine when the laser should convert from being disabled to enabled, and from enabled to disabled. Corresponding encoder positions bounded by [0,8000] are placed in rising edge and falling edge vectors, $[R]$ and $[F]$ respectively. The current software only accomodates 100 elements in $[R]$ and $[F]$ each while utilizing 40% of the FPGA resources. The edge vectors are sent to the FPGA along with the starting laser state (enabled or disabled) at $\theta = 0$.

With the centrifuge spinning, the software waits for the zero rotary encoder position to occur $\theta = 0$. LabVIEW reads the encoder position as [0,7999]. A bolean yes to the indexing tick scenario triggers the writing processes to begin. The current encoder position is read, and three scenarios are checked. If the current encoder position is 0, and the initial laser condition is to be enabled ($\theta = 0$ & $LP(i, 0) \neq 0$) then the laser is enabled. If the current

encoder position is an element of the rising edge vector ($\theta \in [R]$), the laser is enabled. If the current encoder position is an element of the falling edge vector ($\theta \in [F]$) the laser is disabled. If none of the conditions are met, the laser state is not updated. The software is continuously checking for the last encoder count in one revolution, 7999. Encoder position is continuously read and the laser enable/disable pin set accordingly until the final count, at which the laser is reset to its disabled state. The row number i is subsequently incremented, and LabVIEW repeats the process to write at new axial and circumferential positions.

The aforementioned protocol implements a raster-scan approach to laser-based direct-write lithography on the centrifugal caster setup. The current implementation takes the FPGA 15 μs to identify the encoder position, and actuate the laser acccordingly. The laser can be modulated up to 200 kHz, placing a factor of safety of 3 on the rastering algorithm. The cycle duration places a constraint on centrifuge speeds used in writing. Implications of the cycle time are discussed in Chapter 4.

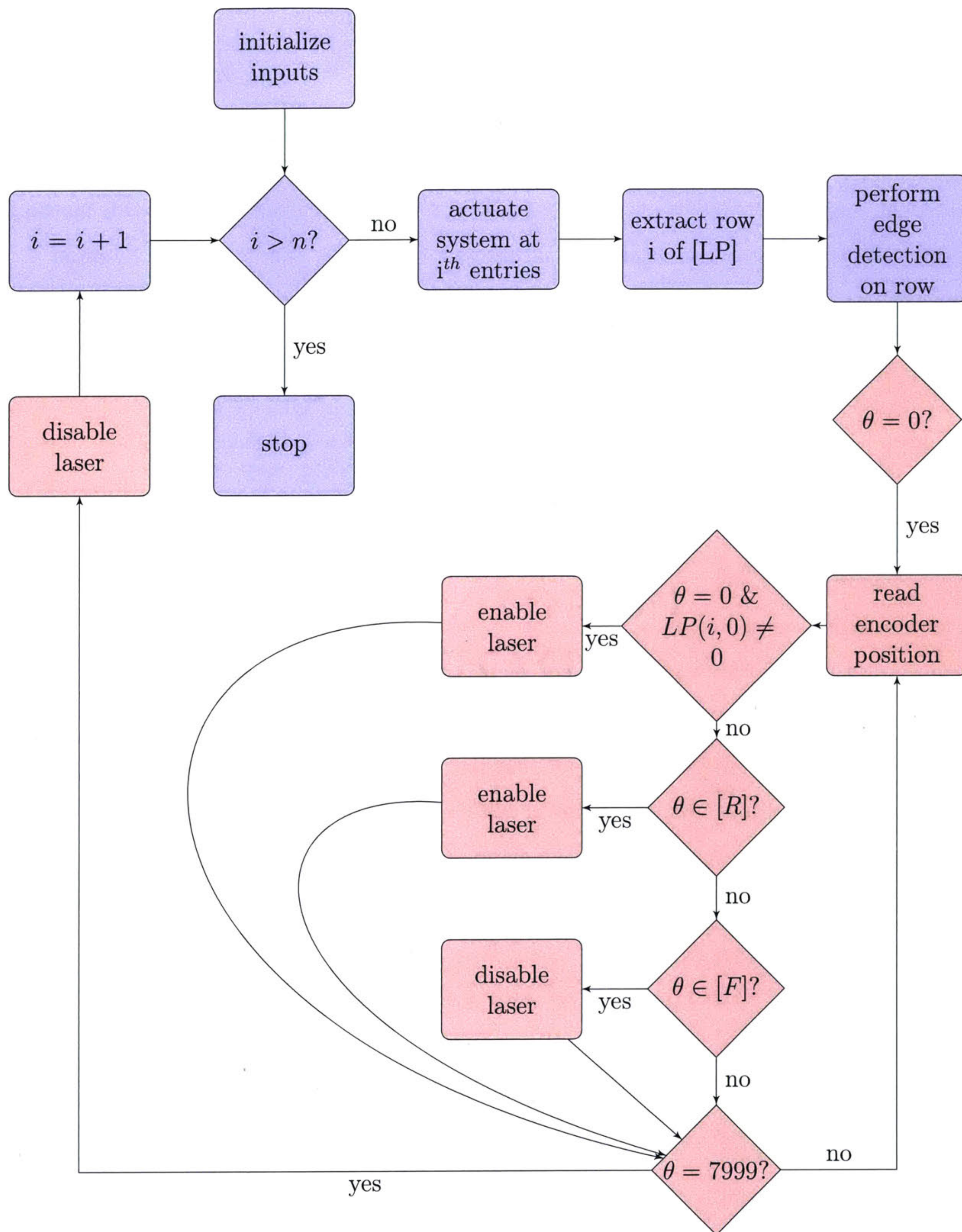

Figure 3-6: A flowchart of the raster-scan direct-write protocol in LabVIEW. Blue blocks denote operations beformed on the host PC. Red blocks are operations executed on the FPGA, which require fast and precise timing.

3.3 Design for Imaging Arbitrary Patterned Tools

Non-destructive forms of stamp metrology are required for scaled-up μCP. In mass production stamps cannot be continuously sacrificed as method of quality control. Prior to this thesis, PDMS stamps were cut so that cross sections could be viewed under a standard optical microscope. Assuming that the cutting does not strain or damage the features, this method provides a very accurate view at stamp feature geometry. but eliminated the potential for any future printing with the stamp in the roll-to-roll system, Furthermore, the method also never provided a complete picture of feature geometry metrics throughout the tool-making process.

No ground truth for PDMS replication of the photoresist mold exists for the cylindrical stamp-casting system. For arbitary patterning, this measurement is key. The contribution of the photoresist as a mold for PDMS must be understood. A directional sensitivity, reshaping of the photoresist over time and or castings, or even inaccurate replication of certain exposure feature types, have huge implications on the feasibility of creating arbitrarily patterned tooling. Additionally, direct measurement of tool feature geometry without destroying or compromising on the printing abilities of a PDMS stamp is paramount for fast tool production rates. This ability would also be particularly useful for features geometries not ideal for dissection. To address these metrology necessities, an episcopic microscope was designed and built for imaging the photoresist patterning layer. Furthermore, an exisiting episcopic microscopy tool for visualizing tool contact was modified and put to use.

3.3.1 Episcopic Microscopy of the Patterning Layer

An episcopic microscope was designed for viewing the photoresist mold inside the centrifuge drum. Figure 3-7 shows a CAD model of the microscope key components labeled. A microscopic objective lens is secured with its optical axis parallel to the spin axis of the drum. A 90° mirror mounts in front of the lens to reditect light from the image into the lens. Through a series of optics outlined in Figure 3-8, the image is observed on a camera sensor. A light source is mounted to the optical assembly to provide coaxial light to the imaging surface through the objective lens itselft. The entire optical assembly is mounted to two translation

stages in series, which provide orthogonal translations relative to the machine's x-axis. The stages are mounted to an identical kinematic coupling baseplate used by the laser-optics. The microscope accessory can be mounted on the stage in place of the optics. In this configuration, the caster's linear stage provides axial translation, the vertical stage focuses the optical system on the resist surface, and the horizontal stage can be adjusted to ensure the image is centered in the centrifuge.

Figure 3-8 presents all of the micrscope's optical components. The image path is represented by the blue line, while the yellow line shows the path of the episcopic light source. A 5x objective lens images the photoresist. A 16 mm (length dimesion) mirror redirects the image for observation given the obvious space constraint. A 30 mm mirror redirects the image another 90°. A beam splitter redirects the image to the optical axis of the camera, where a tube lens converges the light rays on a C-mount camera with a 1/2" sensor. A rotatable polarizer filter mitigates reflections off of the aluminum drum in the image, and a cutoff filter (maximum wavelength 700 nm) lastly adjusts the image. The beams splitter allows a for a co-axial light source to be placed in the system. The light intensity can be adjusted by the aperture, before traveling the image path in reverse through the lens to illuminate the photoresist at the image location.

A large number of components are left unlabeled in Figure 3-7, even with the additional optical information provided in Figure 3-8. The extra components are purely structural and accurately place optical components relative to each other.

Table 3.2 lists the supplier and part number of each optical component for reference. The strongest factor dictating the microscope design was the space constrain of peering inside the drum, and imaging perpendicular to the photoresist surface. The objective lens that was chosen (5X Mitutoyo Plan Apo Infinity Corrected Long WD Objective) had a long working distance, compact size, and satisfactory optical properties to allow imaging through a mirror. The lens selection significantly influenced the remainder of the design, as other optical components were chosen to match Mitutoyo's optical system specifications at the geometric sizes required for mating them together. Lens specifications are listed in Table 3.3.

A photograph of the microscope in operation is shown in Figure 3-9. Numerous images

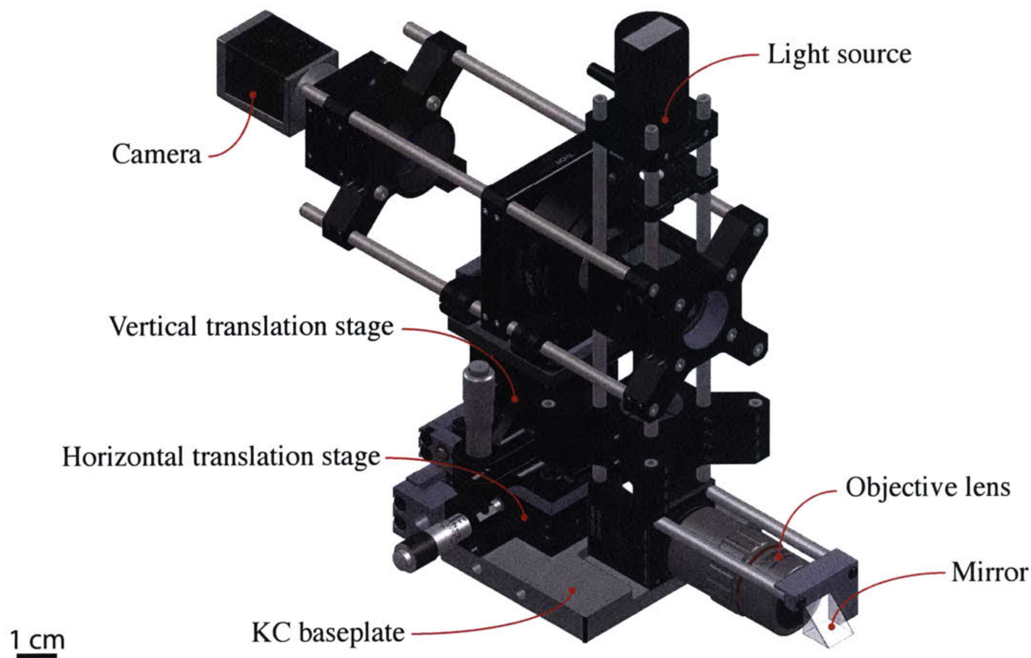

Figure 3-7: A CAD schematic of the episcopic microscope for photoresist imaging with key components labeled.

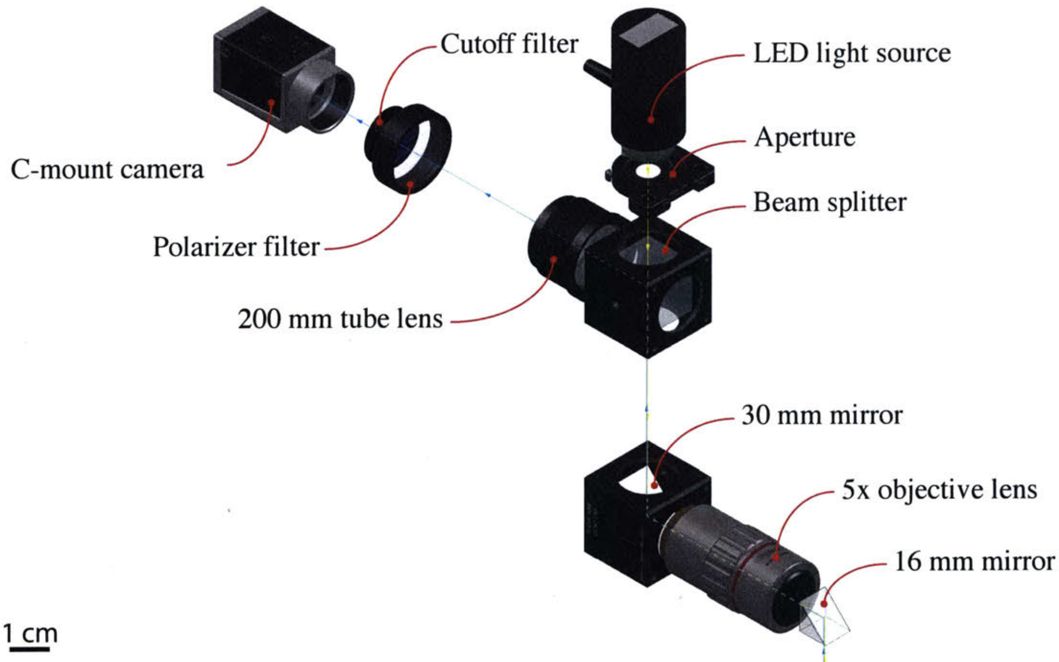

Figure 3-8: A labeled optical schematic from CAD of the episcopic microscope for photoresist imaging. The image path is traced out in blue, the coaxial light path is yellow.

Component Name	Supplier	Part Number
Cutoff filter	Thor Labs	FES0700
Polarizer filter	Edmund Optics	64897
200 mm tube lens	Thor Labs	ITL200
Beam Splitter	Thor Labs	CCM1-BS013
30 mm mirror	Thor Labs	CCM1-E02
5x objective lens	Thor Labs	MY5X-802
16 mm mirror	Thor Labs	MRA15-E02
LED light source	Thor Labs	MCWHL5
Aperture	Thor Labs	CP20S

Table 3.2: Part name, number, and supplier info for the optics shown in Figure 3-8.

Parameter	Value
Depth of Focus	14 μm
Working Distance	34 mm
Resolution	2 μm
Field of View (1/2" sensor)	1.28 mm x 0.96 mm
Numerical Aperture	0.14

Table 3.3: Manufacturer reported specifications of the Mitutoyo 5x objective lens. The depth of focus defines an arbitrary distnace of moderate focus at which the image information is still discernible. This lens allowed for sufficiently viewing nominally 15 μm tall photoresist features. The optical resolution and field of view were adequate for extracting dimensional data over a large number of features.

of photoresist features, a descriptions of using the microscope as a metrology tool are located in Chapter 5.

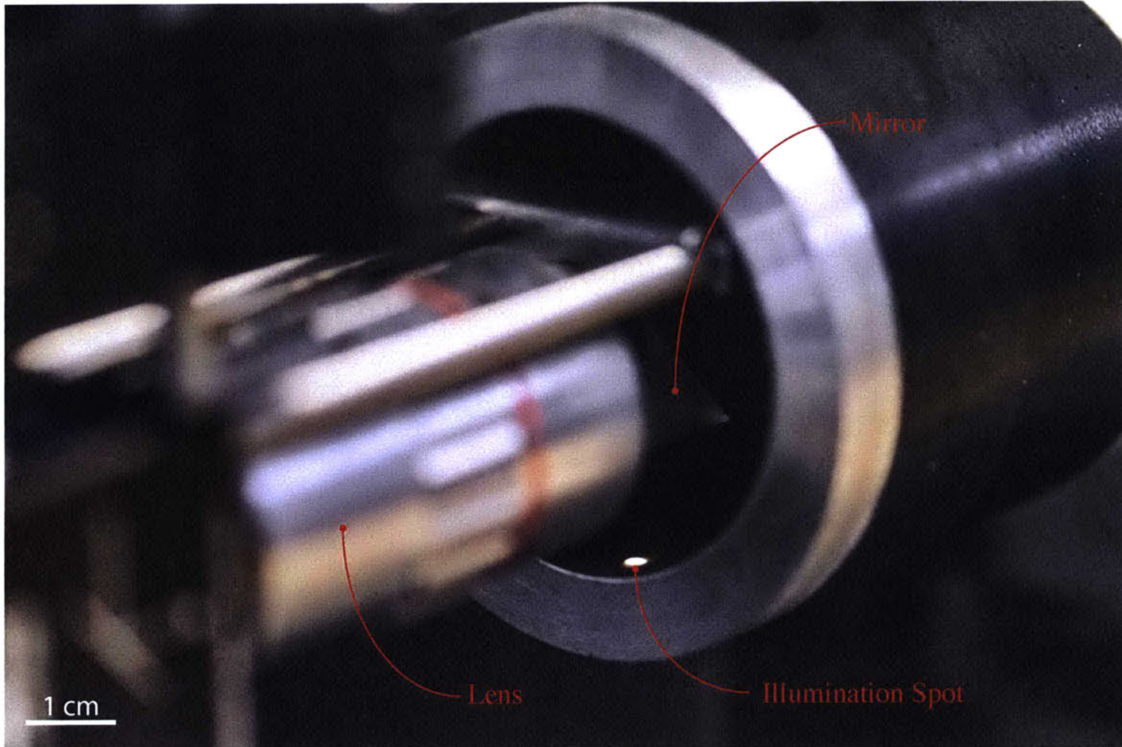

Figure 3-9: A photograph of the episcopic microscopy system imaging the photoresist mold. The illumination spot on the patterning layer is clearly visible.

3.3.2 Episcopic Microscopy of Tool Contact

Scott Nill developed an epsiscopic microscope for visualizing contact between the PDMS stamp and the glass impression roll, wherein total internal reflection of a compressed composite stamps creates an image focused on the black-pigmented backing through regions of feaure contact [29]. While there is currently no data to support that the contact visualized through this method directly matches prints at the same location, the understandings of μCP with thiol inks on gold suggest that any region of the tool in contact will transfer ink [6]. Therefore, contact visualization provides a powerful understanding of the print geometries regardless of cross section feature shape.

The system built by Nill previously operated on the roll-to-roll machine, situated inside a hollow glass impression roll [29]. However the holllow rolls could not be properly constrained in the impression roll assembly designed by Libert (for a solid glass roll), and fractured [12]. A benchtop setup of Nill's system was design and built to accomodate the hollow rolls so

the informative contact metrology setup would not be lost.

A labeled CAD model of the benchtop contact system is shown in Figure 3-10. Nill's microscope was reoriented and placed on three orthogonal translation stages. The configuration allows for focusing, raising or lower the microscope to view midline of contact, and permits the microscope to traverse parallel to the stamp's axial length. When enabled, the printhead assembly brings the PDMS stamp into contact with a hollow glass impression roll of 3 mm thickness. The roll is constrained such that it can only rotate about its spin axis. Radial and axial (thurst) constraints have some compliance to handle roughly 600 μm of roll runout. Two rubber wheels and an adjustable-shoulder cam follower are located at each end of the glass roll for radial constraint. Axial constraint is applied through two cam followers at the base of the glass roll at either opening. The thrust constraint followers include one fixed, and one adjustable shoulder model to take up geometric errors in the impression roll's axial coordinate. Radial constraint is handled with a set of two rubber wheels, and an adjustable cam follower at both openings as well.

A photograph of the benchtop episcopic microscopy setup for contact visualization is presented in Figure 3-11. Chapter 5 contains images taken with the system and discusses specific imaging techniques used to acquire quantitative data for stamp feature contact.

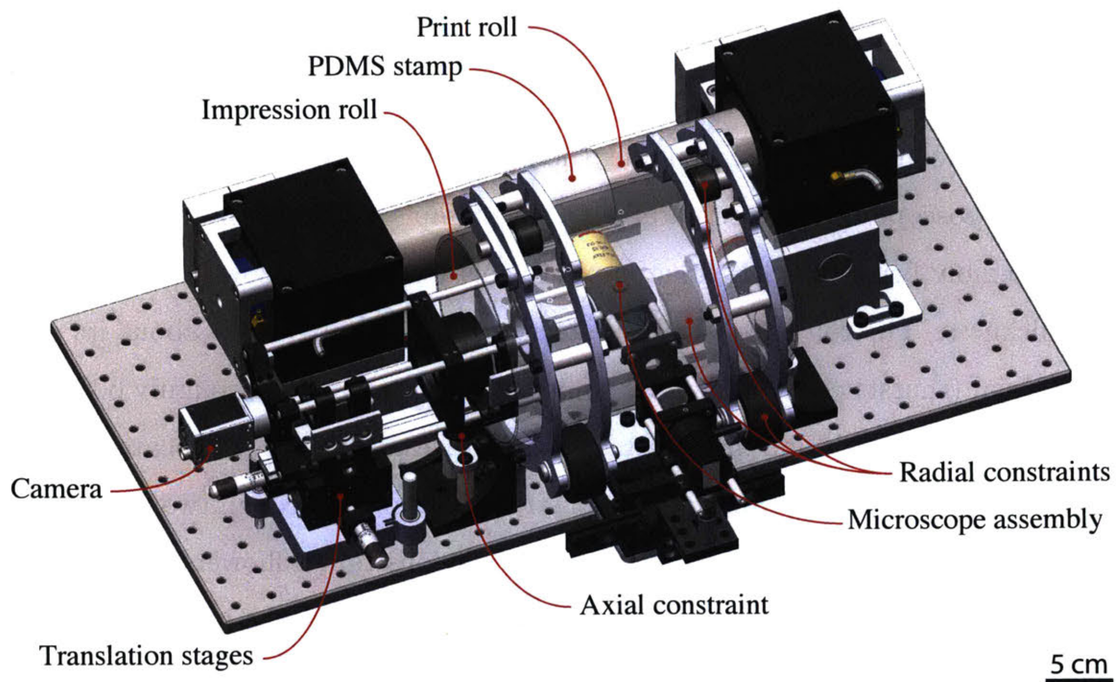

Figure 3-10: A labeled CAD model the bechtop contact visualization setup. The print head is installed on the setup in this image.

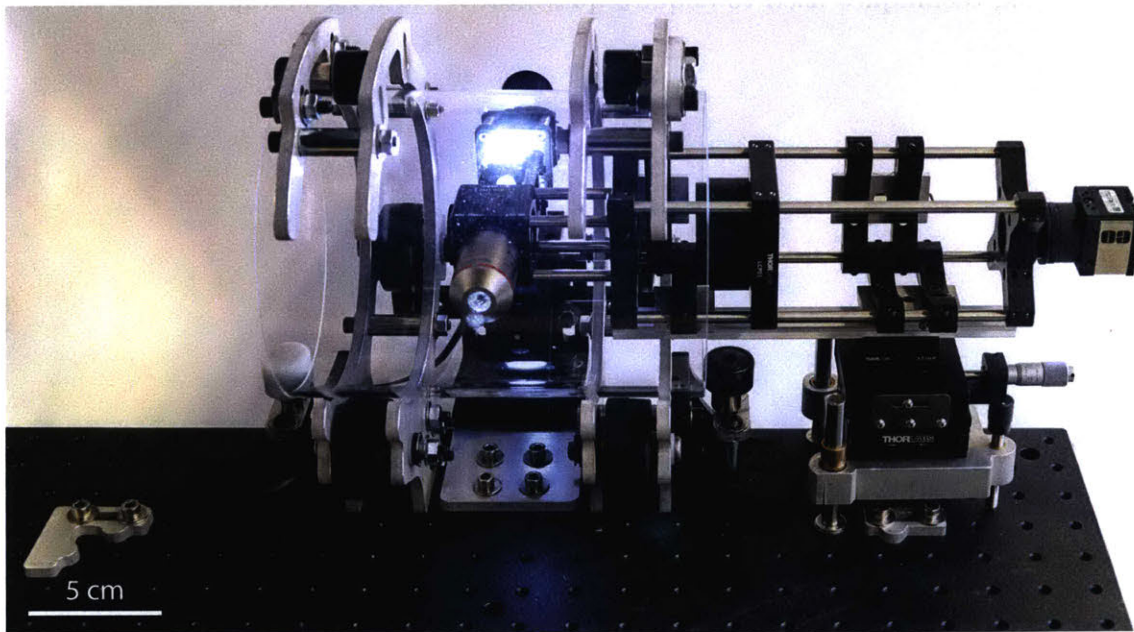

Figure 3-11: A photograph of the benchtop contact system. Kinematic couplings (not shown in Figure 3-10) locate the printhead assembly with high repeatability.

Chapter 4

Process Window for Tool Fabrication

Every manufacturing process exhibits some natural variation in the finished product. Tools for μCP are no exception. Nietner observed significant changes to tool feature shape as a function of centrifuge axial position for identical exposure settings [16]. She also verified that varying the exposure dose impacts feature geoemtry. Clearly, parameters of the tool fabrication process play significant roles. To succesfuly create arbitrarily patterned stamps for μCP it was critical to understand the most influential controllable inputs and noise. Therefore, this chapter investigates the manufacturing process window for seamless, cylindrical, PDMS tooling.

Primary emphasis was placed on analyzing the AZ 9260 photoresist. PDMS is shown to replicates molds down to 30 nm wide and 2 nm deep [2]. Section 5 verifies replication and repeatability at the working micron-level scale of the centrifugal caster setup. Therefore, it was assumed that the observable variation and defects in feature shape and general PDMS stamp quality were based in the patterning layer. The properties and shape of the AZ 9260 mold are governed by the processing prior to exposure (such as bakes), exposure (dose and focus), and development. Understanding the controllability, precision, and consequences of errors in these three stages would lead to the most informed and robust tool fabrication process.

Analyitcal and physical experimentation was performed to hone the creation of the patterning layer. Exposure simulations of AZ 9260 varying the dose and laser focus will illustrate that cross section feature geometry can be altered. Characterizations of errors in the cen-

trifugal caster identify critical sources of noise in the current setup. Finally, literature review and tool-making experimentation verified the effects of these errors and the procedure was re-optimized for the most controllability in fabrication.

4.1 Lithography Simulation

A spatial and temporal model of the exposure of AZ 9260 photoresist was created and verified by Nietner [16], wherein the conversion of the photoactive compound (PAC) to its developer-soluable state through ultraviolet irradiaiton is simulated. Adjustments were made to the analytical model to control the location of the focal point and the angle of incidence of the focused laser beam. A computationally efficient method of simulating overlapping exposures was also developed. Analysis of the feature sizes and shapes demonstrate key trends in creating useful feature geometries for μCP tools.

4.1.1 Governing Physics for an Analytical Model

A 2D model of the fraction of the remaining PAC simulates the exposure of the AZ 9260 photoresist patterning layer. In development, locations of low PAC fractions are washed away while locations with PAC fractions of unity or thereabout are vitrually inert. Exposure by ultraviolet radiation of a diazonaphthoquinone-based (DNQ) positive photoresist converts the PAC into a base-soluable indene acid, which is removed from the photoresist during development. Simulating the distribution of the PAC concentration in time and space throught exposure shows the patterning layer vacancies creating in development, which will be filled in by PDMS during tool casting. Thereby presenting the specific tool feature geometry. The MATLAB code for the analytical model is located in Appendices K, L, M, N.

Dill et al [30] proposed a standard model for resist conversion. The conversion rate is governed by Equation 4.1, where $M(x, y, t)$ is the the remaining PAC concentration (1 representing completely unexposed photoresist and 0 representing completely exposed photoresist), $I(x, y, t)$ is the local radiation intensity, and C is the standard exposure rate constant.

$$\frac{\partial M(x,y,t)}{\partial t} = -I(x,y,t) \cdot M(x,y,t) \cdot C \tag{4.1}$$

Equation 4.1 admits a solution of the form in Equation 4.2, such that the PAC concentration is determined by the cumulative irradiation profile in exposure.

$$M(x, y, t) = \exp\left(-\int_0^t I(x, y, t) \cdot C \, \mathrm{d}t\right) \tag{4.2}$$

C is assumed constant and can be pulled out from the integral in Equation 4.2. The resulting integral, Equation 4.3, represents the exposure dose, which has typical units of $\mathrm{mJ/cm^2}$. While the dose can theoretically take on any value, photoresist manufacturers report benchmark values that are ideal for most applications [31].

$$Dose = \int_0^t I(x, y, t) \, \mathrm{d}t \tag{4.3}$$

The intensity of light from exposure non-linearly propogates through the depth of the photoresist. Light can be refracted laterally during exposure but this phenomenon ignored in this simulation [32]. The absorption coefficient, α, in the Dill model describes ultraviolet absorption in thick resists. Equation 4.4 shows that absorption of ultraviolet radiation depends on photoresist parameters A and B, and on the current PAC concentration. A and B are the absorption parameters of the unexposed and fully exposed (bleached) resist respectively.

$$\alpha(x, y, t) = A \cdot M(x, y, t) + B \tag{4.4}$$

Photoresist properties A, B, and C are known as the Dill photoresist parameters. Typical values of these parameters are provided by photoresist manufacturers and vary depending the wavelength of light used in exposure and exact processing performed on the resist prior to exposure [32]. Nietner tweaked the parameters within a reasonable range such that the simulation best reflected the observed experimental feature geometries [11]. A uniform distribution of the Dill parameter values throughout the simulated resist may be a limitation when compared to error realities of the physical direct-write setup, which will be described in Sections 4.3.2 and 4.2

Returning to first order lithography mechanisms, the intensity is found using the Beer-Lambert law, Equation 4.4, and the assumption that the focused laser diode follows a Gaus-

sian distribution [33] [34] [35]. Equation 4.5 presents intensity at any location x and y^* in the photoresist at any time t, where λ represents the laser wavelength and ω_0 is the focused beam waist.

$$I(x, y^*, t) = I_0 \cdot \left(\frac{\omega_0}{\omega_0 \sqrt{\left(1 + \frac{y^* \lambda}{\pi \omega_0^2}\right)^2}} \right)^2 \cdot \exp\left(\frac{-2x^2}{\left(\omega_0 \sqrt{\left(1 + \frac{y^* \lambda}{\pi \omega_0^2}\right)^2}\right)^2} \right) \cdot \exp\left(- \int_0^{y^*} \left(A \cdot M(x, y, t) + B\right) \mathrm{d}y \right) \tag{4.5}$$

Equation 4.6 represents the theoretical peak laser intensity, where P represents the laser power. However, optical and laser errors of the form of fluctuating power, optical focal length accuracy, and beam non-circularity can cause a deviation in the physical system from the theoretical value. Consequently, Nietner emperically determined the peak intensity that created the feature shapes most well matched to experimental results [11].

$$I_0 = \frac{2P}{\pi \omega_0^2} \tag{4.6}$$

Figure 4-1 shows a schematic of the resulting lithography simulation. The numerical simulation iteratively solves the above equations. The photoresist cross section is discretized, and matrices of $I(x, y, t)$ and $M(x, y, t)$ are created to represent the values at each mesh node. The laser beam is constructed in cyclindrical coordinates (r, z) with a maximum intensity at the focal point, f. A coordinate transformation maps the beam's intensity distribution into the resists's rectangular coordinates (x, y). The PAC and intensity values are updated in nested *for* loops, beginning from the initial condition of $M = 1$ at all locations, denoting a completely unexposed photoresist. The laser power, focal point, angle of incidence, and spatial and temporal simulation boundaries and resolutions comprise of the simulation inputs. Laser beam parameters, such as waist and wavelength, and the Dill parameters are fixed constant at values reflecting the physical setup.

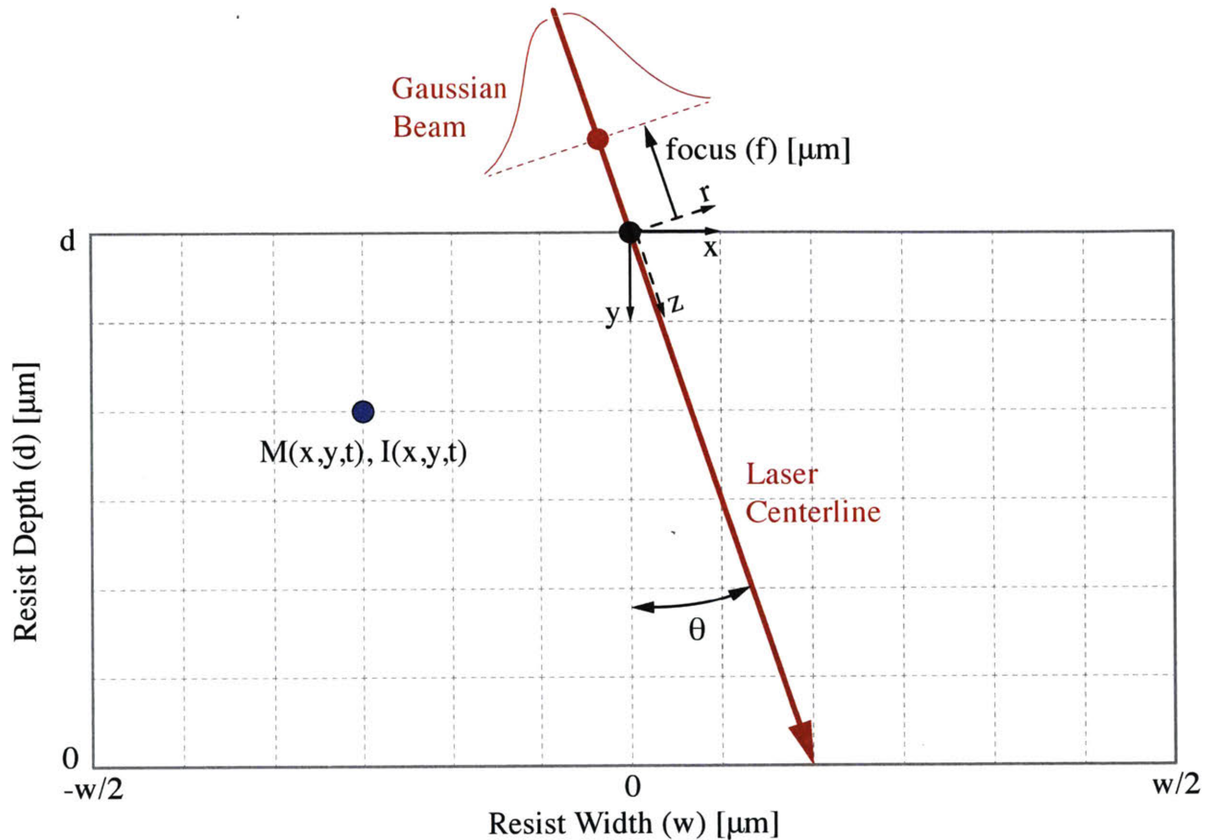

Figure 4-1: A schematic of the lithography simulation. A numerical integration of $M(x, y, t)$ and $I(x, y, t)$ is performed to track the exposure of the photoresist and conversion of the PAC. The model allows for the laser focus and angle of incidence to be adjusted from the previously fixed $x = y = \theta = 0$ scenario.

Equation 4.2 can be expanded to study how more complicated exposure patterns and timing impact feature geometry. Using a two exposure example, Equation 4.2 can be rewritten as Equation 4.7. I_1 and I_2 can be any two exposures. They could represent a complicated change in laser and optics that results in totally different incident distribution applied at the same focal point and angle of incidence. More simply, the same laser parameters applied at a different location on the resist can be used to test creating a coninuous feature through multiple exposures.

$$M(x, y, t) = \exp\left(-\left(\int_0^{t_1} I_1(x, y, t) \cdot C \text{ dt} + \int_{t_1}^{t_2} I_2(x, y, t) \cdot C \text{ dt}\right)\right) \tag{4.7}$$

Equation 4.7 can be rewritten as the multiplication of the results of the two independent exposures, as shown in Equation 4.8. Furthermore, the n-exposure case thus admits

the form in Equation 4.9. This multiplicative property was used to simulate subsequent overlapping exposures. The process was computationally verified by comparing the resulting PAC concentration of simulations that stepped in time through both exposures to the same overlapped scenario constructed from two identical single exposure results offset from eachother.

$$M_{net}(x, y, t_2) = M_1(x, y, t_1) \cdot M_2(x, y, t_2 - t_1) \tag{4.8}$$

$$M_{net}(x, y, t_n) = \prod_{i=1}^{n} M_i(x, y, t_i - t_{i-1}) \tag{4.9}$$

In summary, Equation 4.1 through Equation 4.9 outline an analytical method for modeling laser-based lithography in positive photoresists. A numerical simulation of the model was implemented to study feature geometries created by single and multiple exposures.

4.1.2 Single Exposure Features

Single exposure simulations were run to study the effects of changing focus, exposure dose, and resist thickness on the patterning layer feature geometry. At full laser power, Nietner observed minimum variation in feature dimensions when exposing AZ 9260 at centrifuge speeds between 1 and 2 rev/s for resist thickness between 10 μm and 25 μm [11]. Additionally, Merian successfully inked and printing using a tool with features exposed at 1.5 rev/s in an AZ 9260 photoresist thickness of 15 μm [6]. Experimentation outlined in Section 4.3 found that dose could only be succesfully varied by changing the write speed, since features in the AZ 9260 photoresist would only form when exposed at full laser power. These results established a baseline in experimentation and simulation scope.

Comparison of experimental findings to manufacturer recommended exposure doses[1] served as sanity checks for the process window bounds. Dose benchmarks of 2100 mJ/cm^2, 1500 mJ/cm^2, and 900 mJ/cm^2 for AZ 9260 photoresist thicknesses of 24 μm, 12 μm, and 4.6 μm respectively were provided by the manufacturer of AZ 9260 [31]. Exposure time t for

[1]Provided doses were values experimentally obtained by the manufacturer that yielded satisfactory results, and are suggested as starting points for wafer-based photolithography applications.

the continuous laser-scribing scenario is calculated using the exposure dose and peak laser intensity according to Equation 4.10 (Equation 4.3 rearranged at constant intensity). The associated centrifuge angular veloctiy is found using Equation 4.11, where D represents the internal centrifuge diameter.

$$t = \frac{Dose}{I_0} \tag{4.10}$$

$$\omega_{centrifuge} = \frac{2P}{D\omega_0} \cdot \frac{1}{Dose} \tag{4.11}$$

Using the full laser power of 80 mW, beam waist of 5 μm, the nominal centrifuge diameter of 52.8 mm, and peak laser intensity of 103,000 W/cm^2, exposure times and centrifuge speeds were found for a range of doses. The AZ 9260 manufacturer suggests testing 50% to 200% of the recommended dose since photoresist responses may vary slightly between applications [36]. Figure 4-3 plots the recommended dose range and the associated centrifuge speed. Similarly, Figure 4-2 displays the same dose range but plots the corresponding exposure time. Dose values were linearly interpolated from the manufacturer specifications. While the centrifugal caster cannot achieve the full dose range suggested for thinner resists, the full range can be tested at the 15 μm starting point. Note that 1.5 rev/s (9.42 rad/s) is just inside the suggested test range. Nietner did successfully create features at even higher doses (slower speeds) [16]. The time range of about 5 ms to 35 ms reported in Figure 4-3, created a starting point for simulation temporal bounds.

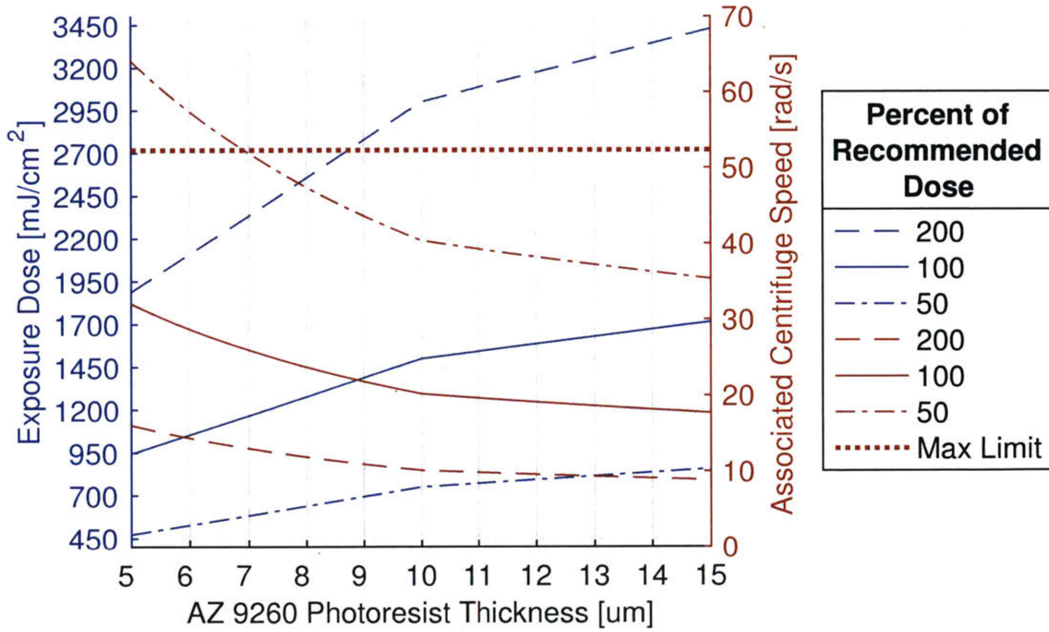

Figure 4-2: Interpolated exposure dose [31] and centrifuge speed requirements for AZ 9260 at varying photoresist thicknesses. Curves for 50%, 100%, and 200% of the recommended dose at the given thickness are plotted in blue. The corresponding centrifuge speeds to apply 50%, 100%, and 200% of the recommended dose at full laser power are shown in orange. The maximum limit represents the maximum centrifuge speed at which the LabVIEW software can enable/disable the laser without missing a tick of the 8000 counts/rev centrifuge rotary encoder. Therefore, the centrifugal caster machine cannot achieve centrifuge speeds higher than this value, and the corresponding dose values are unachievable with the current hardware and software setup.

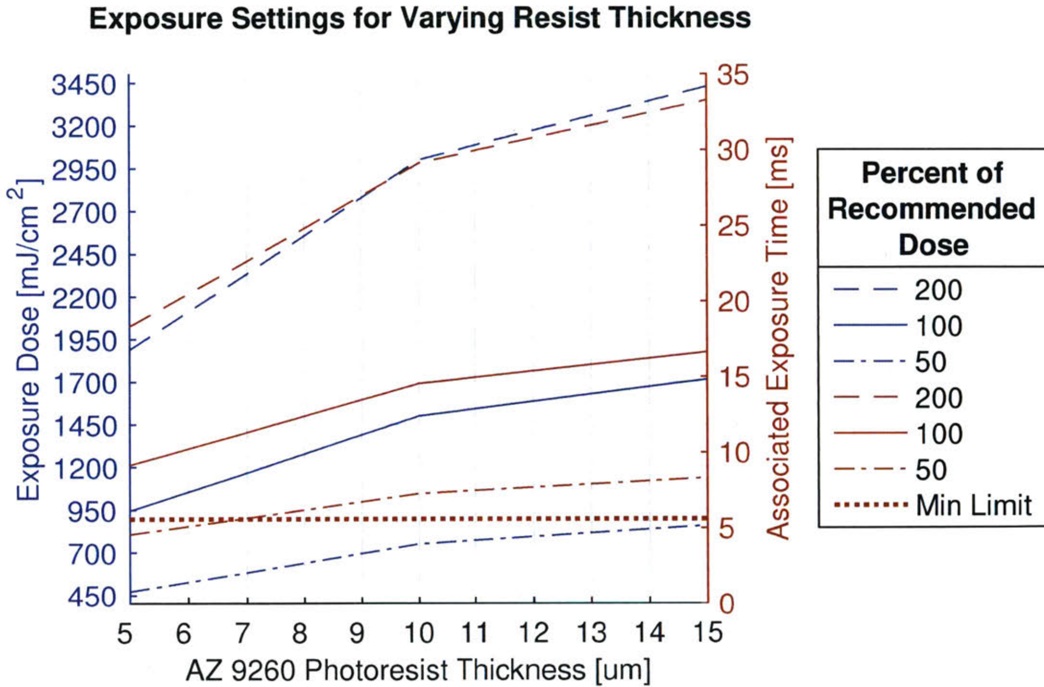

Figure 4-3: Interpolated exposure dose [31] and exposure time requirements for AZ 9260 at varying photoresist thicknesses. Curves for 50%, 100%, and 200% of the recommended dose at the given thickness are plotted in blue. The corresponding exposure time to apply 50%, 100%, and 200% of the recommended dose at full laser power are shown in orange. The minium limit represents the fastest exposure time, which is determined by how quickly the LabVIEW software can enable/disable the laser without missing a tick of the 8000 counts/rev centrifuge rotary encoder. Therefore, the centrifugal caster machine cannot achieve exposure times smaller than this value, and the corresponding dose values are unachievable with the current hardware and software setup.

With insight into simulation bounds, the analytical model was run over many interations to study dose and focus effects on AZ 9260 feature shapes. Table 4.1 lists fixed parameter values for simulation. Table 4.2 contains the test scenario parameters and their value ranges. The focal point location was changed, along with resist thickness. Note that the resist depth value was fixed. Results for any thickness less than or equal to depth can be generated by eliminating data at values of y larger than the desired thickness. Finally, Table 4.3 presents the moments in simulated exposure time where PAC data was extracted, the corresponding centrifuge speed assuming the time represents a complete exposure, and the associated theoretical dose. Note that different simulation times are effectively different doses, which are physically implemented through different centrifuge speeds. The studied doses extended beyond the 50% to 200% bounds shown in Figure 4-3. Simulations encompassed 25% to 200%

of the dose associated with the 9.42 rad/s benchmark centrifuge speed. Results illustrate the effects of dose, focus, and resist thickness on feature root width, top width, and height.

Parameter	Value
A	0.36 μm^{-1}
B	0.01 μm^{-1}
C	0.005 cm^2/mJ
Resist Width (x)	30 μm
Δx	0.25 μm
Resist Depth (y)	15 μm
Δy	0.25 μm
Simulation Time (t)	52 ms
Δt	0.5 ms
P	80 mW
ω_0	5 μm
I_0	103,000 W/cm^2
θ	0 rad

Table 4.1: Values of fixed parameters in the numerical simulation. A spatial step size of 0.25 μm is so small that the resist fully bleaches once exposed, signifying no PAC gradient across the element [37]. A resist width of 30 μm was selected such that M remained unity at the x-boundaries for all tested exposure scenarios, allowing for Equation 4.9 to be applied over the entire photoresist area experiencing changes in PAC concentration.

Parameter	Min. Value	Max. Value	Step Size
Focus (f)	-50 μm	50 μm	5 μm
Resist Thickness	5 μm	15 μm	5 μm

Table 4.2: Value ranges (minimum, maximum, and step size) of the adjustable simulation input parameters. Focus is adjusted between -50 μm and 50 μm at 5 μm steps. Resist thickness of 5 μm, 10μm, and 15 μm. Values of f greater than 0 are hereon refered to as above focus, while values of f less than 0 are called below focus. Ideal focus is achieved when f is equal to 0.

Exposure Scenario	Time (ms)	Centrifuge Speed (rad/s)	Dose (mJ/cm^2)
1	7	34.99	866
2	13	18.84	1608
3	20	12.25	2474
4	26	9.42	3216
5	33	7.42	4083
6	39	6.28	4825
7	46	5.32	5696
8	52	4.71	6434

Table 4.3: Simulation times of interest, the associated centrifuge speed during writing, and the corresponding exposure dose. Each dose was studied for each focus position and resist thickness tested.

Four sample exposures are shown for example prior to reporting the complete simulation results. Figure 4-4 shows a simulated ideal feature, with a focus of 0 μm and 26 ms exposure time. Figure 4-5 is a simulated above focus feature, with a focus of 20 μm and 26 ms exposure time. Figure 4-6 displays a simulated below focus feature, with a focus of -35 μm and 26 ms exposure time. Finally, Figure 4-7 demonstrates the effect of tilting the beam ($\theta = 10°$) on a simulated below focus feature, with a focus of -30 μm and 26 ms exposure time. Subfigures (a) show the PAC concentration after exposure. Subfigures (b) present a binarized image of the theoretical feature shape where only locations of PAC concentrations less than 0.01 are shown in black. Development chemistry is difficult to analytically model, though a number of theories exist [32]. For simplicity, and based on qualitative observation in experimentation, it was assumed that any portion of the resist with a PAC concentration at least three orders of magnitude less than unity would be removed in developmnet, and the resulting vacancy filled in with PDMS to create the tool feature.

Figure 4-4 shows the ideal scenario of a vertical sidewall. The above focus feature exhibits rounding as depth into the resist increases, while the below focus feature shows a tapered but nearly straight sidewall. Both features follow characteristic obervations recorded by lithography pioneer Mack regarding feature shape changes as a function of focus (shifting

plane highest light intensity) [32]. Figure 4-7 presents an asymmetric feature cross-section, one similar to experimentally observed features in PDMS [11]. For creating more complex and varying feature geometries, the focal point can be shift wihtin the exposure time [38].

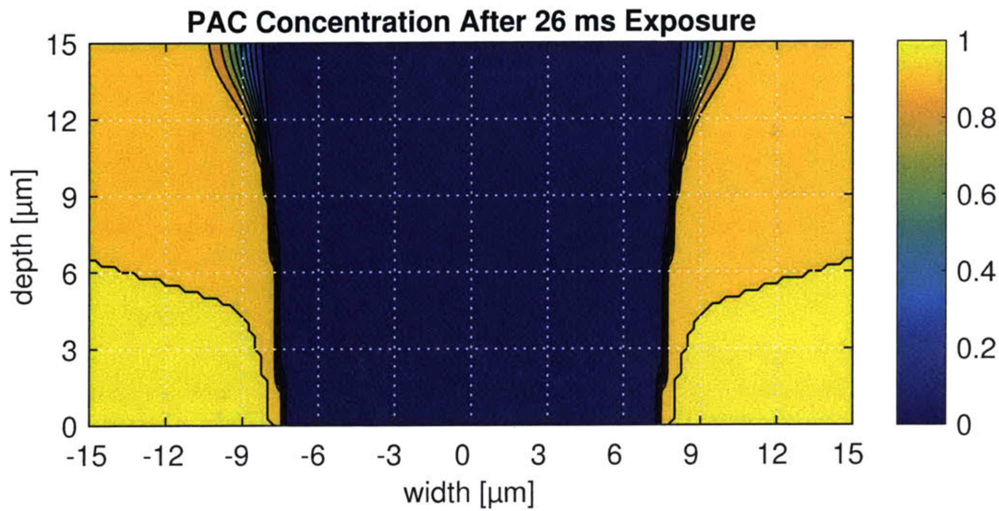

(a) Simulated photoactive compound (PAC) concentration for a focus of 0 microns

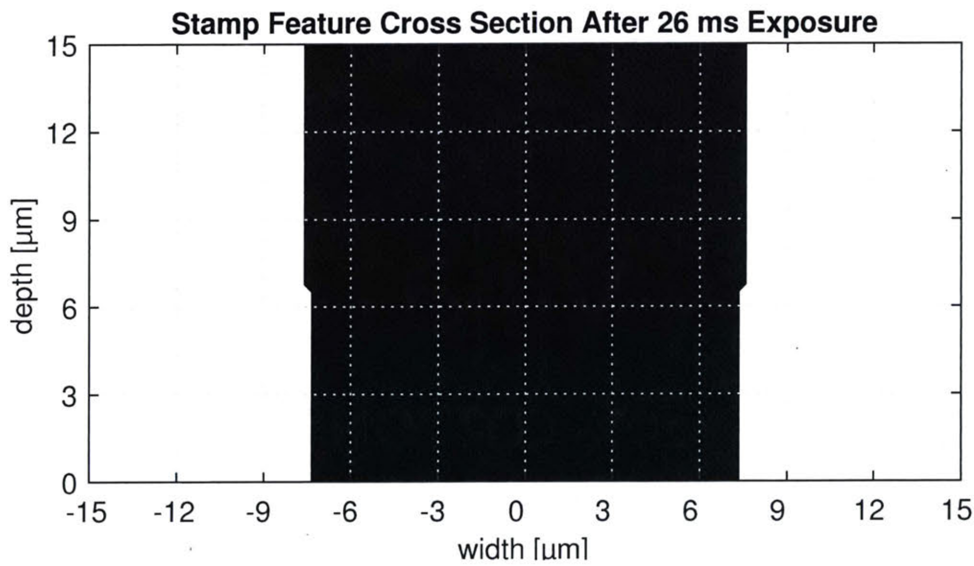

(b) Simulated stamp cross section shape (PAC < 0.01) for a focus of 0 microns.

Figure 4-4: A single exposure simulation for a focus of 0 microns and 26 ms exposure time. The ideal focus position of f=0 yields vertical feature sidewalls.

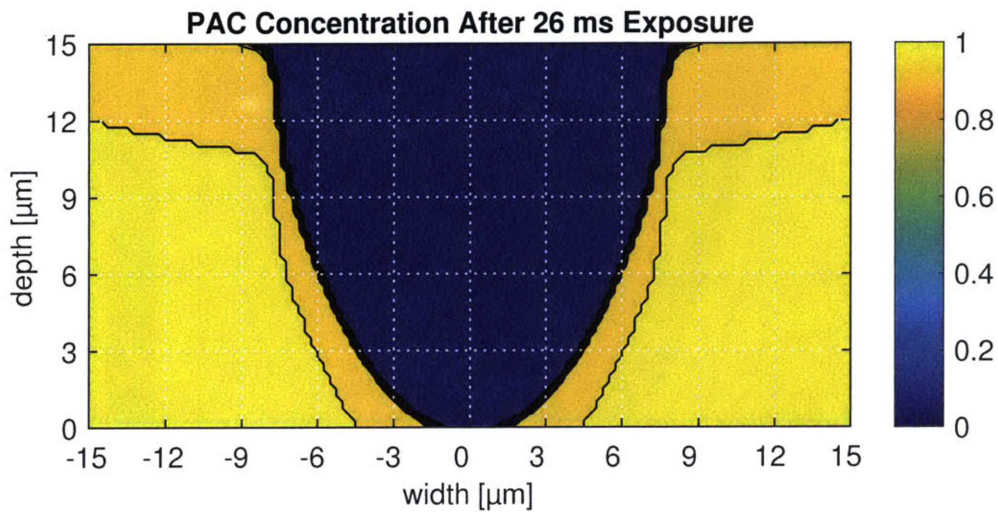

(a) Simulated photoactive compound (PAC) concentration for a focus of 20 microns.

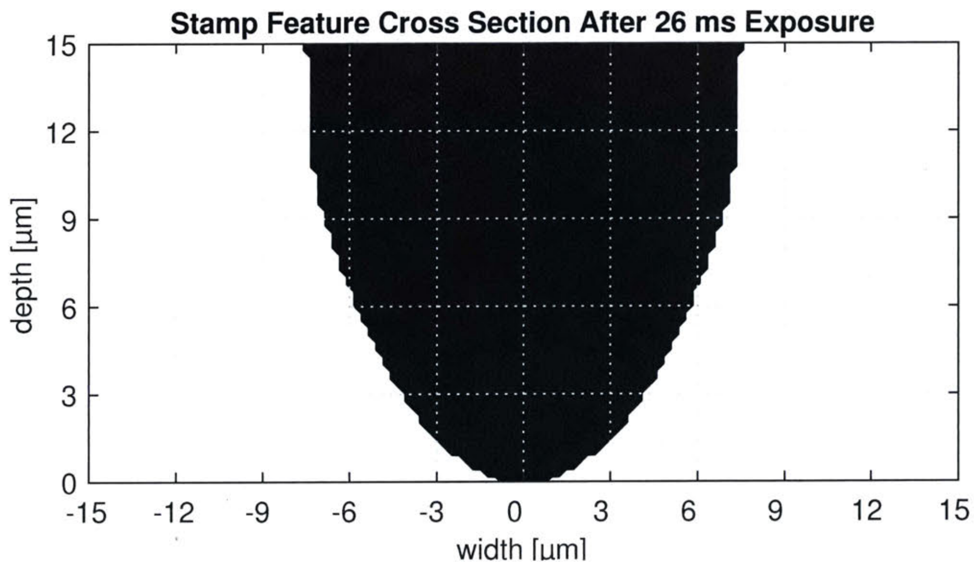

(b) Simulated stamp cross section shape (PAC < 0.01) for a focus of 20 microns.

Figure 4-5: A single exposure simulation for a focus of 20 microns and 26 ms exposure time. Rounded features are characteristic of of an above focus scenario.

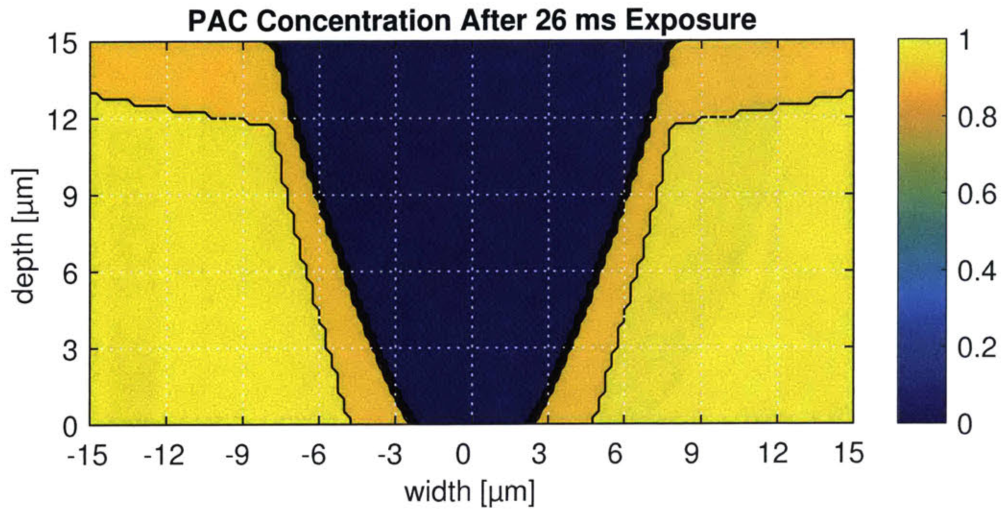

(a) Simulated photoactive compound (PAC) concentration for a focus of -35 microns.

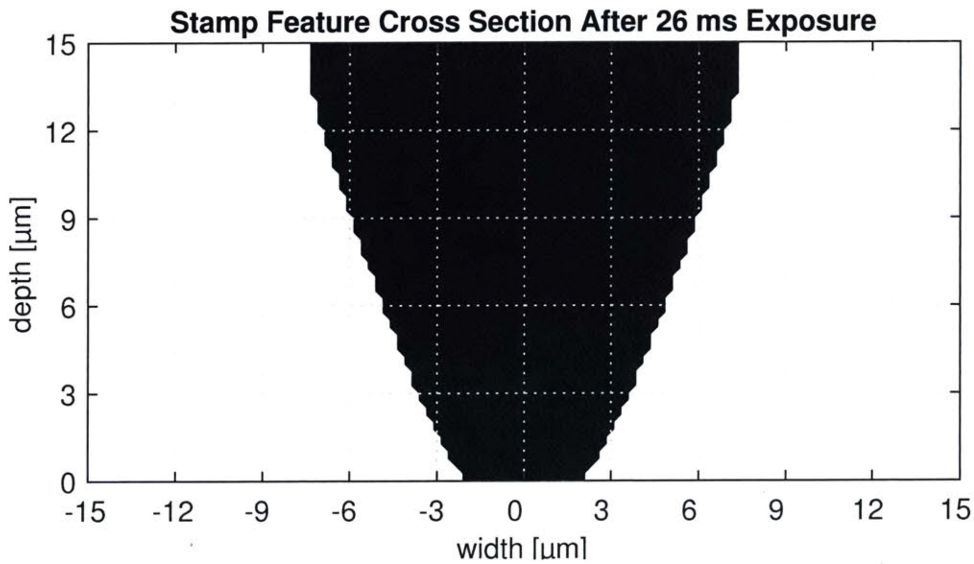

(b) Simulated stamp cross section shape (PAC < 0.01) for a focus of -35 microns.

Figure 4-6: A single exposure simulation for a focus of -35 microns and 26 ms exposure time. Straight, tapered sidewalls are indicitive of a below focus feature.

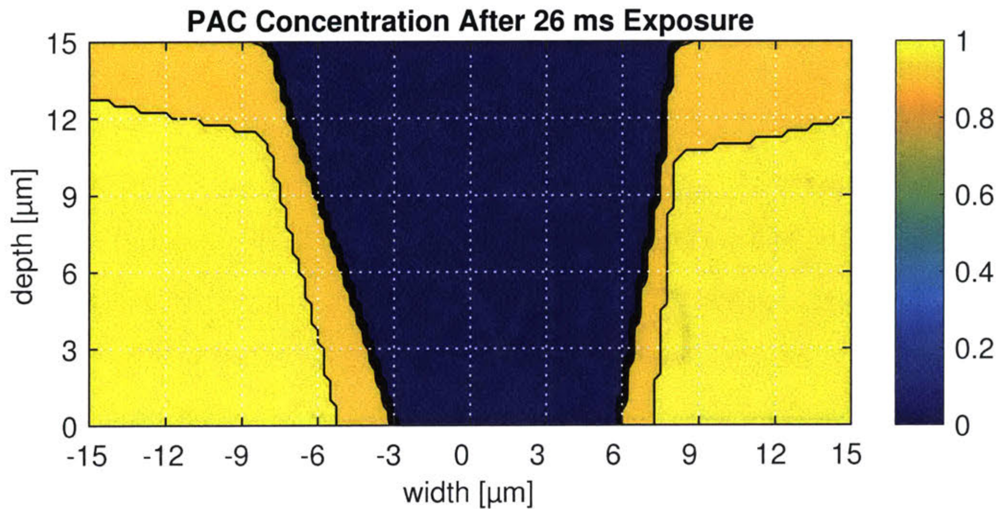

(a) Simulated photoactive compound (PAC) concentration for a focus of -35 microns and beam tilt of 10 degrees.

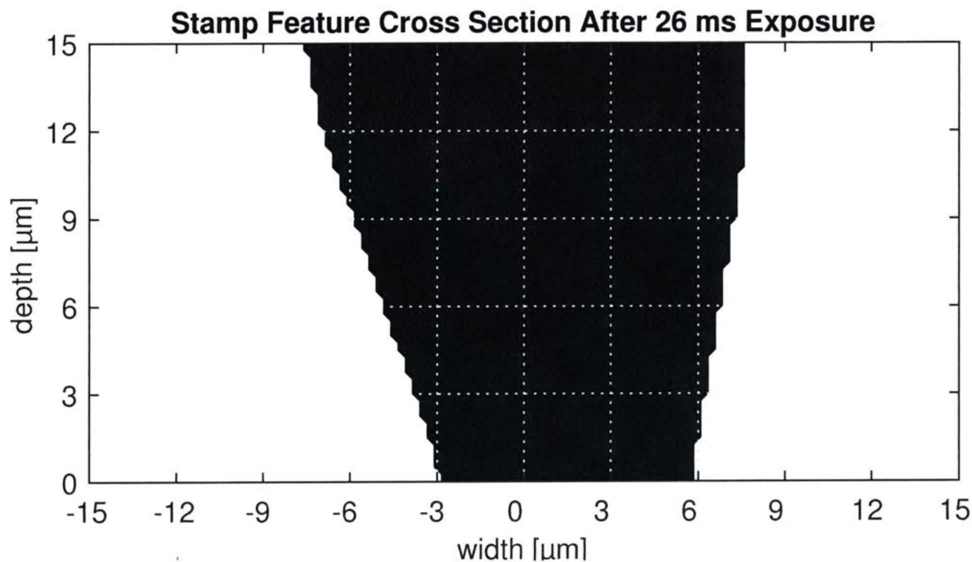

(b) Simulated stamp cross section shape (PAC < 0.01) for a focus of -35 microns and beam tilt of 10 degrees.

Figure 4-7: A single exposure simulation for a focus of -35 microns, beam tilt of 10 degrees, and 26 ms exposure time. The deviation from perpendicularity of the beam axis relative to the photoresist top surface yields an asymmetric feature

Figures 4-8, 4-9, and 4-10 present plots of the simulated feature root width as function of focus and exposure time for resist thicknesses of 5 μm, 10 μm, and 15 μm respectively. The simulation shows that root width is independent of exposure and nearly independent of focus. The 0.5 μm observed step is a mesh artifact (0.25 μm sidelength in a symmetric simulation). Figures 4-11, 4-12, and 4-13 displays plots of the corresponding feature top widths for resist thickness of 5 μm, 10 μm, and 15 μm respectively. Top width is measured as the width of the feature that intersects the line $y = thickness_{photoresist}$ in the schematic's coordinate system. If the feature does not intersect this line, corresponding to an exposure that does not bottom out against the SU8 planarizing layer, top width is reported as zero. Top width appears only slightly asymmetric with focus, and decerease as focus deviates from zero. Top width logically decreases with exposure dose, as less radiation propogates into the resist. Most importantly the range of focus values promoting a maximum top width of 15 μm decreases from a 20 μm window to a 10 μm window at the current resolution, as resist thickness increases from 5 μm to 15 μm at the benchmark exposure time of 26 ms.

Finally, Figures 4-14, 4-15, and 4-16 show feature height trends at 5 μm, 10 μm, and 15 μm respectively. Height was measured as the maximum y value along the x-axis of the binarized geometry. Similar to top width, feature height is very sensitive to exposure dose. AS dose increases, light propogates further into the resist and more PAC is converted. Additionally, height exhibits a more pronounced asymmetry to focus. Below focus features bottom out for larger absolute values of focus than above focus features. Recall the example features. An above focus scenario rapidly rounded the feature, while a below focus scenario merely tapered the sidewall (at much more significant focus error). The difference in response is caused by the plane of maximum laser intensity (focal point) penetrating into the resist in below focus while above focus scenarios perform the opposite effect of decreasing the intensity incident on the photoresis.

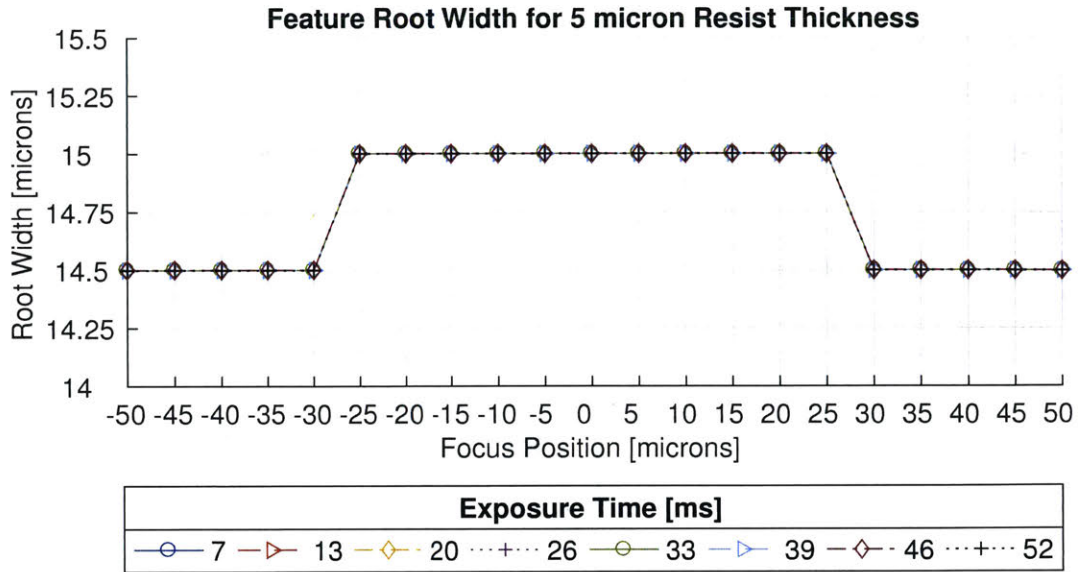

Figure 4-8: Feature root width for a single exposure in 5 micron thick photoresist. Root width appears virtually invariant with changes to exposure time (dose) and focus.

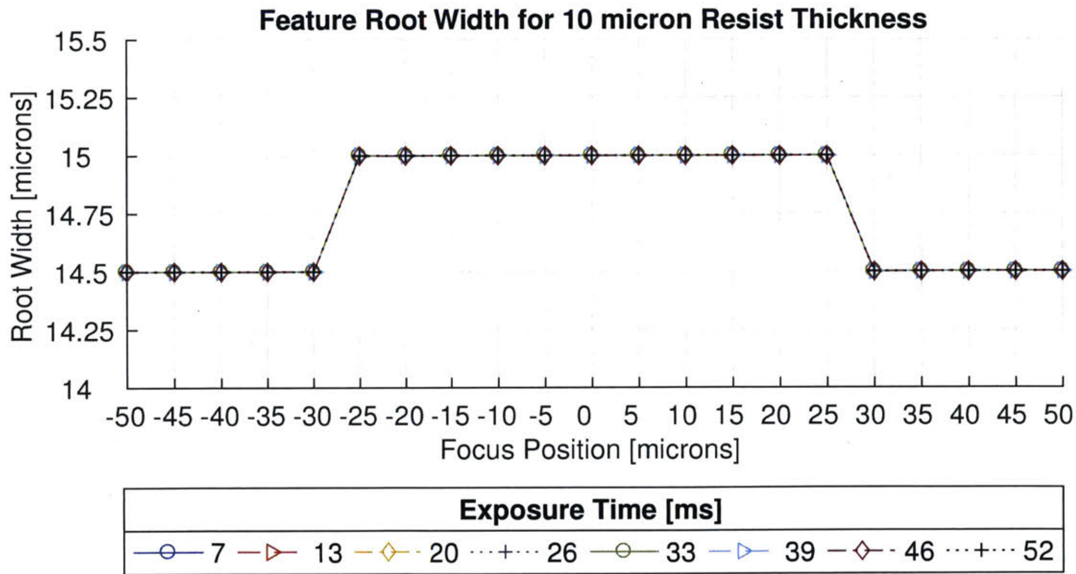

Figure 4-9: Feature root width for a single exposure in 10 micron thick photoresist. Root width appears virtually invariant with changes to exposure time (dose) and focus.

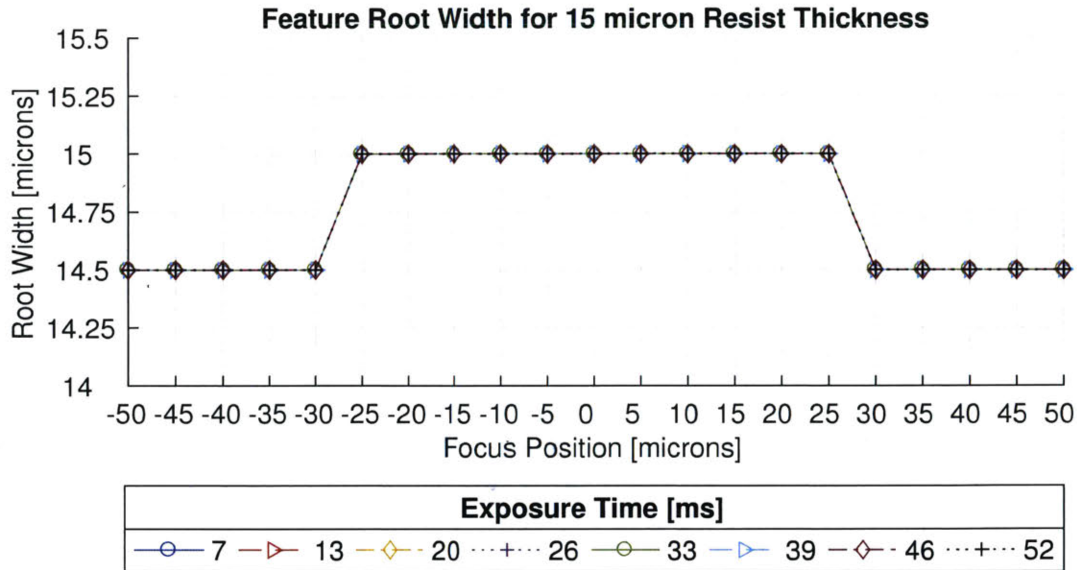

Figure 4-10: Feature root width for a single exposure in 15 micron thick photoresist. Root width appears virtually invariant with changes to exposure time (dose) and focus.

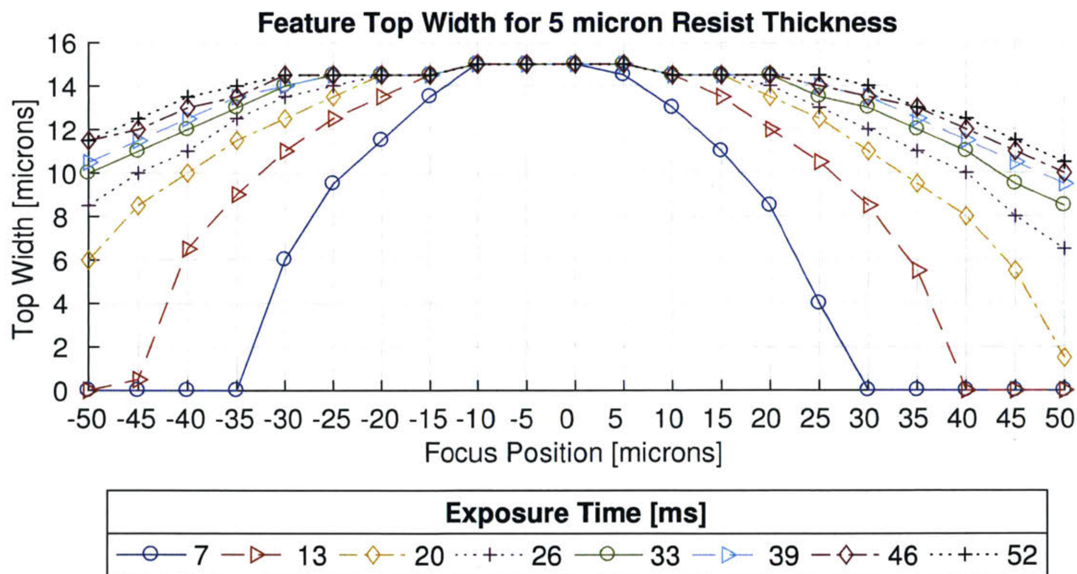

Figure 4-11: Feature top width for a single exposure in 5 micron thick photoresist. Top width decreases significantly with focusing errors, though is slightly less sensitive to below focus. Focusing errors can be compensated for by increasing exposure time (dose), which minimizes dimensional sensitivity to focus.

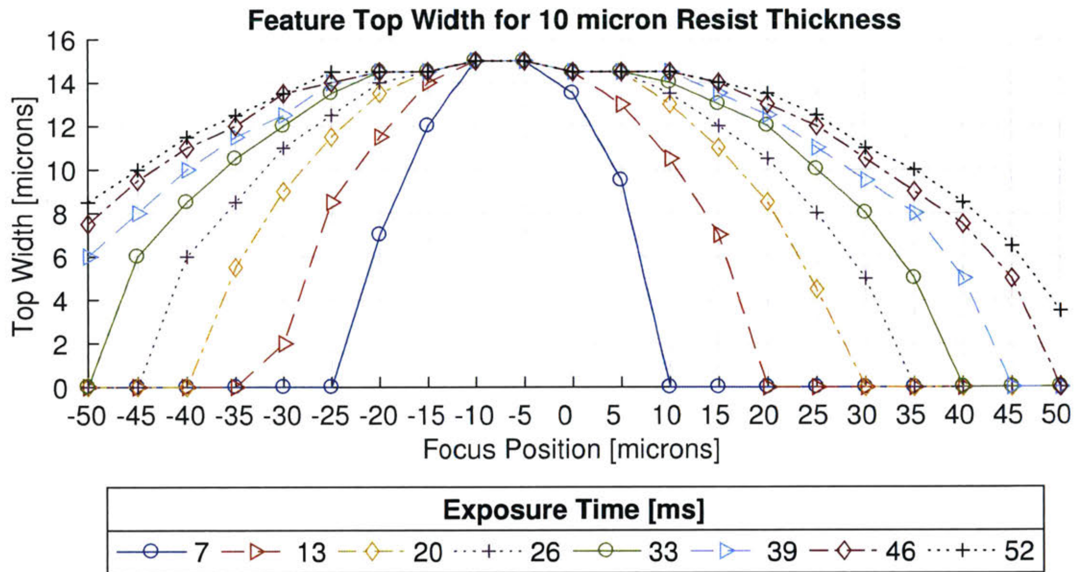

Figure 4-12: Feature top width for a single exposure in 10 micron thick photoresist. Top width decreases significantly with focusing errors, though is slightly less sensitive to below focus. Focusing errors can be compensated for by increasing exposure time (dose), which minimizes dimensional sensitivity to focus

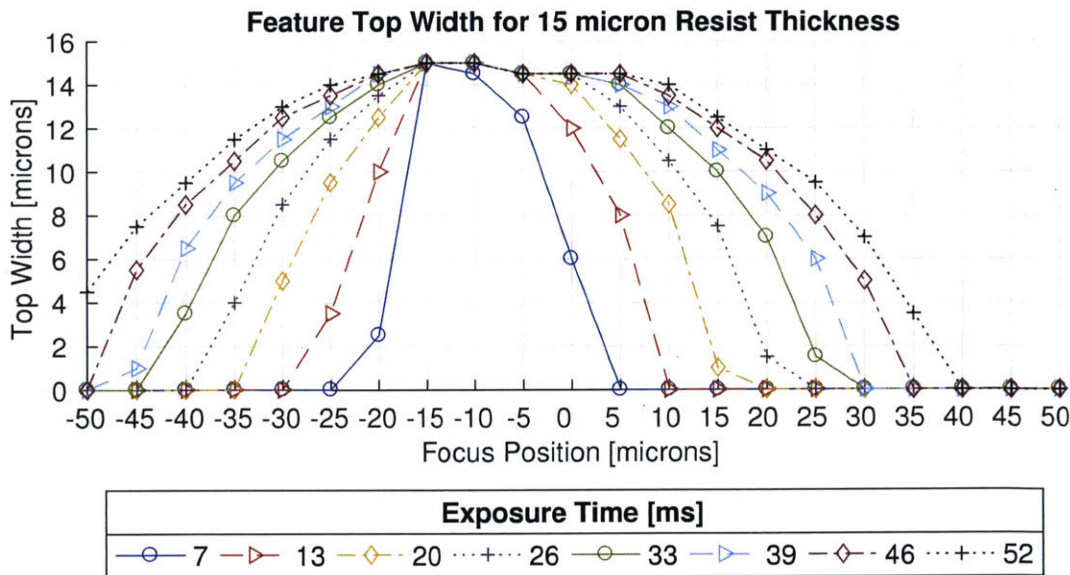

Figure 4-13: Feature top width for a single exposure in 15 micron thick photoresist. Top width decreases significantly with focusing errors, though is slightly less sensitive to below focus. Focusing errors can be compensated for by increasing exposure time (dose), which minimizes dimensional sensitivity to focus

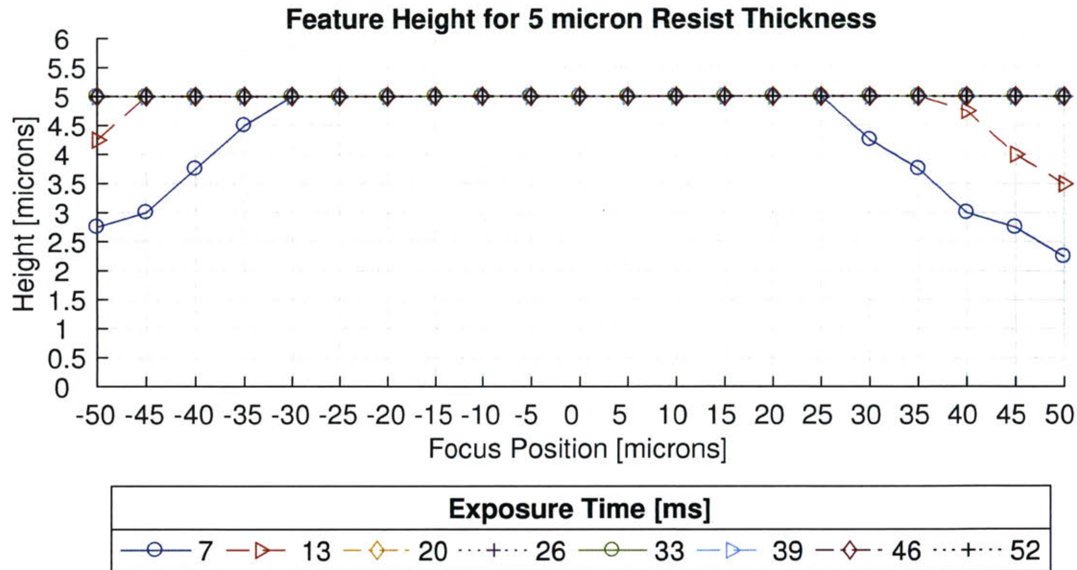

Figure 4-14: Feature height for a single exposure in 5 micron thick photoresist. Height decreases with deviations in focus, but is less sensitive than the top width dimension. Longer exposure times (higher doses) promote bottoming out the exposure against the SU8 substrate, and exhibit a favorable asymmetry towards below focus.

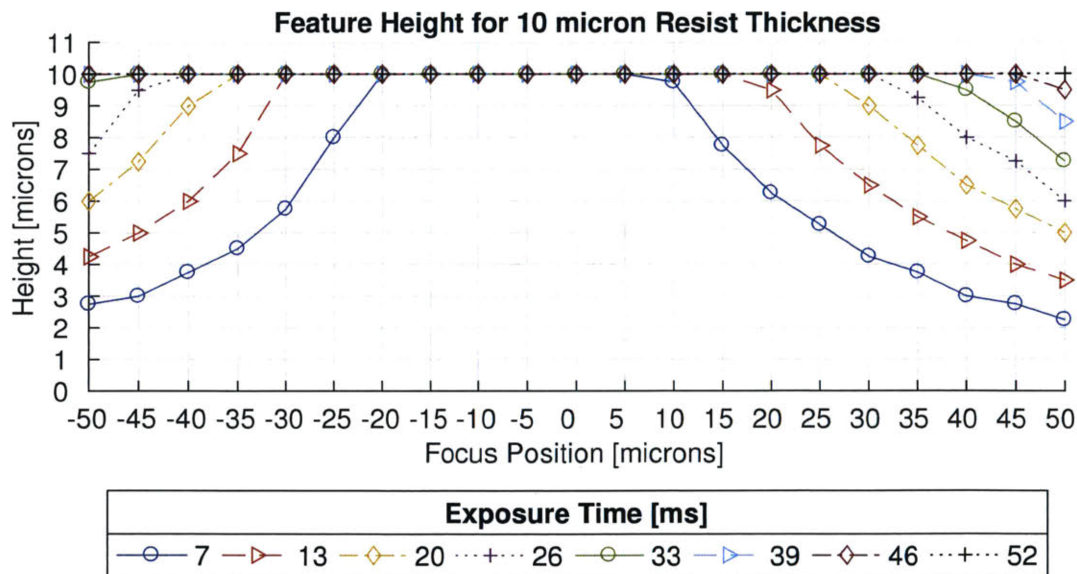

Figure 4-15: Feature height for a single exposure in 10 micron thick photoresist. Height decreases with deviations in focus, but is less sensitive than the top width dimension. Longer exposure times (higher doses) promote bottoming out the exposure against the SU8 substrate, and exhibit a favorable asymmetry towards below focus.

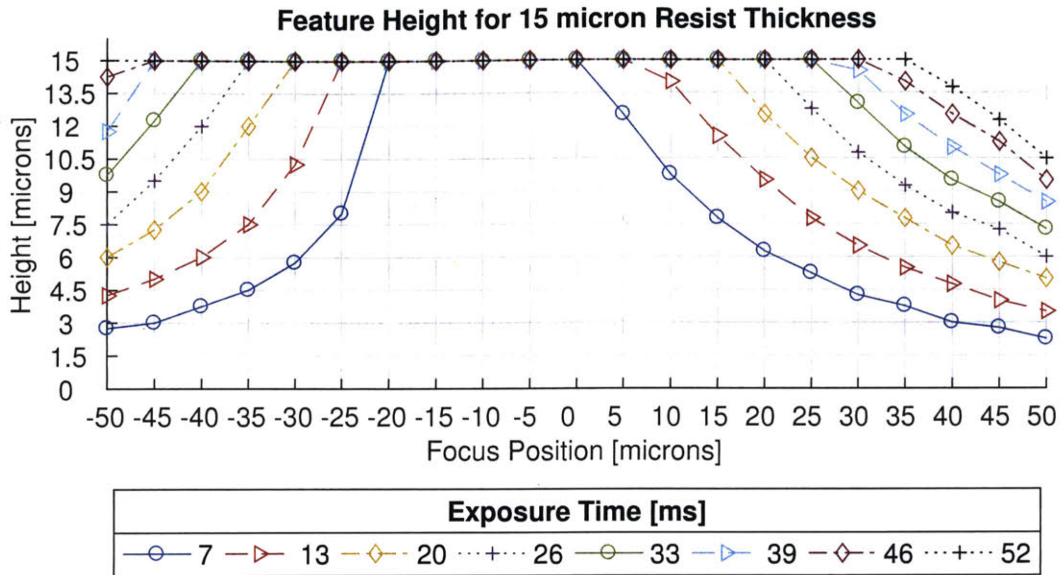

Figure 4-16: Feature height for a single exposure in 15 micron thick photoresist. Height decreases with deviations in focus, but is less sensitive than the top width dimension. Longer exposure times (higher doses) promote bottoming out the exposure against the SU8 substrate, and exhibit a favorable asymmetry towards below focus.

Overall, these single exposure simulation results provide a few key insights. A thinner photoresist is less sensitive to focus and dose variations, leading to more uniform feature shapes. Deviations from $f = 0$ to below focus can tolerate larger errors than above focus scenarios before losing a distinct top width, and full-thickness feature height. Additionally, below focus features exhibit tapered sidewalls compared to rounded sidewalls in above focus features. Lastly, higher doses can compensate for focusing errors. Logically, adding additional exposure time for a decreased incident intensity will increase the amount of absorbed radiation. These results yield a theoretical path for increaseing feature uniformity: err on the side of higher doses, below focus, and thinner resist films when possible.

4.1.3 Multi-Exposure Features

Single expouse simulations provided an understanding for general feature shape. However, a direct-write, laser-scribe approach to lithography severely limits feature geometries to what can typically be formed in a single exposure. Overlapping subsequent exposures, or different lasers and optics sets could be used to change the effective exposure size and shape, as well as the intensity distribution. In the centrifugal caster setup, the concept of using multiple partially-overlapping exposures gives way to new feature types useful for proving the flexiblity of the centrifugal casting system at creating a diverse set of features for μCP tools. Circumferential features could be widened by writing two slightly offset lines, and even axially-oriented features could be constructed by overlapping dots.

Single exposure results were combined via the multiplicative method in Equation 4.9 to simulate two partially overlapping exposures. A third input, the axial offset of exposures, ranging from 1 μm to 20 μm in 1 μm increments was created. Root width, top width, and feature height were again studied, but now as a function of three input variables. Figure 4-17 shows a simulated feature created via two identical exposures (the scenario in Figure 4-6, offset by 6 μm). All overlapping exposure simulations were created with two identical single exposure scenarios, axially offset from eachother. The example double exposure feature nearly doubles the top width and root width dimensions. However, the sidewall profile remains consistent with the single exposure result. From a PAC-conversion standpoint, multiple exposures can clearly adjust feature geometry. For large offsets between exposures, the local cumulative dose on the resist remains close to that of a single exposure and features widen while maintaining the same sidewall profile, possibly to the extent that the top width is discontinuous. For small offsets, the cumulative dose approaches the sum of the individual exposures and feature geometry change is less severe.

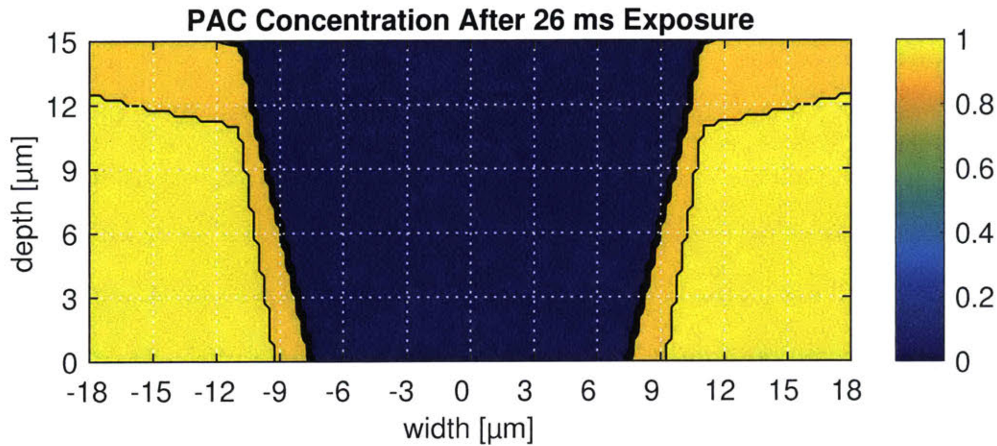

(a) Simulated photoactive compound (PAC) concentration for an overlapping feature with focus of -35 microns and exposure offset of 6 microns.

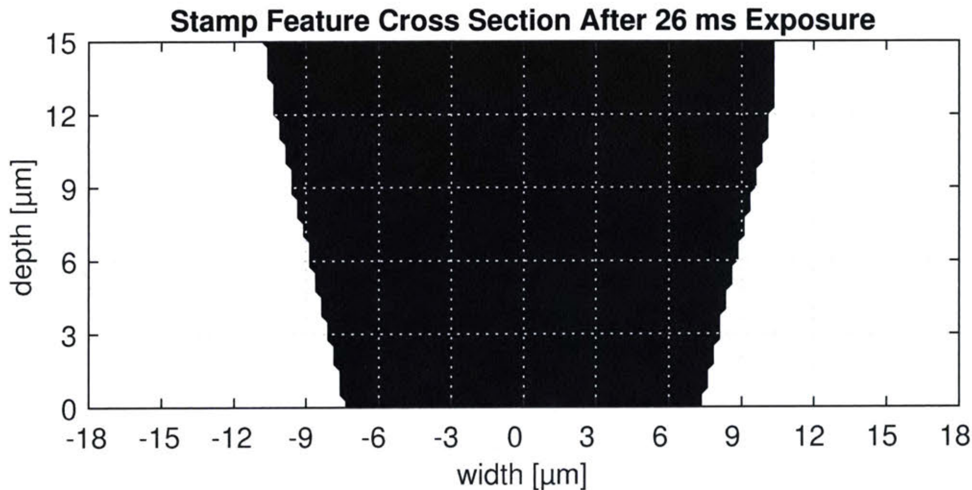

(b) Simulated stamp cross section shape (PAC < 0.01) for an overlapping feature with focus of -35 microns and exposure offset of 6 microns.

Figure 4-17: An overlapping exposure simulation for a focus of -35 microns and an exposure offset of 6 microns. The 26 ms exposure refers to each individual exposure, indicating that this feature require a net 52 ms exposure time.

Root width, top width, and height for multiple exposures present the same conclusions of the single exposure simulations. Similarly, feature uniformity was shown to be more easily achieved by using higher exposure dose, thinner resist thickness, and targeting ideal or below focus scenarios. Three new findings arose, which significantly impact the concept of

arbitrarily patterned tools. First, as shown in Figure 4-17, sidewall profiles remain consistent with the singe exposure result. Second, top widths can be increased with an increasing offset between subsequent exposures (Figure 4-18). Note the favorable bias towards below-focus exposures in the top width trend. Finally, a desired top width, root width, or height can be achieved by various exposure scenarios. Referring to Figure 4-18 for example, a top width of 20 μm can be created using an offset of 13 μm and a focus of 20 μm, or an offset of 6 μm and focus of -20 μm. This claim is in the context of PAC conversion. Therefore, physical lithography limitations can potentially be overcome by a different set of inputs should the real system respond negatively due to unmodeled factors or hardware and software constraints.

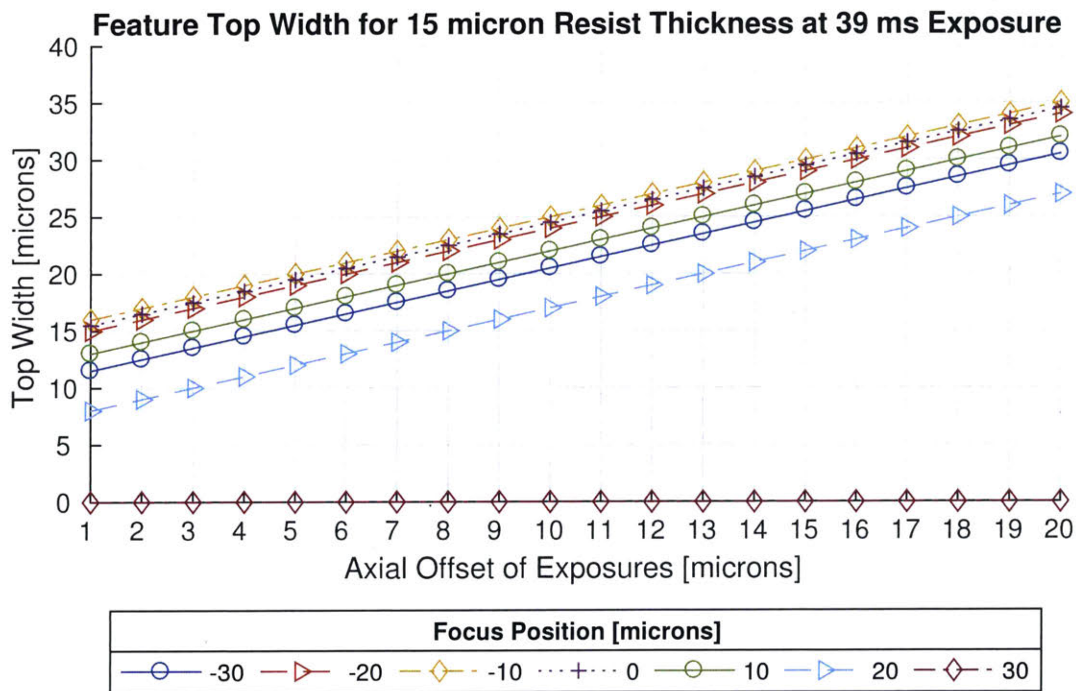

Figure 4-18: Feature top width for two exposures of 39 ms each, in 15 micron thick photoresist. Top width linearly grows with increase axial offset at a rate of 1 micron per micron. Null width indicates that the exposure did not permeate full resist thickness.

4.2 Characterization of Machine Errors

Simulation results identified significant correlations between exposure parameters and feature shape. Variations in focus, exposure dose, and resist properties yield different stamp cross section geometries. Concern was placed on evaluating the centrifugal caster setup for intrinsic errors that would impact exposure of the photoresist and the ultimate feature shape. Error motions of the linear stage were measured to understand changes in beam length (focal point position) as the stage traversed the writing locations. An attempt was made at verifying the flatness of the planarizing layer to confirm that bottoming out should result in flat tops. Finally measurements to qualify the uniformity and repeatability of the thermal system were taken since poor thermal control can create a non-uniform distribution of photoresist properties (see Section 4.3.2.

4.2.1 Linear Stage Error Motions

Error motions of the linear stage result in a change in laser beam length in the centrifugal caster setup. The caster does have an autofocus system, therefore, the laser is constantly focused at a fixed distance downsteam of the light path from the diode source. Clearly, motions of the cantilevered optics will change the focus position relative to the photoresist. A fiber optic displacement sensor (muDMS-RC100-T5 by Philtec Inc.) was kinematically mounted to the linear stage, and positioned in the same cantilevered axial location as the 90° mirror to accurately capture Abbe error. A polished stainless steel plate was mounted in place of the centrifuge drum because the sensor required a specular surface for accurate measurement.

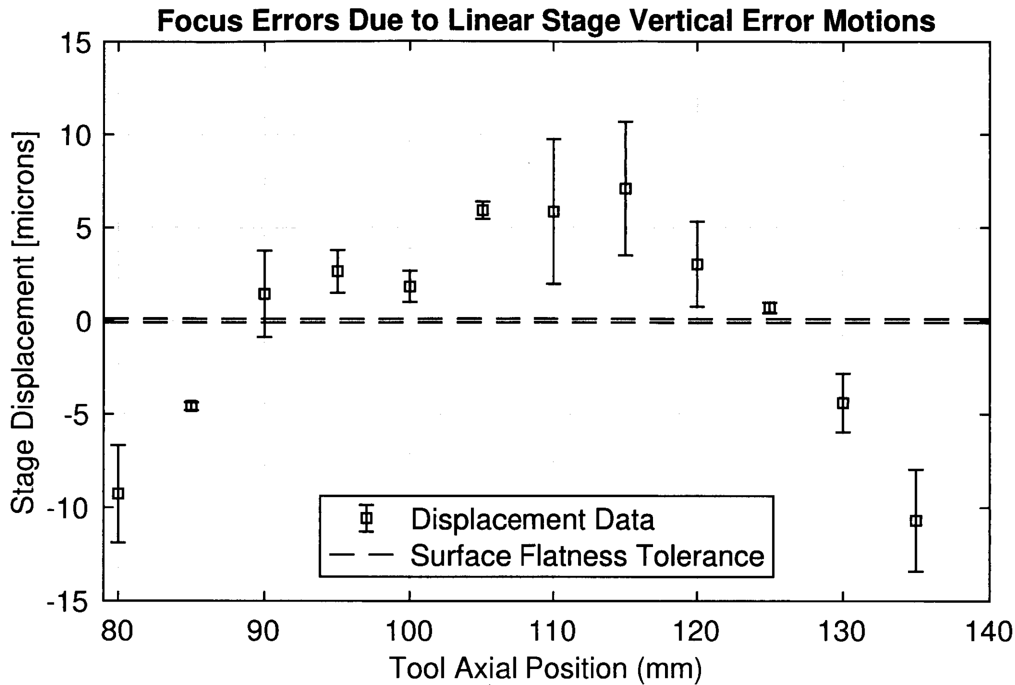

Figure 4-19: Displacement of the linear stage (change in focus) over the axial positions corresponding to tool length. The data presented are mean values recorded from ten trials. Error bars represent one standard deviation above and below the mean value. The data exceed the flatness tolerance of the polished surface used for optical measurement, clearly showing the presence of error motions impacting laser focus.

Figure 4-19 shows the measured relative displacement between the sensor and mirror surface over the writeable axial length of a stamp. Variations in repeatability, and nearly 30 μm displacement spread of the axial length of the stamp indicate critical focus errors. These measurements do not account for drum runnout, eccentricity, or spin axis misalignemnt with the optical axis, all of which undoubtly contribute further to focusing errors. These data help explain the witnessed variations in feature shape and establish the requirement for autofocus in future centrifugal casting systems [16].

4.2.2 Planarizing Layer Flatness

The flatness of the planarizing layer was analyzed to ensure that flat tops should form given proper exposure and focus inputs. A PDMS mold (featureless stamp) of a new SU8 planarizing layer was analyzed with Atomic Force Microscopy (AFM). A Veeco Dimension 3100 SPM in tapping mode measured the surface roughness of a 1 μm by 1 μm section of

PDMS casts against the SU8. Figure 4-20 shows the result, incredibly low roughness of about 10 nanometers. The planaring layer could be damaged over time through patterning layer castings, and tool castings, though it likely will not degrade or reshaped on its own [39]. Fortunately, the data suggests that the planarizing layer at least cures flat as intended.

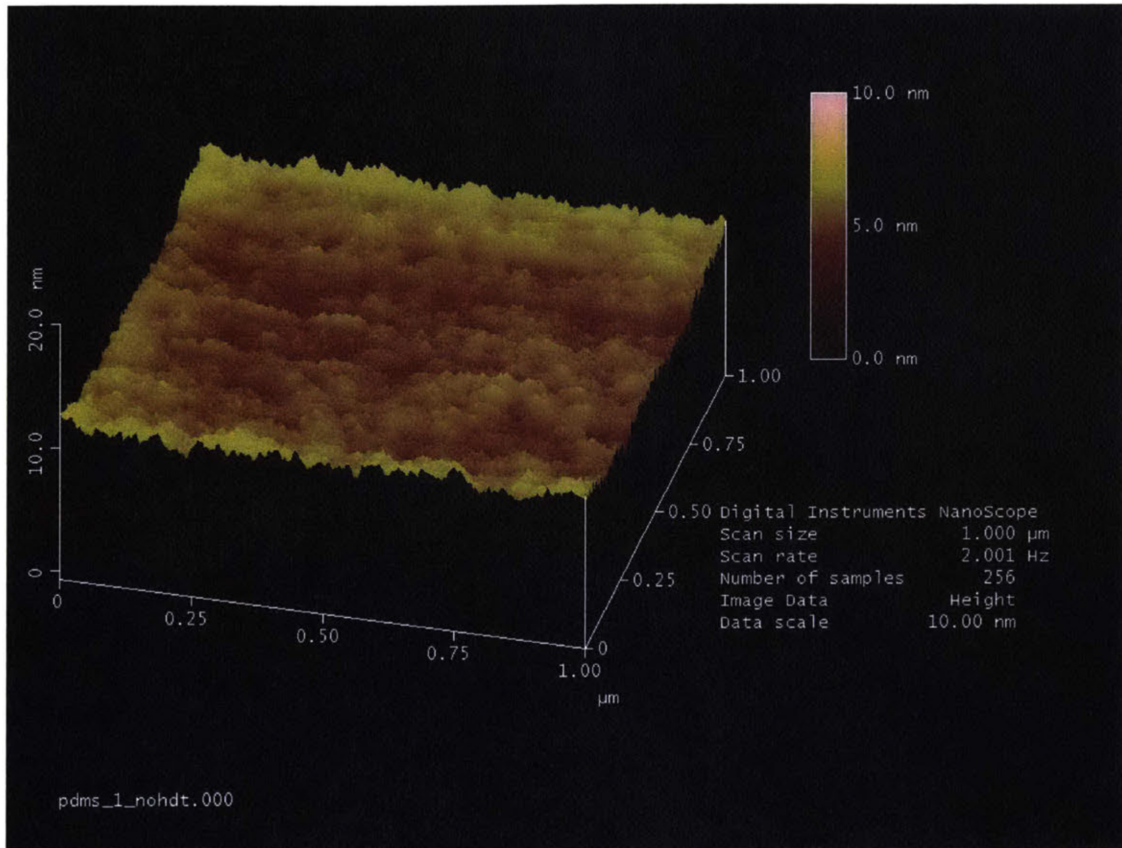

Figure 4-20: Atomic force microscopy (AFM) of a PDMS mold of the SU8 surface. Only a few nanometers of roughness suggest that the planarizing layer is indeed flat after casting.

4.2.3 Thermal Processing Uniformity and Repeatability

Thermal performance of the centrifugal caster was analyzed in two ways. First, measurements of the centrifuge temperature at different axial positions were recorded to check for thermal uniformity. Second, thermal rise trajectories between 60°C and 110°C bakes were obtained to study baking transients.

Figure 4-21 plots a temperature distribution of the axial length of the tool in the centrifuge drum. The thermal system was turned on as it would be in patterning layer casting, but without a set point. Eventually an equilibrium was achieved between the heat gun input

and the forced convective cooling. Once at steady state, the infrared temperature sensor was translated to observe centrifuge temperature at different drum axial positions. The data show an axial temperature distribution on the order of a f5°C. The temperature sensor is nominally mounted at the about the 100 mm axial position, and thus records the highest temperature. It is important to note that thermal equilibirum of the system at full power is very near the softbake operating temperature of 110°C, which may be responsible for large variations in transient rise time to the softbake.

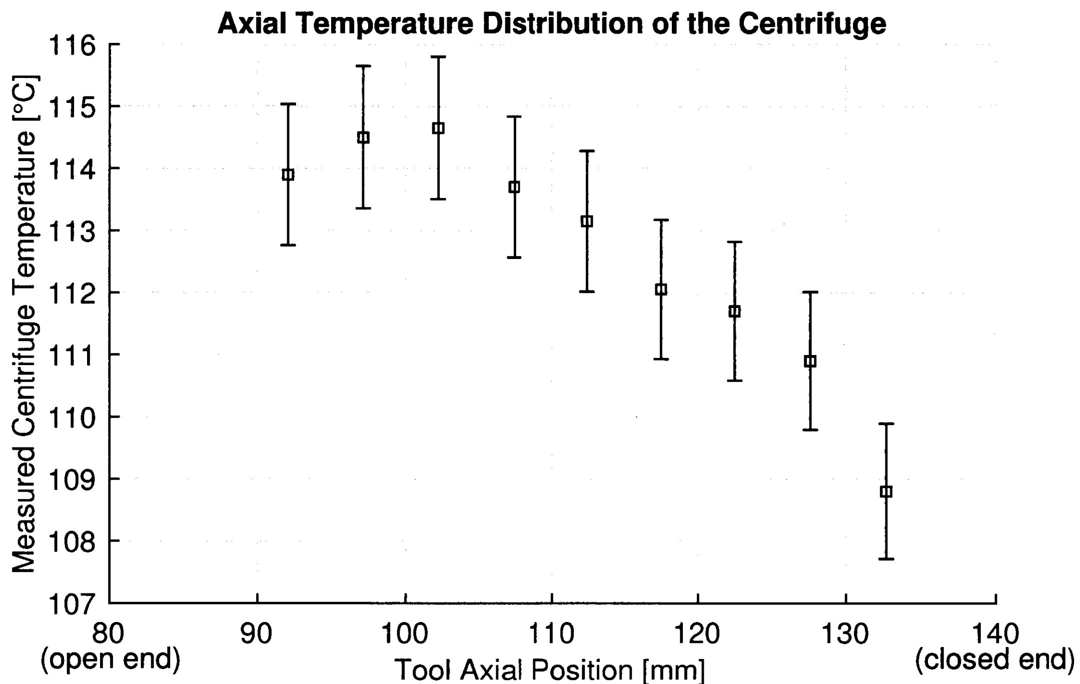

Figure 4-21: Axial temperature distribution of the centrifuge drum at thermal equilibrium. Temperature varies over 5°C. The open end of the drum (near an axial position of 80 mm) is substantially warmer than the mounted end of the drum (near an axial position of 140 mm).

Figure 4-22 plots two closed loop thermal transient rises to the softbake temperature. Again, the thermal system exhibits large variation. The second trial takes nearly 25% more time to reach the set point compared to the first trial. The variation in the data show a lack of tight control in the thermal system. As Section 4.3.2 will expalin, significantly different bake times and temperatures can drastically impact how the photoresist behaves upon exposure. The heating discrepancies, coupled with focusing errors, suggest that features may only be consistent in shape over small areas of the photoresist.

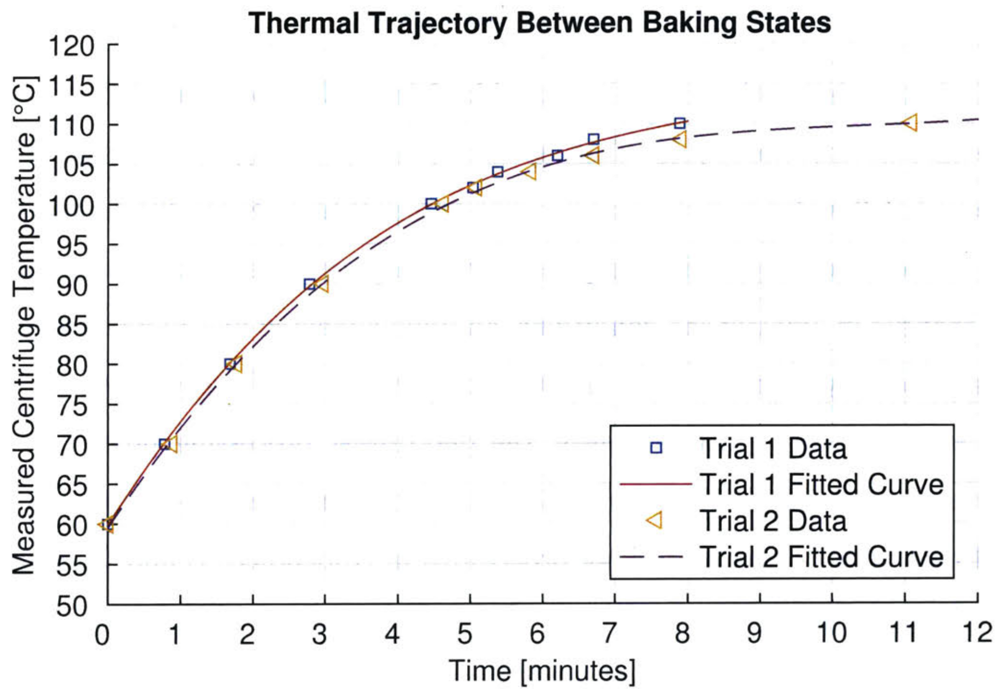

Figure 4-22: Two thermal transisent trajectories to the softbake set point of 110°C. The two trials both take minutes to rise, though the second extends about three minutes longer. The variation shows that the patterning layer cast in the second trial received about 25% more energy input due to the transient process.

4.3 Photoresist Processing

A number of photoresist defects were observed throughout this thesis. This sections summarizes experimental results, details procedural changes in the casting process, and presents findings in the literature surrounding the processing of thick-film photoresists. A working procedure for casting the planarizing layer is proposed, and is discussed in the context of photoresist processing chemistry.

4.3.1 Defects and Processing Optimization

The AZ 9260 photoresist casting procedure used by Nietner led to severe defects when tools started to be cast for this thesis [11]. Castings took place following the redesign of the LabVIEW software to allow for raster-scanning exposure patterns. Some fundamental change had occured. Differences in chemical response between photoresist batches, severe and undocumented changes in ambient lab conditions, an undocumented and unintentional process step having a secondary effect, or even undetected hardware / software issues, were all possible sources of discrepency. Consequently, the photoresist processing procedure required thorough testing and reoptimization. For documentation purposes, this section outlines the experimental path used to create working procedures in Appendices B and C. Section 4.3.2 thoroughly references processing guidelines, theoretical reaction mechanisms, and experimental observations from literature that guided the process.

Many photoresist and PDMS casting tests were run. Generalized experimental sets are outlined below to summarize the defects, parameter adjustments, and results utlimately leading to a working casting process. Parallel literature review, disccussions with MEMS experts, and experimental outcomes guided the re-optimization path. Recommendations from literature were ignored if they contradicted with experimental results for this application. Unless otherwise noted, features were written at 1.5 rev/s, full laser power, and an axial pitch of 100 μm to replicate the tool succesffuly used by Merian for printing [6].

1. Nietner's procedure yielded bubbling and peel-off defects that appeared during the casting of the PDMS stamp. Figure 4-23 shows photographs of the defects in the photoresist planarizing layer cast inside the centrifuge drum. Figure 4-24 presents

the corresponding macroscopic-level defects transfered onto a PDMS tool. Figure 4-25 provides microscopic images of the PDMS, which reveal significant damage to the stamp features. Obviously unusable tools were created. Further experiments adjusting parameters were run to isolate the problematic step in the tool-making process.

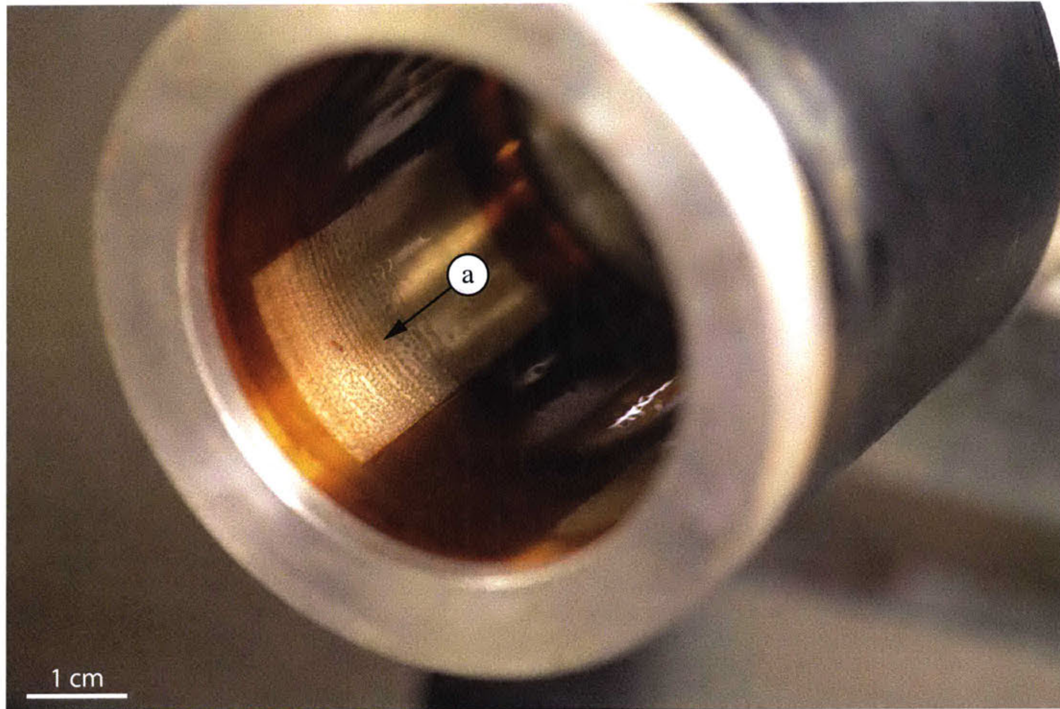

(a) Bubble (a) defects in the exposed region of the AZ 9260 photoresist after casting but prior to tool removal.

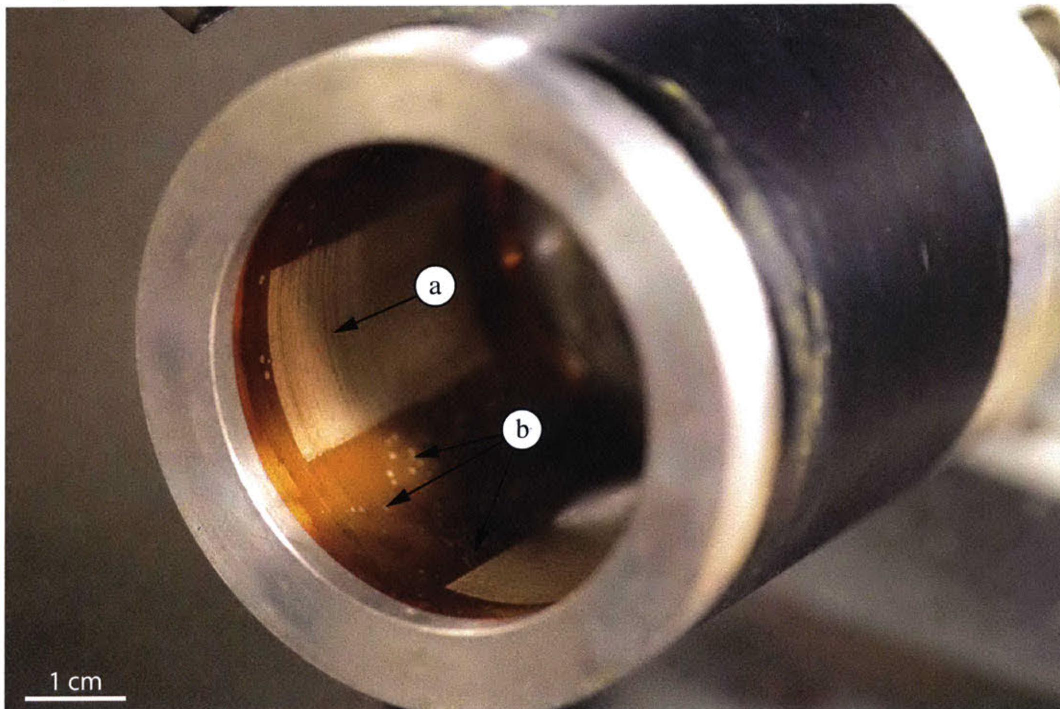

(b) Bubble (a) and peel-off (b) defects in the AZ 9260 photoresist after tool casting and removal.

Figure 4-23: Defects in the AZ 9260 photoresist using Nietner's tool fabrication process [11]. Bubbles emerged during the PDMS casting step. Removal of the tool introduced additional resist peel-off defects in the exposed (white) and unexposed regions (amber).

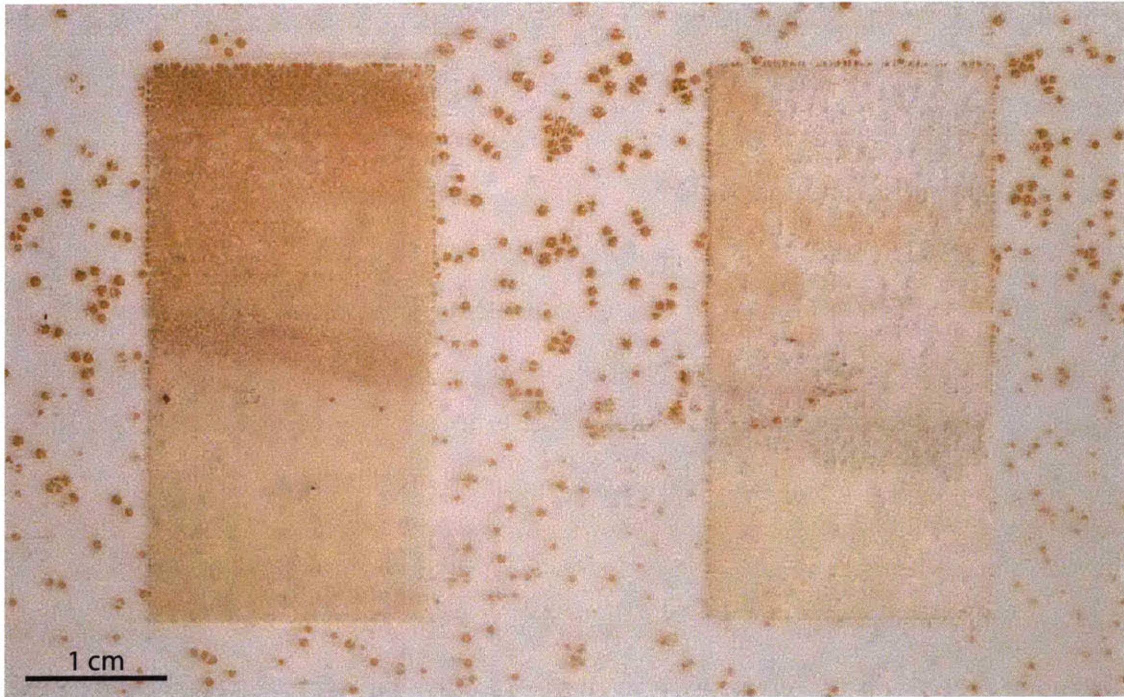

Figure 4-24: Photoresist peel-off and bubble defects in the PDMS tool cast in Figure 4-23. The photograph shows one-half of the clear, PDMS tool against a white background.

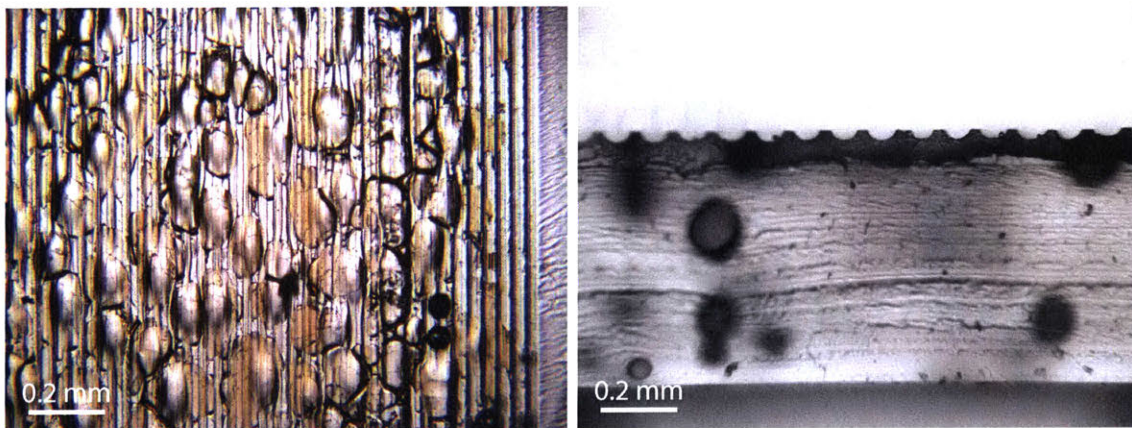

(a) A microscopic top view of bubbling and resist peel-off (amber) transfered onto a PDMS tool.

(b) A microscopic cross section view of damaged features and gas bubbles that did not fully diffuse through the PDMS during tool casting.

Figure 4-25: Microscopic images of bubbles and peel-off defects replicated by the PDMS tool.

2. Experiments were condected to test the hypothesis that improper exposure was the most significant issue. The patterning layer was cast following the original procedure

but exposure skipped, and then a PDMS tool cast. No defects were evident in the photoresist or tool. Using the same patterning layer, exposure was then performed, followed by development and tool casting. Defects emerged as described, placing significant fault on the exposure step of the process, with an understanding that prior processing steps could be inadequately preparing the photoresist for exposure. The resulting bubbles could formed via residual solvent attempting to evaporate during heated PDMS curing, and or exposure products similarly trying to escape the photoresist. Resist peel-off could have been due to insufficient water content in the resist, which is also required for the exposure reaction to proceed properly [36].

3. A one hour process delay between softbake and exposure was added for photoresist rehydration through diffusion of water in the air (humidity). Extended softbake times were also tested in an attempt to evaporate additional solvent. Experimental results showed that the rehydration delay (without humidity control) elminated peel-off in unexposed regions of the resist. Hotter and longer softbakes (such as 5 minutes at 110°C) decreased bubbling and peel-off in the exposed regions of the photoresist but did not eliminate them. Too hot or long of softbakes (such as 15 minutes at 110°C or 5 minutes at 115°C) decomposed too much of the PAC for any features to develop in exposure. Subsequent concern was placed on testing for exposure products since extended softbakes should have eliminated delayed solvent evaporation [36] [39].

4. Assuming exposure products were the issue, and given a correct exposure dose, the reactivity of the PDMS was tested. The observed bubbling could have be exposure products trapped by the PDMS, or reacting with PDMS at the AZ 9260 - PDMS interface. Nietner's procedure with a slightly extended softbake (5 minutes at 110°C) and the included rehydration delay were used in testing. A simulated stamp (no PDMS deposited in the drum, but the centrifuge spun and heated according to tool casting procedures) scenario was run. Bubble defects still emerged in the exposed regions of the photoresist during the thermal processing used to cure the PDMS. Nitrogen gas is produced during exposure if the reaction proceeds properly. Since the defects were clearly not based on a PDMS interaction, effort was then placed outgasing the nitrogen

in a defect-free manner [39].

5. Returning to the original softbake conditions and still implementing a rehydration delay, another hour-long process delay for outgassing was added between exposure and development. Similarly, the PDMS tools were cast the following day after patterning layer casting and cured at room temperature for 24-72 hours. The centrifuge was only spun for the first 8 hours, allowing the PDMS to set. The lack of subsequent heating and additional time delay yielded no photoresist defects. However, room temperature curing times were not consistent and such long cure times would be a huge setback to a scaled-up μCP process. Further system investigation located an error in the LabVIEW software, which led to inconsistent laser performance. Circumferential lines could be written between 100% and 500% the intended dose for a feature written at 9.42 rad/s. Even higher doses were tested by Neitner without defects, demonstrating the complexity of change(s) that occured to the system [11].

6. Proper single exposure (100% dose), the original softbake parameters, a reyhdration delay, and an outgassing delay led to much more functional stamps. A more narrow workable write speed range was determined to be 1 rev/s to 3 rev/s. However, tools could only be cast the day after photoresist casting, and even the PDMS curing would sometimes lead to photoresist features turning a bright red color, and or the emergence of minimal but present bubbling and peel-off. A decrease in PDMS curing temperature was implemented to minimize thermally-induced outgassing and to minimize the chance of the hydrostatic and thermal stresses of tool casting reshaping the resist [40] [41].

7. The final working procedure included a 3 minute and 20 second softbake at 110°C, a one hour process delay between softbake and exposure for rehydration, a one hour process delay between exposure and development for outgassing, followed by an immediate PDMS casting and cure at 60°C for two hours.

To summarize, Table 4.4 presents the generalized procedure and reasoning behind steps and values. The complete procedure is located in Appendices B and C.

Step	Procedure	Reasoning
1	Bake at 60°C for 30 minutes	Taken from Nietner [11], no negative impact observed
2	Soft bake at 110°C for 3 minutes and 20 seconds	Taken from Nietner [11]. Experimentally observed to evaporate sufficient solvent without desensitizing the photoresist, or causing bubbling/foaming
3	1 hour process delay for photoresist rehydration	Experimentally observed to eliminate peel-off defects in unexposed regions of the photoresist
4	Expose the photoresist at full laser power	Experimentally observed poor or no feature formation when laser power was not set to the full 80 mW
5	1 hour process delay for outgassing	Experimentally observed to mitigate bubbles forming in the photoresist following PDMS casting
6	Develop the photoresist at room temperature for 3 minutes and 40 seconds	Taken from Nietner [11], no negative impact observed
7	Cure PDMS stamp at 60°C for 2 hours	Experimentally observed to prevent defects from forming in the PDMS casting step

Table 4.4: procedure

4.3.2 AZ 9260 Photoresist Processing Literature Review

The processing of AZ 9260 in the centrifugal caster, and in most other applications contains three main steps. A pre-exposure bake, exposure, and development. Some applications implement post-exposure and or post-development bakes, though these are very uncommon

for AZ 9260 [32] [36]. AZ 9260 is a positive thick-film resist [31]. Thick resists are cast at film thicknesses larger than the wavelength of light used in exposure. In positive resists, exposed areas are dissolvable in the corresponding developer solution. This section summarizes key lithography physics and observations specifically pertaining to the baking, exposure, and development of AZ 9260, and other thick-film photoresists.

Soft Bake

After applying the photoresist to the substrate, the resist is heated. This step, refered to as the softbake, solidifies the resist, promotes adhesion of the resist to the substrate, and prepares the resist for exposure [42]. Baking should be a tightly controlled and repeatable process. The thermal histroy of the resist should be considered. Time warming up, baking at the desired temperature, and cooling down all impact the resulting resist properties. Typical wafer-based photolithography applications use hot plates and chill plates at the desired baking and cool-down temperatures where repeatable thermal transients are on the order of seconds [32]. For AZ 9260, conductive heating through the substrate leads to the best resist performance. Air convection over the free surface as a dominant heating method, such as using a convection oven, dries the free surface of the photoresist, preventing the evaporation of much of the solvent volume [36].

The softbake evaporates solvent from the photoresist, decomposes the PAC, and impacts the development rate. AZ 9260 is diluted in PGMEA[2] (solvent) for deposition to the substrate , increasing the solvent volume but decreasing photoresist viscosity [43] [44]. The resist itself already contains some solvent, though the exact amount and resulting resist viscosity depends on storage conditions and age [45]. Too much solvent in the resist allows diffusion of developer reactants into the unexposed resist increasing the undesirable dark erosion rate [42]. Conversely, some solvent presence is required for the diffusion of exposure products [32].

The trade-off to lengthier or hotter baking is the decomposition of the PAC. AZ 9260 uses the common sensitizer diazonaphthoquinone (DNQ) as the PAC. Most positive DNQ resists exhibit sensitizer decomposition at temperatures above 70°C. While a compromise between

[2]Propylene glycol monomethyl ether acetate

PAC decomposition and solvent evaporation can lead to a range of workable softbakes for a given process, too short and cool, or too hot and long of softbakes both lead severe defects in the form of embrittling and bubbling of the photoresist [46]. If no softbake benchmark is available, 1 min/μm of film thickness at 100°C is recommended for AZ 9260. However, manufacturer soft bake recommendations for 24 μm and 10 μm film thickness of 240 seconds at 110°C and 165 seconds at 110°C respectively, yield an interpolated soft bake of 3 minutes and 10 seconds at 110°C for a film thickness of 15 μm [31].

Rehydration

The photoresist must rehydrate between softbake and exposure. During baking, the water concentration of the photoresist film signficantly drops. Water is required for the DNQ reaction in exposure and to achieve a reasonable development rate [32]. Water diffuses back into the resist through air humidity. Thin films typically rehydrate within seconds. For thick films, experimental concensus suggests a one hour rehydration delay in at least 40% humidy yields 100% rehydration of the photoresist [47] [48]. In the laboratory setup for this thesis, indoor humidity was not controlled, and varied day-to-day. Rehydrations for one hour at 16-45 %RH were witnessed and eliminated peel-off defects.

Exposure

The exposure reaction is a microscopic absorption process. The exact kinetics are governed by the exposure intensity, radiation flux, and photon absorption rates. Upon UV exposure, the DNQ sensitizer converts to an idene intermeidate product, and releases nitrogen. Water is required to proceed to the final product, a carboxylic acid. A distribution in resist composition prior to exposure, and variations in exposure will signifantly impact how the reaction proceeds [32]. Therefore, 50-200% of the theoretically required exposure dose should be tested when optimizing new processes [37].

Development

Development is a straightforward process compared to exposure and baking. The PAC acts as an inhibitor to the development reaction. The specific development solution used creates

a contrast in how quickly the exposed resist developes (development rate) compared to the development of unexposed regions (dark erosion rate). The rates are temperature dependent. The AZ 400K developers used for AZ 9260 will develop unexposed resist on the order of nanometers assuming suffient baking and a reasonable development time [49]. Development procedures can be optimized but do not impact the formation of the defects observed on a first order analysis, unlike the softbake and exposure. Multiple models for exist for computing the developed shape of an exposed feature (a PAC distribution). Therefore, the analytical model presented in this thesis could be expanded to produce the final photoresist structure if desired [32].

PDMS Casting

The thermal processing of PDMS operates at temperatures similar to a hardbake (baking after development) [50]. Hardbake of AZ 9260 is typically used to induce reflow, softening the resist to round out features [40]. A 15 μm thick film of AZ 9260 has a softening point around 110°C [41]. However, the mechanical and thermal stresses from PDMS casting at 90°C and centrifugally amplified hydrostatic pressure (approximately 200 g of acceleration) could create a glass-transition temperature/pressure regime softening the resist well below the reported value. Hardbakes above 150°C will cross-link AZ 9260, which harden resist structures and makes resist removal difficult (the substrate will appear stained) [51].

Laser Scribing

Clearly, tight control over baking, exposure and development steps are required in all lithography applications. Unfortuantely, laser scribing adds futher complexity to the process, frequently leading to bubble and burning defects in photoresists. A high nitrogen generation rate in laser scribing exposures can lead to gas bubbles in photoresist. The AZ 9260 contains a low PAC concentration relative to other positive high contrast resists, making it one of the most suitable resists on the market for laser scribing. Laser exposure rapidly transfers a densly packed energy burst to the photoresist. Severe local temperature increases can significantly decompose the PAC, cross-link the resist, and induce thermal stresses causing cracks that scatter light [52] [53].

Summary

The facts presented in this literature review helped guide the process reoptimization. However, they also highlight numerous error sources and unknowns that could still be impacting patterning layer performance. First, poorly controlled heating, and lack of cooling and humidity control could easily lead to different exposure kinects between patterning layer experiments. Even within one film, a varying axial temperature distribution in softbake would cause different sensitizer decompositions across the writeable stamp area. The effects on feature shape could potentially be studied by adjusting the analytical model's Dill parameters [32]. After baking, variations in focus and potentially poor laser performance could provide different doses across the resist. Again, there is therefore no gaurantee that two adjacent features would be identical. Finally, the intensity of burning the resist from laser scribing could also vary with position and time, caused by laser focusing and performance variations. One concern with the centrifugal caster is that flat feature tops are not always observed even if features exhibit the correct height. A corresponding hypothesis would be the below-focus exposure crosslinking portions of the resist, adhereing them to the SU8 substrate, thus decreasing it's flatness over time. Similarly, the PAC at the SU8 - AZ 9260 could be thermally decomposed during writing itself, and the feature therefore would not bottom out.

4.4 Minimization of Laser Focusing Errors

Simulation results presented clear correlations between focus variation and μCP stamp feature shapes. Literature review of photoresist processing confirmed that exposure reaction kinects are easily varied by the exact irradiation energy transfer and flux. Additionally, machine characterization measured intrinsic stage error motions impacting focus. Though no formal measurement exists, it was assumed that runnout and eccentricity errors in the centrifuge drum were also present, leading to addtional misalignments between the optical and spin axes of the system. Withough an autofocus system for the laser, a focus shift was forced in the structural loop to verify feature shape changes and locate a range of axial and circumferential tool positions.

Multiple tools were created from different pattering layers to study and determine focus. Shim stock was placed in the kinematic contacts of the centrifuge subsystem to tilt the drum vertically about its spin axis. The shift would force a linear change in focus over the axial length of the drum, with an ideal focus of $f = 0$ located at the axial center of the writable length of the drum.

4.4.1 Experiment 1: 400 Micron Focus Shift

First, a 400 μm focus shift was imparted (Figure 4-26). Exposure near the open end of the drum was intended to create an above focus feature, while exposures towards the fixed end of the drum should have created below focus features. Recall that the centrifugal caster's laser system has a depth of field of about 200 μm. Therefore, extreme above and below focus tests were also to be implemented on the same tool. The patterning layer was exposed with circumferential lines at 100 μm axial pitch and a centrifuge speed of 9.42 rad/s. Figure 4-27 shows features in expected above (Figure 4-27a) and theoretical below (Figure 4-27b) focus positions in the PDMS tool. The geometries agree with the single feature simulation results, suggesting that focus can be manipulated. However, no features with vertical sidewalls were observed, nor were a lack of features in regions theoretically outside the depth of focus. Therefore, it is possible that theoretical focus shift was not exactly applied due to errors in the system

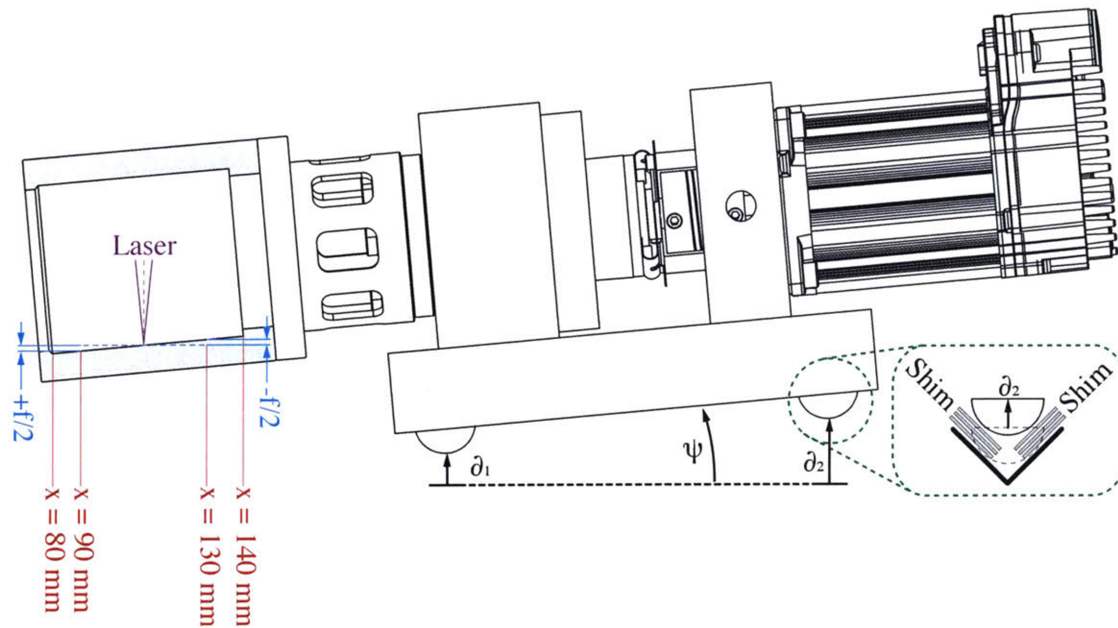

Figure 4-26: A schematic demonstrating the setup for imparting a focus shift. A change in focus, f over the axial length of the drum, specifically over the patterned area of the stamp between $x = 90$ mm and $x = 130$ mm, was created by tilting the drum an angle ψ through shimming the kinematic couplings for vertical displacements δ_1 and δ_2. The fixed laser focus should result in $f = 0$ at the axial center of the drum, and $\pm f/2$ at opposite ends.

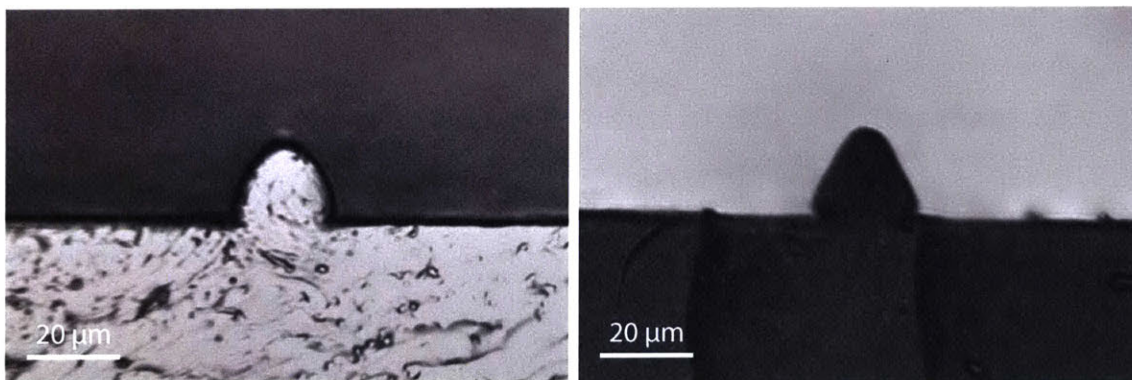

(a) A cross section view of a PDMS tool feature. This feature formed from a portion of the photoresist mold theoretically exhibiting above focus. The rounded feature shape agrees with the simulated geometry.

(b) A cross section view of a PDMS tool feature. This feature formed from a portion of the photoresist mold theoretically exhibiting below focus. The straight, tapered sidewalls agree with the simulated geometry.

Figure 4-27: Cross sections of above and below focus feature in a PDMS tool.

4.4.2 Experiment 2: 200 Micron Focus Shift

In the end, a tool with a 200 μm theoretical focus shift was implemented (Figure 4-26). 0.028 inches of shim was placed at each of the four kinematic contacts located closest to the centrifuge drum. 0.045 inches of shim was placed at each of the two kinematic contacts towards the centrifuge motor. The shims were placed directly between each ball and groove contact point. Once again, the theoretical shift should have placed zero-focus directly in the axial center of the writeable area of the centrifuge (axial position of 110 mm). The focus shift spanned over 40 mm of axial length. Circumferential lines were written with centrifuge speeds varying from 6.28 rad/s to 12.56 rad/s, with each dose written at multiple axial locations.

Figure 4-28 displays two stamp features, which were written into the photoresist at 6.28 rad/s. The two features were taken from opposite axial ends of the tool, and the centrifuge drum. As such, the features should have been exposed with the most significant difference in focal plane position. However, they exhibit very similar cross section profiles. Similar to the previous focus test, no features with vertical sidewalls were observed over the axial length of the tool. Fortunately the high exposure dose seems to have led to general feature uniformity that also utilized full resist thickness in the advantageous trapezoidal shape. As such the ideal writing speed of 6.28 rad/s was chosen. The ideal axial position of 120 mm was also selected for presenting robust and uniform set of adjacent features at 6.28 rad/s.

Even though the features in Figure 4-28 may be ideal for experimentation since they showed low sensitivity to focus variations, the observed geometries relative to exposure inputs disagree heavily with simulation results. The stamp features measure nearly twice as large in root width as the model predicted. This could be caused by lateral refraction of the laser beam within the resist, which is not captured by the analytical model. Additionally, a characterestic above focus rounding shape was not observed. This discrepancy is most likely caused by the physcial system maintaining a below focus configuration for all axial positions, despite the shimming procedure.

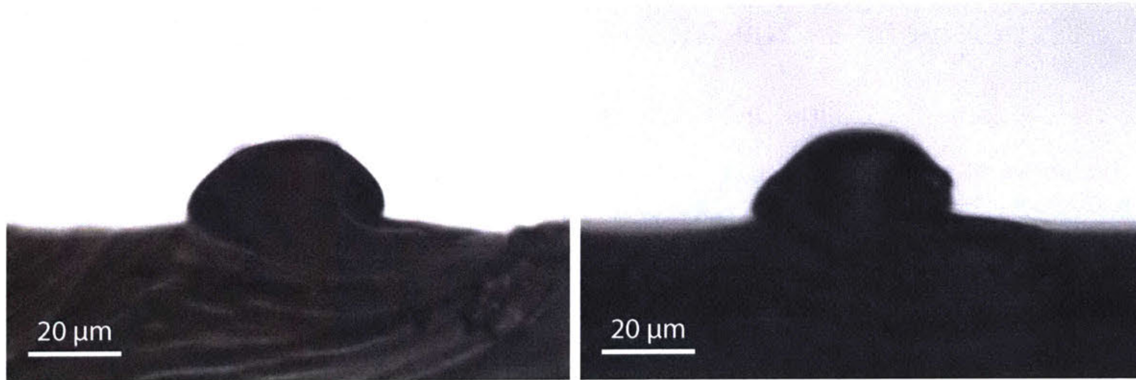

(a) A cross section view of a PDMS tool feature. This feature formed from a portion of the photoresist mold theoretically exposed above focus.

(b) A cross section view of a PDMS tool feature. This feature formed from a portion of the photoresist mold theoretically exposed below focus.

Figure 4-28: Cross sections of two features in a PDMS tool, from the same axial traverse that should have experienced a 150 μm difference in laser focal point position. However, the features are very similar in size and shape.

4.4.3 Summary of Focus Experiments

Figure 4-27 demonstrated the ability to alter feature shape by changing the position of the laser focal plane. However, high uniformity in feature shape was required for experimentation. Consequently, an ideal dose at a centrifuge write speed of 6.28 rad/s (Figure 4-28) produced features with minimal change in profile geometry, which is effectively an insensitivity to variations in focus. The relatively high dose of 4825 mJ/cm^2 agrees with the simulations results demonstrating proper top width and height formation at high exposure times even with large focusing errors.

Chapter 5

Experimentation

5.1 Goals

The core focus of experimentation for this thesis sought to investigate the contribution of the tool (also refered to as the stamp) in the μCP process. With this in mind, emphasis was also placed on demonstrating the manufacturing utility of creating tools with varying feature types and patterns. For efficient experimentation and a demonstration of arbitrary patterning, a single photoresist pattern with varying features was fabricated.

The work of Petrzelka and Hardt [23] demonstrated the ability to centrifugally cast seamless μCP tooling on a cylindrical photoresist mold. The subsequent contributions of Nietner and Hardt [16] optimized the photoresist of choice and exposure settings for advantageous tool feature cross section geometry and ease of fabrication. Finally, Merian [6] continuously inked and printed with Nietner's tools. However, the lack of estabilished ground truths between intended tool feature cross section geometry and the resulting print was of significant concern. As such, establishing understandings of the repeatability of the photoresist mold, the accuracy of PDMS replication of photoresist features, the portion of the tool brought into contact when printing, and whether printed geometries matched contact profiles was of high priority.

Towards the goal of manufacturing flexibility, creating new feature types and a variety of features on a single tool would be considered a signifcant metric of progress. The use a raster-scan direct write method permits the creation of tool sections with different patterns,

which could potentially feature line segments, dots, and even features formed via partially overlapping exposures. Therefore, fabricating an experimental tool with a multitude of features, some of them being attempts at creating new geometries, would be an impactful demonstration of tool fabrication capabilities.

5.2 Methods

5.2.1 Experimental Parameters and Feature Types

Four tools were cast from a single photoresist mold. Figure 5-1 shows the photoresist and subsequent general tool pattern, which contains sixteen sections approximately 1 cm by 1 cm in size. An axially oriented gap separates each section. The gap is consistenlty 1 mm in thickness, except between sections D1 and A1, and sections A1 and B1, where the gaps are 2 mm and 1.5 mm respectively. The gaps assists in distiguishing between the stamp sections, serve as fiducial markers, and the change in width allows one to easily locate the 0-count and 1000-count circumferential tool positions. One can then simply count sections from the 0 mark to easily determine which physical stamp pattern corresponds to which theoretical section. Table 5.1 contains exposure settings and general feature information for the photoresist pattern.

Section	**Axial Pitch (μm)**	**Features Written**	**Laser Power (mW)**	**Centrifuge Speed (rad/s)**	**Dose (mJ/cm^2)**
A	100	100	80	6.28	4825
B	200	50	80	6.28	4825
C	200	50	80	6.28	4825
D	1000	10	80	6.28	4825

Table 5.1: Exposure and general feature information for each tool section. Axial Pitch and Features Written denote the number of each feature and its linear axial density written per each section (1 cm in length). Laser Power and Centrifuge Speed control the exposure dose supplied to the photoresist. The reported dose denotes the theoretical dose per single exposure (not cumulative in the case of an overlap) at the given settings.

Each of the four sections, A, B, C, D represent four different feature types. Sections labeled A (A1, A2, A3, and A4) contain circumferential single line features at a fine axial

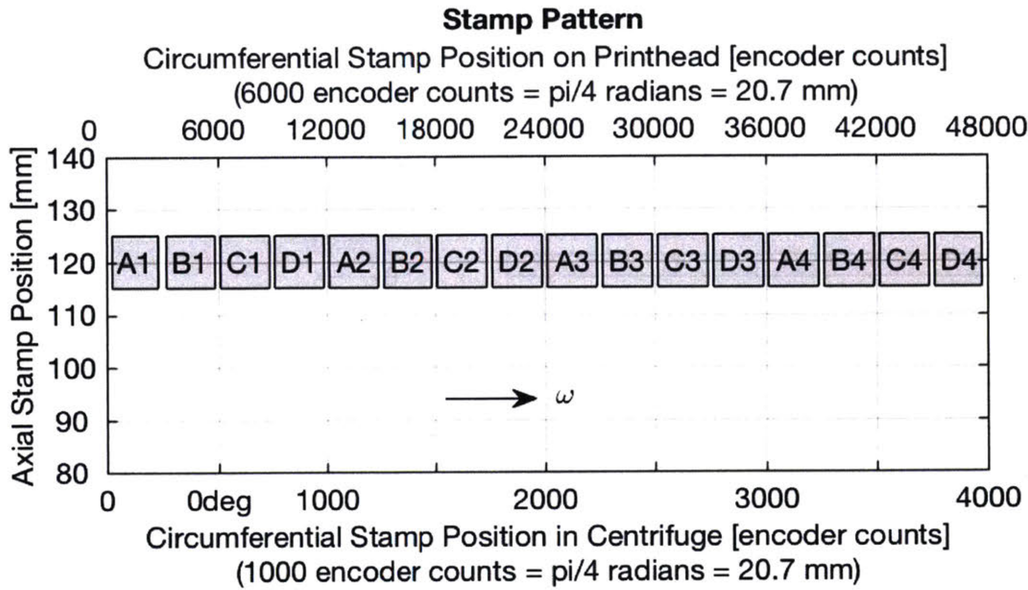

Figure 5-1: A general schematic of the photoresist pattern, and subsequent stamp pattern. Four feature sets, A, B, C, and D are each repeated four times over the circumference of the centrifuge and subsequent tool. Each set (such as A1, A2, A3, and A4) should theoretcally be identical and thus allows any physical circumferntial variation to be noted should it arise. Note that 0 and 8000 centrifuge counts correspond to 0° and 360° respectively, giving rise to the centrifuge rotation direction ω.

pitch. Sections labeled B (B1, B2, B3, and B4) are comprised of circumferential single line features at a coarse axial pitch. Secions labeled C (C1, C2, C3, and C4) possess pairs of partially overlapping lines for the creation of wider features. Sections labeled D (D1, D2, D3, D4) have sets of eleven short circumferential line segments overlapped to create axially oriented features. Creating feature types A and B was previously performed by Nietner [11]. However, feature types C and D are first attempts at creating features via overlapping exposures in this novel direct-write lithography system.

Figures 5-2, 5-3, 5-4, and 5-5 are generelized schematics of exposure paths and typical cross sections for A, B, C, and D features respectively. A and B features were chosen for quantifying tool contributions from standard single-exposed features. C and D features were chosen to test and investigate creating new feature geometries in this centrifugal system via cumulative, overlapping laser scribe paths, and their impact on the tool.

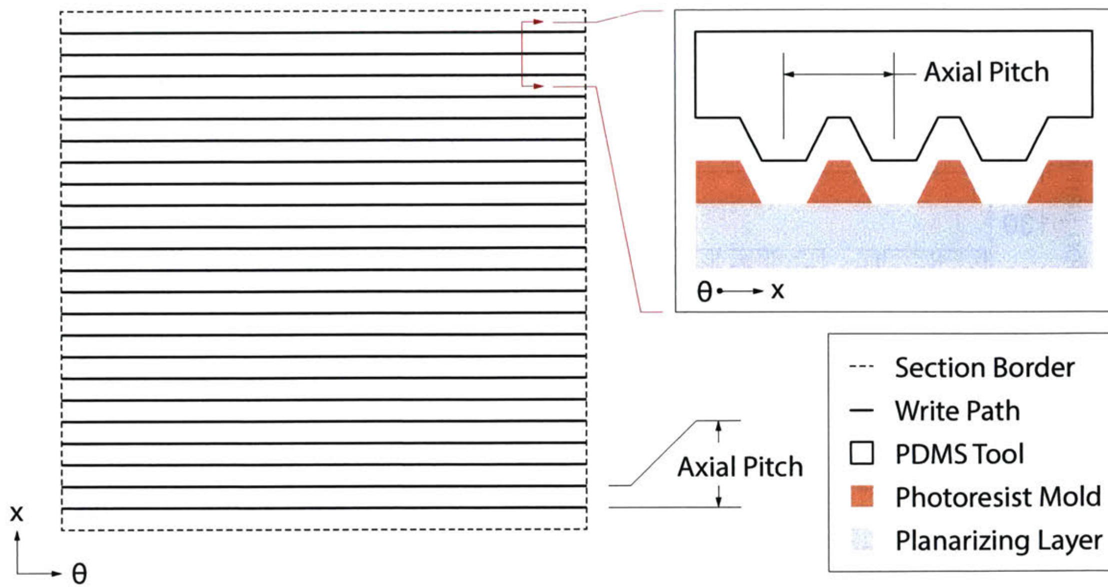

Figure 5-2: A generalized schematic of section A, consisting of 100 circumferential (θ-oriented) lines of 100 μm axial (x-oriented) pitch. The features, shown as the expected shape from simulation in an advantageous below-focus configuration, are created in the photoresist mold through single exposures and yield the resulting PDMS tool shape.

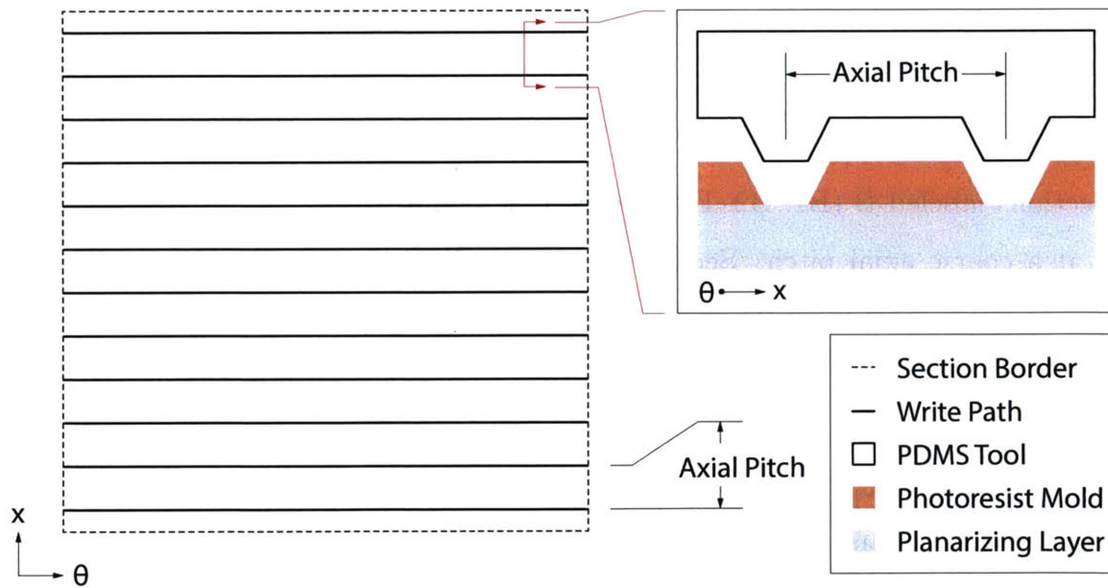

Figure 5-3: A generalized schematic of section B, consisting of 50 circumferential (θ-oriented) lines of 200 μm axial (x-oriented) pitch. The features, shown as the simulated shape in an advantageous below-focus configuration, are created in the photoresist mold through single exposures and yield the resulting PDMS tool shape.

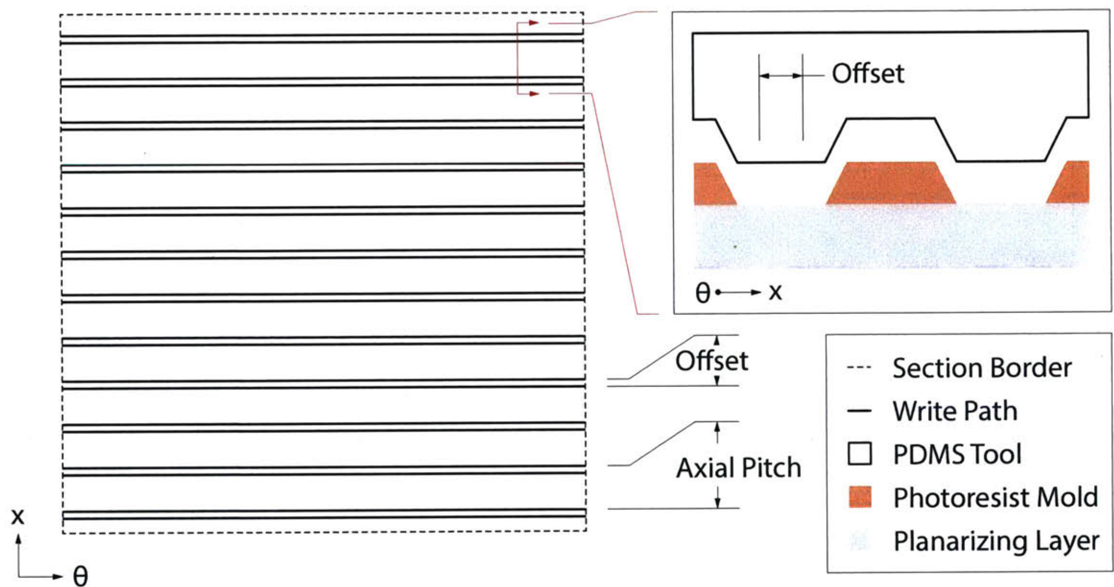

Figure 5-4: A generalized schematic of section C, consisting of 50 circumferential (θ-oriented) lines of 200 μm axial (x-oriented) pitch. The features, shown as the simulated shape in an advantageous below-focus configuration, are created in the photoresist mold through two partially overlapping exposures and yield the resulting PDMS tool shape. Exposure offsets of 5, 10, 15, 20, and 25 μm, were tested 10 times each and were expected to form wider features than A and B.

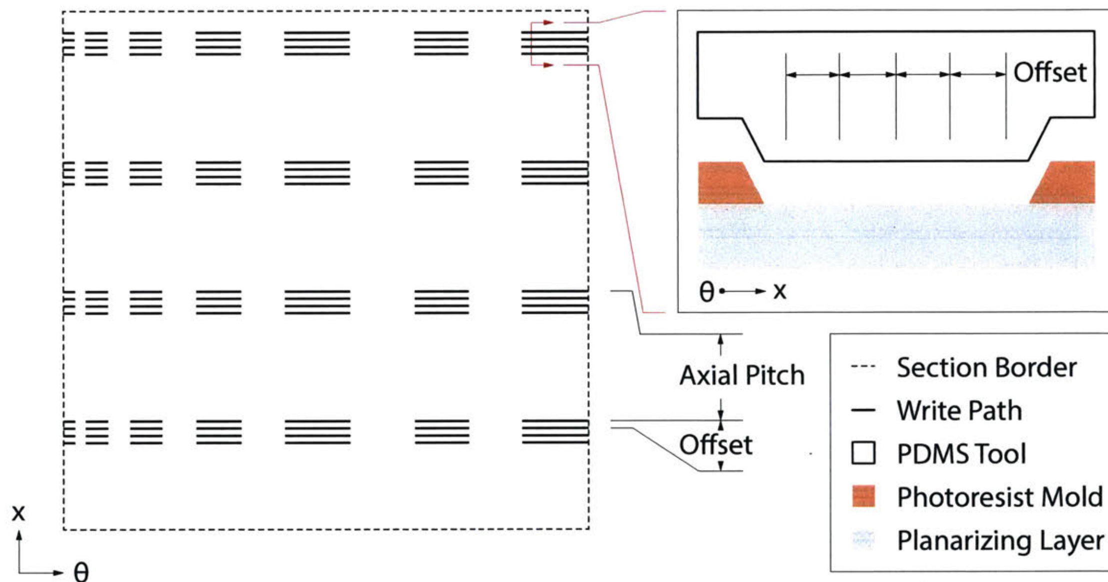

Figure 5-5: A generalized schematic of section D, consisting of 10 circumferential (θ-oriented) line segments of varying length of 200 μm axial (x-oriented) pitch. The features, shown as the simulated shape in an advantageous below-focus configuration, are created in the photoresist mold through eleven partially overlapping exposures and yield the resulting PDMS tool shape. Exposure offsets of 5, 10, 15, 20, and 25 μm (fixed value for each 11-exposure feature), were tested twice each and were expected to form features with a significant axial dimension, some even appearing as axially-oriented lines..

5.2.2 Procedure

The patterning layer for experimentation was cast using the procedure in Appendix B on an existing planaring layer, which was cast using the procedure in Appendix A. 0.565 g of AZ 9260 and 5.189 g of PGMEA were used in photoresist casting. The ambient room temperature during casting was 23°C and the indoor humidity was 23 %RH. There is noticable variation to the baking rise times in casting. For documentation purposes Figure 5-6 displays the measured temperature of the centrifuge drum while baking the photoresist. The MATLAB code containing the direct-write exposure settings specific to the cast pattern is located in Appendix E. Running the script or performing the computation by another method will yield the exact writing information at much greater detail than in Figures 5-1 through 5-5 and Table 5.1. In the exposure step only, the centrifuge drum was angled such that the laser focal point shifted vertically across the axial length of the drum exactly according to the setup described in Section 4.4. Following development of the photoresist to form the patterning layer, the photoresist was imaged and four PDMS tools were cast.

Immediately following development, the photoresist was imaged using the methods described in Section 5.3.2. Characteristic photographs of all 16 sections were taken. Following this imaging, and in the same day as patterning layer casting, a single-layer PDMS stamp (S1) was cast according to the procedure in Appendix C. 6.004 g of the elastomer base and 0.614 g of the elastomer curing agent were used to create the tool. Immediately following this casting and the removal of tool S1 from the centrifuge drum, the same 16 locations of the photoresist were photographed.

The following day (the first day after patterning layer casting), tool S1 was dissected and imaged according to the methods detailed in Section 5.3.1. The stamp locations of the best A, B, C, and D features were identified. The photoresist was then photographed at these locations. On the same day, a dual layer black tool (S2) was cast according to the procedure in Appendix D. The clear layer contained 3.143 g of the elastomer base and 0.308 g of the elastomer curing agent. The black layer was created using 3.002 g of the elastomer base, 0.352 g of the elastomer curing agent, and 0.209 g of the black dye. Ambient temperature and indoor humidity on this day were observed to be 23°C and 23 %RH.

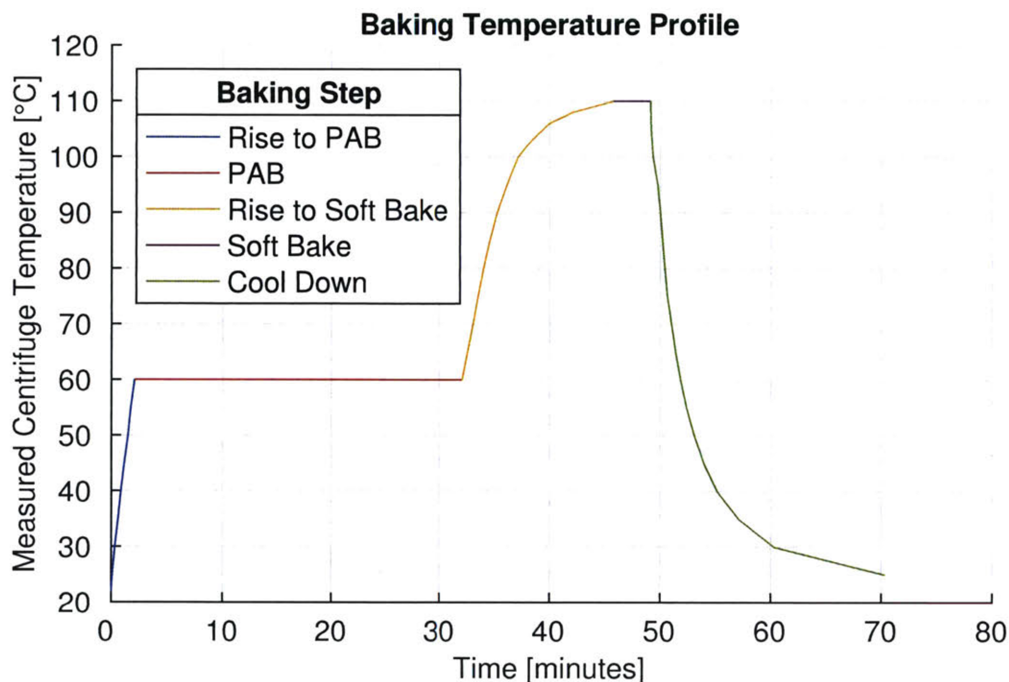

Figure 5-6: The measured centrifuge drum temperature for baking steps during photoresist casting of the experimental patterning layer. The casting procedure calls for a 30 minute post apply bake (PAB) at 60°C followed by a soft bake for 3 minutes and 20 seconds at 110°C. In addition to displaying these bakes, the plot also shows the rise trajectory to each bake and the cool down trajectory to ambient temperature. All baking steps, except cool down, are performed using closed loop temperature control.

The next day (the second day after patterning layer casting), another single layer tool (S3) was cast using 6.075 g of the elastomer base, and 0.606 g of the curing agent. Immediately following the removal of tool S3, all 16 A, B, C, and D characteristic photoresist locations were photographed again, along with the best A, B, C, and D locations identified by tool S1. Ambient temperature was 23°C and indoor humidty was 25 %RH on this day. Finally, one day later (the third day after patterning layer casting) one final dual layer tool (S4), was cast using 7.090 g of the elastomer base and 0.942 g of the elastomer curing agent for the clear layer. The black layer used 2.6 mL of a mixture comprised of 3.153 g of the elastomer base, 0.324 g of the elastomer curing agent, and 0.218 g of the black dye, to top of the 10 mL volume of the centrifuge drum. Ambient conditions on this day were 23°C and 16 %RH.

Figure 5-7 contains photographs of the centrifuge interior throughout the tool-making process. Figure 5-7a shows the drum with only the SU8 planarizing layer. Figure 5-7b displays the adhered but unexposed AZ 9260 photoresist patternling layer. Figure 5-7c is

an image of the AZ 9260 photoresist patterning layer after exposure. Finally, Figure 5-7d presents the AZ 9260 photoresist patterning layer after development. The photoresist pattern is clearly evident after exposure and prior to development, otherwise the photoresist appears as a uniform amber film. Figures 5-8a and 5-8b are photographs of tools S1 and S2 respectively.

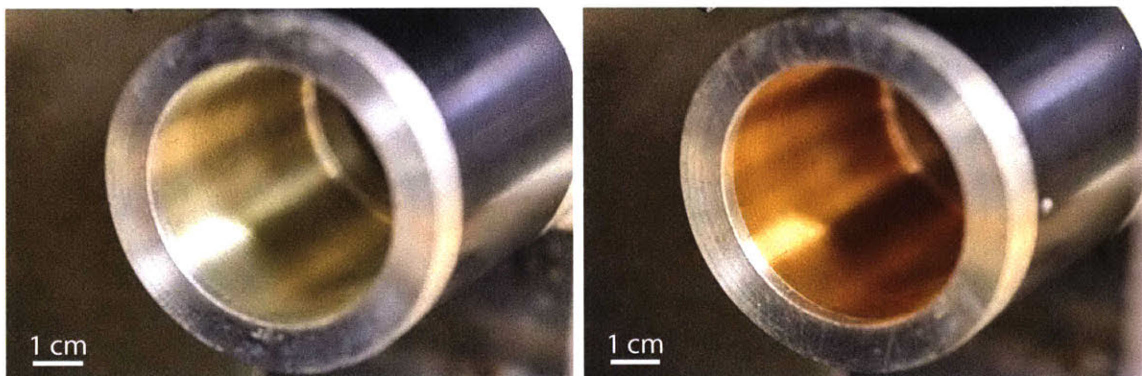

(a) The SU8 planarizing layer in the centrifuge drum. Note that this layer is not opaque and the machining marks from turning the aluminum centrifuge drum show through.

(b) The AZ 9260 photoresist patterning layer in the centrifuge drum after baking and prior to exposure. Note the characteristic amber color of the resist and that the machining marks are still somewhat visible.

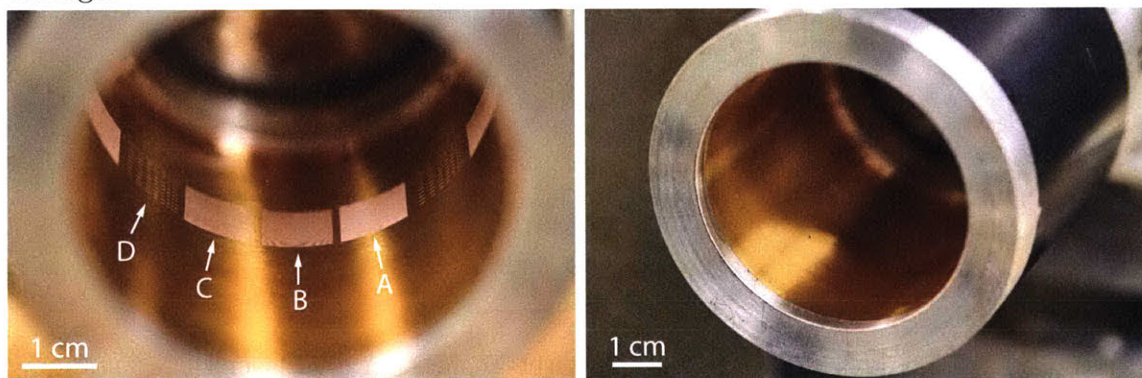

(c) The AZ 9260 photoresist patterning layer in the centrifuge after exposure and prior to development. One visible A, B, C, and D feature section are each labeled. Note that the exposed photoresist exhibits a crisp white aesthetic. The varying feature type and axial density between A, B, and C regions can easily be seen as a difference in the level of whiteness between the sections.

(d) The AZ 9260 photoresist patterning layer in the centrifuge after development. The exposed region is nearly impossible to distinguish from the unexposed resist now. Note that at this macroscopic level the photoresist does not noticeably change from this state over the subsequent stamp castings.

Figure 5-7: Photographs of the centrifuge interior during the patterning layer casting process for the experimentation tools.

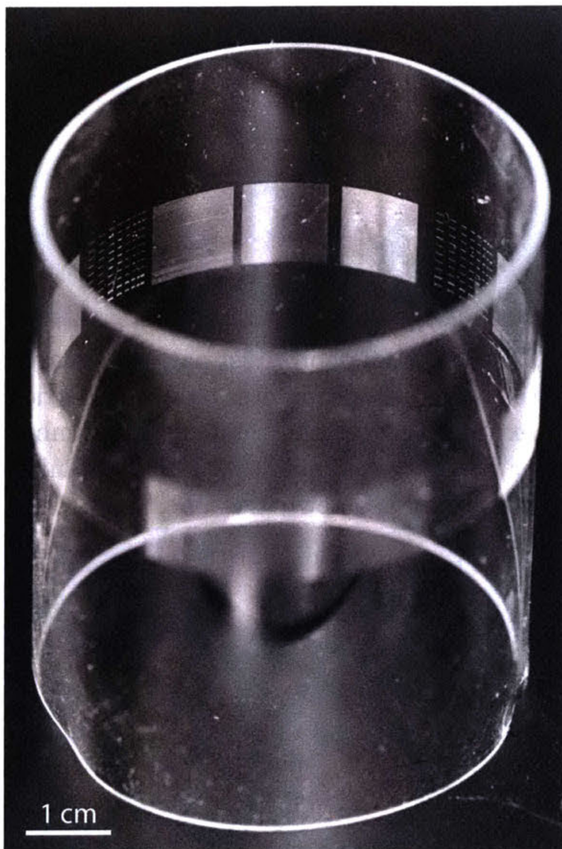

(a) Tool S1 - A single layer PDMS stamp.

(b) Tool S2 - A dual layer PDMS stamp.

Figure 5-8: Photographs of the S1 and S2 PDMS tools, single layer and dual layer respectively, created for experimentation. Note how easily dust particles adhere to the PDMS.

5.3 Tool Measurement Processes

Tools can be assessed by four different methods to yield qualitative and quantitative data. First, single layer tools can be dissected and imaged via standard optical microscopy. Photographs can be taken and geometric dimensions manually extracted using the image scale (μm/pixel). Second, episcopic microscopy of the patterning layer inside the centrifuge drum can be performed. Similarly, photographs and manually gathered geometric dimensions serve as the retrieved data. Third, episcopic microscopy of dual layer PDMS tools (method developed by Nill [29]) can be used to visualize the tool contact region. Photographs can again be taken for pure visualization purposes, but they can also be computationally analyzed to quantify critical dimensions of the contact region. Lastly, HDT prints made with the tool on gold-coated PET substrates can be analyzed with standard optical microscopy. As with contact visualization, images can be taken, and computationally assessed using an algorithm developed by Merian [6].

5.3.1 Optical Microscopy of PDMS Tools

The PDMS tools can be cut using a razor blade to create smaller sections, which were placed on glass slides for viewing in a standard optical microscope. For this thesis a LW Scientific M-Series LW200 microscope with bottom lighting and 4x, 10x, and 40x objectives was used to image the tool. Top views (looking radially inward if the tool was still in the photoresist mold) and cross sections views (cut perpindicular to the circumferential drum direction) of each A, B, C, and D section were created. From these samples, the best A, B, C, and D regions of the tool were identified. These ideal regions are refered to as A*, B*, C*, and D* respectively. Cross section feature geometries were measured for comparison with the same features in the photoresist and contact imaging. Figure 5-9 shows two cross section and one top view photographs of a PDMS tool imaged by this method. Critical dimensions are identified to demomstrate how cross sections are measured, and their corresponding dimensioning ordinates in top views.

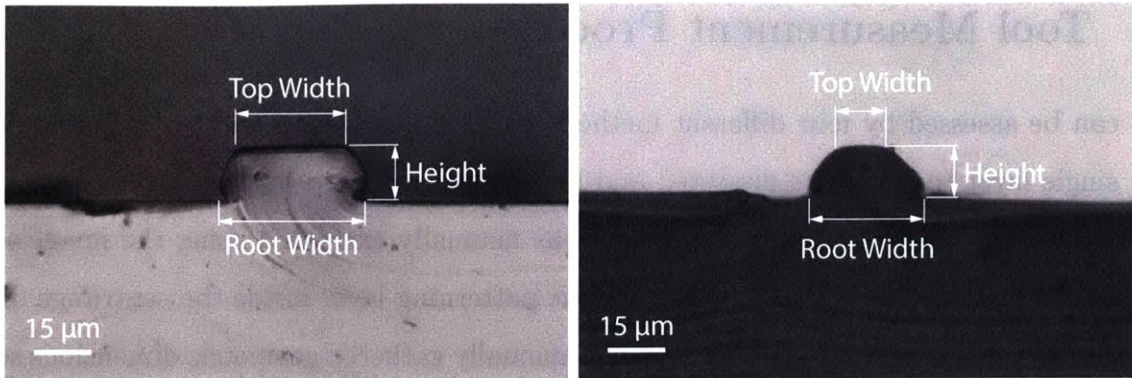

(a) A cross section view of a feature in a PDMS tool with labeled dimensions. A more rectangular geoemtry is used in this example.

(b) A cross section view of a feature in a PDMS tool with labeled dimensions. A more trapezoidal geoemtry is used in this example.

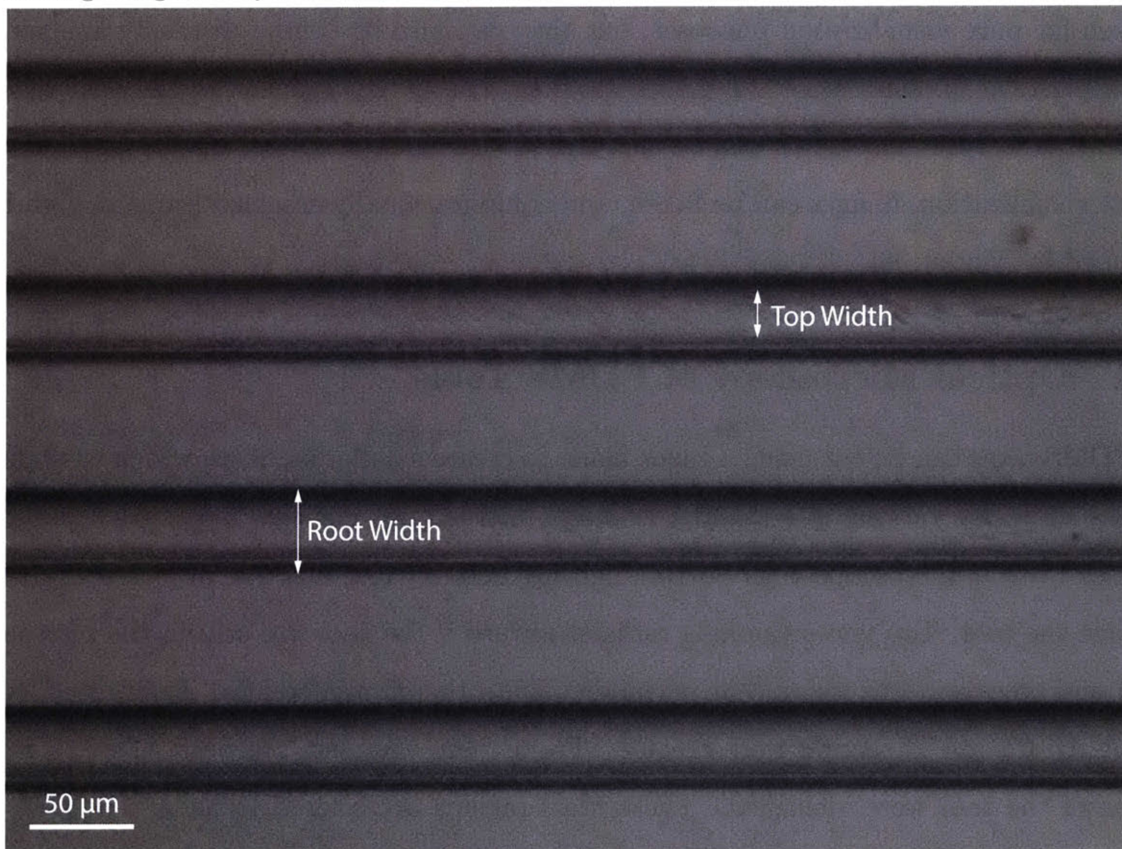

(c) A top view of lines in a PDMS tool with labeled dimensions. There is no crisp black line pair definining the top width like the root width, but shadows and light gray outlines make it easy to identify the top width.

Figure 5-9: Sample photographs of features in a PDMS tool with labeled dimensions (top width, root width, and height). Two extreme feature geometries are shown in cross section to demonstrate the measurement ordinates. Note that root width is always measured from the widest locations, ignoring an undercut if present.

5.3.2 Episcopic Microscopy of the Patterning Layer

The photoresist patterning layer can be imaged using the microscope designed in Section 3.3.1. A sample image of each section (A1-A4, B1-B4, C1-C4, and D1-D4) was recorded after development, after removing PDMS tool S1, and after removing PDMS tool S3. Photographs of ideal regions A*, B*, C*, and D* can also be recorded for every step after removing and analyzing tool S1 for the best regions. This measurment method is used to compare PDMS features to their respective photoresist molds, and to qualitatively assess if the patterning layer undergoes any changes throughout the tool fabrication process. Similar to optical microscopy, geometric dimensions of features can be determined through the image scale. Figure 5-10 shows sample images with labeled features and dimemsions. Figure 5-10a emphasizes the feature sidewalls, the AZ 9260 patterning layer and the SU8 planarizing layer. The striations, white reflections, and speckles are machining marks on the aluminum centrifuge drum refracted through the photoresist films. Figure 5-10c presents interpreted cross sections from images.

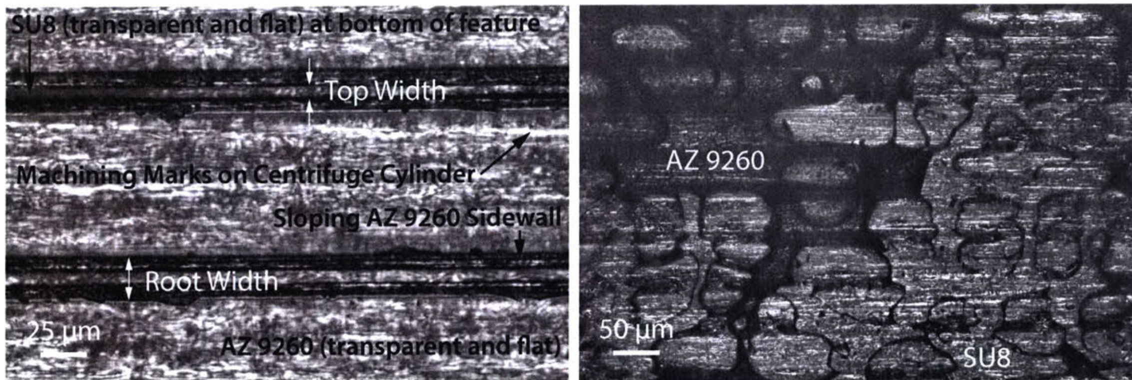

(a) An image of the photoresist patterning layer with labels and dimensions.

(b) An image of AZ 9260 (dark grey) peel off defects exposing the SU8 (light grey).

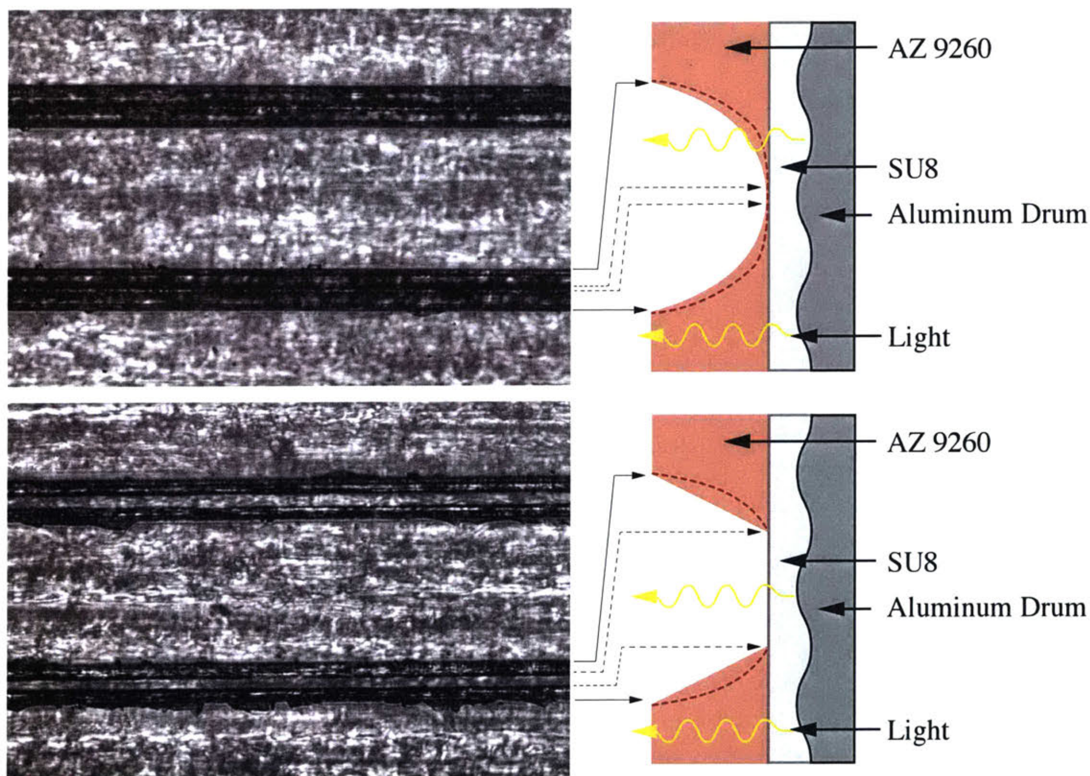

(c) Cross section interpretations of photoresist images. Top: Light reflected off of the aluminum drum passes through the SU8 and AZ 9260. Sidwalls make up most of this feature, with little or no bottoming out against the SU8. Bottom: The SU8 is visible in the feature center, indicating that the exposure bottomed out.

Figure 5-10: Photographs of the AZ 9260 photoresist patterning layer with labeled dimensions for measuring features. The damaged patterning layer compares the aesthetic of AZ 9260 and SU8 in the same image, showing that a bottomed-out feature should have clear top width with a well defined border. Cross section interpretations suggest two types of features through the extend of dark grey portions of the image (the sidewall). Note the dashed red lines indicating other sidewall geometries, since the 2D image makes it impossible to exactly infer the slope shape.

5.3.3 Episcopic Microscopy of Tool Contact

Tool contact on the impression roll (simulated printing) can be visualized using an episcopic microscope developed by Nill [29]. Using reflection and refraction as the driving physics, regions of the tool in contact with the impression roll allow one to see and focus on the black backing of a dual layer tool. The contact images are binarized, and are run through Merian's line width analysis algorithm to quantify dimensions of the contact region [6]. Contact imaging was performed using the benchtop setup described in Section 3.3.2. The optical system has a resolution of 0.3 μm. A*, B*, C* and D* sections were imaged for qualitative contact visualization purposes and quantification of A and B feature geometries. Figure 5-11 shows an original and a processed image created using this contact system. The corresponding line width data are presented in Figure 5-12. The MATLAB code for contact processing and analysis is located in Appendices F, G, I, and J. Many contact images were taken at at 6 N set point for open loop force, which Merian [6] used in printing. This configuration repeatedly measured at 4.9 N of force.

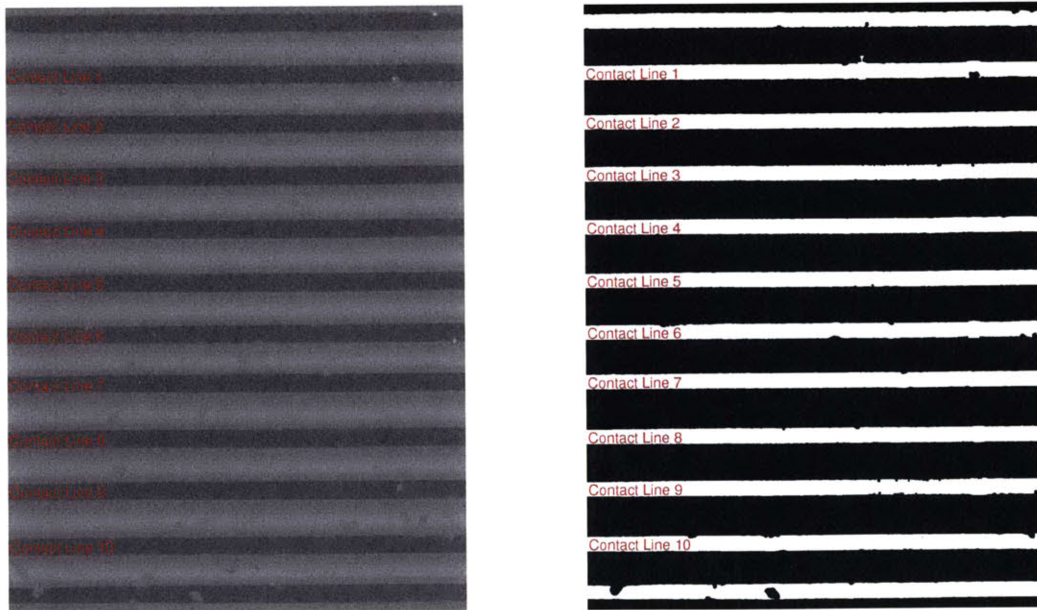

(a) Original image with labeled lines.

(b) Processed image with labeled lines.

Figure 5-11: An example original and the subsequently processed (binarized) contact image at 6.30 N of measured open loop force. Corresponding lines are labeled and the processing algorithm clearly identifies and maintains defects in line continuity.

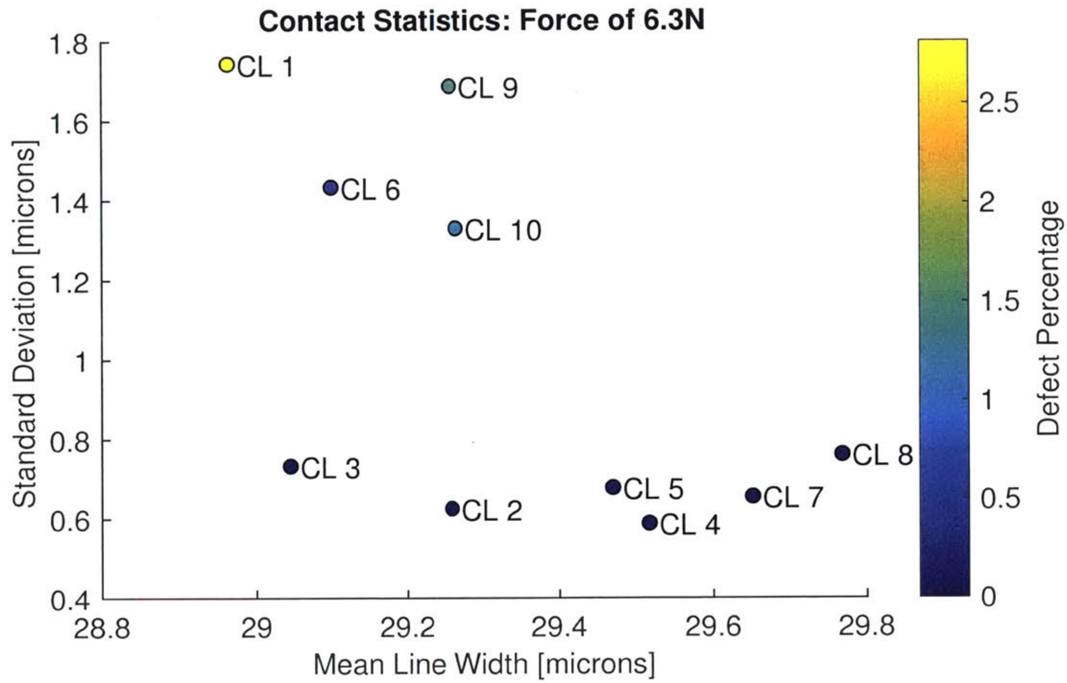

Figure 5-12: Contact data corresponding to the image(s) in Figure 5-11. Note that CL 1 representents Contact Line 1, and so on. For this image, line widths are extremely tight, < 1 μm, suggesting that features dimensions vary minimally over the area of the image.

5.3.4 Optical Microscopy of Prints

Following Merian's printing procedures, the tools were inked and used in printing. The resulting prints can be photographed under the same LW Scientific M-Series LW200 microscope and run through Merian's print width analysis algorithm [6]. Emphasis was placed on obtaining an ideal print in the region of A*, called A**. These prints could be photographed for quantitative line width analysis. Print images of any B, C, and D region were sufficient for pure visualization purposes. Figure 5-13 shows an original and a processed image of one print. The corresponding line width data are presented in Figure 5-14. Non-uniform print pressure, inking, or etching over the span of the image could be responsible for the 5 μm spread. The MATLAB code for print processing and analysis is located in Appendices F, H, I, and J.

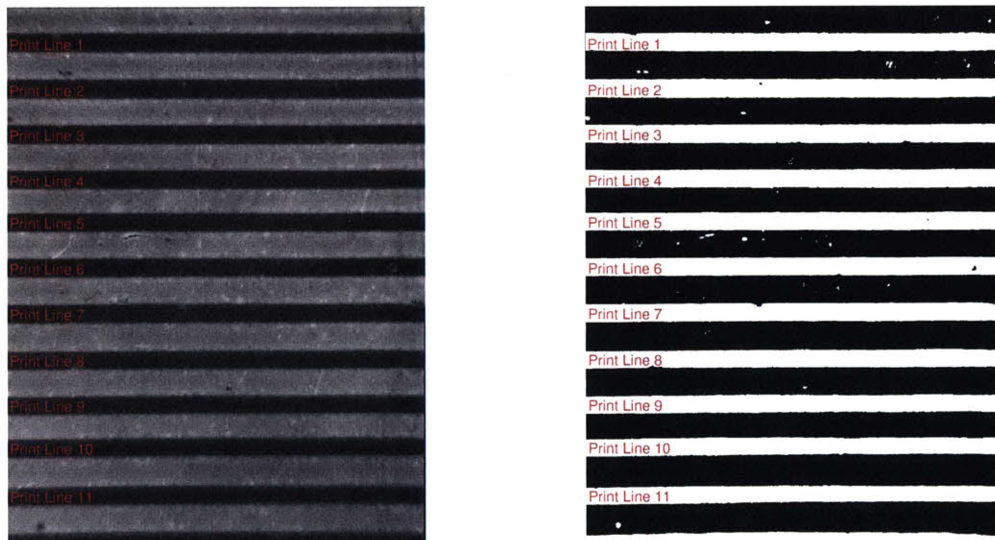

(a) Original print image with labeled lines. (b) Processed print image with labeled lines.

Figure 5-13: An example original and subsequently processed (binarized) print image at a mean closed loop print force of 7.41 N. Corresponding lines are labeled and Merian's processing algorithm clearly identifies and maintains defects in line continuity [6].

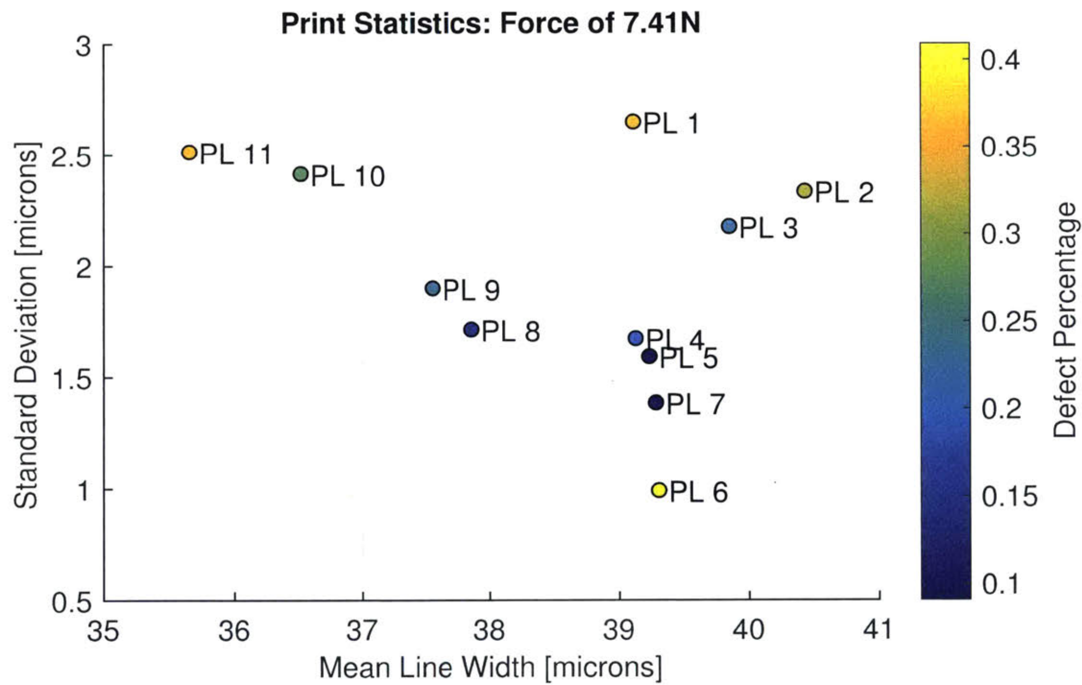

Figure 5-14: Print data corresponding to the image(s) in Figure 5-13. Note that PL 1 representents Print Line 1, and so on. For this image, line widths data encompass a large range, ≈ 5 μm.

5.3.5 Measurement Order

Table 5.2 presents an ordered list of procedure steps. It summarizes the order of photoresist castings, tool castings, and measurement steps.

Step	Process
1	Cast AZ 9260 photoresist
2	Expose AZ 9260 photoresist
3	Develop AZ 9260 photoresist
4	Image the photoresist at locations A1-A4, B1-B4, C1-C4, and D1-D4
5	Cast and remove PDMS tool S1
6	Identify and image S1 PDMS at locations A*, B*, C*, and D*
7	Image the photoresist at locations A1-A4, A*, B1-B4, B*, C1-C4, C*, D1-D4, and D*
8	Cast and remove PDMS tool S2
9	Image contact of tool S2 at locations A*, B*, C*, and D*
10	Cast and remove PDMS tool S3
11	Image the photoresist at locaitons A1-A4, A*, B1-B4, B*, C1-C4, C*, D1-D4, and D*
12	Image the S3 PDMS at locations A*, B*, C*, and D*
13	Cast and Remove PDMS tool S4
14	Print using tool S4 at locations A*, and any B, C, and D locations
15	Image contact of tool S4 at location A*

Table 5.2: An outline of the experimentation procedure.

5.4 Single Exposure Feature Results

This section analyzes A and B features, which were created in the photoresist using single exposures. Qualitative and quantitative analyses are presented to assess patterning layer repeatability, pattern replication and PDMS stamp repeatability, the contact region, and the resulting print.

5.4.1 Patterning Layer Repeatability

The photoresist patterning layer was imaged after development, after casting and removing tool S1, and after casting and removing tool S3. The 16 sample A, B, C, and D locations were photographed each time. This sequence of images was taken to determine whether the photoresist changed. Does casting a PDMS tool reshape the features from their developed dimensions? Do subsequent tool castings cause the photoresist to alter in shape as well?

Figure 5-15, Figure 5-16, Figure 5-17, and Figure 5-18 show images the photoresist in sample areas of A1, A2, A3, and A4 respectively after development (subfigure a), after casting and removing tool S1 (subfigure b), and after casting and removing tool S3 (subfigure c). Similarly, Figure 5-19, Figure 5-20, Figure 5-21, and Figure 5-22 are pictures of the photoresist at sample areas of B1, B2, B3, and B4 respectively. Table 5.3 lists the exact positions of the photoresist imaged; the fidicuial gaps in tool pattern were used to tare out positioning differences between imaging and exposure setups such that the reported values refer to linear stage and centrifuge drum positions during writing.

Section	Axial Position (mm)	Circumferential Position (counts)
A1	124.5	97
A2	124.5	2158
A3	124.5	4132
A4	124.5	6238
B1	124.5	601
B2	124.5	2779
B3	124.5	4761
B4	124.5	6725

Table 5.3: Axial and circumferential positions of the patterning layer that were imaged for photoresist repeatability tests of features created using single exposures.

(a) Photograph of the photoresist at location A1 after development.

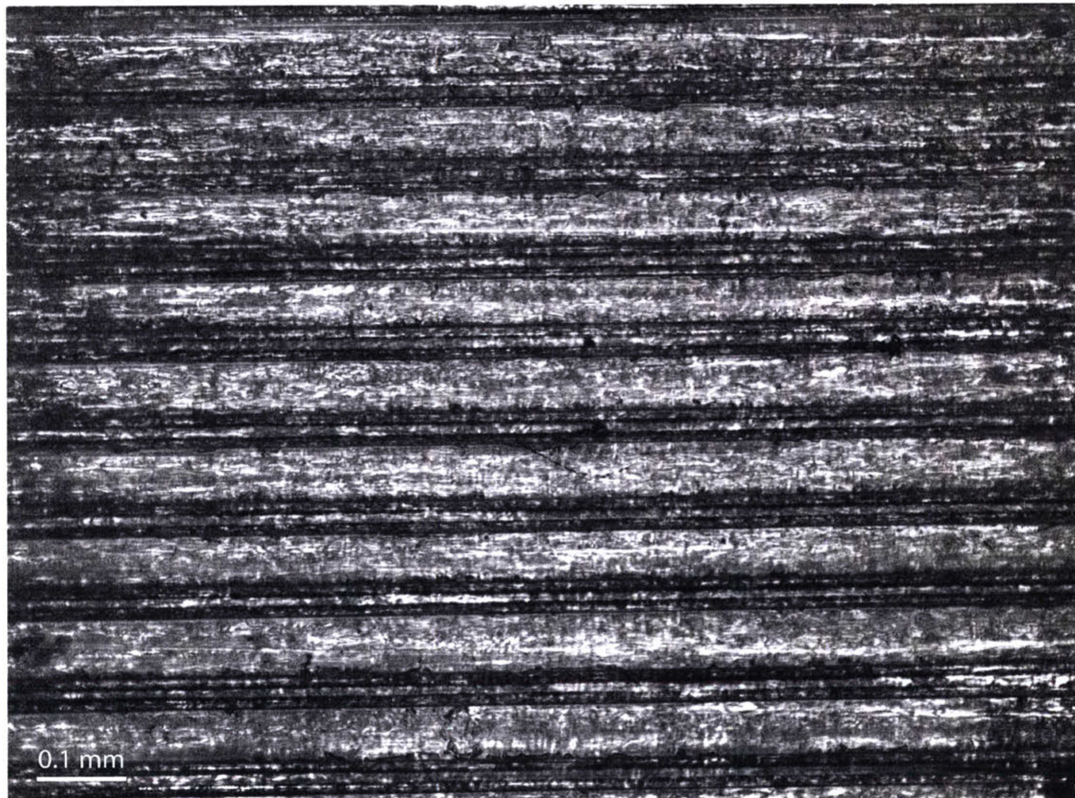

(b) Photograph of the photoresist at location A1 after removing tool S1.

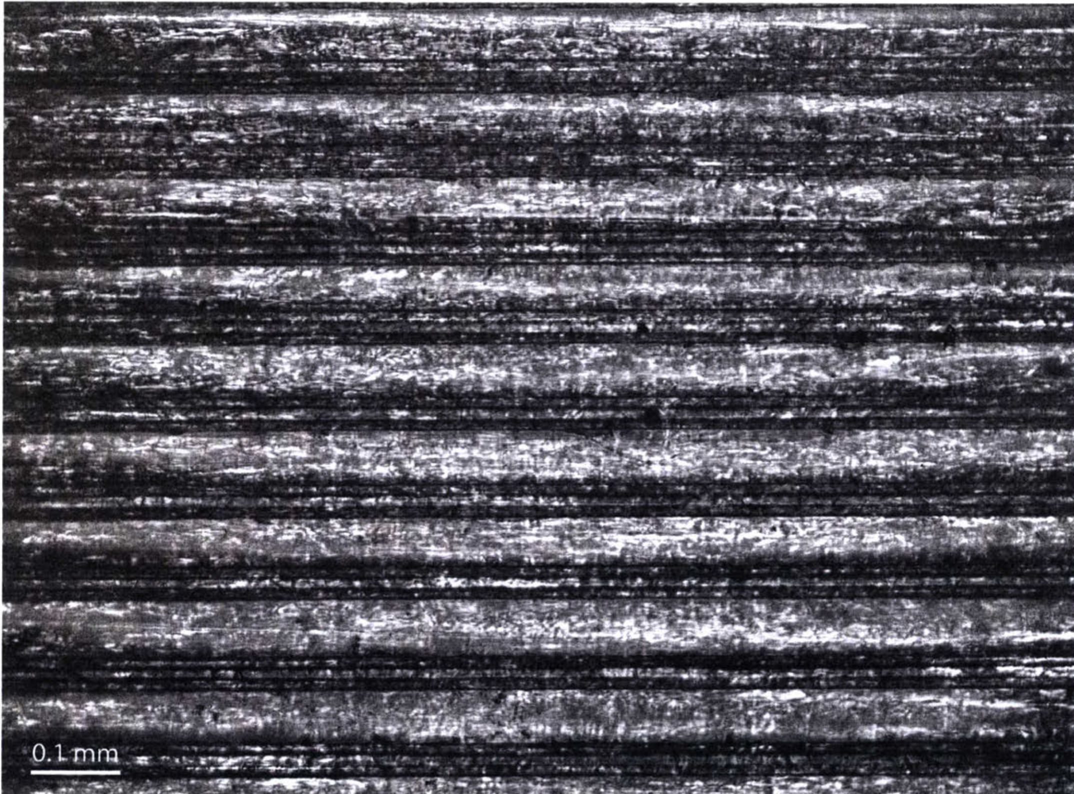

(c) Photograph of the photoresist at location A1 after removing tool S3.

Figure 5-15: Photographs of the photoresist at location A1 throughout the tool-making process. Note the obvious change between Figures 5-15a and 5-15b as if the PDMS casting slanted a previously vertical sidwall. There is no obvious alteration to the photoresist between casting tool S1 (Figure 5-15b) and tool S3 (Figure 5-15c), minor root width edge roughness and defects are consistent between the two. Both S1 and S3 molds also exhibit bottomed out features, where the exposure propogated all the way through to the SU8 planarizing layer.

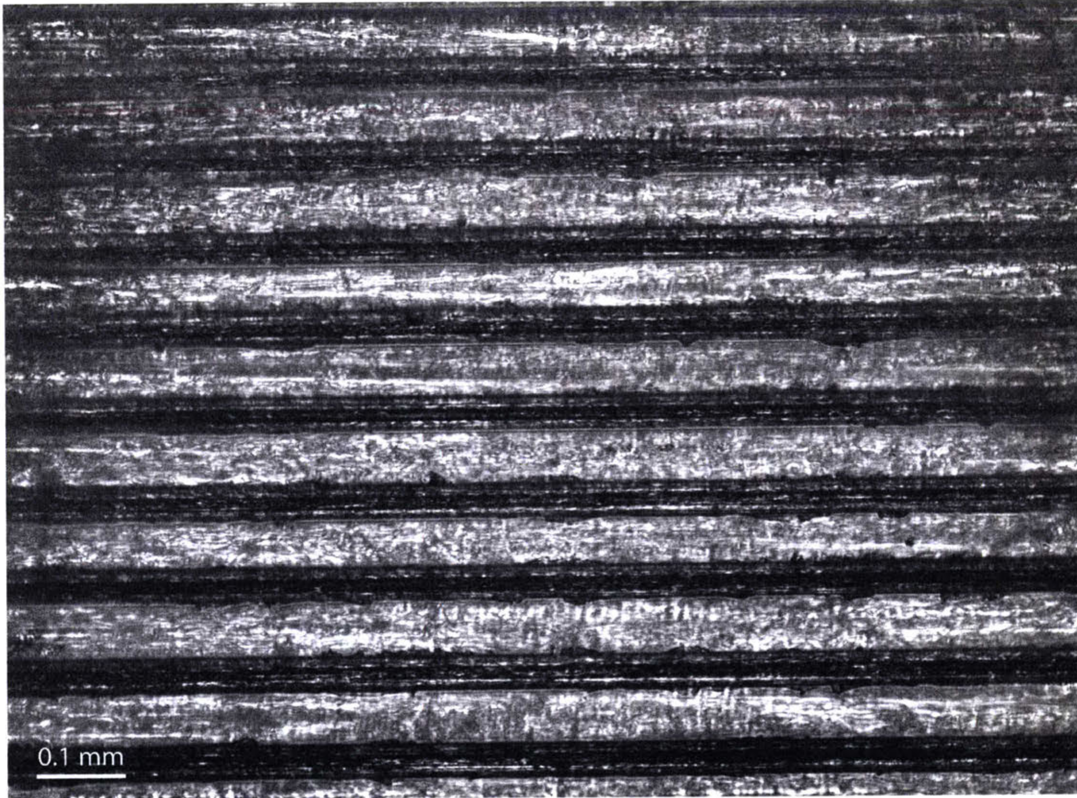

(a) Photograph of the photoresist at location A2 after development.

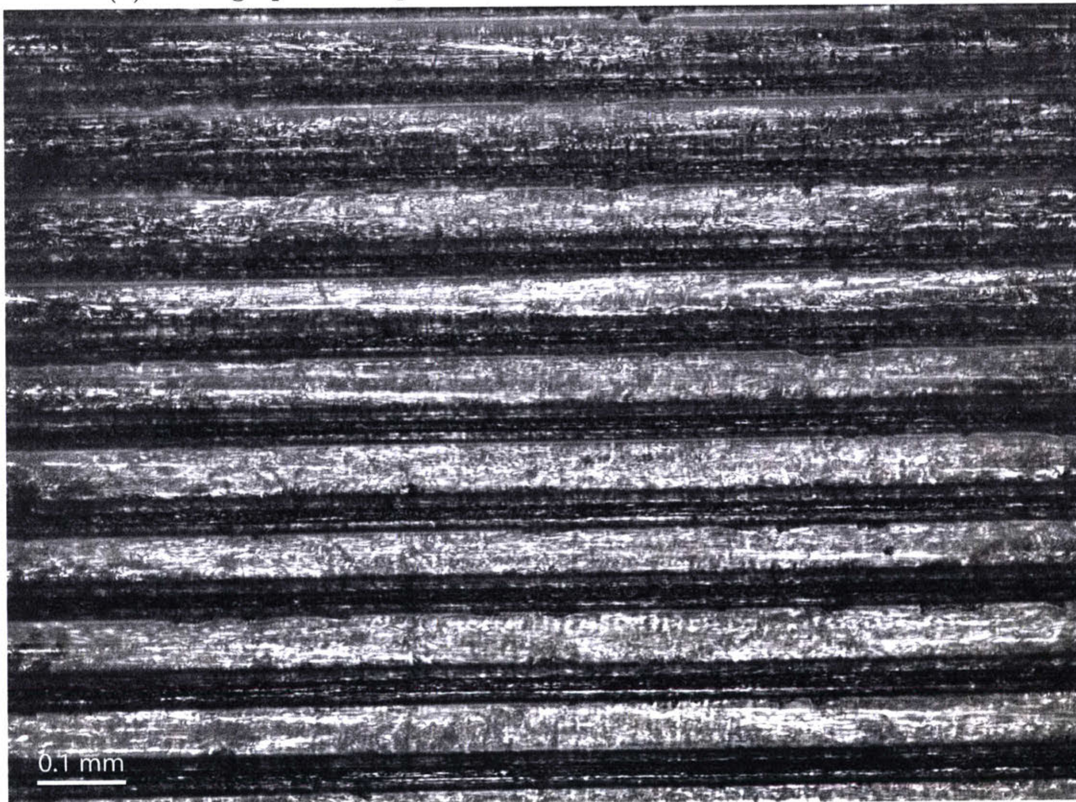

(b) Photograph of the photoresist at location A2 after removing tool S1.

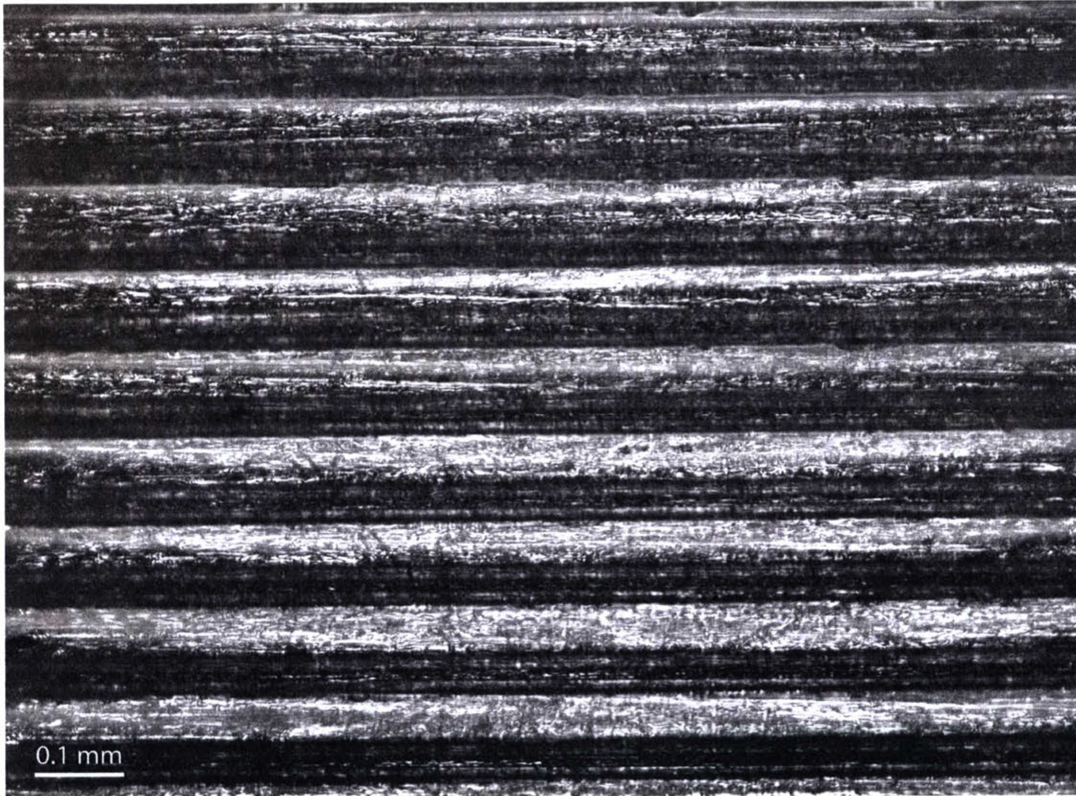

(c) Photograph of the photoresist at location A2 after removing tool S3.

Figure 5-16: Photographs of the photoresist at location A2 throughout the tool-making process. There are no apparent changes between development (Figure 5-16a) and subsequent tool castings (Figure 5-16b and Figure 5-16c). Features obviously bottom out and mild edge defects are visible and consistent between images.

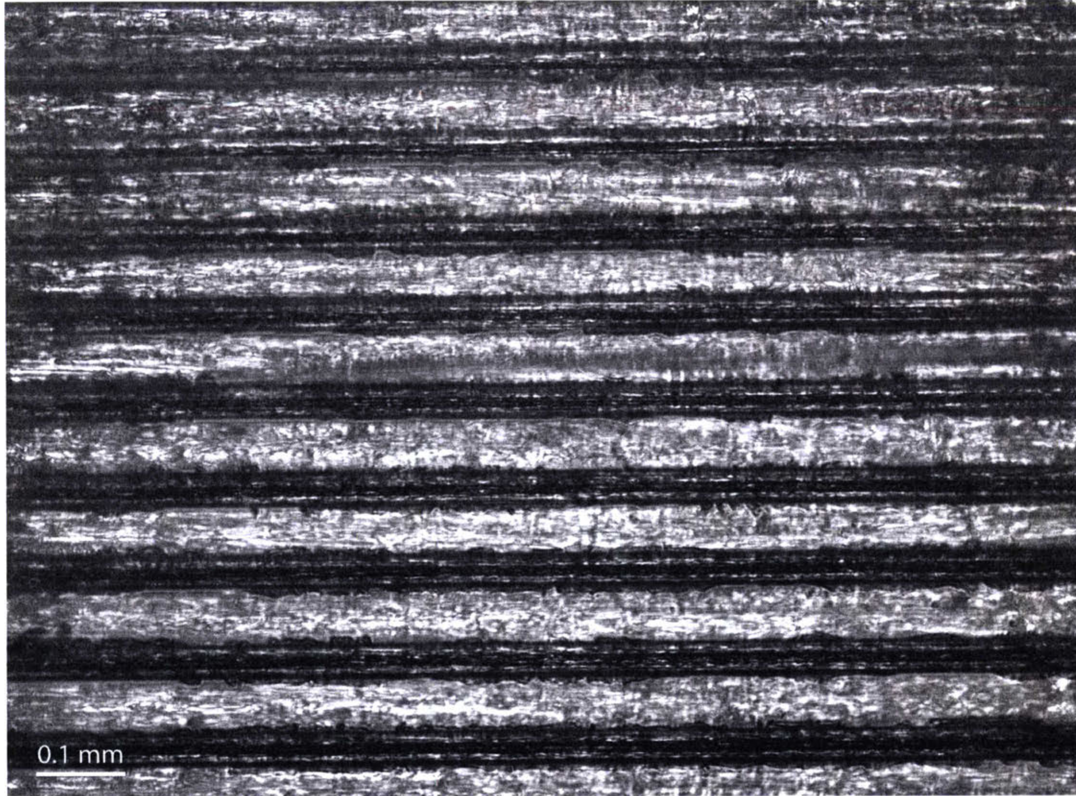

(a) Photograph of the photoresist at location A3 after development.

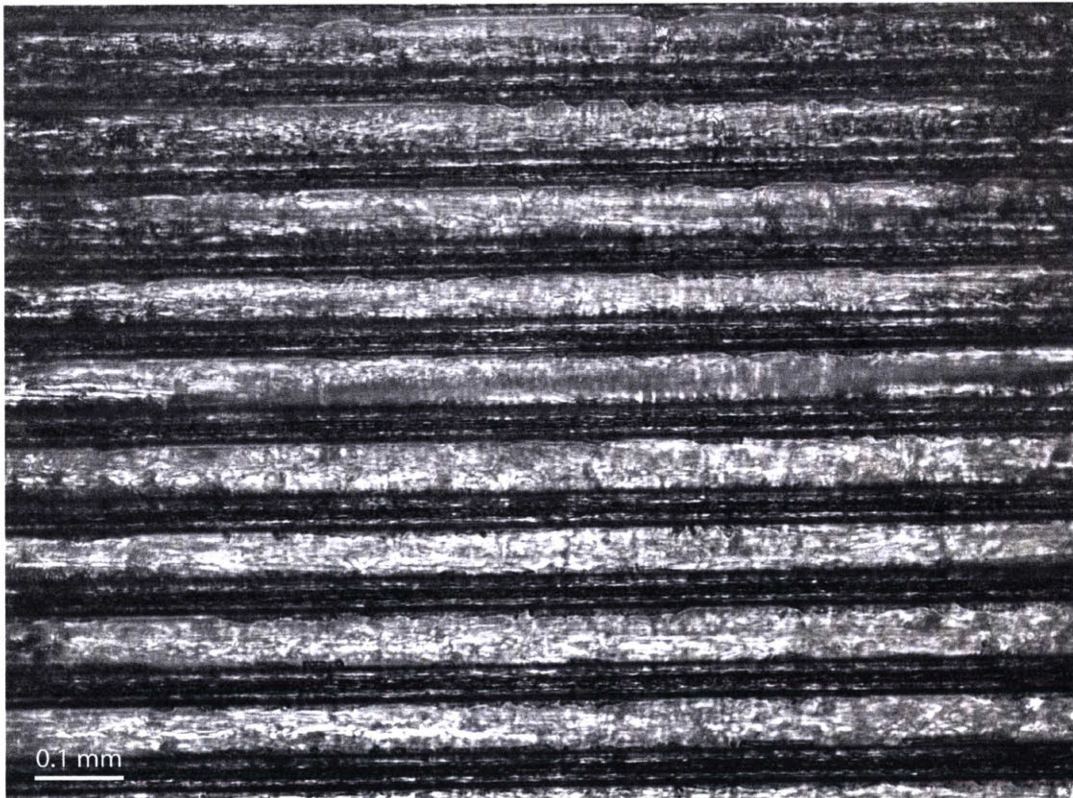

(b) Photograph of the photoresist at location A3 after removing tool S1.

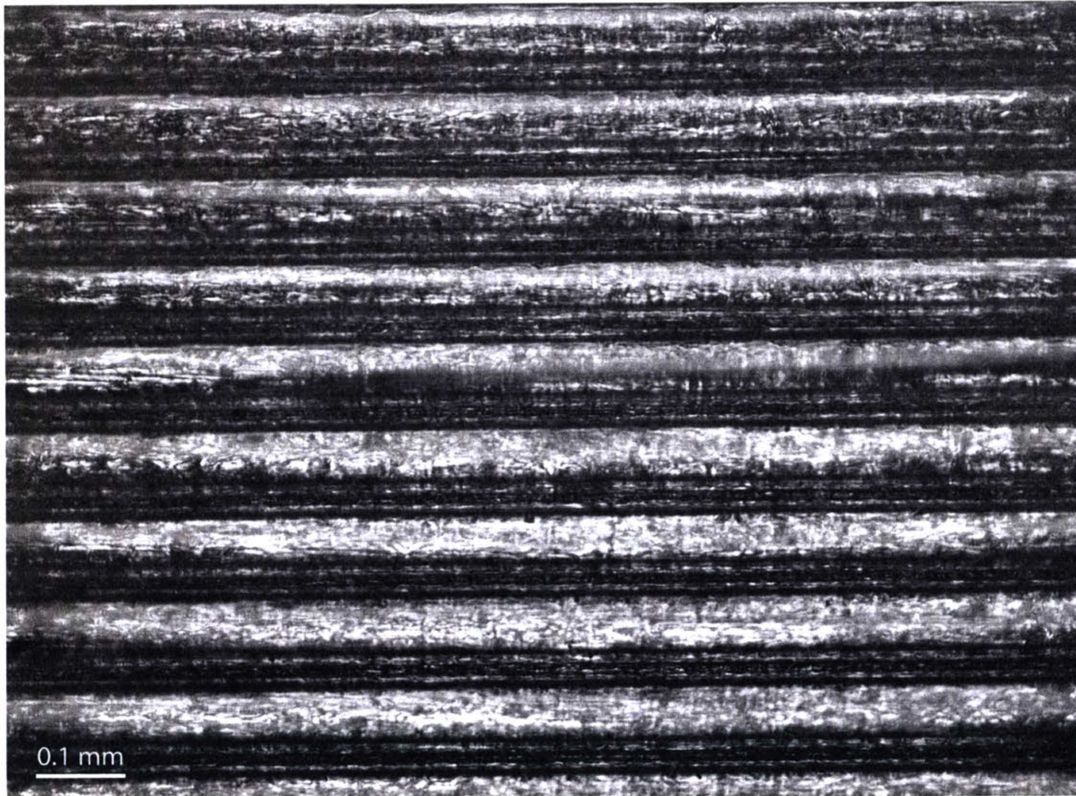

(c) Photograph of the photoresist at location A3 after removing tool S3.

Figure 5-17: Photographs of the photoresist at location A3 throughout the tool-making process. There are no apparent changes between development (Figure 5-17a) and subsequent tool castings (Figure 5-17b and Figure 5-17c). Features obviously bottom out and mild edge defects are visible and consistent between images.

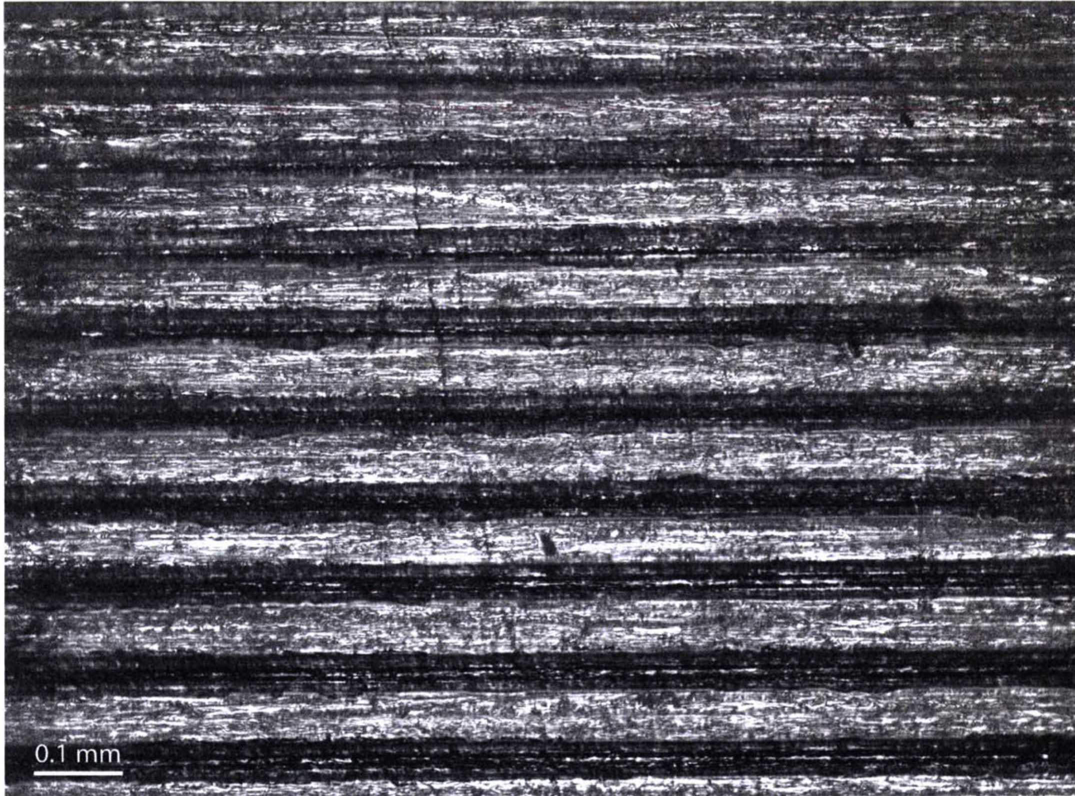

(a) Photograph of the photoresist at location A4 after development.

(b) Photograph of the photoresist at location A4 after removing tool S1.

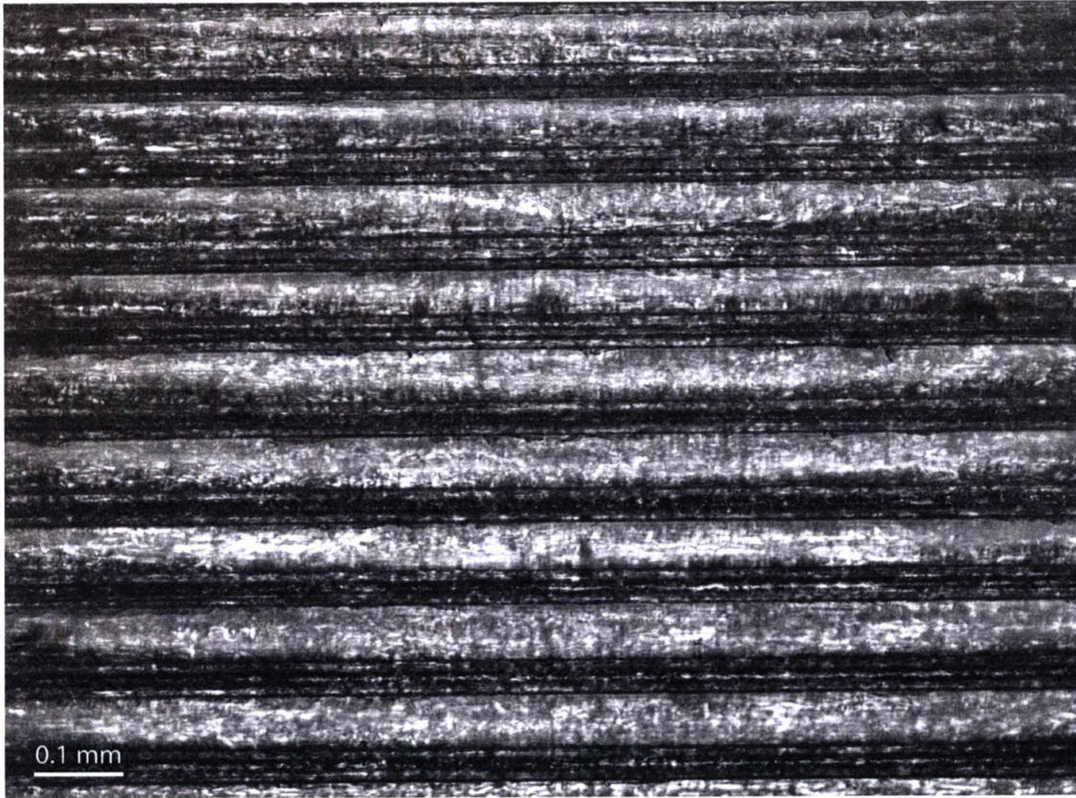

(c) Photograph of the photoresist at location A4 after removing tool S3.

Figure 5-18: Photographs of the photoresist at location A4 throughout the tool-making process. There are no apparent changes between development (Figure 5-18a) and subsequent tool castings (Figure 5-18b and Figure 5-18c). Features obviously bottom out and mild edge defects are visible and consistent between images. Most notable, the roughly vertical *scar* in the middle of this resist section is still visisble after each process step.

(a) Photograph of the photoresist at location B1 after development.

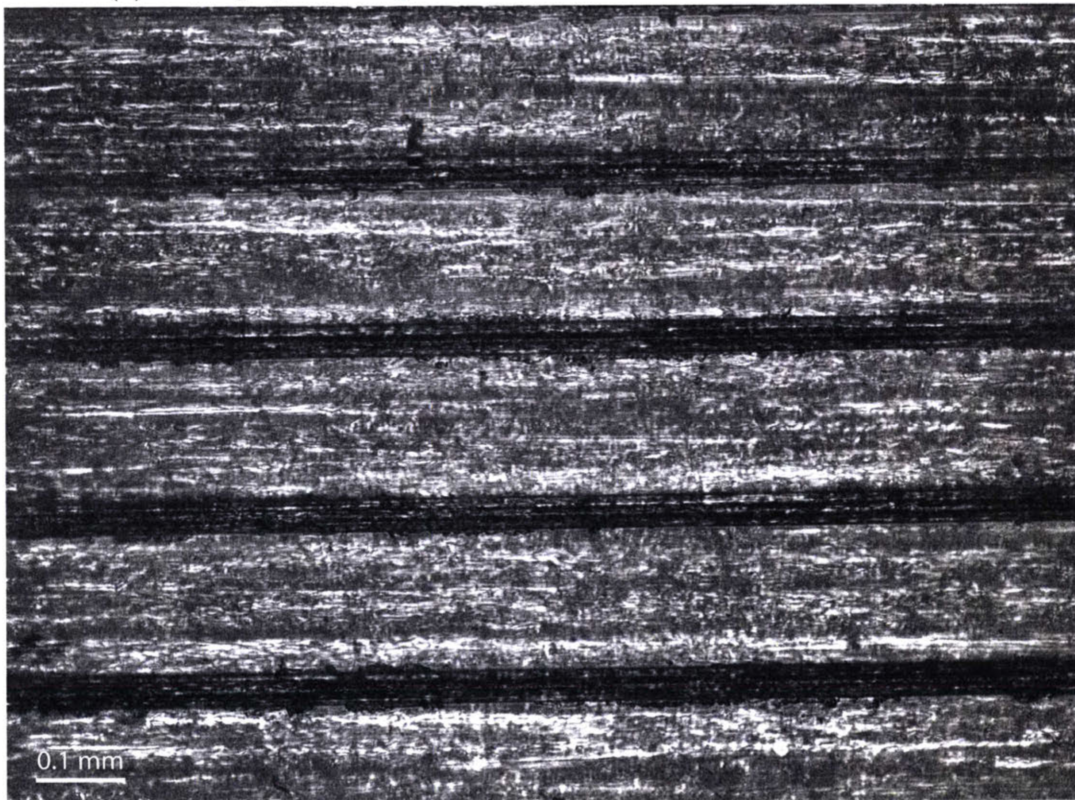

(b) Photograph of the photoresist at location B1 after removing tool S1.

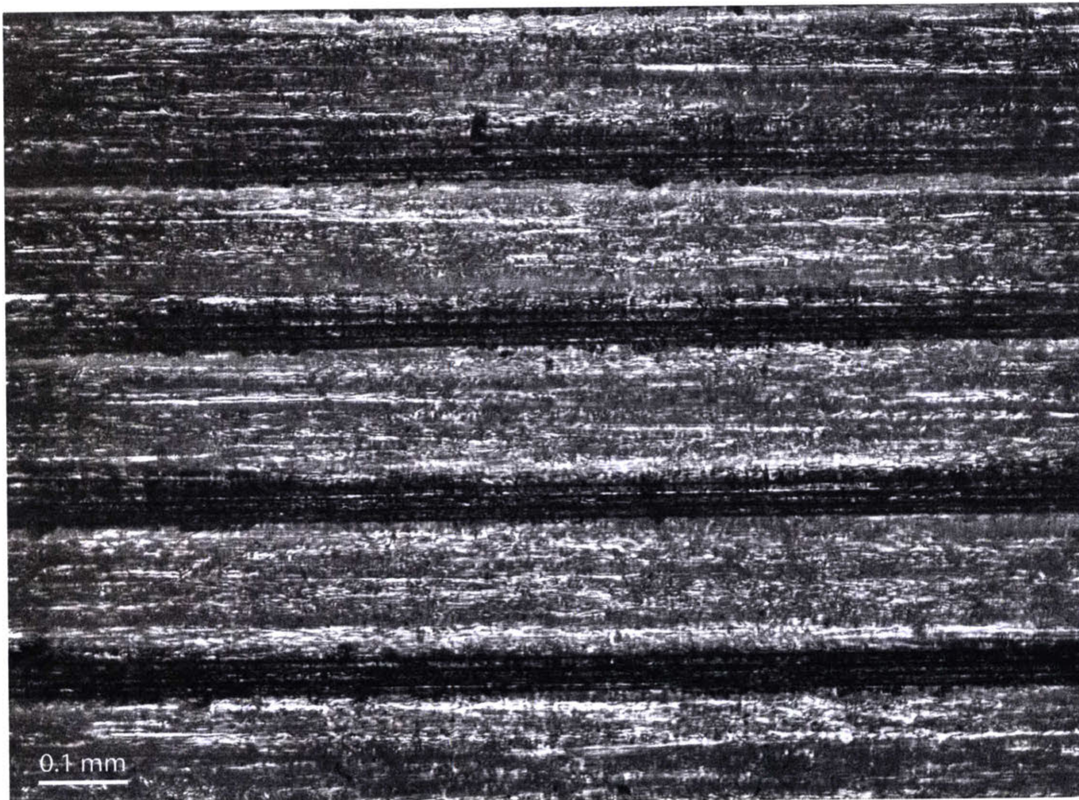

(c) Photograph of the photoresist at location B1 after removing tool S3.

Figure 5-19: Photographs of the photoresist at location B1 throughout the tool-making process. Note the obvious change between Figures 5-19a and 5-19b as if the PDMS casting slanted a previously vertical sidewall. There is no obvious alteration to the photoresist between casting tool S1 (Figure 5-19b) and tool S3 (Figure 5-19c), and minor root width edge roughness and defects are consistent between the two. Both S1 and S3 molds also exhibit bottomed out features, where the exposure propogated all the way through to the SU8 planarizing layer.

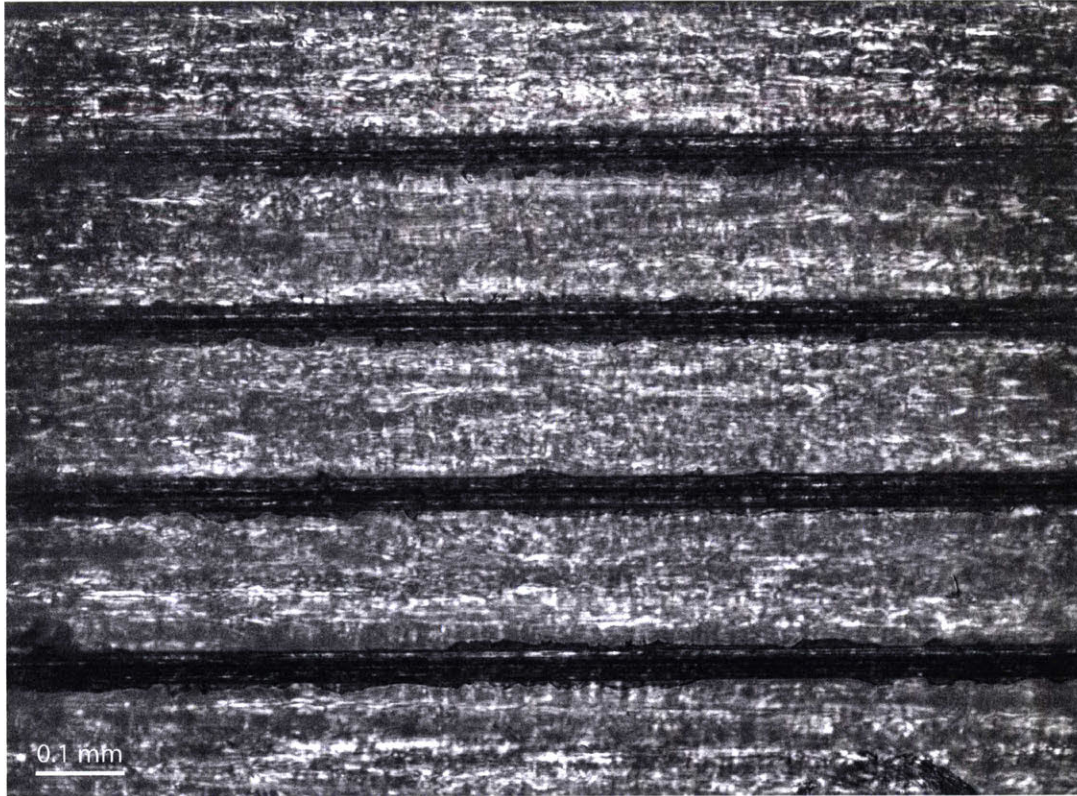

(a) Photograph of the photoresist at location B2 after development.

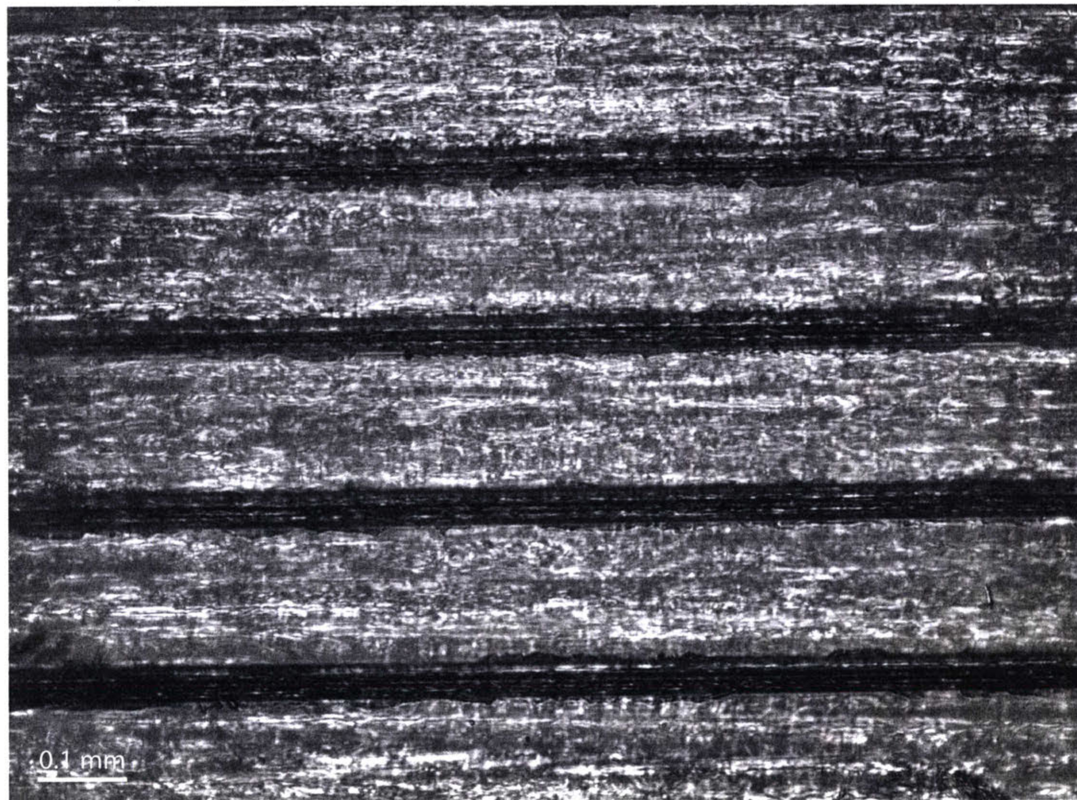

(b) Photograph of the photoresist at location B2 after removing tool S1.

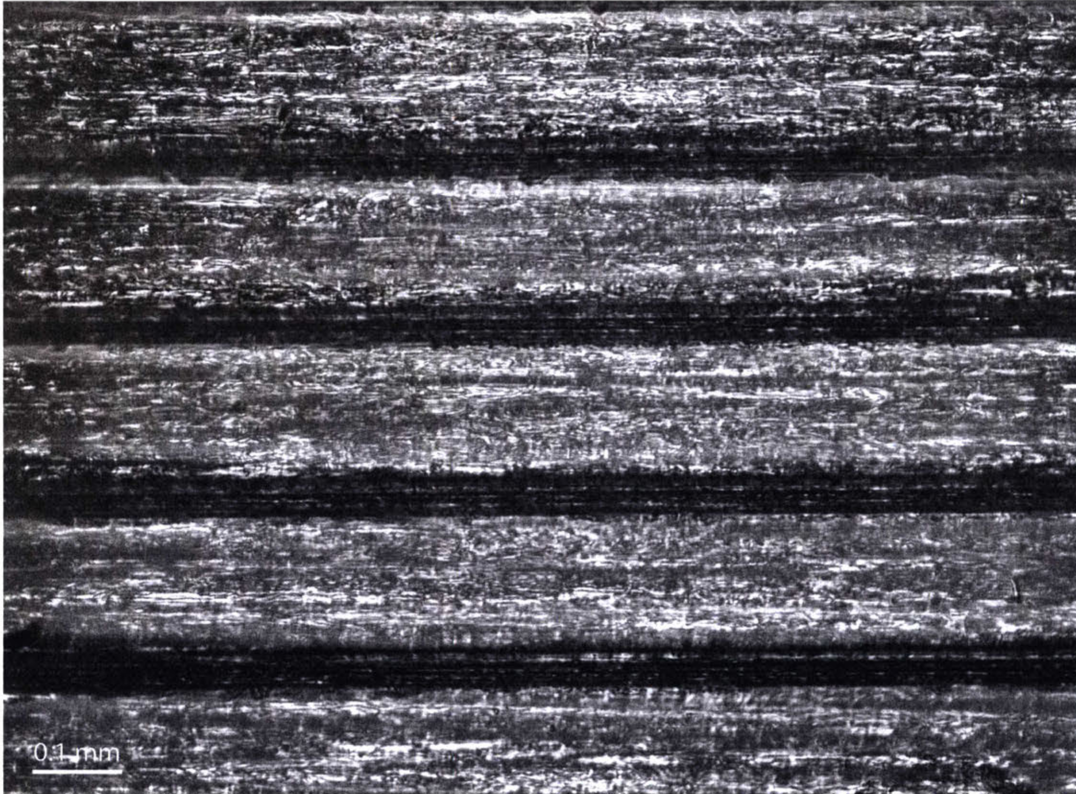

(c) Photograph of the photoresist at location B2 after removing tool S3.

Figure 5-20: Photographs of the photoresist at location B2 throughout the tool-making process. There are no apparent changes between development (Figure 5-20a) and subsequent tool castings (Figure 5-20b and Figure 5-20c). Features obviously bottom out and mild edge defects are visible and consistent between images.

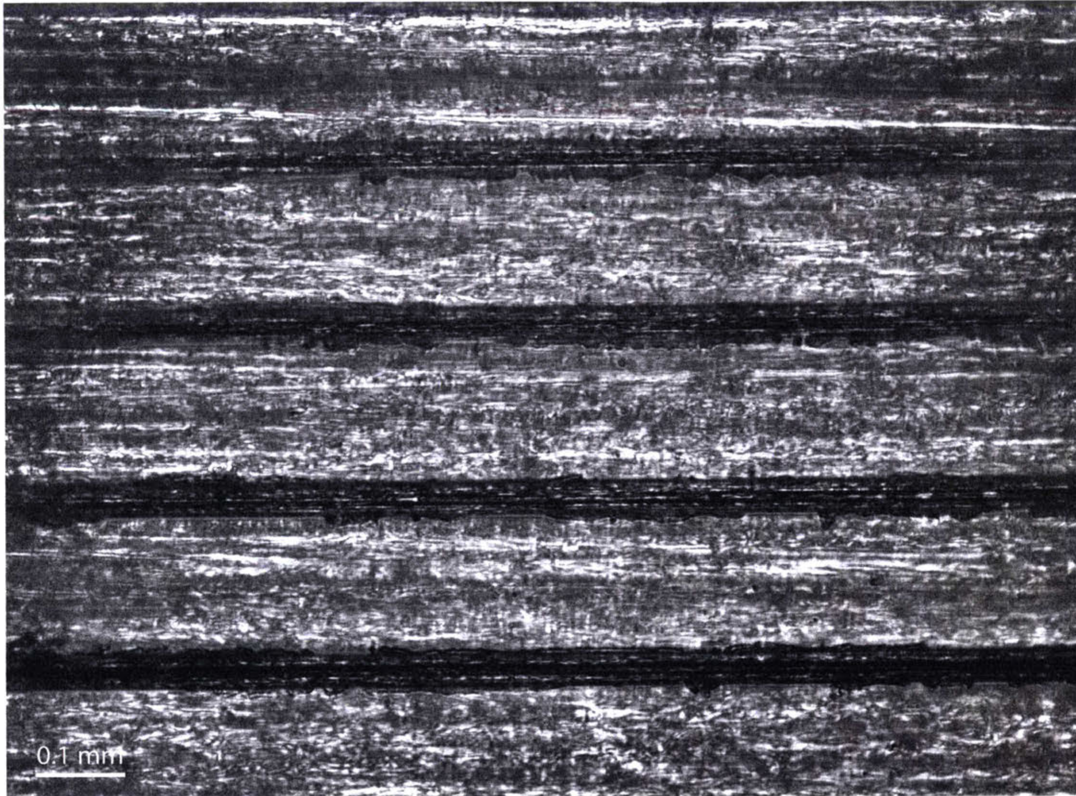

(a) Photograph of the photoresist at location B3 after development.

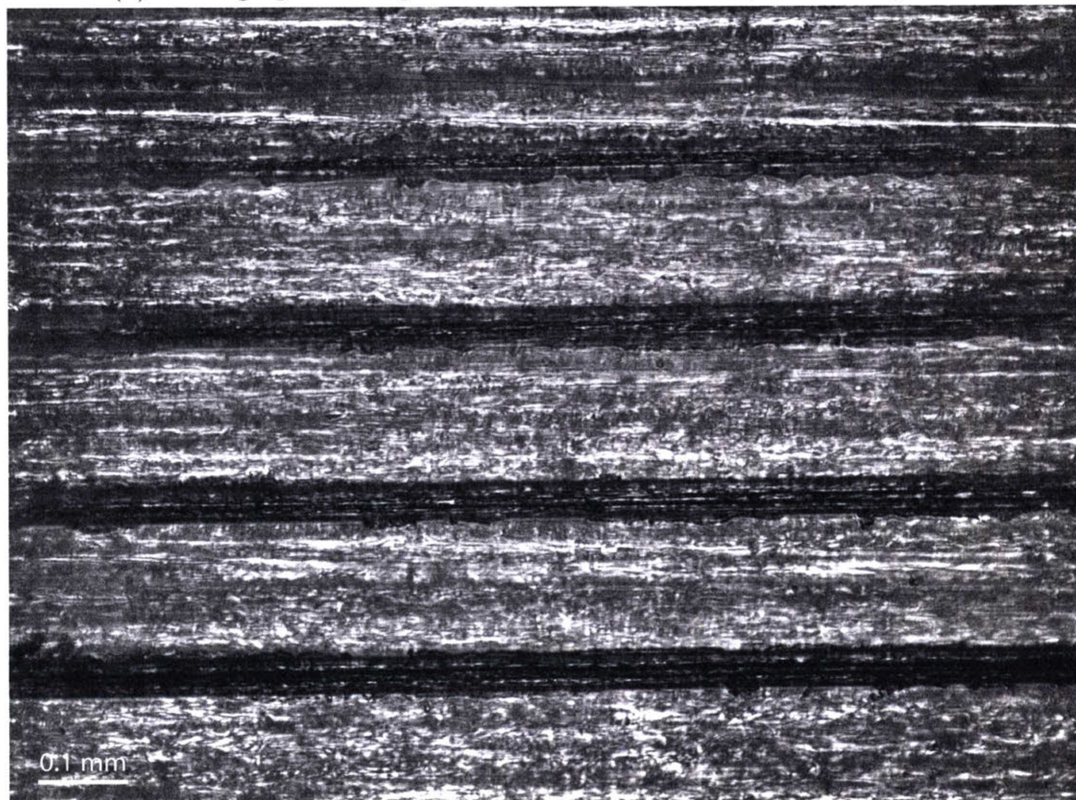

(b) Photograph of the photoresist at location B3 after removing tool S1.

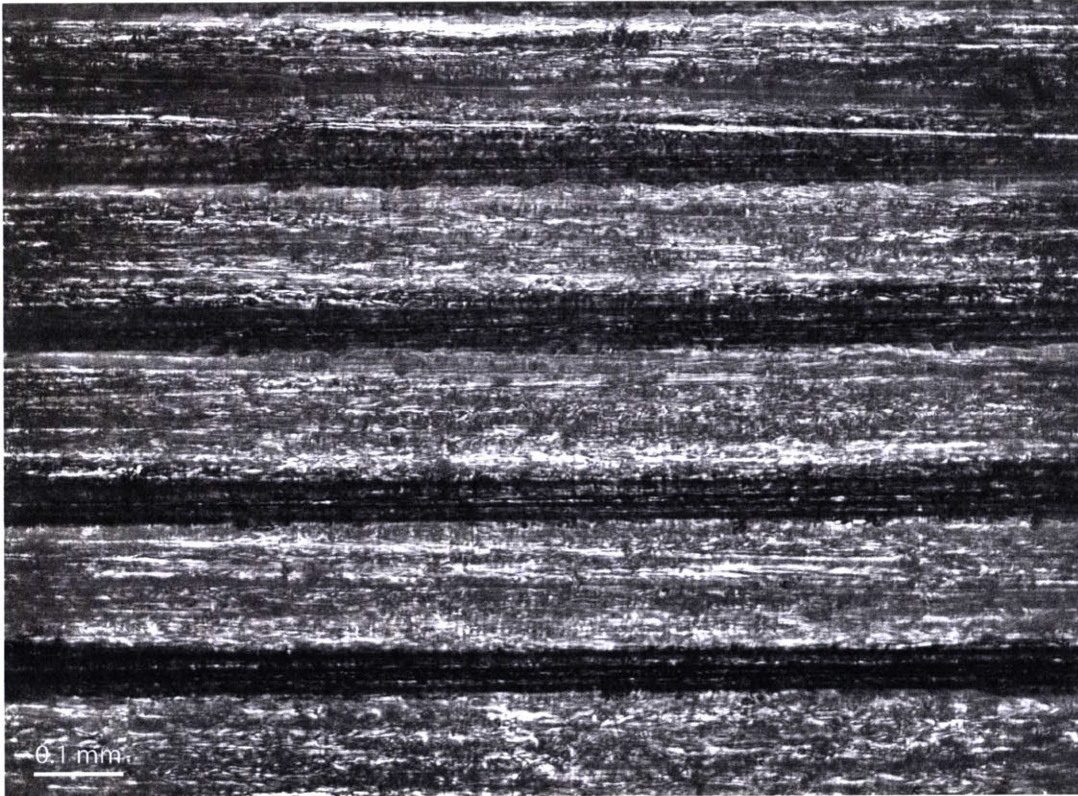

(c) Photograph of the photoresist at location B3 after removing tool S3.

Figure 5-21: Photographs of the photoresist at location B3 throughout the tool-making process. There are no apparent changes between development (Figure 5-21a) and subsequent tool castings (Figure 5-21b and Figure 5-21c). Features obviously bottom out and mild edge defects are visible and consistent between images.

(a) Photograph of the photoresist at location B4 after development.

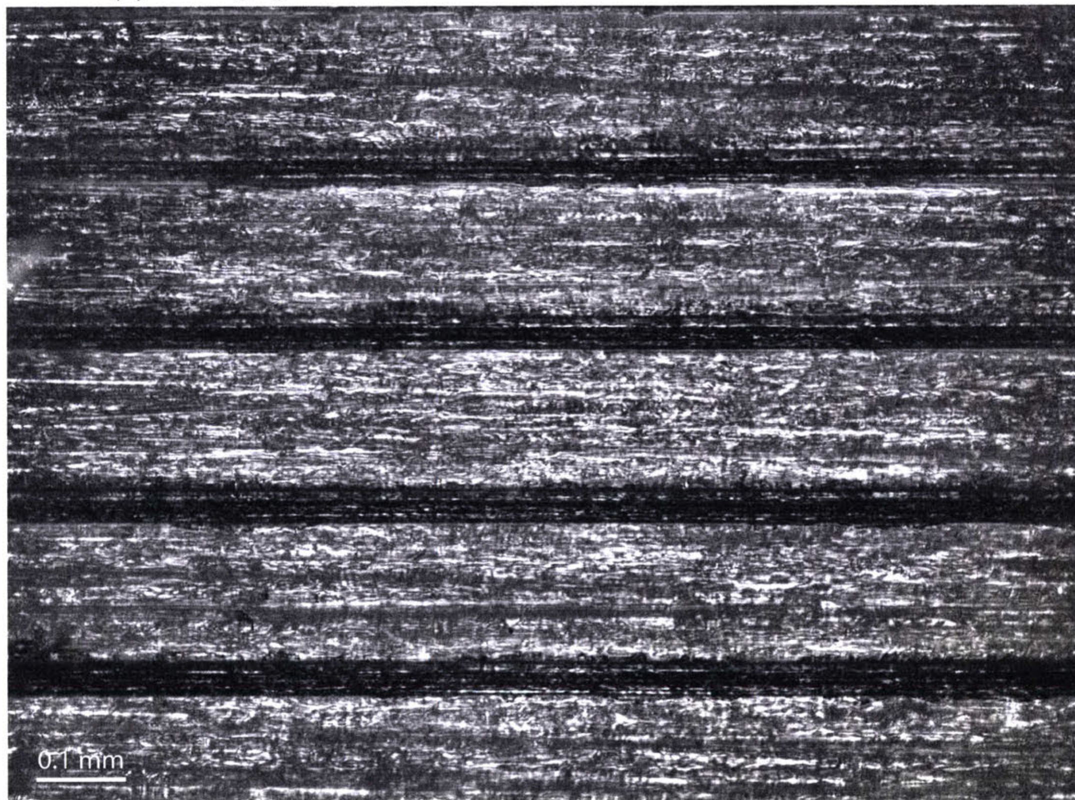

(b) Photograph of the photoresist at location B4 after removing tool S1.

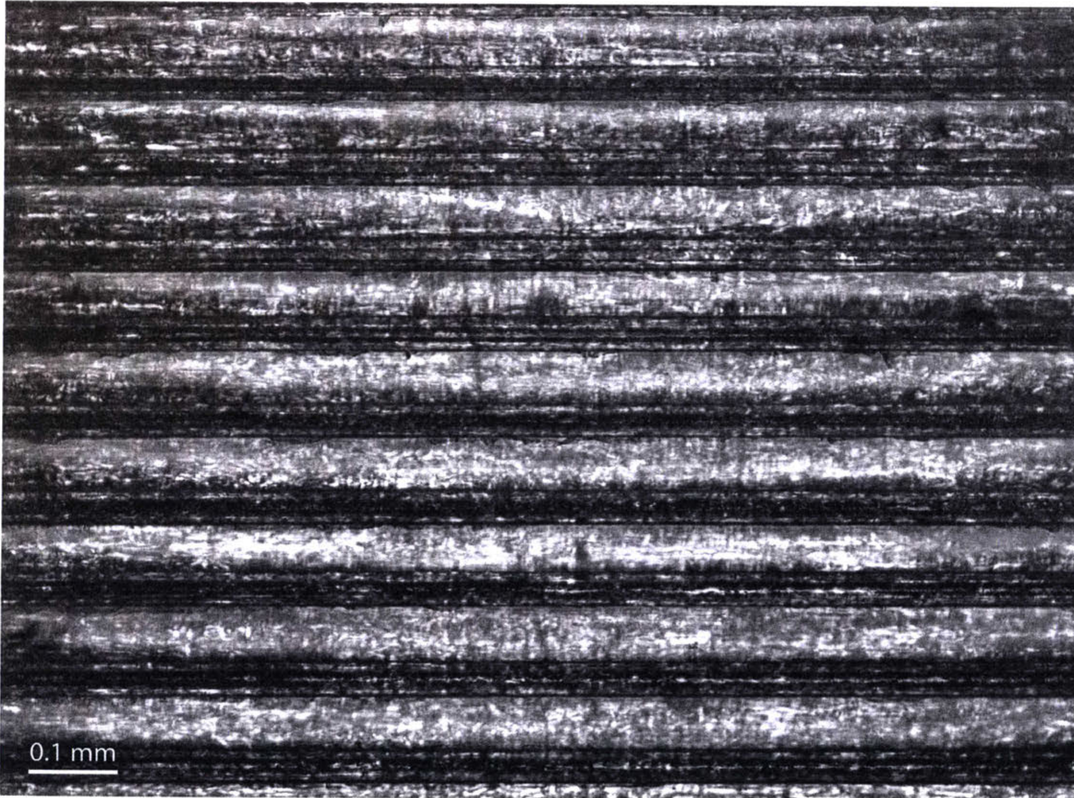

(c) Photograph of the photoresist at location B4 after removing tool S3.

Figure 5-22: Photographs of the photoresist at location B4 throughout the tool-making process. There are no apparent changes between development (Figure 5-22a) and subsequent tool castings (Figure 5-22b and Figure 5-22c). Features obviously bottom out and mild edge defects are visible and consistent between images.

A1 and B1 clearly show changes in the patterning layer between development and removing tool S1. No other sections in A and B exhibit this property. However, all photoresist sections remain consistent between subsequent tool castings. This suggests that there are mechanisms by which the AZ 9260 photoresist can be deformed between development and the removal of the first tool from the mold. However, the photoresist is visually repeatable over the time span and processing steps involved in casting PDMS tools S1 through S3.

5.4.2 Pattern Replication and PDMS Stamp Repeatability

For the manufacturing scale-up of μCP, it is paramount for the patterning layer mold to yield repeatable PDMS tools over multiple castings. Two process repeatabilities are critical to demonstrating the multi-use utility of a single patterning layer. First, the stamp features must accurately and continuously replicate the photoresist mold over multiple castings. Second, the PDMS stamp features must exhibit the same critical dimensions, implying that the resist too must not change between tool castings.

To test replication and repeatability, PDMS features of tool S1 and S3 were compared, along with the corresponding locations in the patterning layer after each respective casting. The locations for this comparison, A* and B*, were determined by imaging cross sections of A1-A4 and B1-B4 in tool S1, and identifying a group of the most uniform, clean, and characteristic features. Measurements of the PDMS cross sections between S1 and S3 assessed tool repeatability, while measurements of PDMS features in S1 compared to measuremenst of photoresist geoemtries after casting tool S1 provided insight into pattern replication by the PDMS. Comparisons between S3 PDMS and photoresist also sought to investigate pattern replicaiton.

Table 5.4 lists the stamp and patterning layer locations of the A* and B* regions. Figure 5-23, Figure 5-24, Figure 5-25, and Figure 5-26 show photographs of the A* features in tool S1, A* features in tool S3, B* features in tool S1, and B* features in tool S3 respectively. All four cross sections exhibit the same trapezoidal feature shape, demonstrating high PDMS tool repeatabilitity. Figure 5-27 contains pictures of the A* location in the photoresist patterning layer following the removal of tools S1 and S3 while Figure 5-28 displays the same images but for B*. Just as with the patterning layer images of A1-A4 and B1-B4, A* and B* do not exhibit observable changes to the photoresist between casting and removing tool S1 and S3. Qualitatively, this indicates that the photoresist mold does not change over the short term of multiple tool castings.

Section	Axial Position (mm)	Circumferential Position (counts)
A*	116.5	6250
B*	120	750

Table 5.4: Axial and circumferential locations of ideal features A* and B*.

(a) A cross section photograph of PDMS tool S1 at location A*.

(b) A top-view photograph of PDMS tool S1 at location A*.

Figure 5-23: Photographs of PDMS tool S1 at location A*. Note the near-trapezoidal cross section feature geoemtry with approximately flat tops. Crisp lines and edges are evident in the top view.

(a) A cross section photograph of PDMS tool S3 at location A*.

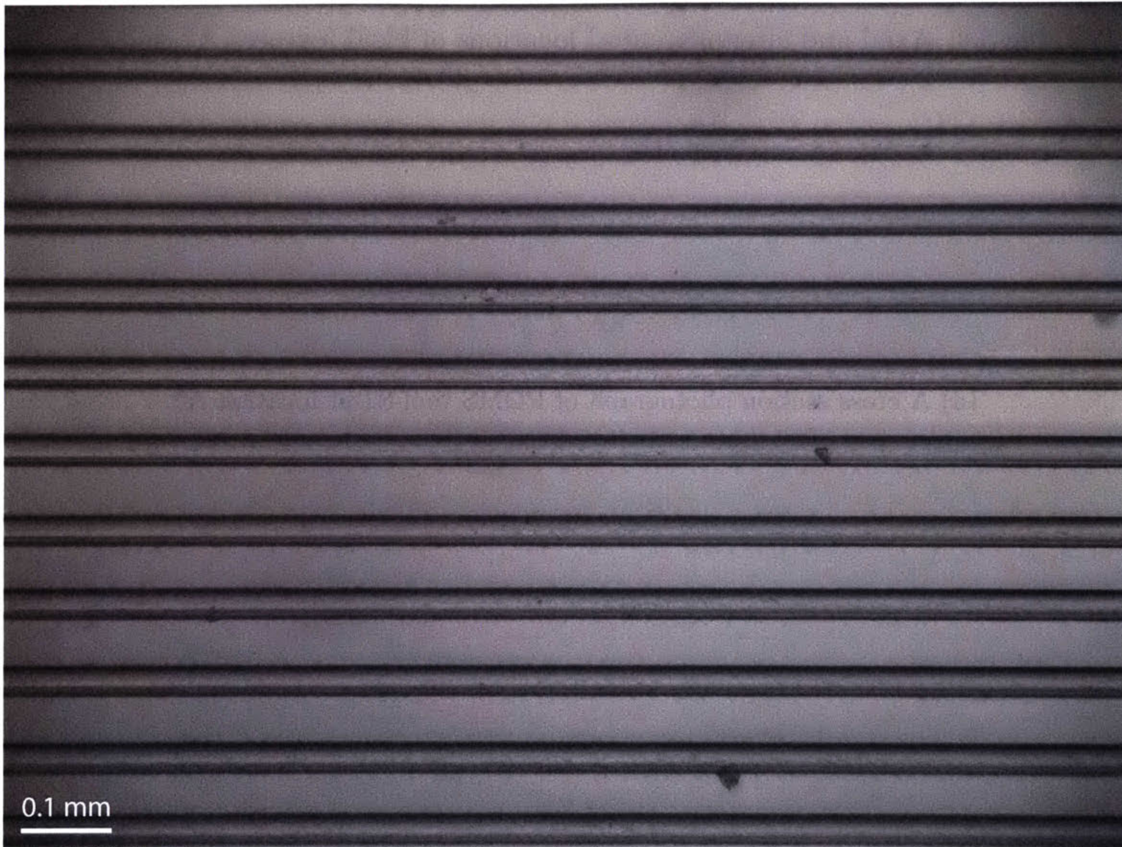

(b) A top-view photograph of PDMS tool S3 at location A*.

Figure 5-24: Photographs of PDMS tool S3 at location A*. Again, note the near-trapezoidal cross section feature geoemtry with approximately flat tops, and crisp liines in the top view.

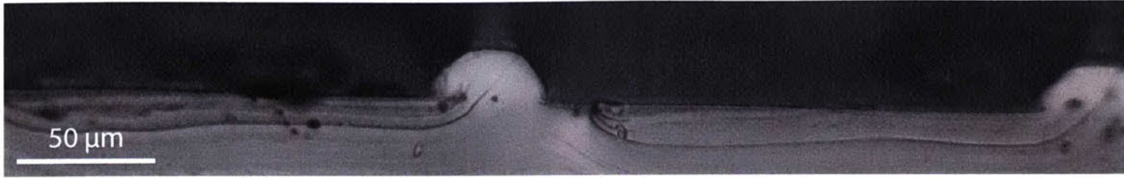

(a) A cross section photograph of PDMS tool S1 at location B*.

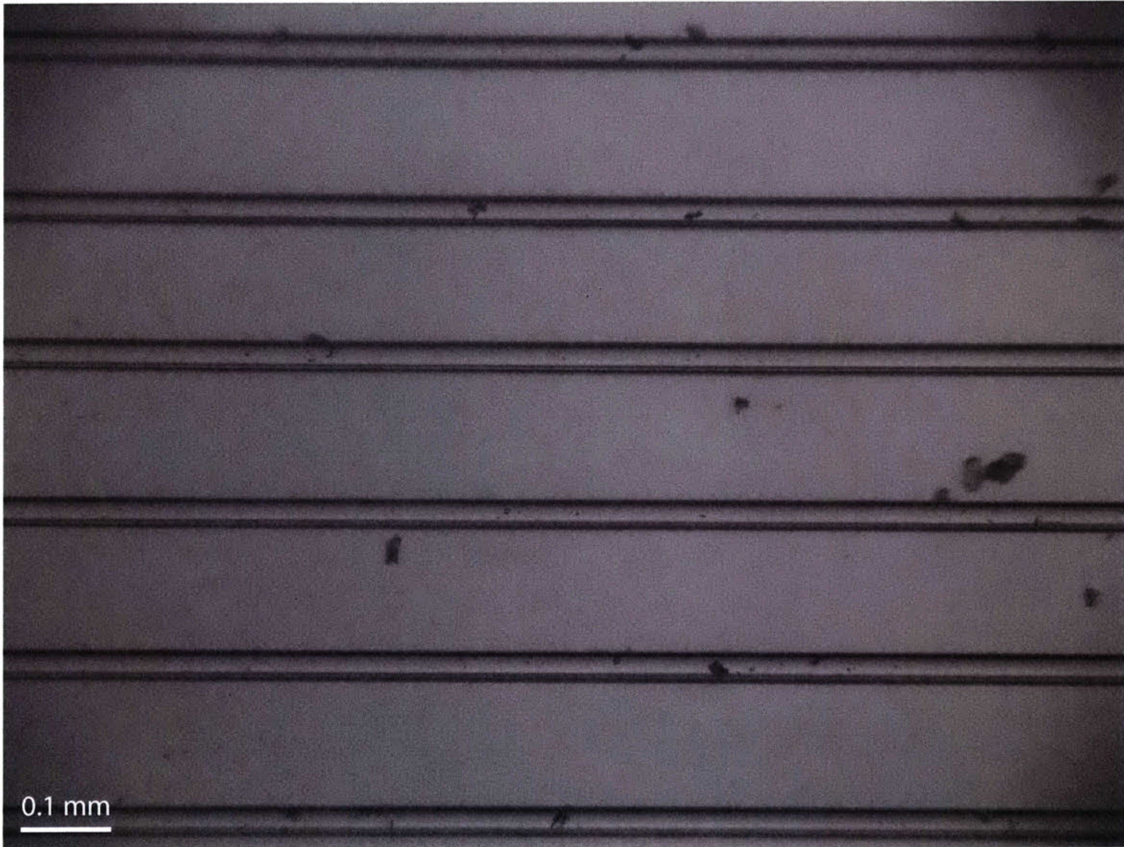

(b) A top-view photograph of PDMS tool S1 at location B*.

Figure 5-25: Photographs of PDMS tool S1 at location B*. Note the near-trapezoidal cross section feature geoemtry with approximately flat tops, as seen in A*. Crisp lines and edges are evident in the top view as well.

(a) A cross section photograph of PDMS tool S3 at location B*.

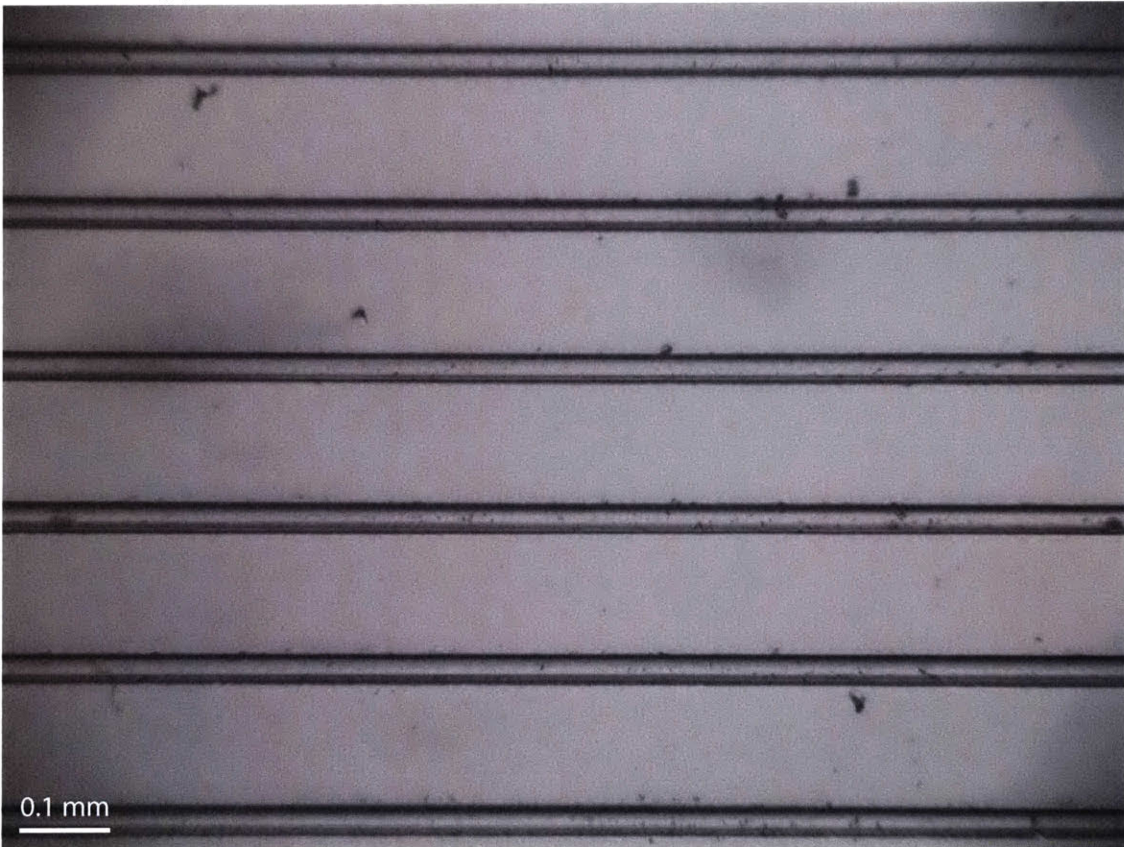

(b) A top-view photograph of PDMS tool S3 at location B*.

Figure 5-26: Photographs of PDMS tool S3 at location B*. Again, note the near-trapezoidal cross section feature geoemtry with approximately flat tops. and crisp liines in the top view.

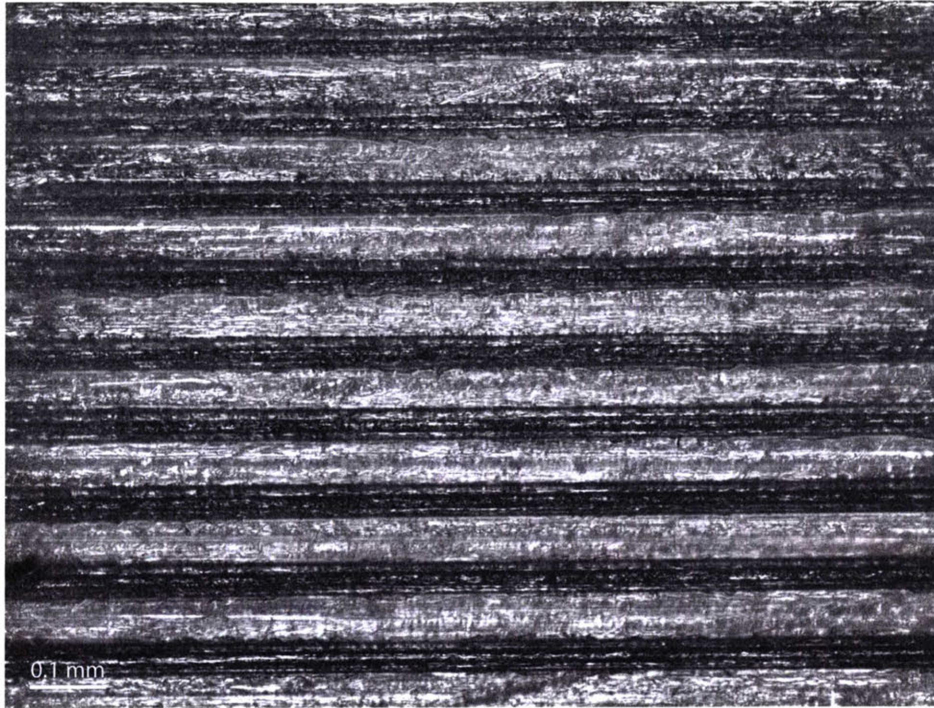

(a) Photograph of the photoresist at location A* after removing tool S1.

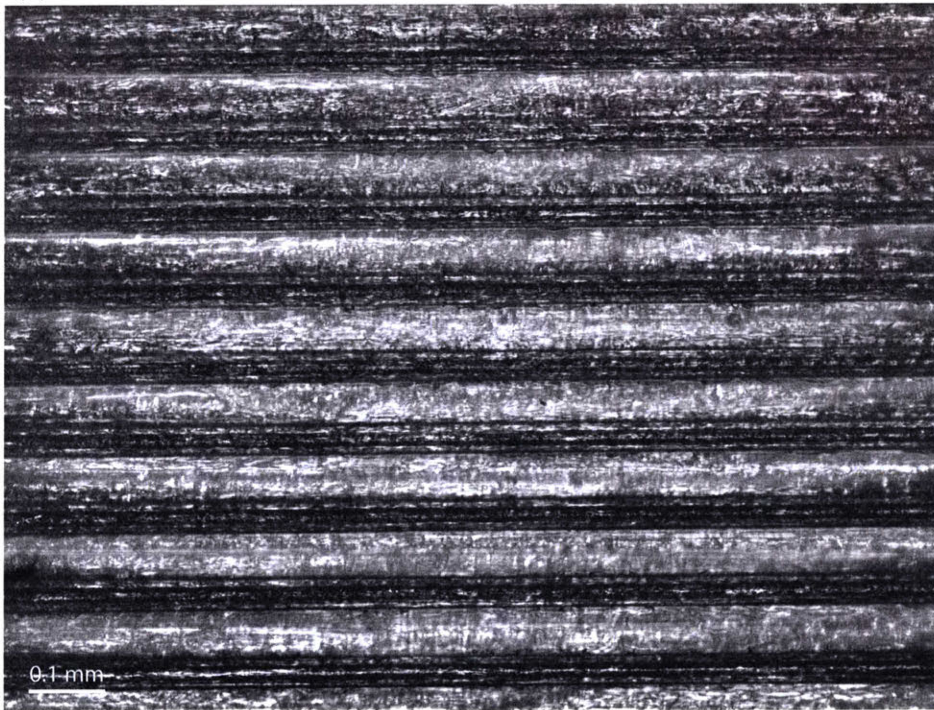

(b) Photograph of the photoresist at location A* after removing tool S3.

Figure 5-27: Photographs of the photoresist at location A* throughout the tool-making process. There are no apparent changes between casting tool S1 (Figure 5-27a) and tool S3 (Figure 5-27a). Although the features in the A* PDMS looked most ideal, the corresponding photoresist location may not look the best. Note the lack of colorlessness of the bottomed out region compared to A1 (Figure 5-15b).

(a) Photograph of the photoresist at location B* after removing tool S1.

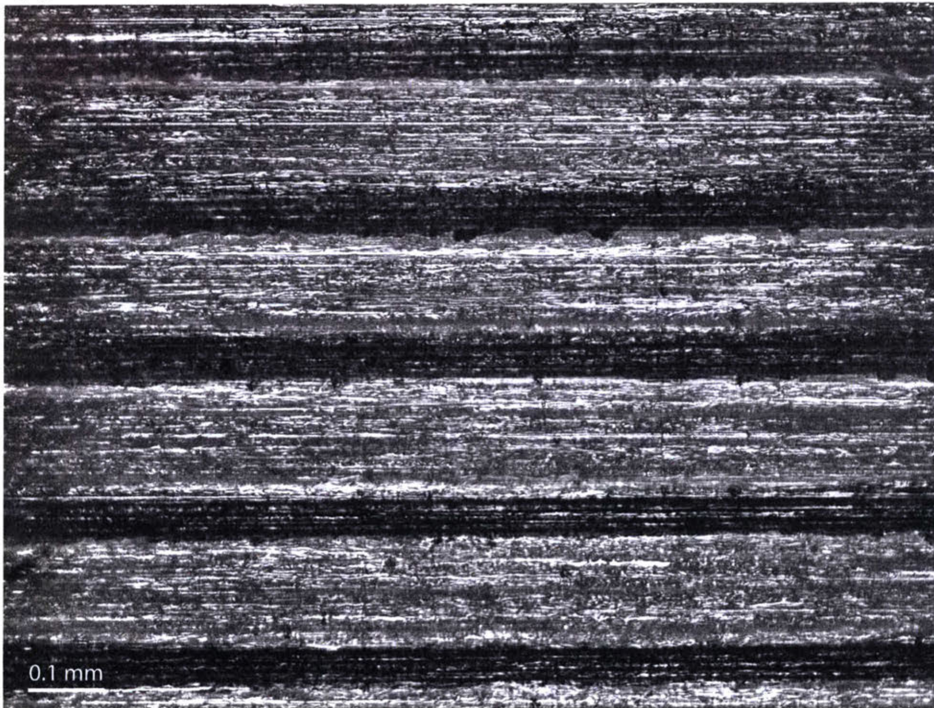

(b) Photograph of the photoresist at location B* after removing tool S3.

Figure 5-28: Photographs of the photoresist at location B* throughout the tool-making process. There are no apparent changes between casting tool S1 (Figure 5-28a) and tool S3 (Figure 5-28a).

Measurements of feature root widths, top widths, and heights were taken for quantitative analysis. Figure 5-29 shows the mean measured top widths of A* and B* features in tools S1 and S3, as well as in the photoresist following the removal of tools S1 and S3. Figure 5-30 presents mean measured root widths of A* and B*. The presented root width data are tightly bound, and originate from the same distribution with a confidence level of 95% (using a two sample Kolmogorov-Smirnov Test). The top width data similarly all belong to the same distribution with 95% certainty. The rejection of the null hypothesis suggests that the PDMS tool successfully replicates the photoresist mold, and that the mold and tools are repeatible over the investigated time-scale and associated thermal and mechanical processes. Therefore, it can be said that A and B single exposure features have a root width of 41.99 $\pm$ 2.39 μm and a top width of 16.19 $\pm$ 1.80 μm. Heights could only be measured using the PDMS cross sections. Figure 5-31 illustrates a tight height data spread, with a mean of 15.77 $\pm$ 1.21 μm. Again, features are consistent in this critical dimension, and the patterning layer achieved the intended procedural height. However, the height data sets only originate from the same distribution to 84 % confidence.

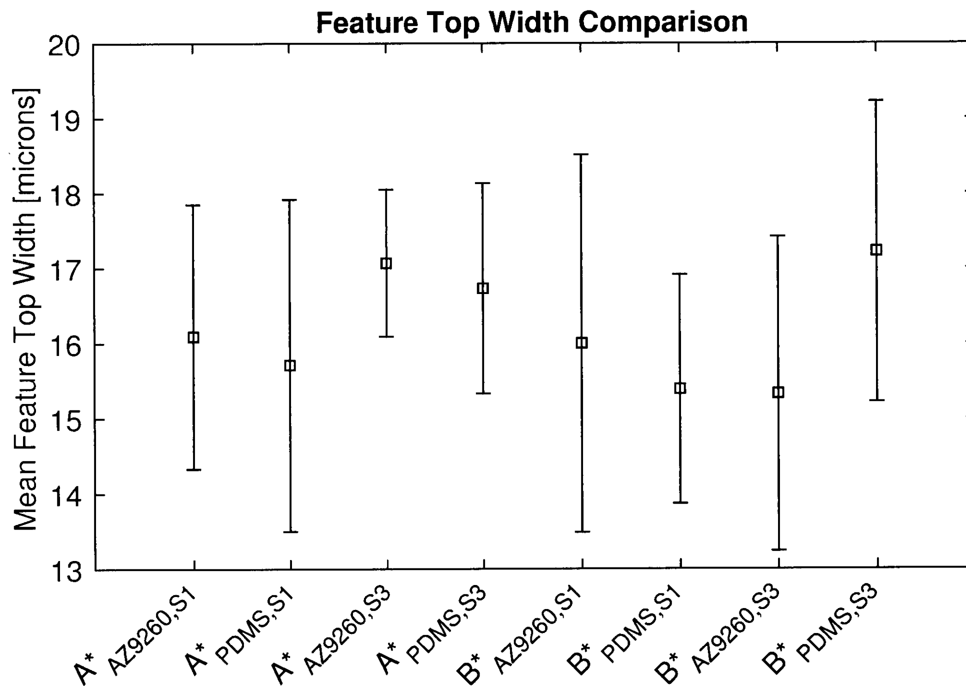

Figure 5-29: Measured A* and B* feature top widths in PDMS tools and in the photoresist patterning layer. Data presented are mean values. Error bars span one standard deviation above and below.

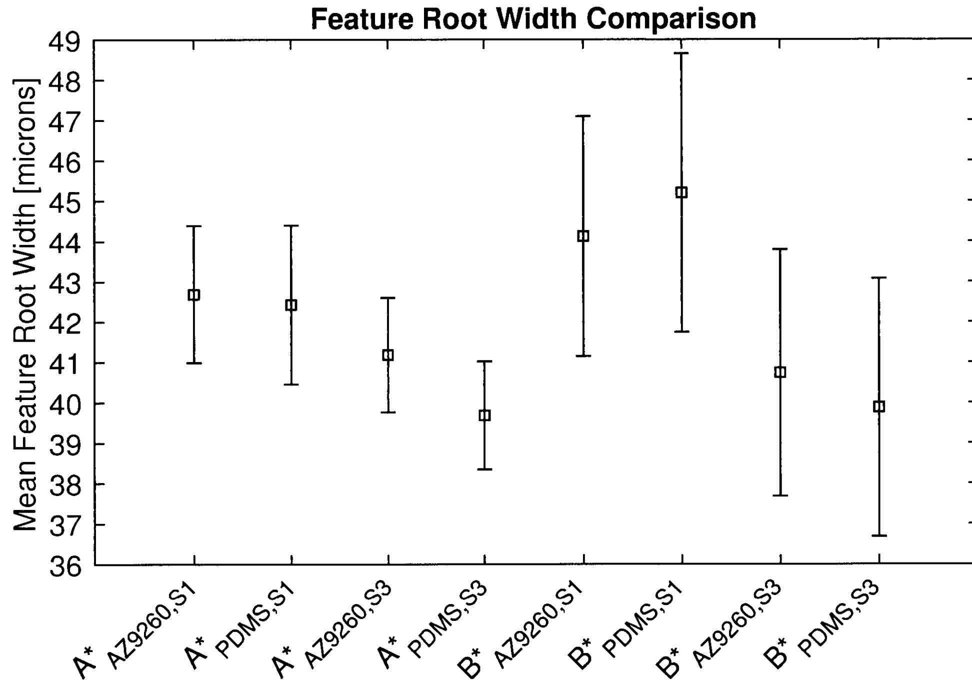

Figure 5-30: Measured A* and B* feature root widths in PDMS tools and in the photoresist patterning layer. Data presented are mean values. Error bars span one standard deviation above and below.

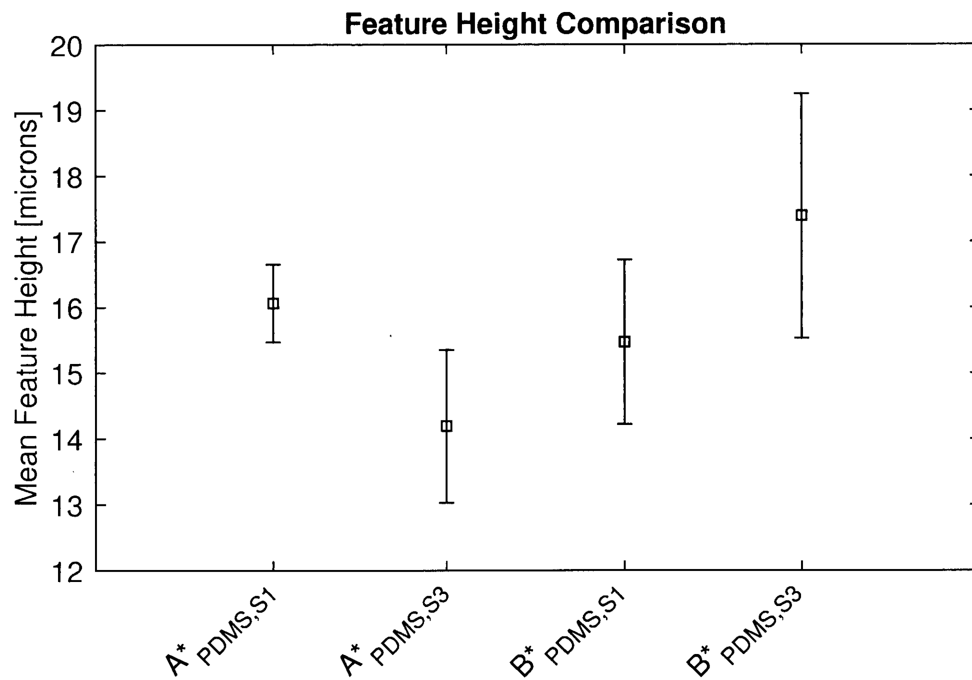

Figure 5-31: Measured A* and B* feature heights in PDMS tools. Data presented are mean values. Error bars span one standard deviation above and below.

To summarize, images of the photoresist between tool castings S1 and S3 at locations A* and B* show no visible difference. Root width and top widths appear constant in size, and minor root width edge defects are consistent between castings. Photographs of cross sections of the PDMS tools show similar trapezoidal feature shapes. Root width data from PDMS tools S1 and S3, and from the AZ 9260 photoresist mold for tools S1 and S3 agree to 95% confidence. The same can be said for top width. Therefore, presented qualitative and quantitative data suggest that the photoresist mold does not change over the span of three tool castings and that the PDMS features accurately replicate photoresist topology.

5.4.3 Contact Visualization and Analysis

When printing with HDT on a gold substrate, it is theorized that the ink transfers only when the PDMS tool makes direct contact with the substrate. Therefore, understanding the contact behavior of tools provides insight into potentially realizable print geometries. To analyze the contact of A and B features, tool S2 was imaged via the episcopic microscopy method described in Section 5.3.3. In an attempt to document quasi-static behavior, the tool was brought into contact with the hollow glass impression roll by applying a 1 N open loop force command. The open loop force command was then incremented in 0.2 N steps every 5 seconds. Every 1 N (1 N, 2 N, 3 N, etc.) the system was refocused, a picture taken, and the net measured force recorded. Although the dynamics of printing could lead to different contact responses for the same region of the tool, the quasi-static approach was chosen since it minimizes PDMS-glass adhesion and subsequent hysteresis effects visible with large force command steps and the subsequent overshoot.

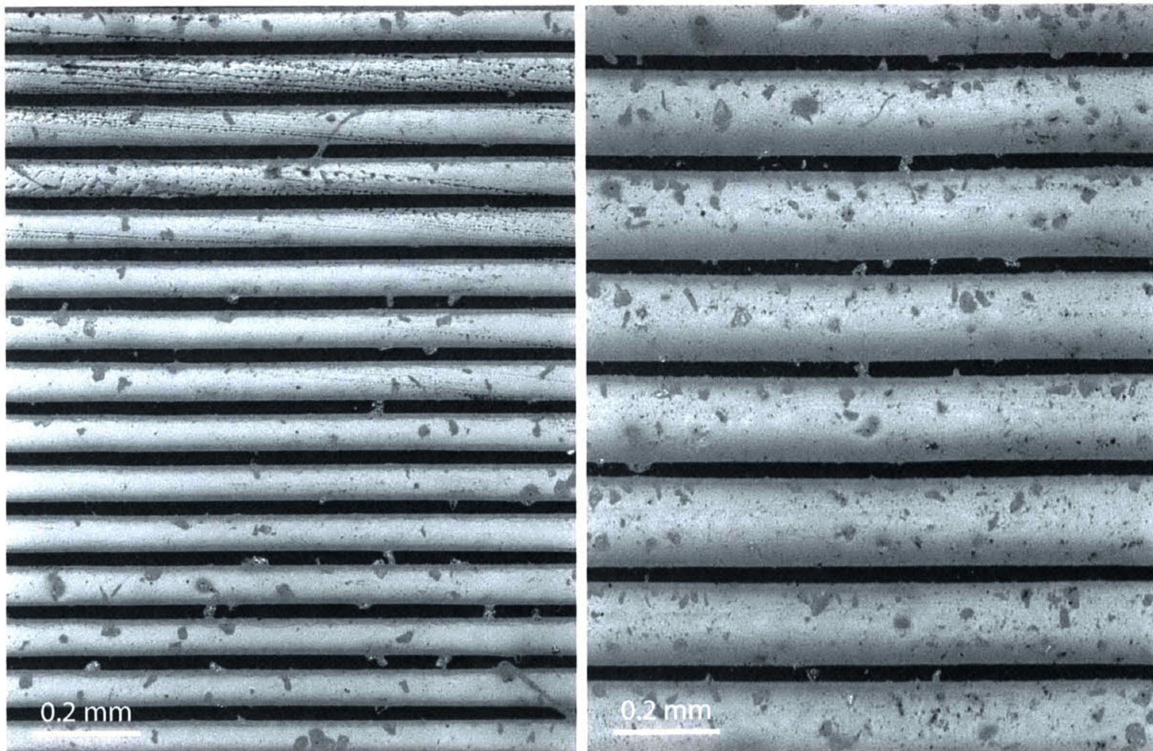

(a) Contact visualization of A* on tool S2. (b) Contact visualization of B* on tool S2.

Figure 5-32: Unprocessed images of A* and B* contact regions at measured open loop forces was 4.91 N and 4.84 N respectively. The spots and discontinuities are dust particles.

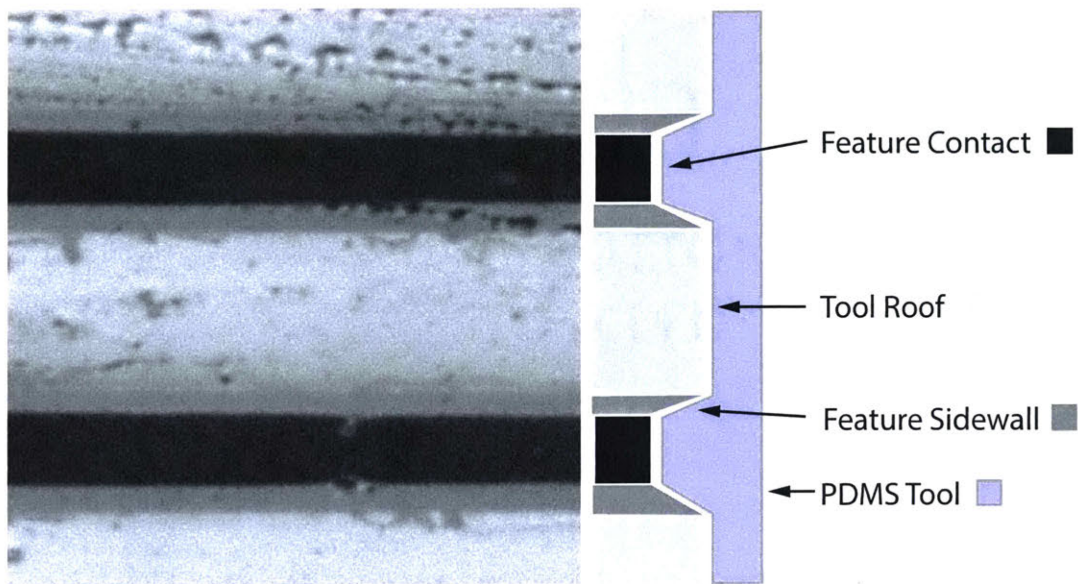

Figure 5-33: A schematic showing the theoretical compressed tool cross section corresponding to contact.

Contact trendlines for the A* and B* locations of tool S2 were generated using the described approach. The binarization algorith was calibrated use an A* and B* image both at 4.9 N of measured force. Figure 5-32 shows unprocessed photographs of A* and B* contact regions at the calibration settings visualization purposes. Figure 5-33 presents a cross section intepretation of the contact images. Speckles and discontinuities are assume to be debris (dust) on the PDMS and or on the impression roll. As expected, B* features appear wider than to A* features since they should displace further under the same load due to their coarser axial pitch. Figure 5-34 plots mean contact widths of A* and B* features as a function of the applied force (the measured open-loop force), and also displays fitted linear trendlines. The ratio of the slope of B*'s linear fit to A*'s is 1.57, which is on the order expected for this scenario, which cab simplified in concept to a collection of elastic columns loaded in parallel. Columns would displace twice as much at half the spatial density given the same load.

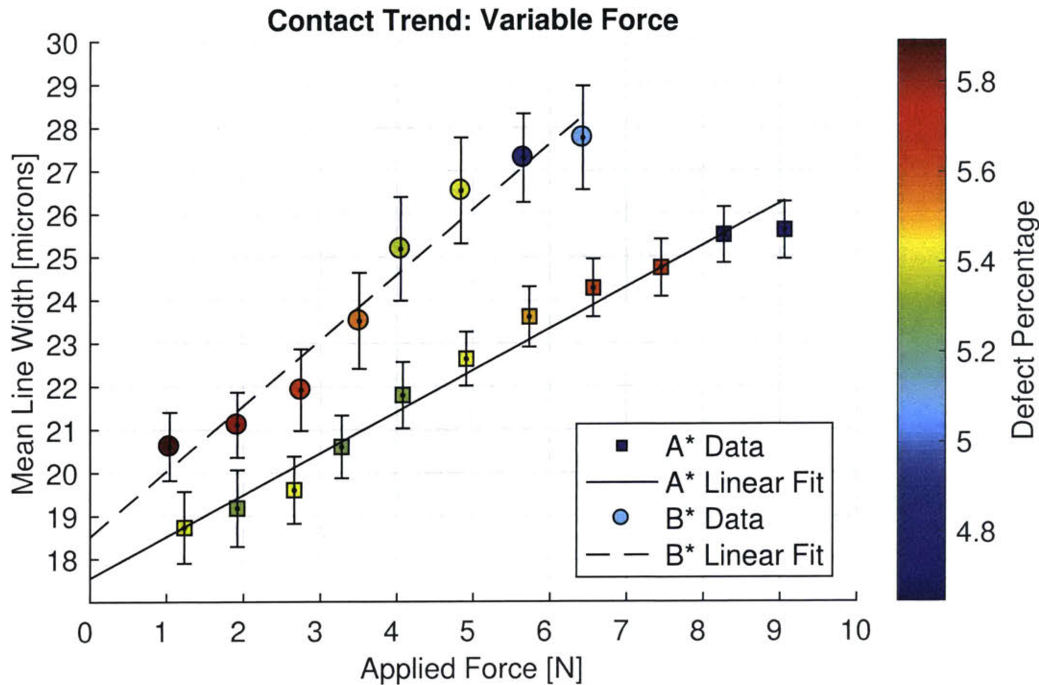

Figure 5-34: Mean contact line width as function of the measured applied force for single exposure lines of differerent axial pitches (features A and B). The contact response of A* is fit with $y = 0.97x + 17.55$ with $R^2 = 0.98$. B* is fit with $y = 1.52x + 18.52$ with $R^2 = 0.96$.

The data presented are the mean and standard deviation over the entire processed image. Comparison of line pairs in the calibration images (thousands of data points per line) through a two-sample Kolmogorov-Smirnov Test showed that any two lines belongs to the same continuous distribution at a 95% confidence level. This rejection of the null hypothesis allowed contact widths to be assessed over the whole image, rather than analyzing each line individually.

The top width of A* and B* features can be calculated from the linear fits in Figure 5-34 evaluated at 0 N applied force. Figure 5-35 presents the mean top widths in Figure 5-29 plus the estimated top widths from contact width. The data agree highly, with a 95% confidence from a one-sample Kologmorov-Smirnov test, denoting they belong to the same standard normal distribution. This result signifies that the feature top widths initially comes in contact. The top width surface either then physically widens in compression, or PDMS from the sidwall is pushed into the same surface defining the top width as the applied load on the tool increases. The additional contact measurements of A* and B* yield an updated mean top width of 16.46 ± 1.59 μm.

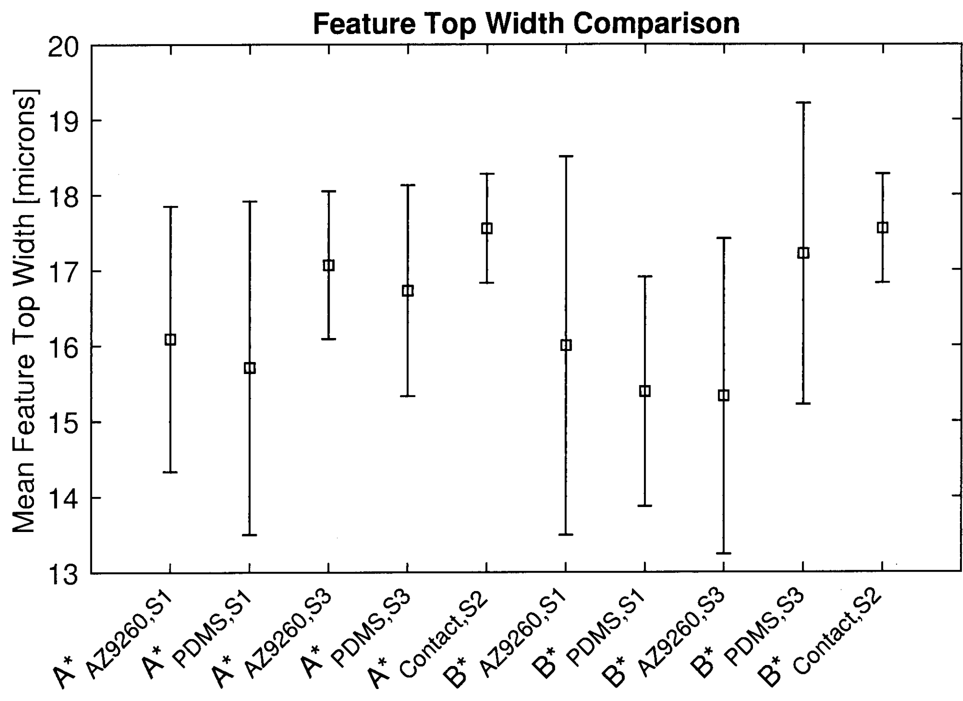

Figure 5-35: Measured A* and B* feature top widths in PDMS tools and in the photoresist patterning layer, and top width estimations from contact imaging. Data presented are mean values. Error bars span one standard deviation above and below. Note that all data belong to the same continuous distribution and therefore represent the same measurement.

5.4.4 Print Visualization and Analysis

A comparison of A* contact and print widths was performed using tool S4[1]. A* was printed multiple times using HDT on gold, with closed loop force control at a 6 N set point, web speed of 0.25 in/s, and open loop web tension of 2 lb. Tool S4 was not remounted between trials. After printing, S4 was placed in the contact system, similarly without moving the stamp on the print shaft. Multiple contact images of A* while changing the impression roll position were captured at a closed loop force of 7.1 N, the mean measured printing load.

One contact image and one print image of A* are presented in Figure 5-36. Both pictures exhibit similar line widths[2]. A histogram of the computionally analyzed line widths from two prints and two contact images are shown in Figure 5-37. The two distributions are very similiar in shape but with two obviously separate peaks. The line widths in printing were 38.45 $\pm$ 2.67 μm, while the respective lines in contact were 32.98 $\pm$ 4.92 μm. A two sample Kolmogorov-Smirnov test indicates that the two data sets belong to the same distribution with a shift and scaling at a 95% confidence level. Consequently, the data suggests a deterministic adjustment factor between contact geometry and the resulting print. Stamp swelling during inking, the aggressiveness of etching, stamp adhesion and hysterisis in contact, and print dynamics on stamp features could all be possible contributors.

This is a promising first analysis of the contribution of the tool in printing. There may be large variation over the entire stamp and subsequent print, but corresponding locations (axial and circumferential matching of features) should exhibit predictable and repeatable performance.

[1] S4 was the final cast stamp, which was intended for comparing print and contact.

[2] Refer to Figure 5-33 for interpreting contact. Ink transfers in regions of contact only during printing. The black lines in the a print image reflect the gold protected by ink in etching, and therefore should replicate tool contact.

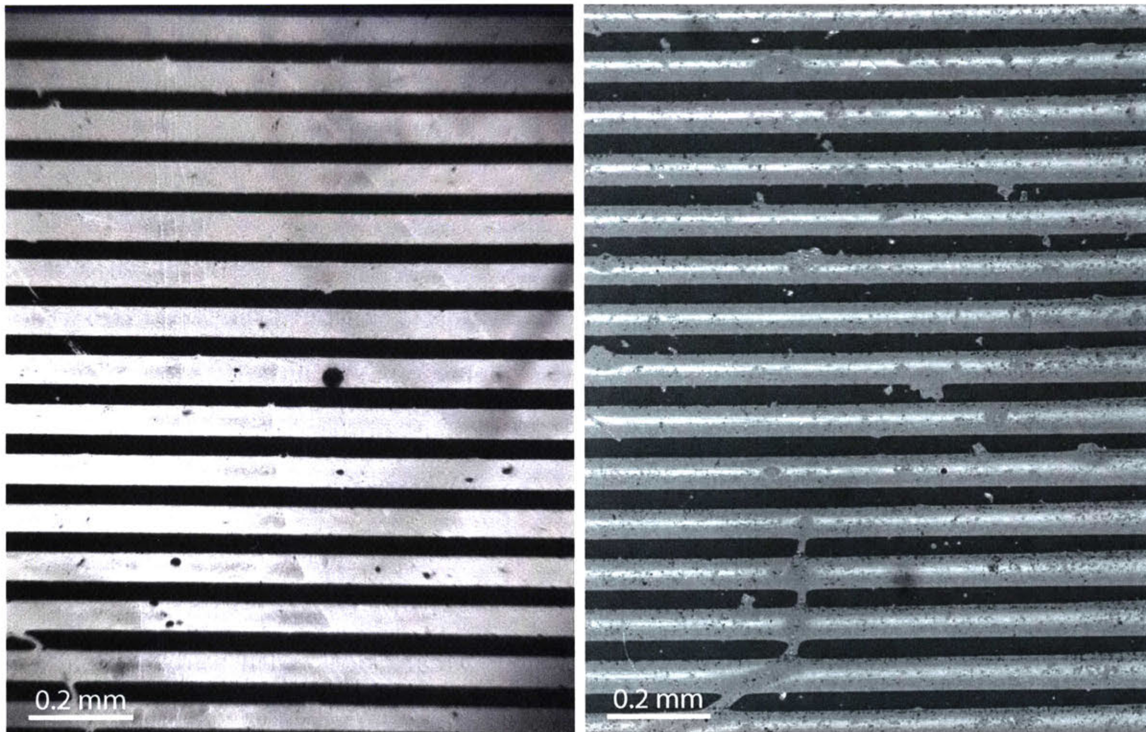

(a) Print image. (b) Contact image.

Figure 5-36: Sample print and contact images of A* features using tool S4.

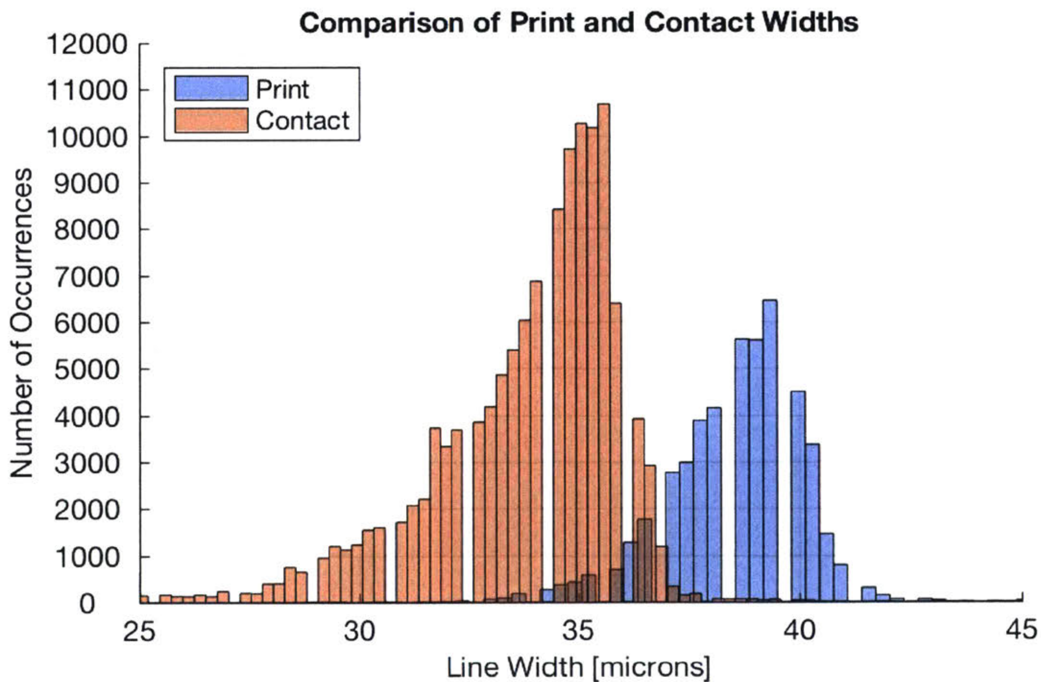

Figure 5-37: A histogram of print and contact line widths for A* features. The two data sets exhibit a ≈ 5 μm mean shift.

5.4.5 Summary

The AZ 9260 photoresist patterning layer was imaged at locations A1-A4, and B1-B4 after development, after casting and removing PDMS tool S1, and after casting and removing PDMS tool S3. All locations, except A1 and B1, remained visually unchanged. However, A1 and B1 features appeared to widen signifantly between development and tool S1, suggesting that there may exist a mechanism by which the photoresist can be reshaped during the first tool casting. The photoresist was also imaged at locations A* and B* after casting and removing tools S1 and S3. Again, no visual changes were observed between tool castings. Cross sections images of PDMS tools S1 and S3 showed geometrically similar profiles of the desirable trapezoidal shape. Quantitative comparisons of root and top widths in the PDMS and photoresist of tools S1 and S3 demonstrated accurate PDMS replication of the mold and repeatable feature geometry at 95% confidence. Mean root width and top width were measured to be 41.99 $\pm$ 2.39 μm and 16.19 $\pm$ 1.80 μm respectively. Contact analysis of A* and B* features exhibited a linear increase in contact line width with increasing applied force. Extrapolating the trends at 0 N of force presented top widths agreeing with measured data at 95% confidence. Finally, a comparison of print widths of A* features to contact widths exhibited a 5 μm mean shift of the data distribution.

5.5 Multiple Exposure Feature Results

This section analyzes C and D features, which were created using multiple overlapping exposures in the photoresist. C features were two partially overlapping exposures, intended to make slightly wider circumferentially oriented lines. D features were 11 consecutively overlapping exposures, intended to result in axially oriented features from fused line segments. Primarily qualitative data were obtained for these new feature attempts. In addition to visually checking for the intended feature shape, the data were still used to analyze successes and faults of C and D features in patterning layer repeatability, pattern replication and PDMS stamp repeatability, the contact region, and the resulting print.

5.5.1 Patterning Layer Repeatability

Figure 5-38, Figure 5-39, Figure 5-40, and Figure 5-41 show images of the photoresist in sample areas of C1, C2, C3, and C4 respectivey after development (subfigure a), after casting and removing tool S1 (subfigure b), and after casting and removing tool S3 (subfigure c). Similarly, Figure 5-42, Figure 5-43, Figure 5-44, and Figure 5-45 are pictures of the photoresist at sample areas of D1, D2, D3, and D4 respectively. Table 5.5 list the C and D locations, reporting the values for the posiitons of the drum and linear stage during writing. It is important to note that D features formed significantly different than anticipated. See Section 5.5.5 for an details on the expected D geometry.

Location Name	Axial Position (mm)	Circumferential Position (counts)
C1	124.5	1334
C2	124.5	3185
C3	124.5	5230
C4	124.5	7157
D1	124.5	1741
D2	124.5	3809
D3	124.5	5901
D4	124.5	7814

Table 5.5: Axial and circumferential positions of the patterning layer that were imaged for photoresist repeatability tests of features created using overlapping exposures.

(a) Photograph of the photoresist at location C1 after development.

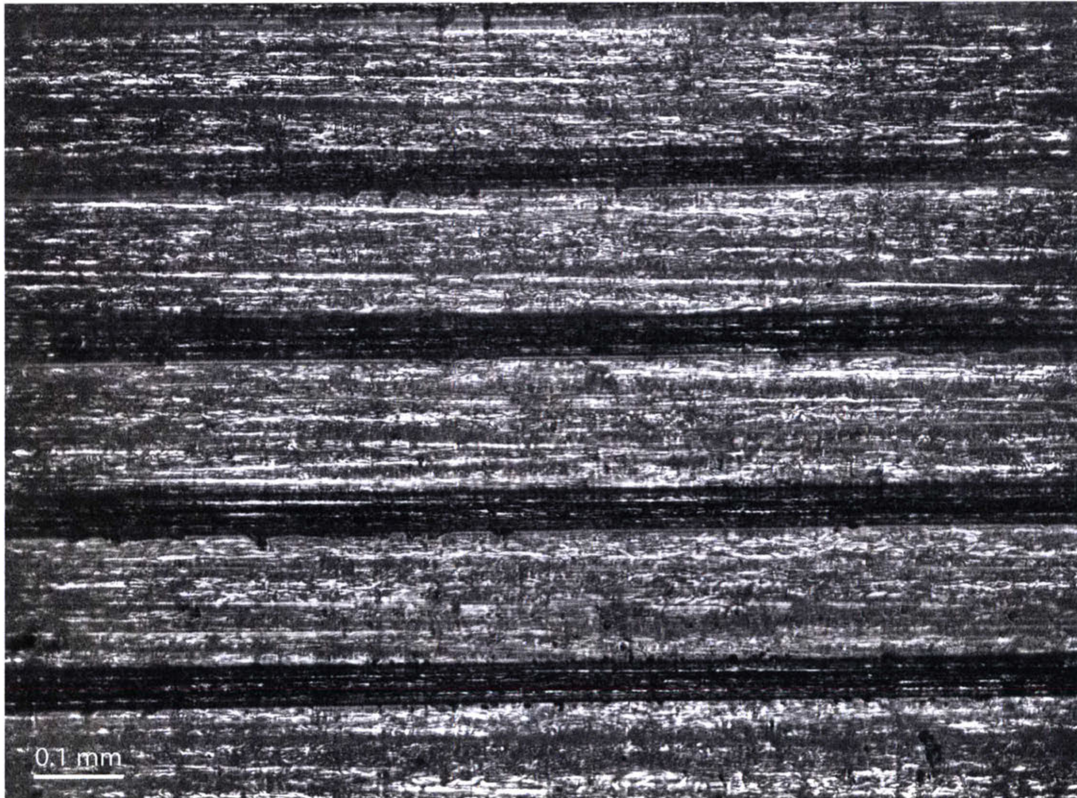

(b) Photograph of the photoresist at location C1 after removing tool S1.

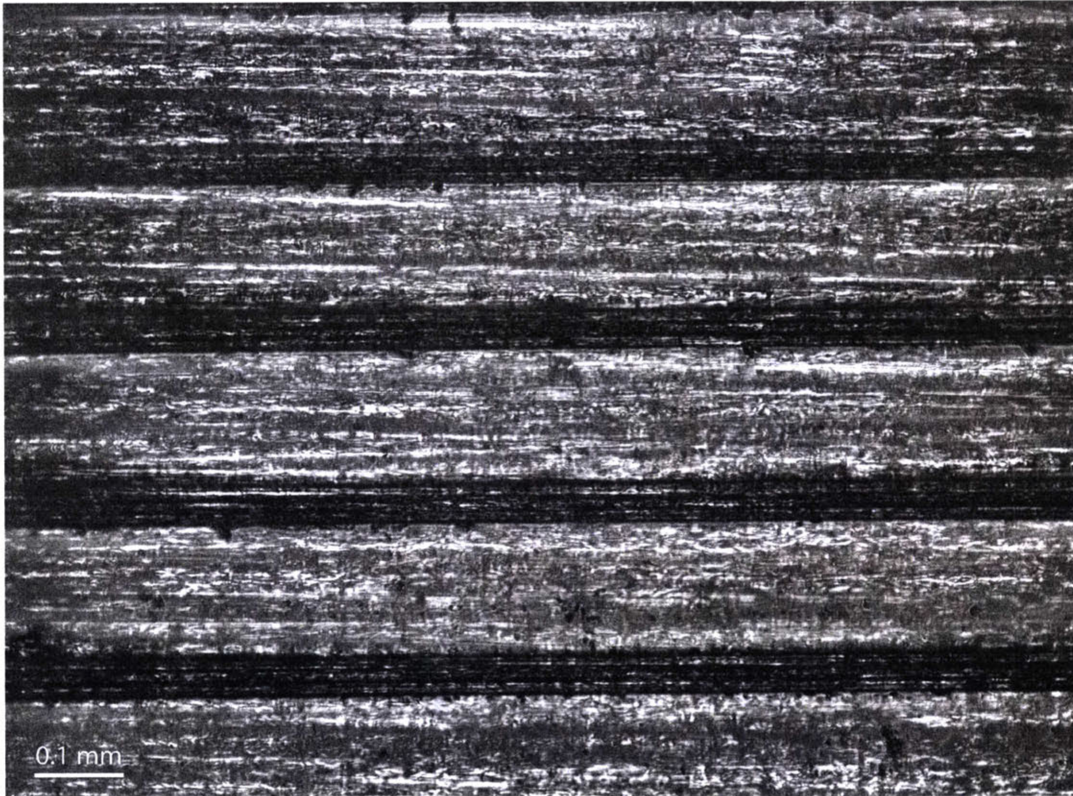

(c) Photograph of the photoresist at location C1 after removing tool S3.

Figure 5-38: Photographs of the photoresist at location C1 throughout the tool-making process. Note the obvious change between Figures 5-38a and 5-38b as if the PDMS casting slanted a previously vertical sidwall. This same phenomenon was observed for A1 and B1 in Figures 5-15 and 5-19. There is no obvious alteration to the photoresist between casting tool S1 (Figure 5-38b) and tool S3 (Figure 5-38c), minor root width edge roughness and defects are consistent between the two. Both S1 and S3 molds also exhibit bottomed out features, where the exposure propogated all the way through to the SU8 planarizing layer.

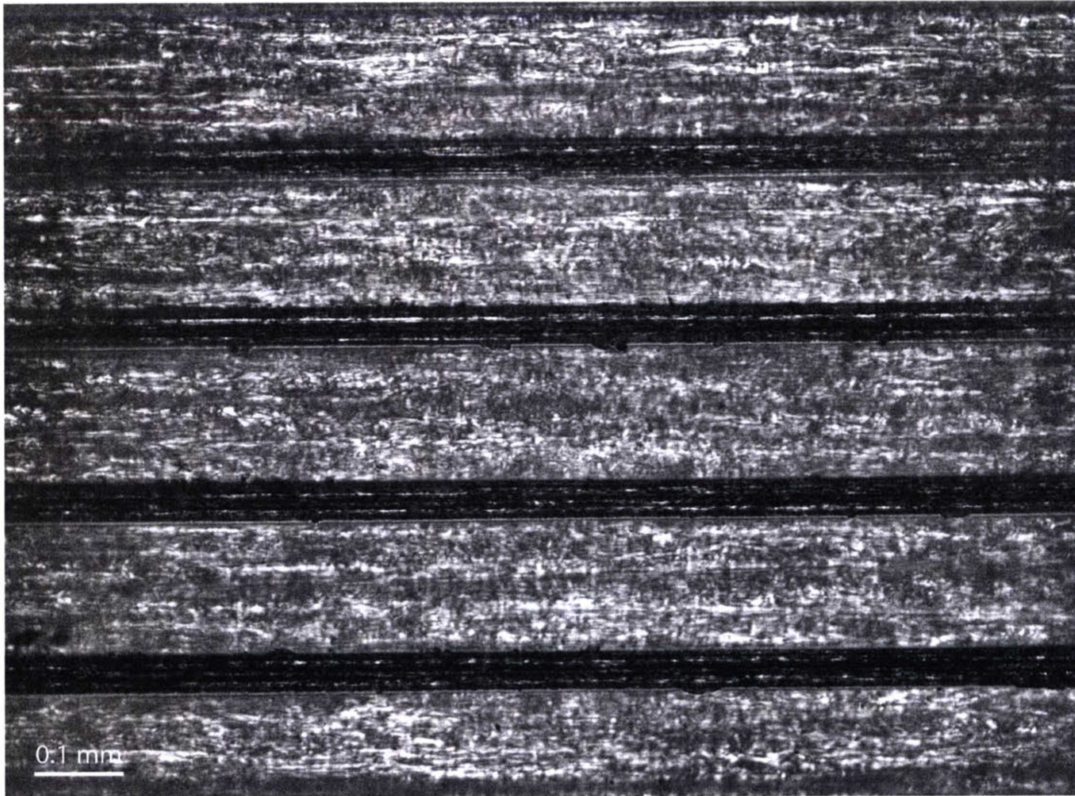

(a) Photograph of the photoresist at location C2 after development.

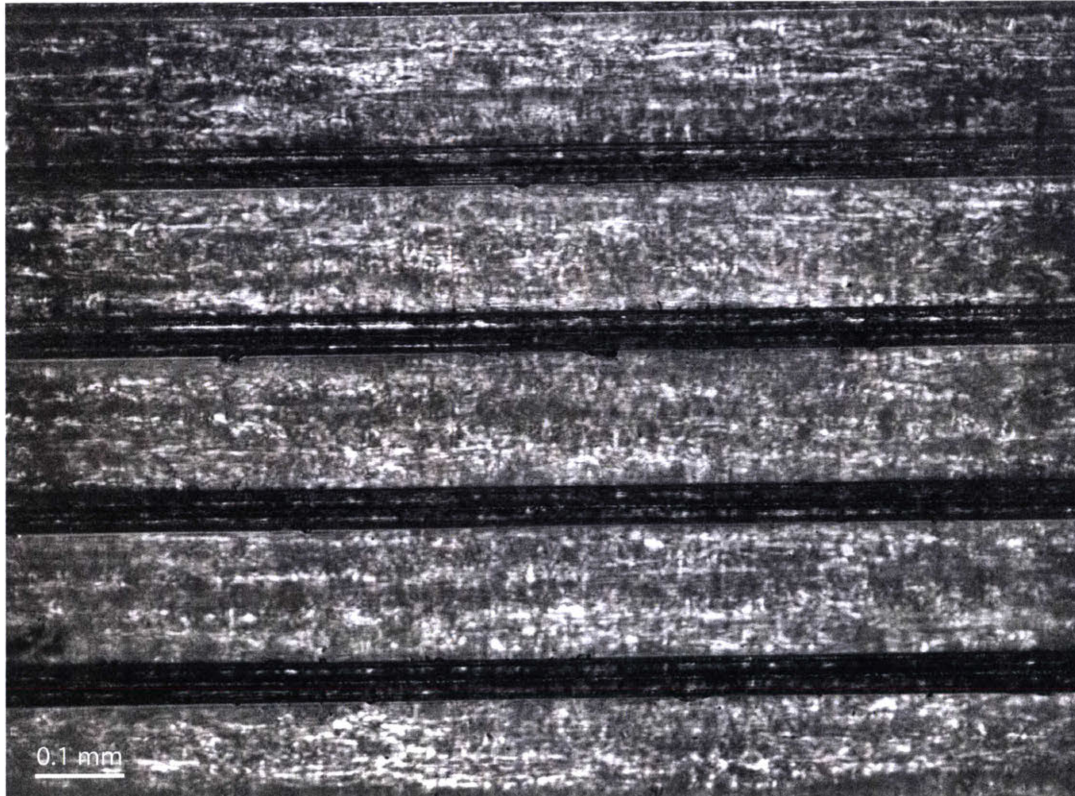

(b) Photograph of the photoresist at location C2 after removing tool S1.

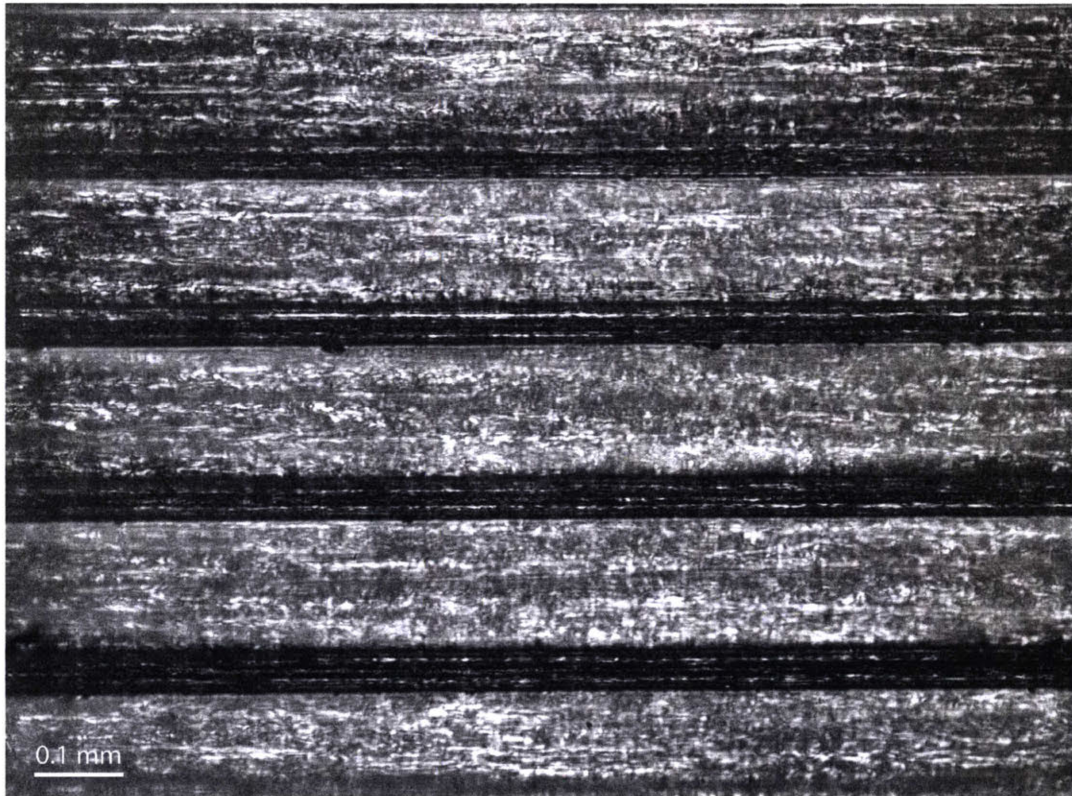

(c) Photograph of the photoresist at location C2 after removing tool S3.

Figure 5-39: Photographs of the photoresist at location C2 throughout the tool-making process. There are no apparent changes between development (Figure 5-39a) and subsequent tool castings (Figure 5-39b and Figure 5-39c). Features obviously bottom out and mild edge defects are visible and consistent between images.

(a) Photograph of the photoresist at location C3 after development.

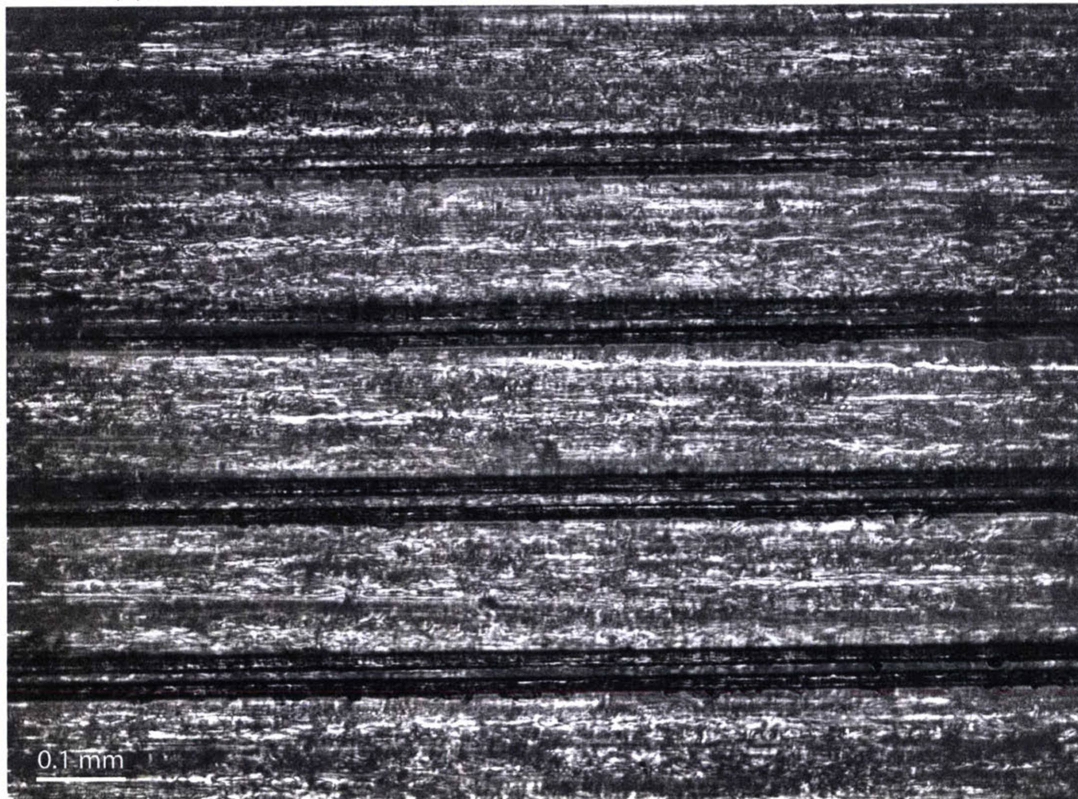

(b) Photograph of the photoresist at location C3 after removing tool S1.

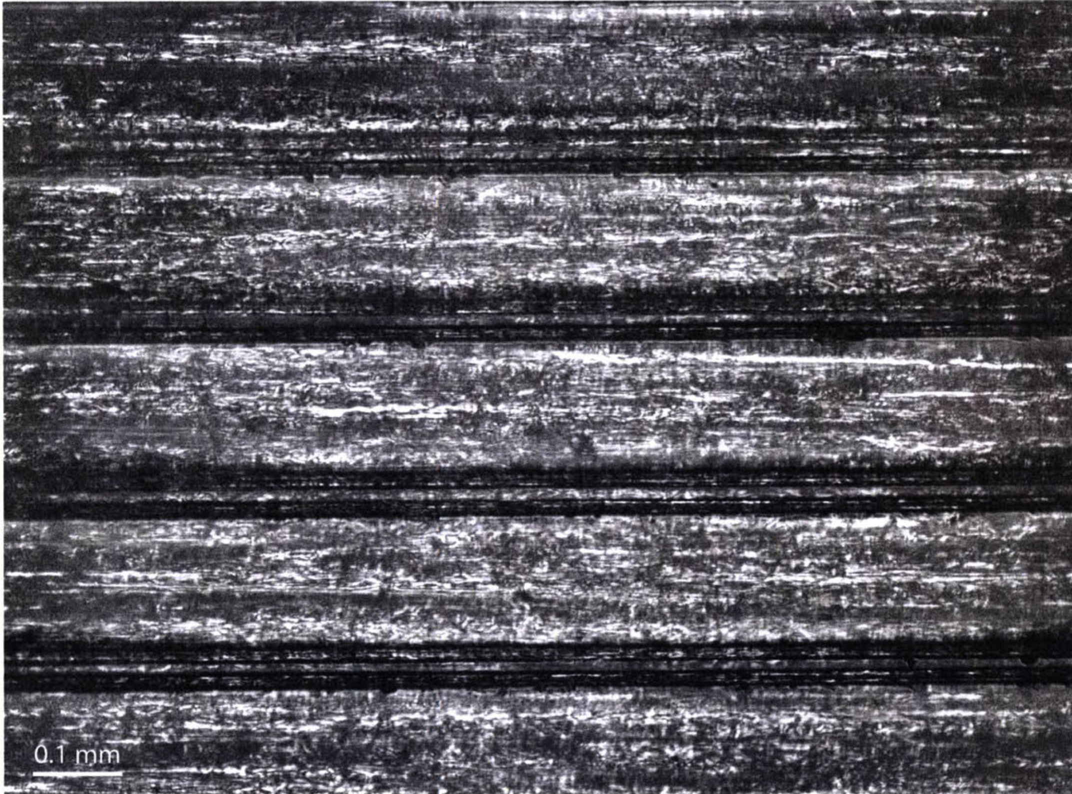

(c) Photograph of the photoresist at location C3 after removing tool S3.

Figure 5-40: Photographs of the photoresist at location C3 throughout the tool-making process. There are no apparent changes between development (Figure 5-40a) and subsequent tool castings (Figure 5-40b and Figure 5-40c). Features obviously bottom out and mild edge defects are visible and consistent between images.

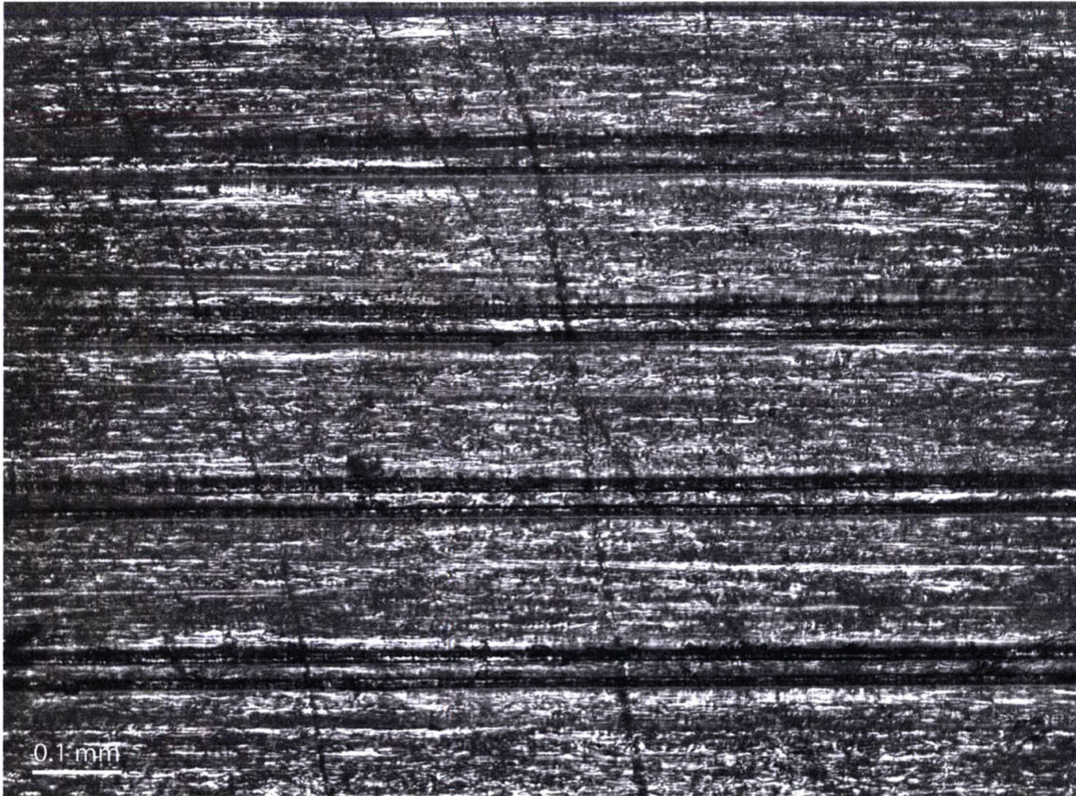

(a) Photograph of the photoresist at location C4 after development.

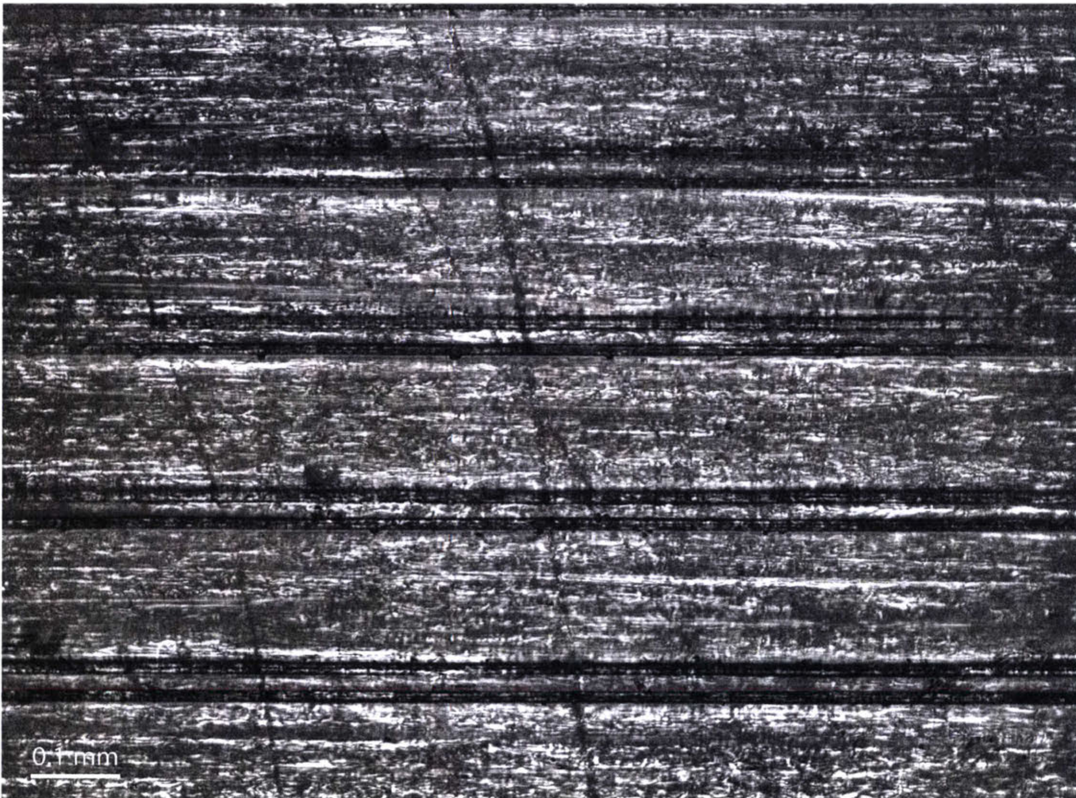

(b) Photograph of the photoresist at location C4 after removing tool S1.

(c) Photograph of the photoresist at location C4 after removing tool S3.

Figure 5-41: Photographs of the photoresist at location C4 throughout the tool-making process. There are no apparent changes between development (Figure 5-41a) and subsequent tool castings (Figure 5-41b and Figure 5-41c). Features obviously bottom out and mild edge defects are visible and consistent between images. Most notably, the near-vertical scratches are present in all three images.

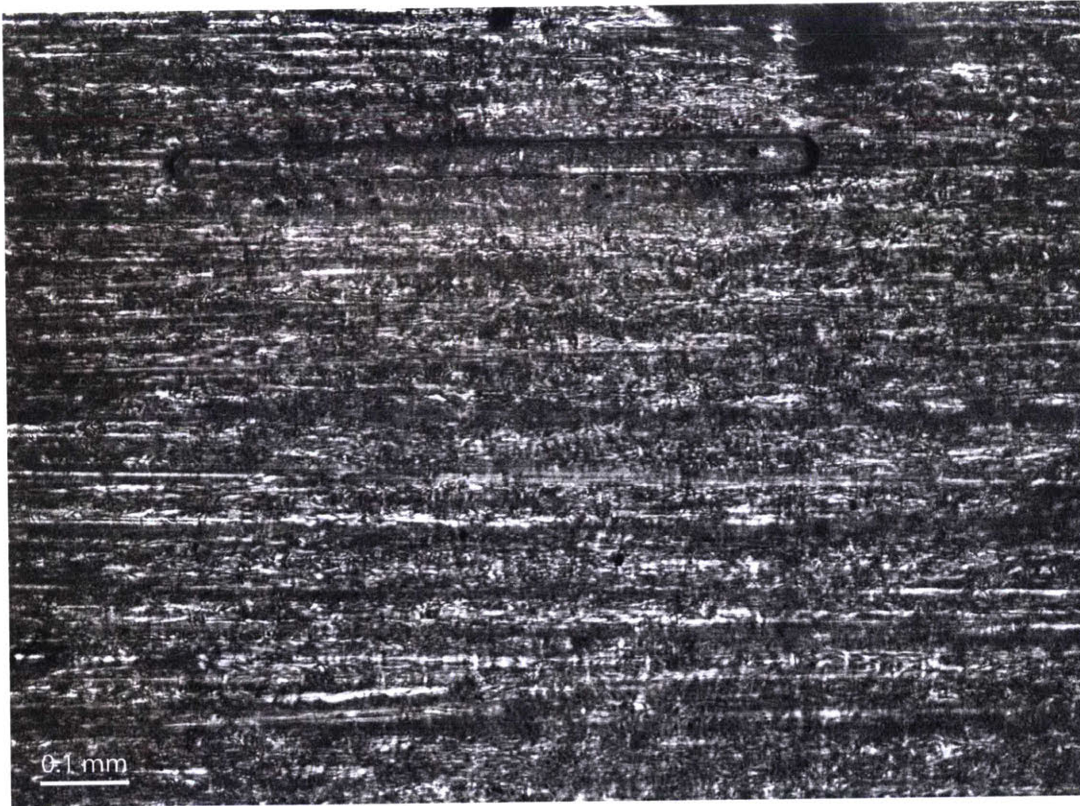

(a) Photograph of the photoresist at location D1 after development.

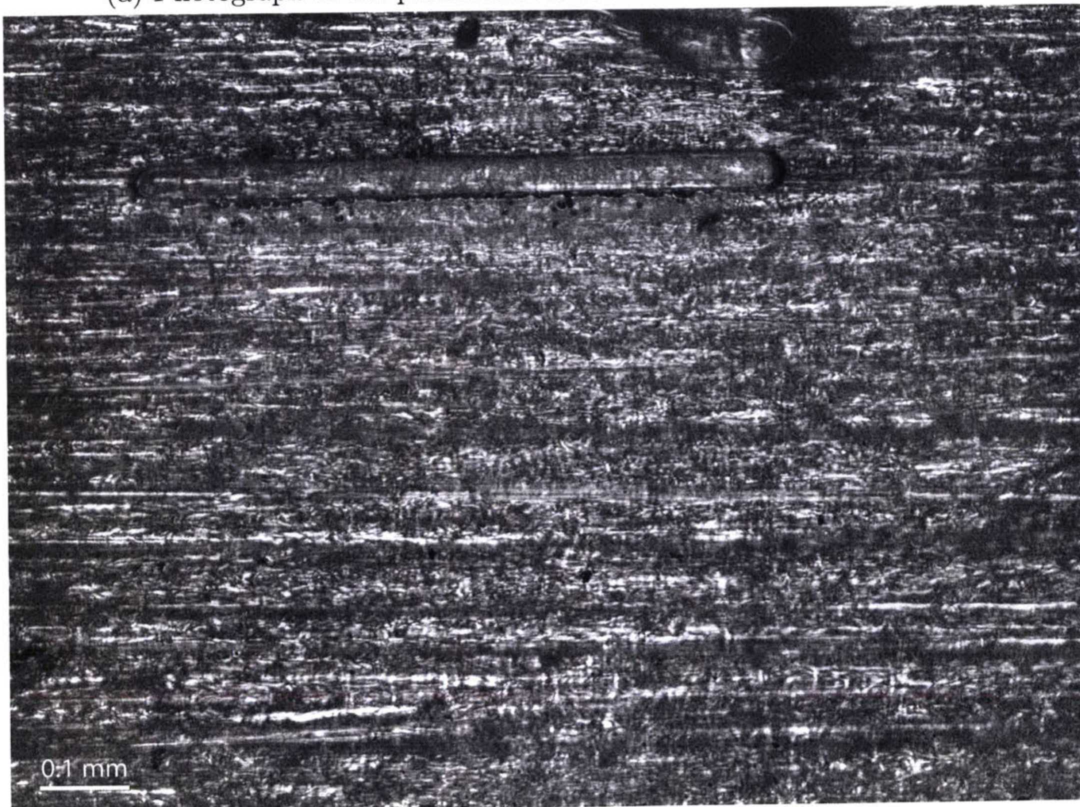

(b) Photograph of the photoresist at location D1 after removing tool S1.

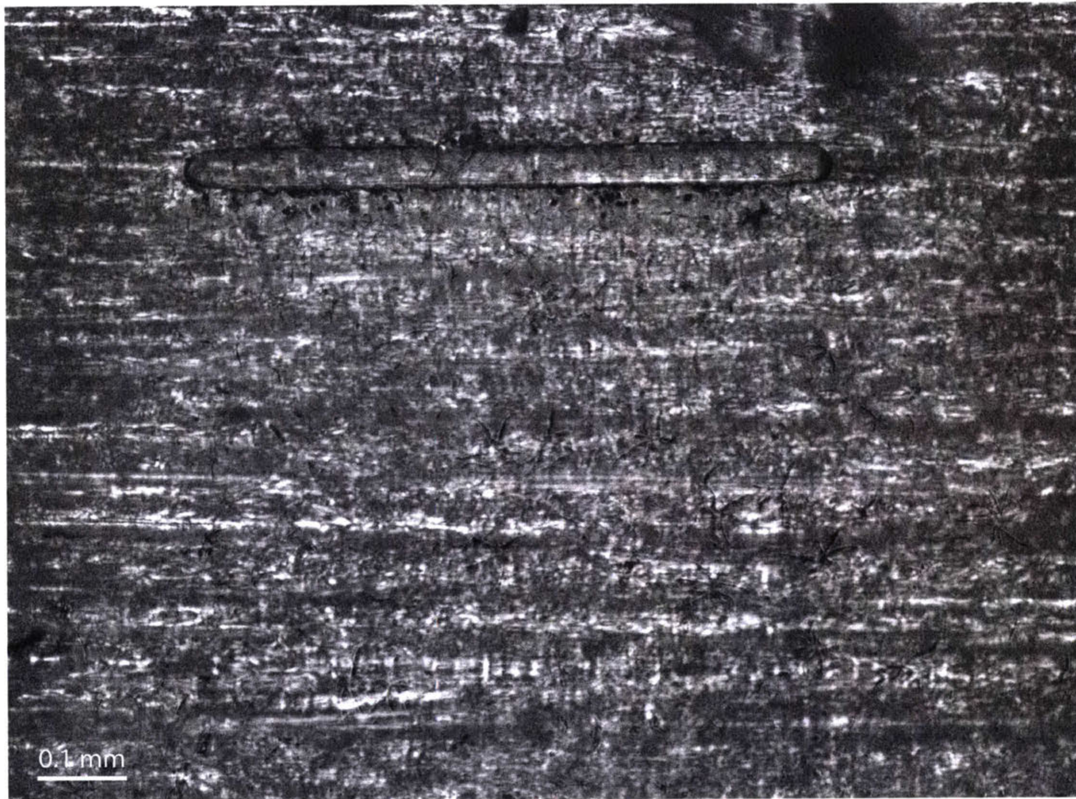

(c) Photograph of the photoresist at location D1 after removing tool S3.

Figure 5-42: Photographs of the photoresist at location D1 throughout the tool-making process. There are no apparent changes between development (Figure 5-42a) and subsequent tool castings (Figure 5-42b and Figure 5-42c). Features obviously bottom out, exhibit steep (near-vertical) sidewalls, have mild edge defects, and are surrounded by small bubble defects. These properties are present in all three images.

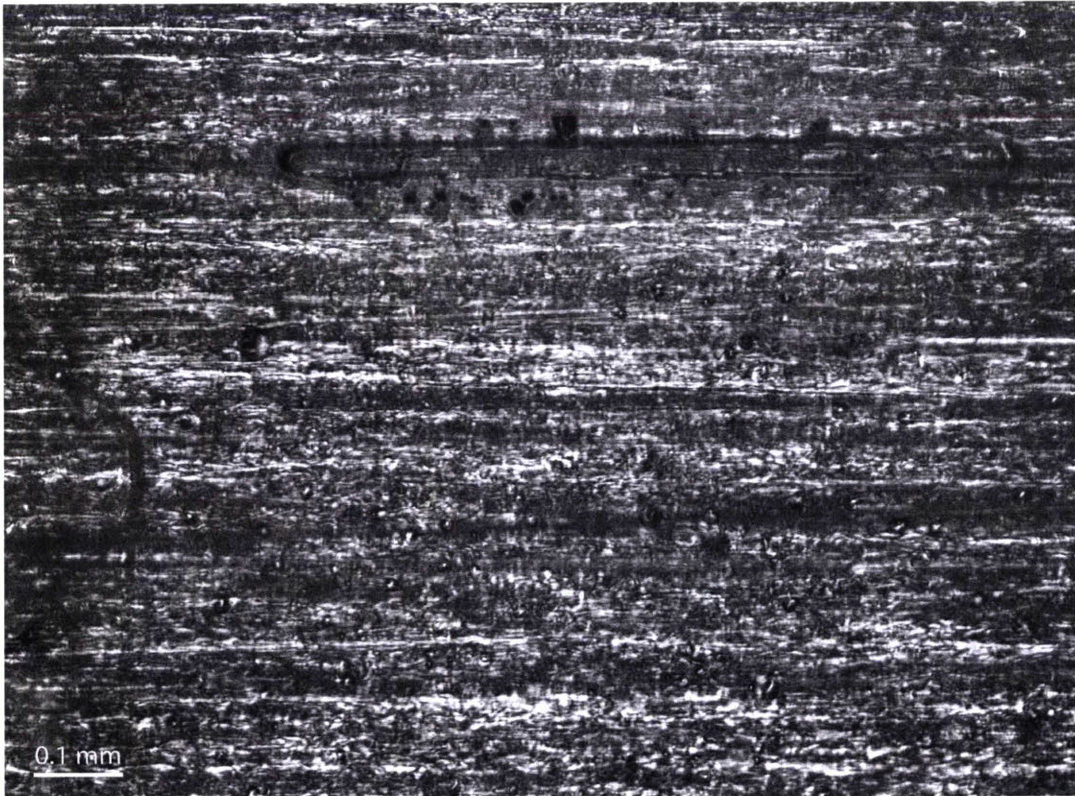

(a) Photograph of the photoresist at location D2 after development.

(b) Photograph of the photoresist at location D2 after removing tool S1.

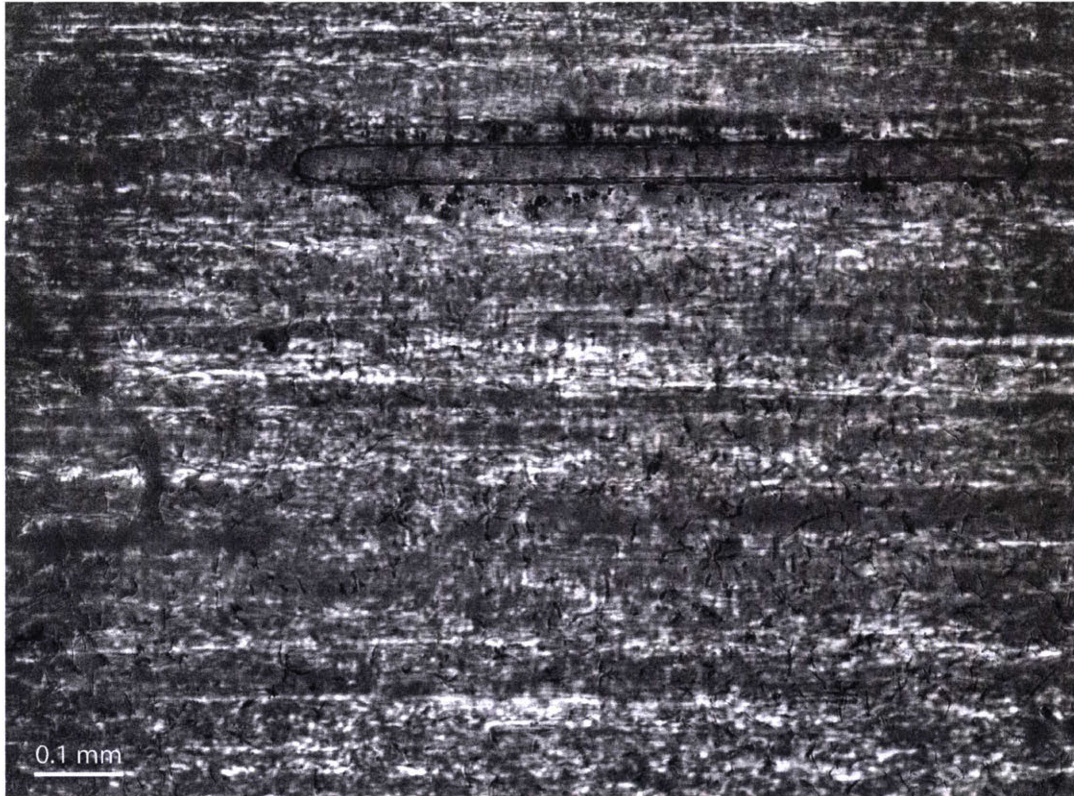

(c) Photograph of the photoresist at location D2 after removing tool S3.

Figure 5-43: Photographs of the photoresist at location D2 throughout the tool-making process. There are no apparent changes between development (Figure 5-43a) and subsequent tool castings (Figure 5-43b and Figure 5-43c). Features obviously bottom out, exhibit steep (near-vertical) sidewalls, have mild edge defects, and are surrounded by small bubble defects. These properties are present in all three images.

(a) Photograph of the photoresist at location D3 after development.

(b) Photograph of the photoresist at location D3 after removing tool S1.

(c) Photograph of the photoresist at location D3 after removing tool S3.

Figure 5-44: Photographs of the photoresist at location D3 throughout the tool-making process. There are no apparent changes between development (Figure 5-44a) and subsequent tool castings (Figure 5-44b and Figure 5-44c). Features obviously bottom out, exhibit steep (near-vertical) sidewalls, have mild edge defects, and are surrounded by small bubble defects. These properties are present in all three images.

(a) Photograph of the photoresist at location D4 after development.

(b) Photograph of the photoresist at location D4 after removing tool S1.

(c) Photograph of the photoresist at location D4 after removing tool S3.

Figure 5-45: Photographs of the photoresist at location D4 throughout the tool-making process. There are no obvious changes between development (Figure 5-45a) and subsequent tool castings (Figure 5-45b and Figure 5-45c). Features obviously bottom out, exhibit steep (near-vertical) sidewalls, have mild edge defects, and are surrounded by small bubble defects. These properties are present in all three images, though the bubbling does appear to grow slightly in size between removing tool S1 and removing tool S3.

Similar to A1 and B1, C1 clearly shows a change in the patterning layer between development and removing tool S1. No other C or D locations exhibit this property. As with all A and B locations, all C and D locations do however show no obvious change in the patterning layer between tool castings. Again, this suggests that there must be some mechanism by which AZ 9260 photoresist can be reshaped between development and casting. A1, B1, and C1 are adjacement stamp sections, which gives merit to the mechanism being related to a eccentricity-related error. Perhaps laser focus is substantially different in these sections. The lack of obvious sidewalls may indicate that ideal features with vertical sidewalls were exposed and developed, but the mechanical and thermal stresses of the first tool casting reshaped the photoresist.

5.5.2 Pattern Replication and PDMS Stamp Repeatability

Ideal locations of C[3] and D[4] features, C* and D*, were analyzed to test the repeatability and replication of the new feature types. The ideal locations, C* and D* were again determined by imaging cross sections of C1-C4, and D1-D4 in tool S1 and identifying the most characteristic location. Pictures of PDMS cross sections between castings S1 and S3 assessed tool repeatability, while photographs of photoresist geometries after casting tool S1 compared to those of the S1 PDMS features provided insight into the pattern replication by PDMS. Comparisons between S3 PDMS and photoresist also investigated feature replication.

Table 5.6 list the stamp and patterning layer locations of the C* and D* regions. C* images feature created with a 15 μm expsoure offset. D* invstigates features created with 5, 15, and 25 μm exposure offsets. Figure 5-46, Figure 5-47, Figure 5-48, and Figure 5-49 show photographs of the C* features in tool S1, C* features in tool S3, D* features in tool S1, and D* features in tool S3 respectively.

Location Name	Axial Position (mm)	Circumferential Position (counts)
C*	120	3750 (a) 3912 (b), 3545 (c)
D*5	124	3736 (a), 3912 (b), 3545 (c)
D*15	120	3736 (a), 3912 (b), 3545 (c)
D*25	116	3736 (a), 3912 (b), 3545 (c)
D*x	116.5	7521 (a)

Table 5.6: Axial and circumferential locations of ideal features C* and D*. D features varied greatly in cross section shape with the amount of overlap. D*5 is a feature constructed with 5 μm offset in exposures. D*15 uses a 15 μm offset in exposures. D*25 has a 25 μm offset. Finally D*x is an additional feature constructed with 25 μm offset in exposures but viewed in a different location to provide extra insight into overlapping exposures. The dashed nature of D features required multiple imaging locations, each best catered to the specific microscopy type. Circumferential positions labeled (a) were used for imaging the photoresist, positions (b) represent PDMS tool cross sections, while (c) locations were used for creating top views of the PDMS tools.

C* features have a very rounded shape and no really obvious top width. Measured PDMS cross sections yield a mean rootwidth of 44.74 $\pm$ 1.62 μm, which is comparable to A* and B* star features. This suggest the partially overlapping exposures simply altered the cross

[3]Circumferentially-oriented lines of theoretically larger width formed via two overlapping exposures.
[4]Theoretically axially oriented features formed through consecutively overlapping exposures.

section shape, but not the overall dimensions. There are however no obvious discrepancies between the patterning layer and the PDMS tools. Similarly, D* features exhibit a much more rectangular cross section than A*, B*, and C*. The machine can clearly create short line segments, however the overlapping exposures did not behave as expected. See Section 5.5.5 for an details on the expected D geometry. Only the D*25 features partially formed into an axially elongated feature set but did not fully fuse. The photoresist and PDMS geometries agree visually, though the small bubble defects in D*25 appear to grow in the photoresist as the number of castings increase. These qualitative data suggest that there are chemical limitations to overlapping exposures for larger features, and too high of a cumulative dose may compromise the repeatability of the AZ 9260 photoresist.

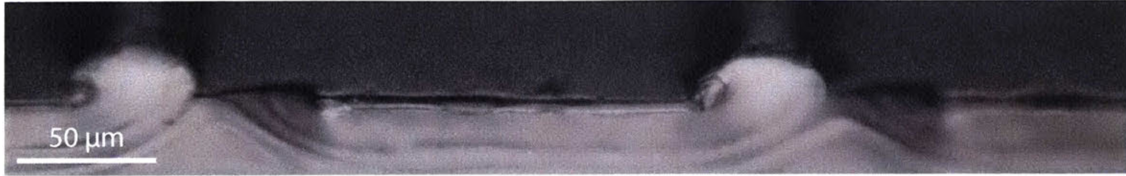

(a) A cross section photograph of PDMS tool S1 at location C*.

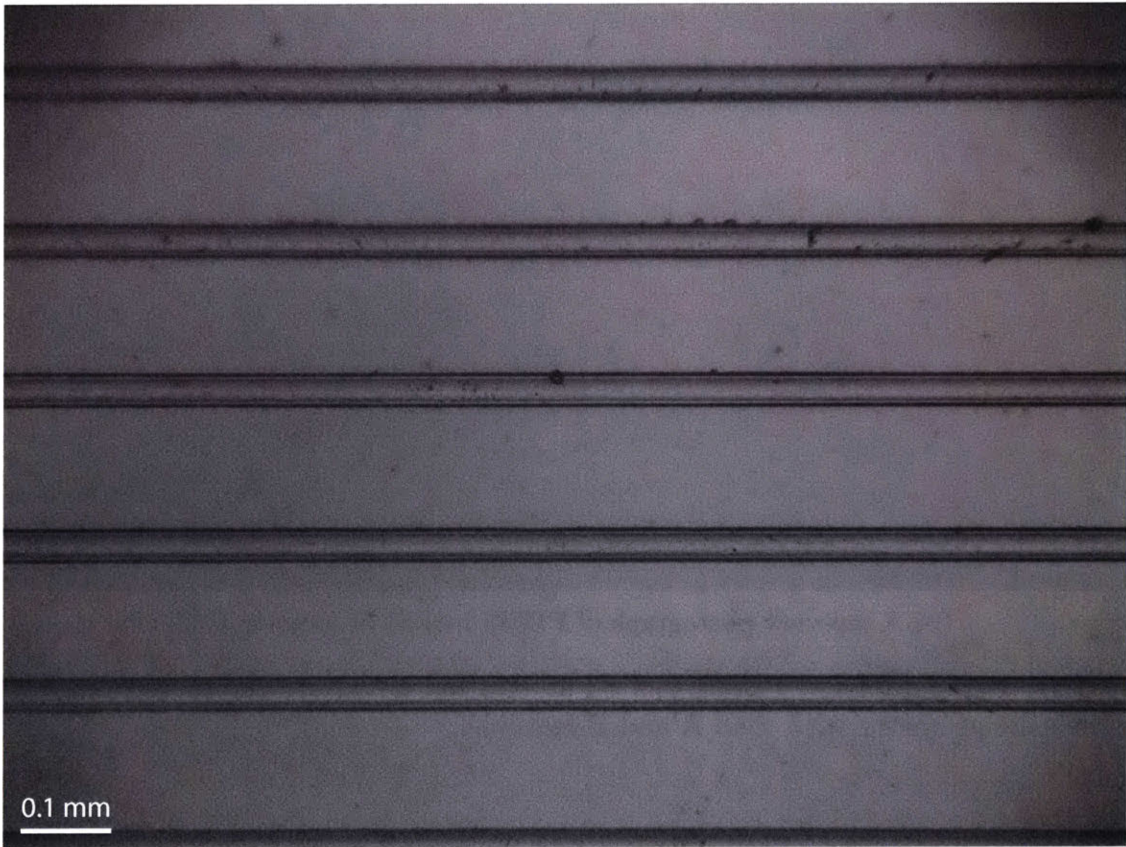

(b) A top-view photograph of PDMS tool S1 at location C*.

Figure 5-46: Photographs of PDMS tool S3 at location C*. Note the more rounded cross section feature geometry with than A and B features.

(a) A cross section photograph of PDMS tool S3 at location C*.

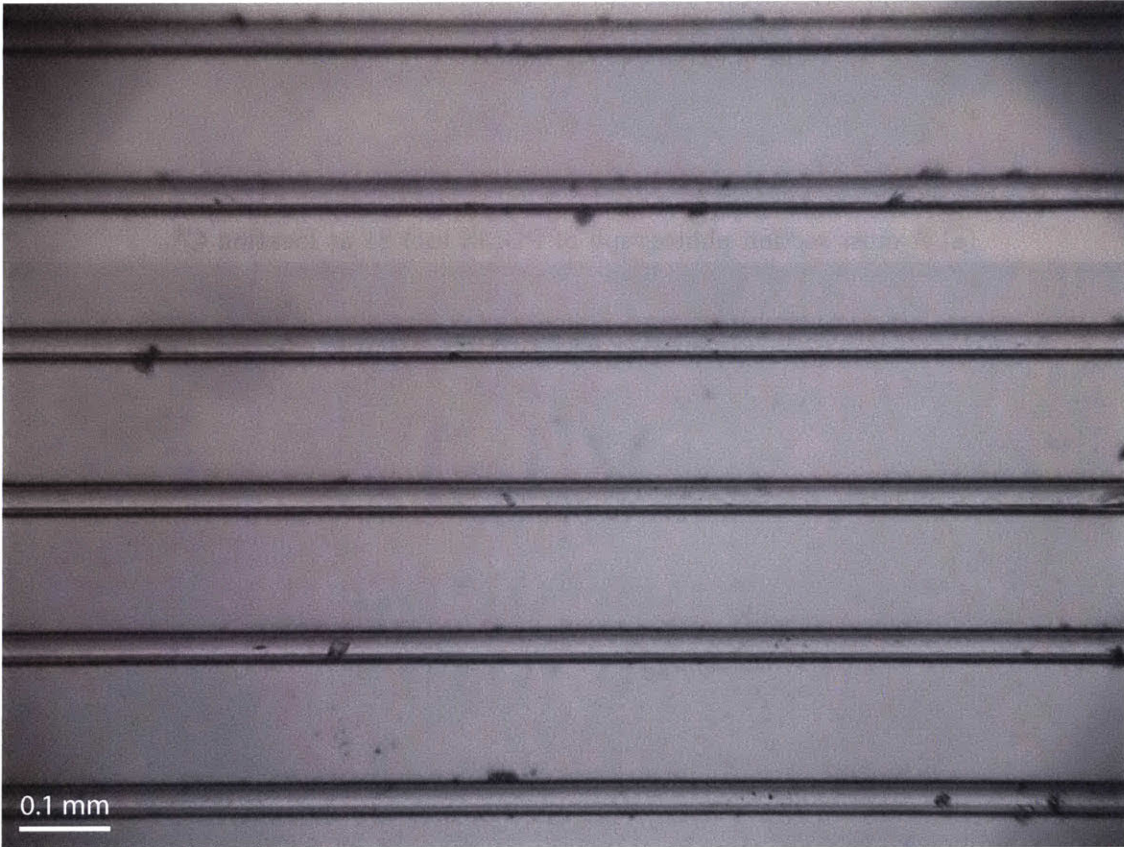

(b) A top-view photograph of PDMS tool S3 at location C*.

Figure 5-47: Photographs of PDMS tool S3 at location C*. Note the more rounded cross section feature geometry with than A and B features.

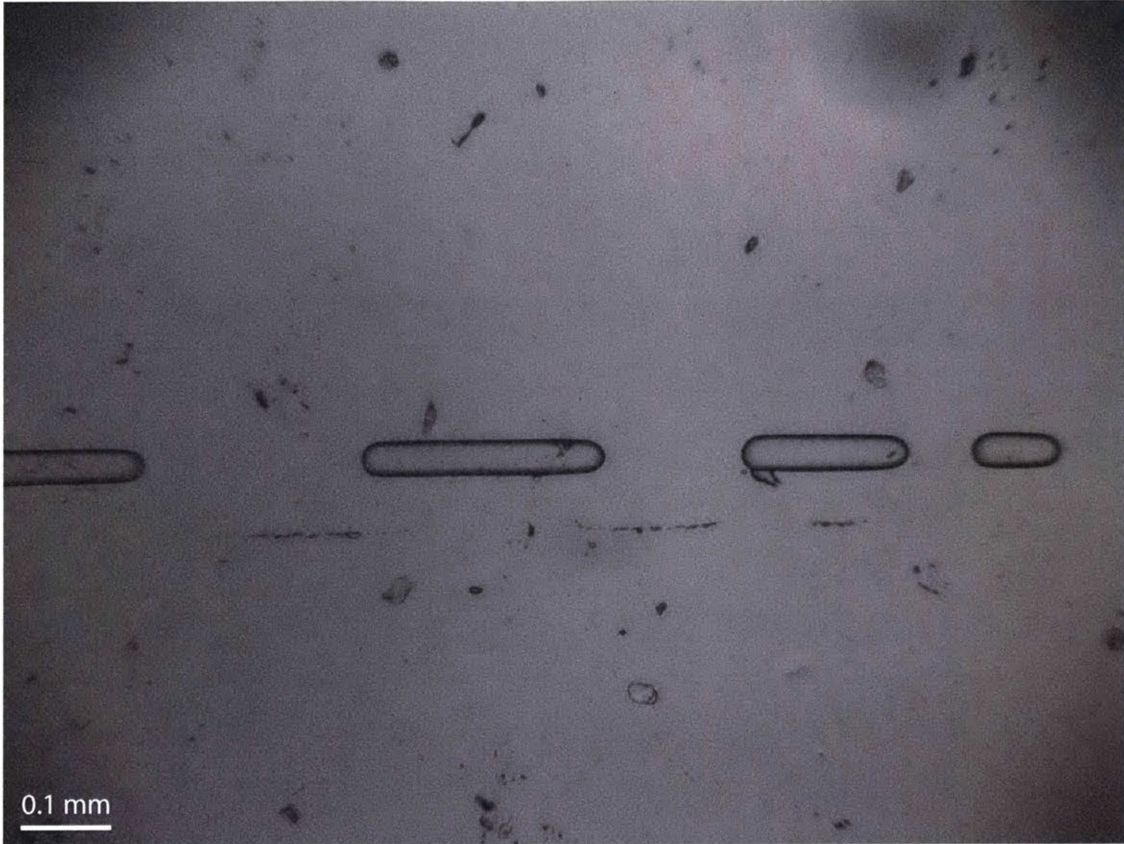

(a) A top-view photograph of PDMS tool S1 at location D*5.

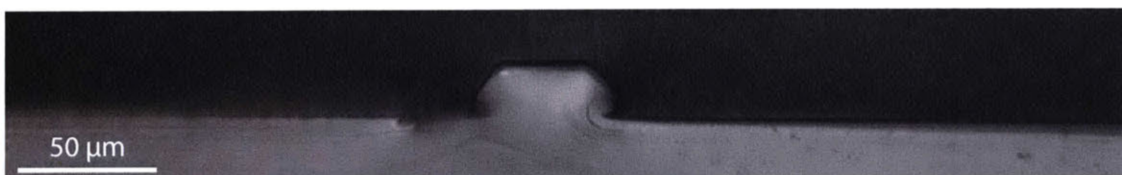

(b) A cross section photograph of PDMS tool S1 at location D*15.

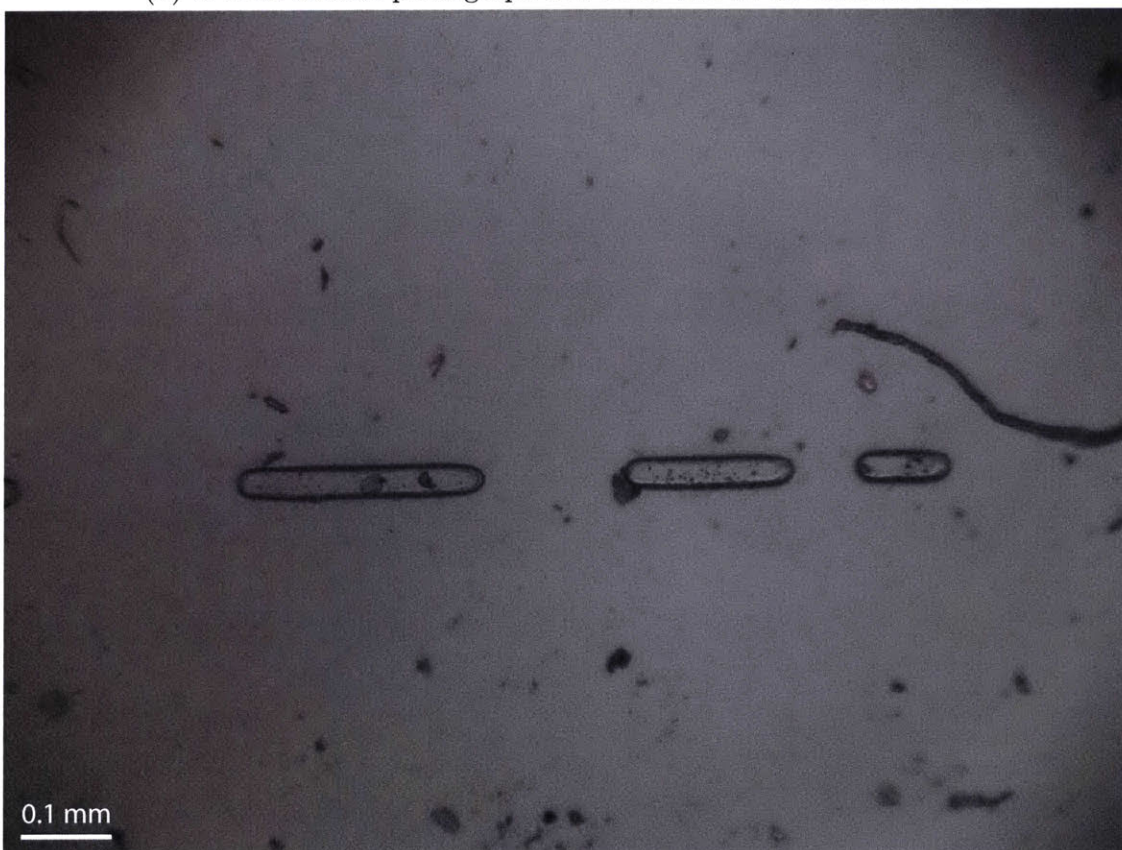

(c) A top-view photograph of PDMS tool S1 at location D*15.

(d) A cross section photograph of PDMS tool S1 at location D*25.

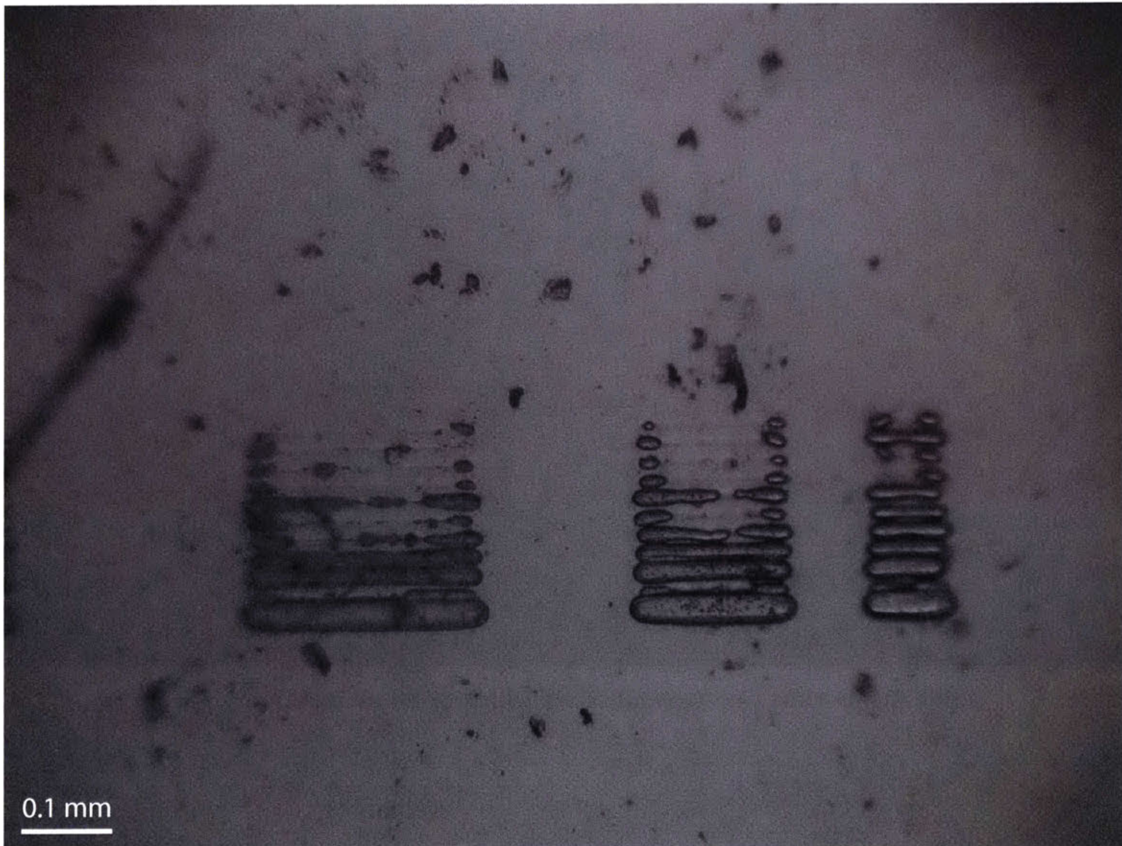

(e) A top-view photograph of PDMS tool S1 at location D*25.

Figure 5-48: Photographs of PDMS tool S1 at location D*. Note the trapezoidal-rectangular cross section feature geoemtry with extremely flat tops. Crisp lines and edges are evident in the top view. Only the features constructed with 25 μm exposure offset exhibit axially-oriented characteristics, in the form of partially formed line segments. In all cases, only the first exposed area of the photoresist developed into a full feature, of notably different geometry than A, B, or C features.

(a) A cross section photograph of PDMS tool S3 at location D*5.

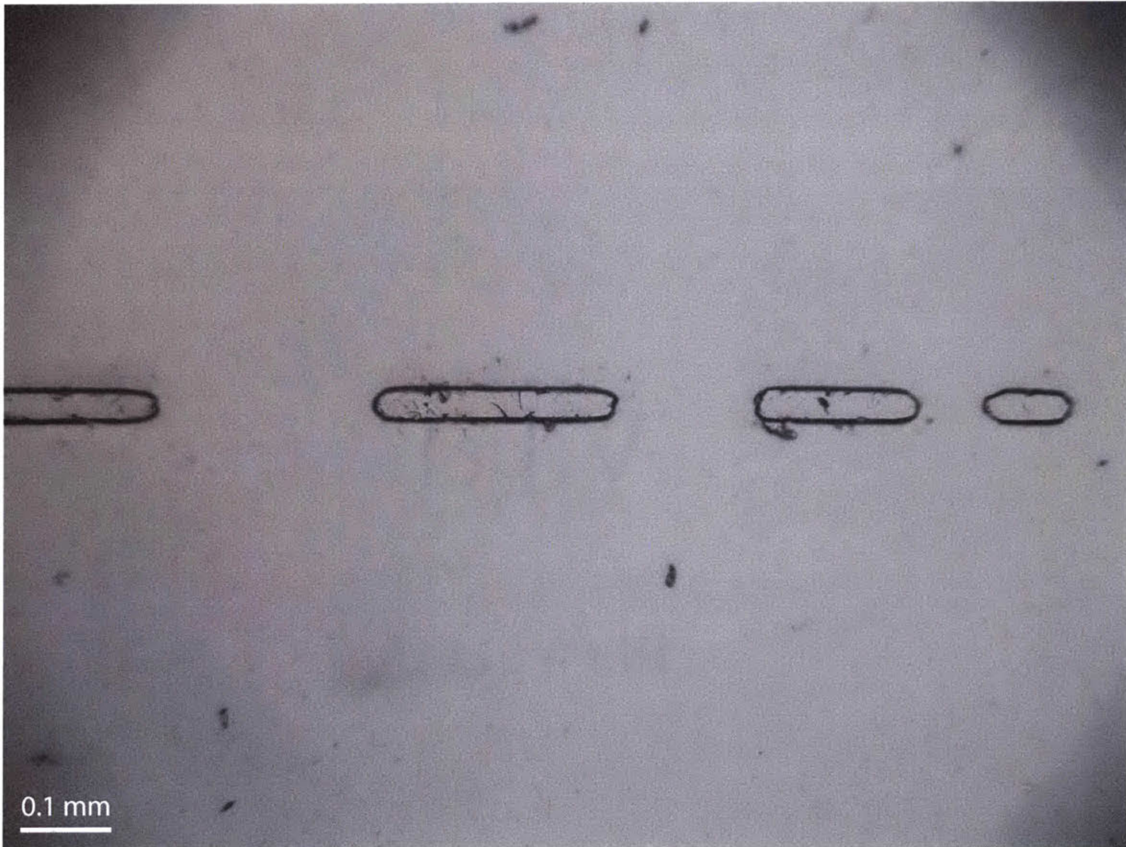

(b) A top-view photograph of PDMS tool S3 at location D*5.

(c) A cross section photograph of PDMS tool S3 at location D*15.

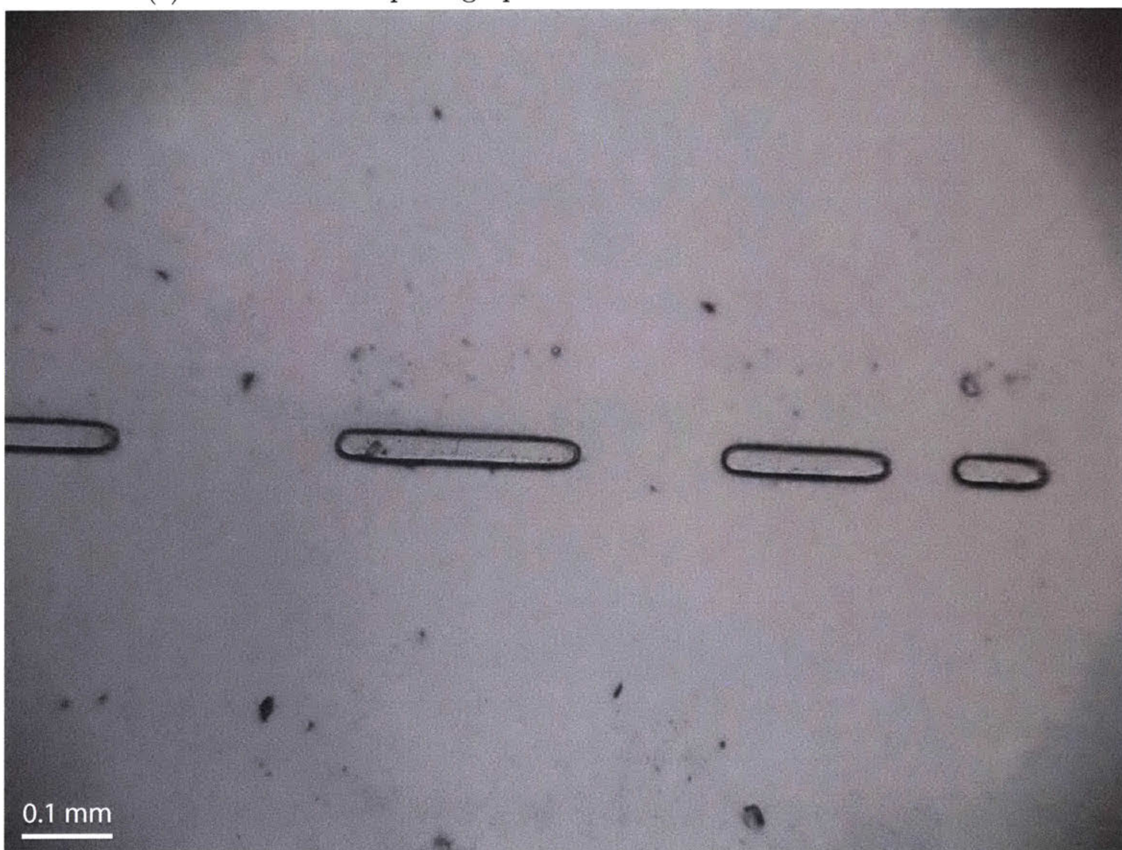

(d) A top-view photograph of PDMS tool S3 at location D*15.

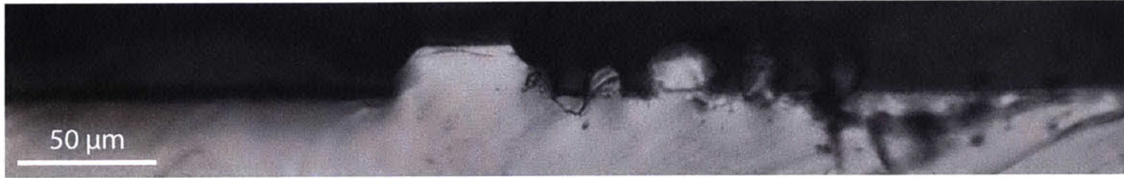

(e) A cross section photograph of PDMS tool S3 at location D*25.

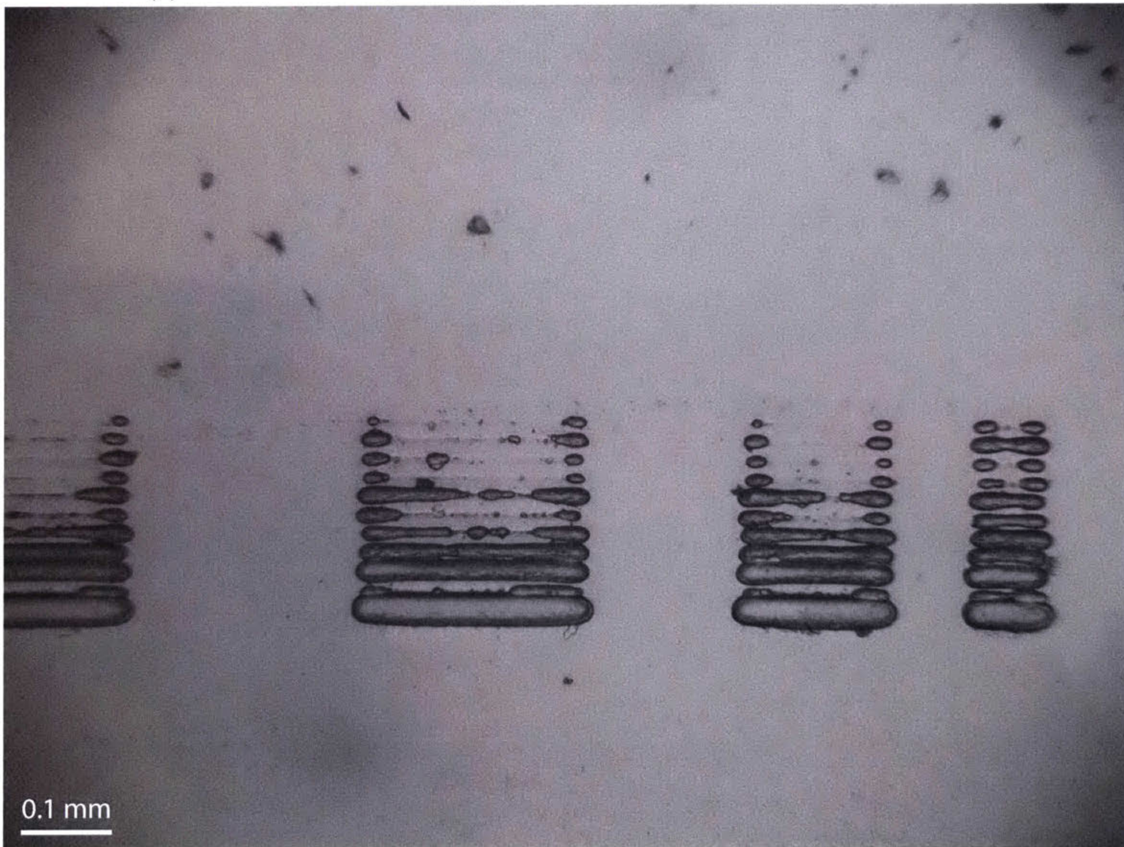

(f) A top-view photograph of PDMS tool S3 at location D*25.

Figure 5-49: Photographs of PDMS tool S3 at location D*. Note the trapezoidal-rectangular cross section feature geoemtry with extremely flat tops. Crisp lines and edges are evident in the top view. Only the features constructed with 25 μm exposure offset exhibit axially-oriented characteristics, in the form of partially formed line segments. In all cases, only the first exposed area of the photoresist developed into a full feature, of notably different geometry than A, B, or C features.

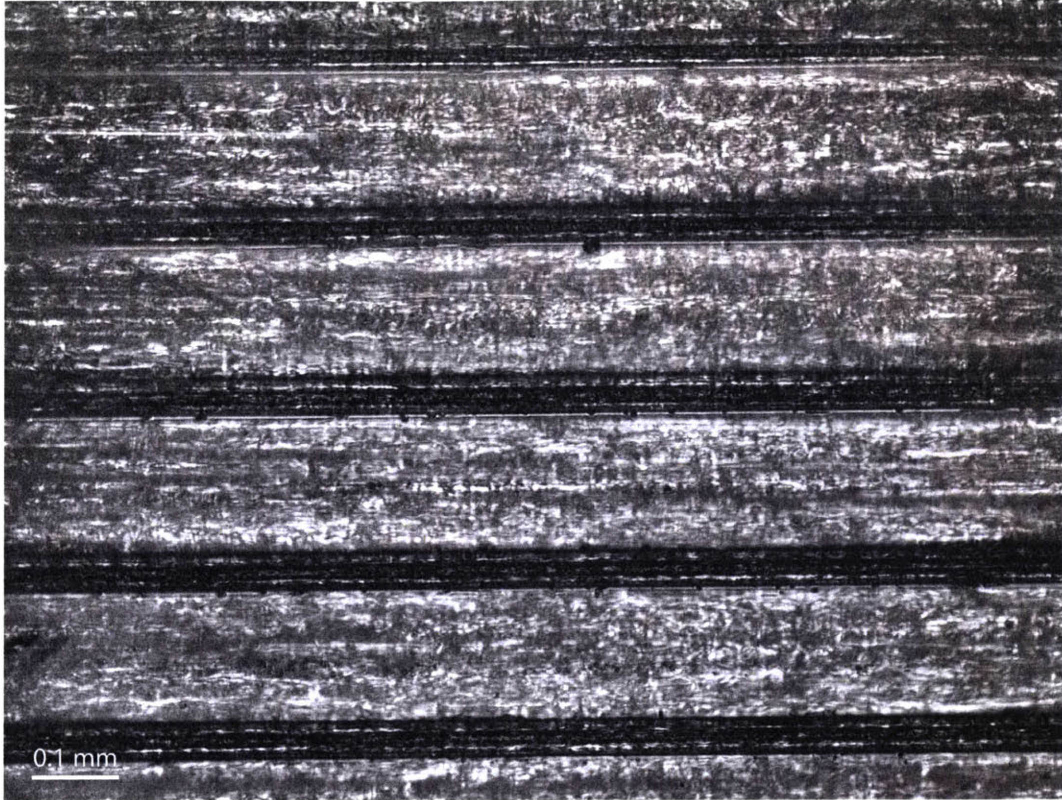

(a) Photograph of the photoresist at location C* after removing tool S1.

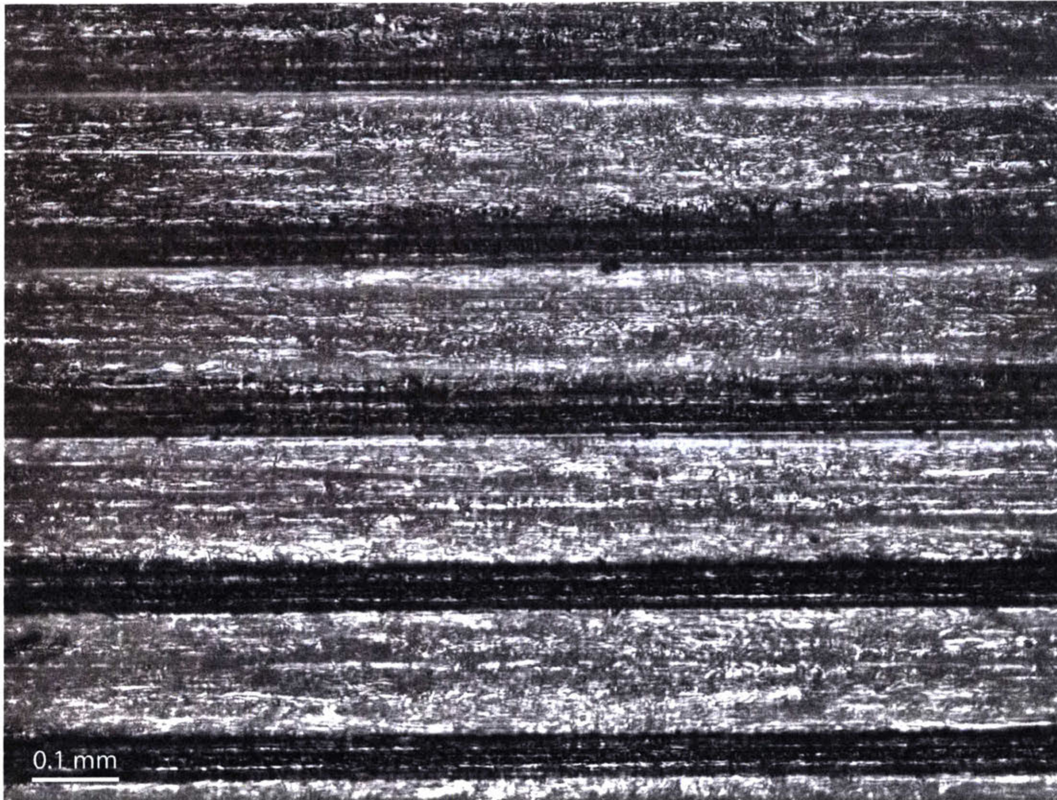

(b) Photograph of the photoresist at location C* after removing tool S3.

Figure 5-50: Photographs of the photoresist at location C* throughout the tool-making process There are no apparent changes between casting removing tool S1 and tool S3. While the C* PDMS looked most ideal, the corresponding photoresist location may not look the best. NOte the lack of colorlessness of the bottom out region compared to C3 (Figure 5-40b).

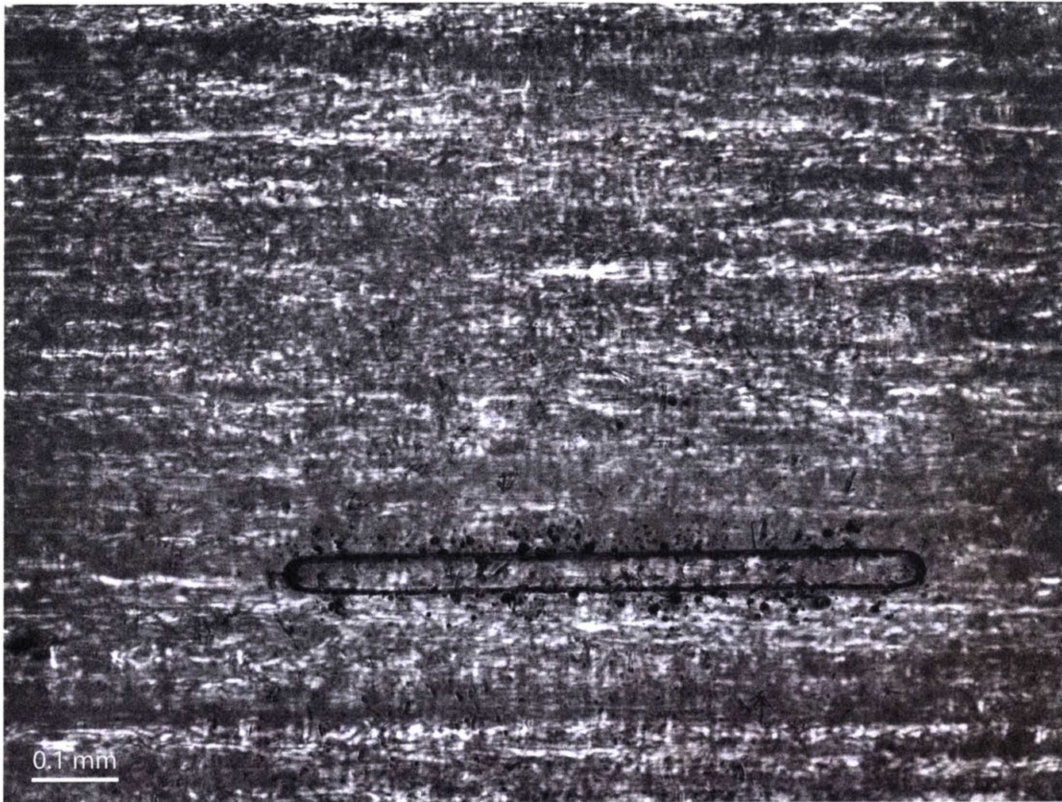

(a) Photograph of the photoresist at location D*5 after removing tool S1.

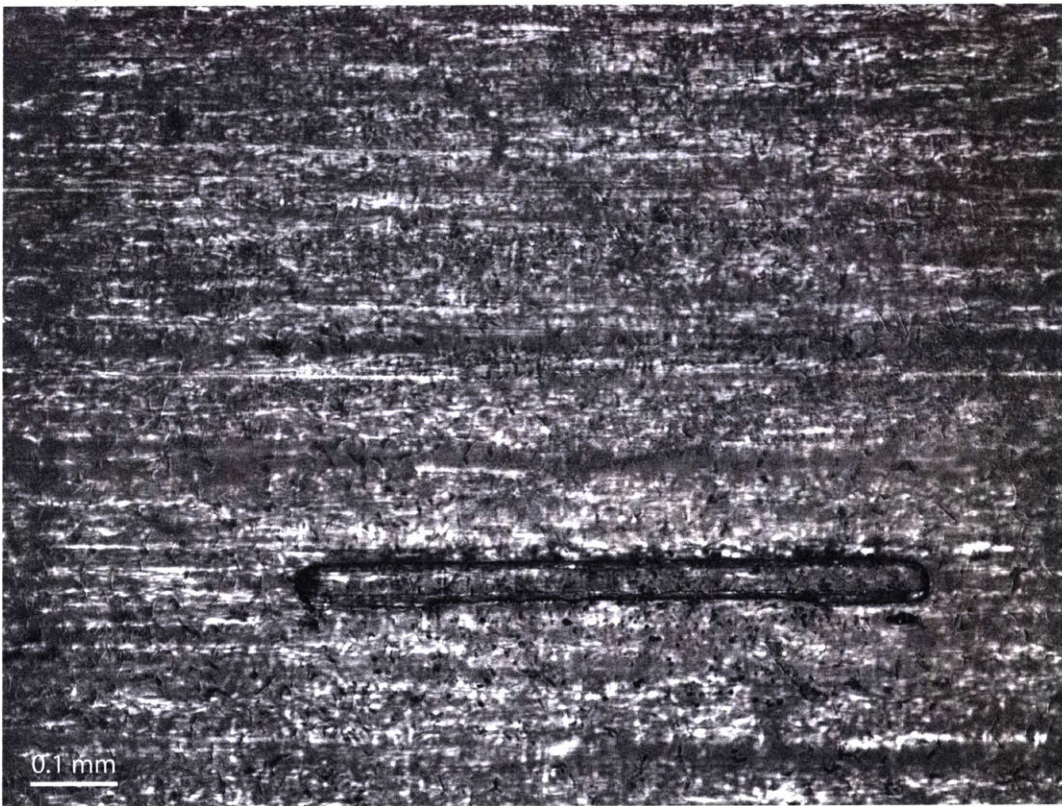

(b) Photograph of the photoresist at location D*15 after removing tool S3.

(c) Photograph of the photoresist at location D*25 after removing tool S1.

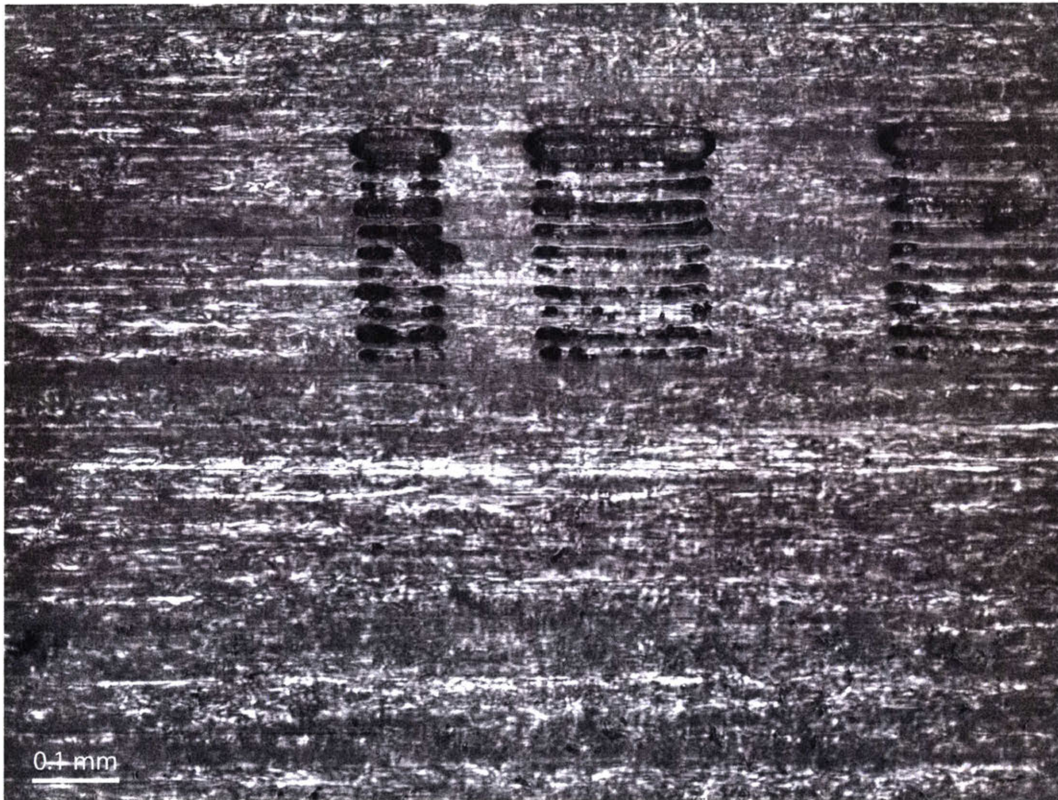

(d) Photograph of the photoresist at location D*x after removing tool S3.

Figure 5-51: Photographs of the photoresist at D* locations throughout the tool-making process. In all cases, the feature clearly bottoms out against the SU8 has a steep sidewall and some minor edge defects. These properties are present both after casting and removing tool S1 and S3. However, the nearby bubbles do appear to grow in size and in the case of features constructed with 25 μm offsets, the only partially formed line segments appear to smooth out over multiple castings.

5.5.3 Contact Visualization

Observing the contact behaviors of C and D features demonstrates whether or not the tool creates the intended contact and to what degree the contact regions differ from A and B features. To visualize contact of C and D features, tool S2 was imaged via the episcopic mircoscopy method described in Section 5.3.3. Copying the loading procedure used to image A and B, C and D features were visualized at a measured open loop force of 4.9 N (6 N set point). While this load may not be the ideal for printing these new features, it was the proven print load for Merian [6] and is therefore the most useful force to test in contact and printing without re-optimizing the inking and printing procedure.

Figure 5-52 shows unprocessed contact images of B* and C* at the same measured applied load. Refer to Figure 5-33 for interpreting what portion of the tool is in contact (black). The average line width of C* is significantly larger. This difference proves a very important attribute: different feature types will exhibit different contact performance. B* and C* are equally axially spaced, and have nearly the same root width, but C* cross sections showed a substantially more curved feature. Perhaps this characteristic allows more of the PDMS to rool into contact the impression roll. Figure 5-53 displays photographs of D*15 and D*25 contact. There is obvious roof collapse surrounding the features but the dots and dashes cleary make contact in accordance with the top-view feature geometry. Overall, C* and D* demonstrate logical contact behavior, though different from the single exposure features. Ideal contact and print forces for these features may be different from A* and B*, and from each other. A truly diverse, arbitrarily patterned tool would then require a dynamically changing printing load to successfully print complex patterns.

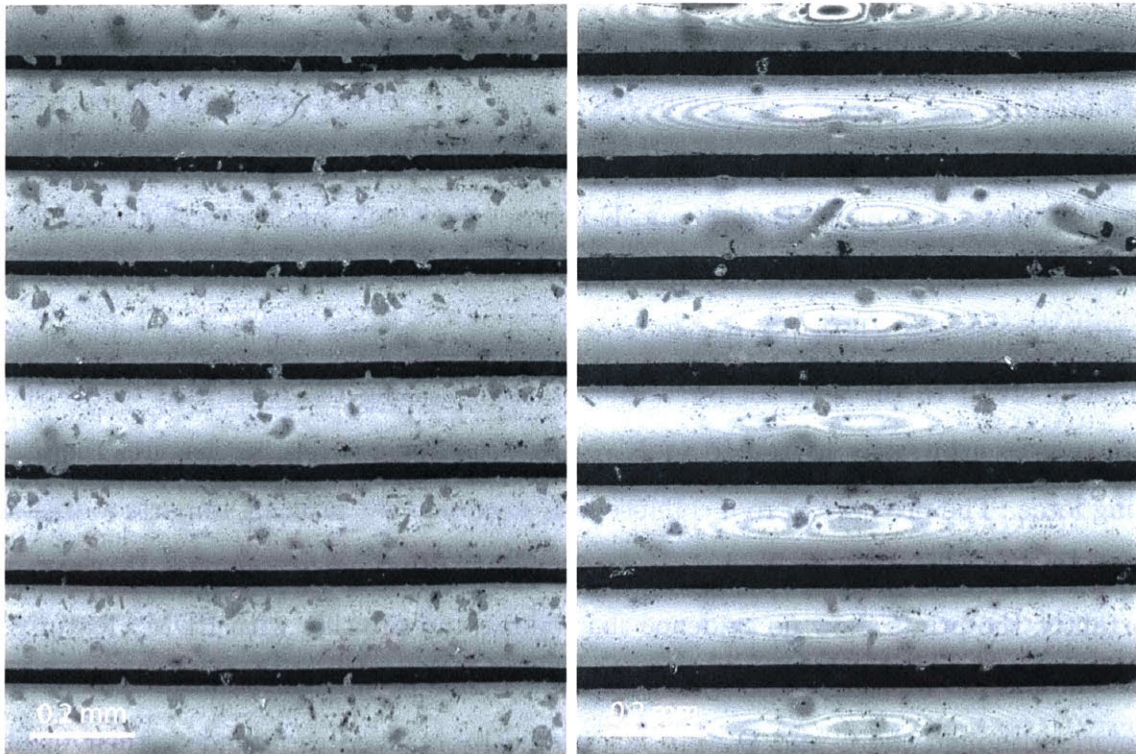

(a) Contact visualization of B* on tool S2. (b) Contact visualization of C* on tool S2.

Figure 5-52: Unprocessed images of B* and C* contact regions at a measured force of 4.9 N. C* contact widths are noticeably larger.

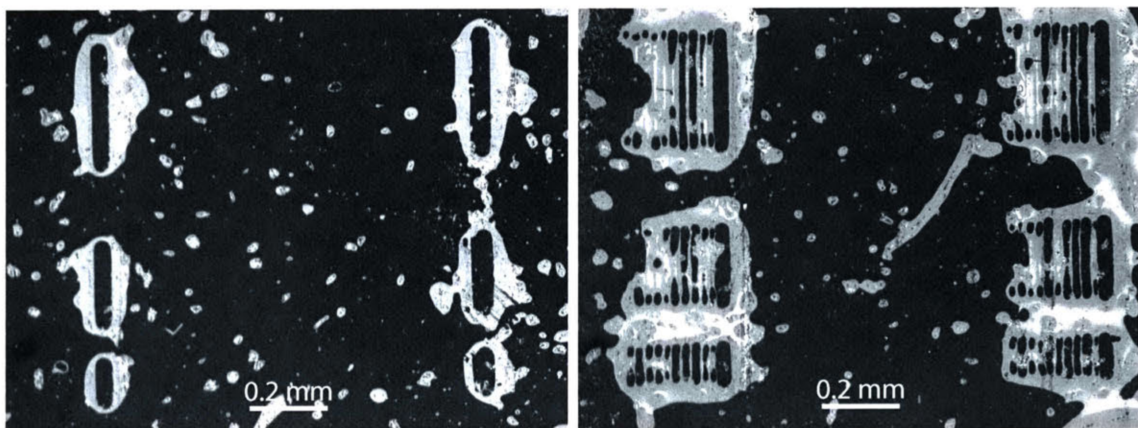

(a) Contact visualization of D*15 on tool S2. (b) Contact visualization of D*25 on tool S2.

Figure 5-53: Unprocessed images of D*15 and D*25 contact regions at a measured force of 4.9 N.

5.5.4 Print Visualization

Similar to contact, visualizing prints of C and D provides information on the role of varying feature types in μCP. Figure 5-54 compares a print of C with a print of B. Even with the same axial pitch, the two prints show different line widths due to different feature geometry. Figure 5-56 shows a D print. Both C and D prints are visually similar to their contact performance, but exhibit large roof collapse. Figure 5-55 shows a tool cross section compared to a print to indicate which ink transfers result from a feature versus roof collapse. This again lends credit to the need for force control and adapting the print load to the specific feature type in arbitrarily patterned tools. In this case, sparse postive features require less printing force. The presence of roof collapse also suggests that printing imparts a drastically different load condition on the tool than quasi-static contact measurements. However, most importantly, the prints show no evidence that inking and printing with PDMS features created from multiple exposures behave any differently than their single exposure counterparts. Therefore, although the C and D were not physically realized as intended, their utility in demonstrating arbitrarily patterned tools and new feature geometries was not severely diminished.

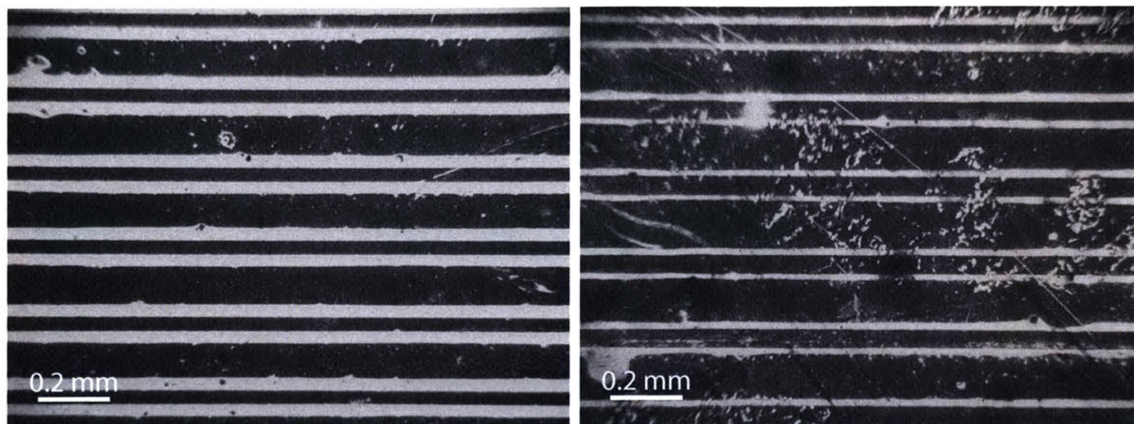

(a) An unprocessed print photograph of section B3. At this printing force roof collapse occured. The thin white lines represent the sidewalls, which did not make contact with the substrate. The thin black line bounded by the white represents the print width of the B feature.

(b) An unprocessed print photograph of section C3. At this printing force roof collapse occured. The thin white lines represent the sidewalls, which did not make contact with the substrate. The thin black line bounded by the white represents the print width of the C feature.

Figure 5-54: Unprocessed images of B3 and C3 prints at a measured print force of 4.9 N. C3 print widths are noticeably larger. Present roof collapse indicates that this was not the optimal print load, but a difference in widths is still noticeable. As with contact in Figure 5-52, C* print widths are much larger than B* at the same loading conditions.

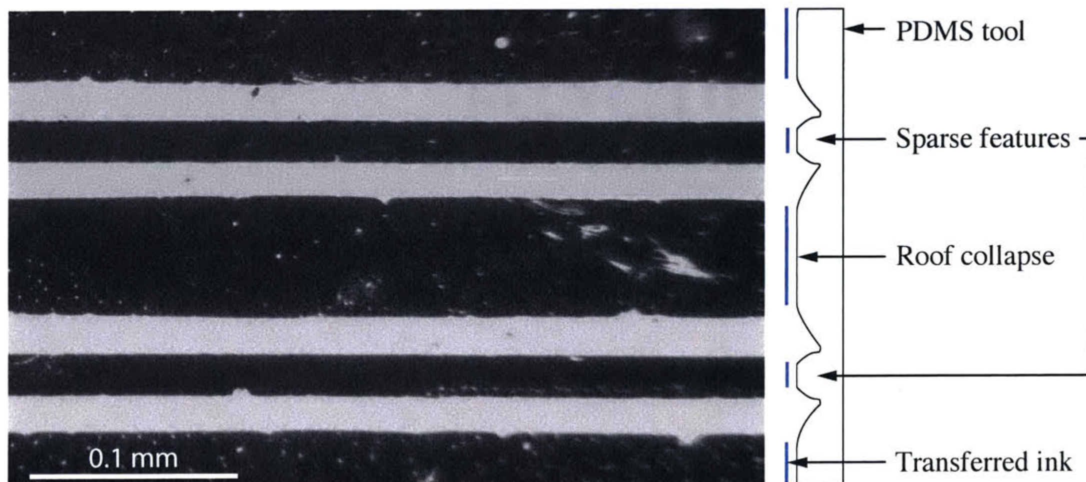

Figure 5-55: A schematic for interpretting prints with roof collapse. Sparse features on a tool loaded with relatively high force will exhibit roof collapse. In this failure mode, PDMS material between features bulges towards the print/contact interface.

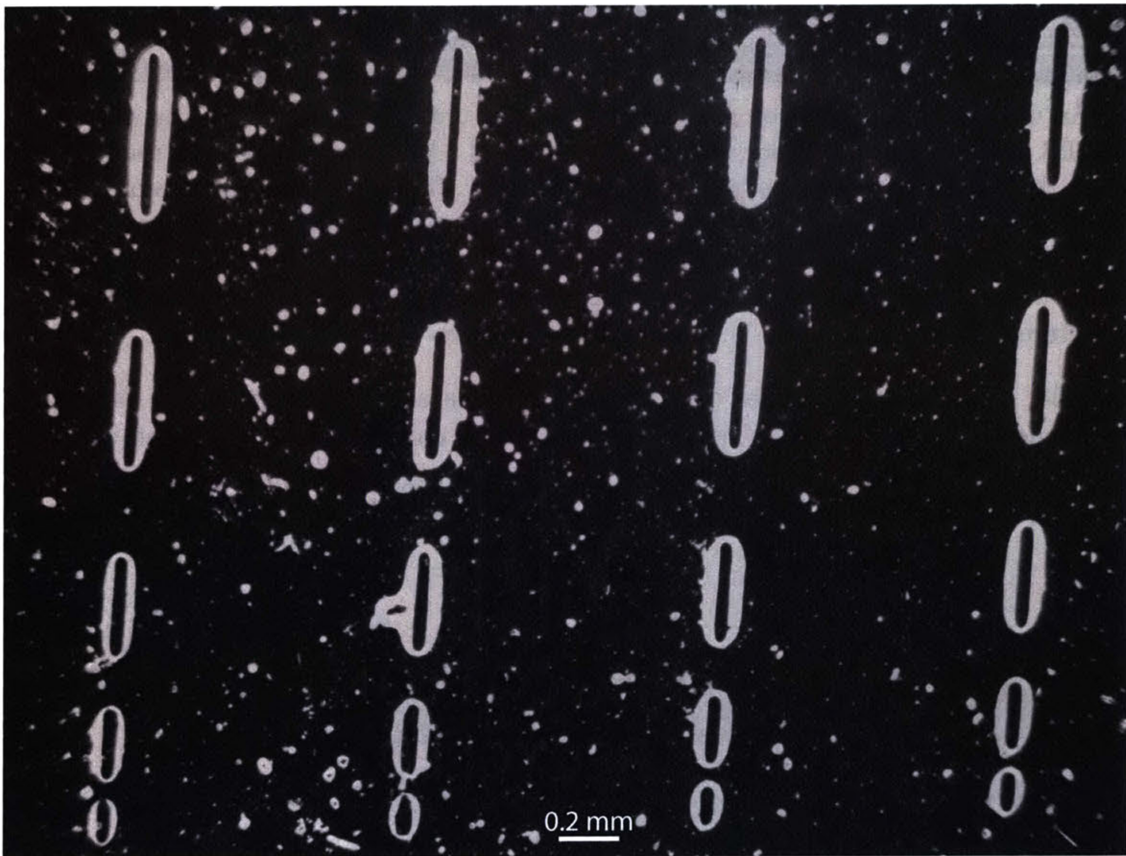

Figure 5-56: An unprocessed print image of D features at 4.9 N measured force. The printed shape agrees qualitatively with the contact geometry at the same applied load.

5.5.5 Overlapping Exposure Failure

It is extremely important to state that D features did not form as anticipated. Figure 5-57 presents a diagram of the expected photoresist structure compared ton a photoresist image. Contrary to simulation predictions, overlapping exposures did not lead to larger fused features. In some cases, only single line segments are present. It appears that only the first axially written feature formed a topology, while subsequent exposures did not yield features (at 5, 10, and 15 μm offsets), or only partially formed features by single exposure standards (at 20 and 25 μm offsets. Furthermore, C features did not widen substantially as expected either, but simpy yielded a very round cross section geometry. The cause of this discrepancy in overlapping exposures is unknown.

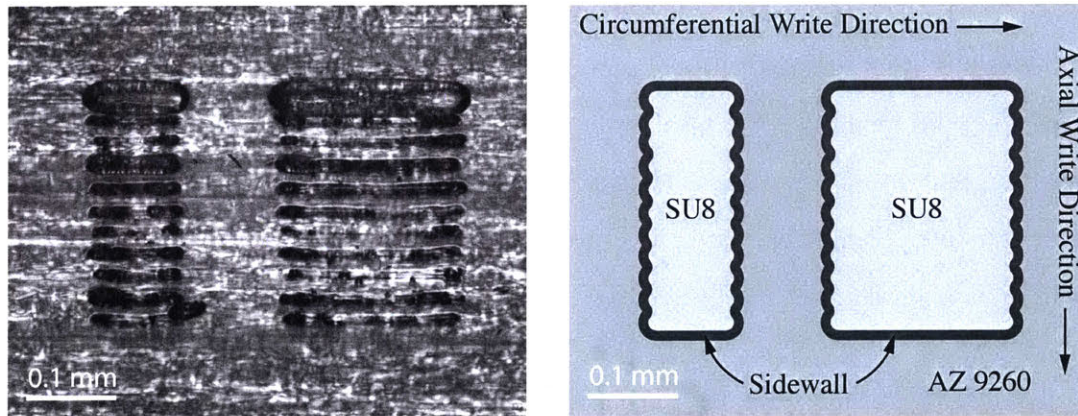

Figure 5-57: A schematic demonstrating how D features fromed in the photoresist (left) versus the intended photoresist geometry (right).

5.5.6 Summary

The AZ 9260 photoresist patterning layer was imaged at locations C1-C4, and D1-D4 after development, after casting and removing PDMS tool S1, and after casting and removing PDMS tool S3. All locations, except C1, remained visually unchanged. C1 features appeared to widen signifantly between development and tool S1, suggesting that there may exist a mechanism by which the photoresist can be reshaped during the first tool casting. The photoresist was also imaged at locations C* and D* after casting and removing tools S1 and S3. No substantial visual changes were observed between tool castings, other than possible enlarging of microscopic gas bubble defects in D* areas. Cross sections of PDMS tools S1 and S3 at C* showed a rounded feature shape of mean root width 44.74 ± 1.62 μm. Cross sections of D* showed the the feature did not form as intended, and some chemical limitation hindered the formation and fusing of adjacent line segments. However, both C* and D* features did visually replicate their corresponding photoresist geoemtries. Contact of C* showed larger contact line widths than B*. Contact of D* clearly presented the contact of short line segments. Similarly, prints of C features led to larger line widths than B features, and prints of D features succesfully yielded line segments as well.

Chapter 6

Discussion

The analytical and physical experimentation described in Chapters 4 and 5 respectively, was intended to demonstrate the fabrication of diverse feature sets on a single tool. Additionally, an understanding of the evolution of features from simulated photoresist geometries, all the way to realized print widths was gathered. The following sections outline the results of these attempts in the context of creating diversely featured PDMS stamps for scaled-up, application ready, μCP.

6.1 Towards Manufacturing Arbitrarily Patterned Tools

The raster-scan approach to photoresist exposure successfully created PDMS stamps with significant spatial variation to the tool pattern. In the experimental stamps for instance, four feature patterns were formed, with each set repeated at four different stamp locations. Additionally features A, B, C, and D, demonstrated the fabrication of features in the axial and circumferential stamp directions. However, the multiple-exposure attempts invoked via the raster-scan method did not create the intended geometries. Experimentation demonstrated practical process limitations to laser scribing, which would not have been eliminated by a vector writing approach. Consequently, a trade off between the manufacturing efficiency of a maskless, direct-write lithography system, and process constraints resulting from laser scribing and photoresist processing was discovered.

Focus and dose changes were shown in simulation and experimentation to create observ-

able changes in feature shape. Consequently, tool patterns and exact cross section geometry can be altered within a reasonable range with only one set of laser-optics. However, an interchangable system of direct-write laser-optics would prove even more useful at creating arbitrary patterns by adding more exposure input options. For example, new laser-optics sets resulting in larger beam waists could overcome the current need for multiple overlapping exposures to form larger features.

6.2 Contributions of the Tool

This thesis attempted to develop a complete picture of how the seamless cylindrical stamp transitioned from simulated feature shapes and associated write-path and exposure parameters, to the resulting microcontact print from the roll-to-roll setup. The following subsections summarize the transition between fabrication steps, highlighting geometric integrity under the context of current knowledge associated with each process step.

6.2.1 Pattern Similarity to Simulation

Single feature simulation trends for top width and height trends as a function of exposure dose were clearly reflected in experimental findings. The characteristic above and below focus feature shapes were also observed. However, the analytical model predicted a nearly constant root width of 15 μm for all focus and dose settings explored. Not only did root width change in practice (increasing with increasing dose) but a centrifuge speed of 6.28 rad/s (281% of the recommended dose at 15 μm resist thickness, 1714 mJ/cm^2) yielded root widths of over double the size, around 40 μm for A and B features.

Multiple exposure features yield further discrepancies. Observed C feature shapes were very round, even when adjacent A and B features exhibited clear trapezoidal cross sections. Additionally, the measured root widths of C features remained unchanged compared to A and B, even with an offset between exposures. D features were the only patterns that exhibited crisp flat tops, although all feature measured the full photoresist thickness. Neither simulation nor prior experimentation anticipated the exact formation or lack thereof of a crisp flat top (from bottoming out) purely from focus. Most importantly, D features did not

axially merge as predicted by the simulation. Clearly, the cumulative exposure method did not result in large width, fused features. From literature review, some physical implication of laser scribing could be a potential cause, but the true source of discrepency is unknown.

In summary, there are clear discrepancies between patterning layer and tool feature geometries seen in practice, compared to those simulated with the analytical model. Observed feature geometries support the single feature analytical trends and shape, but not the exact dimensions. Overlapping features disagree with shape and dimensions. It is unclear whether unmodeled second order processes (such as development or refraction) process faults of the physical system (such as thermal variation or rehydration delay length), and or something more intrinsic, such as centrifugal resist processing are to blame. In any case, the results demonstrate the complexity of modeling the lithography of thick photoresists for μCP stamp molds.

6.2.2 Pattern Replication by PDMS Stamp

Feature dimensions from PDMS cross sections and photoresist top views served as the basis of comparison. Data for the measured root widths and top widths of A* and B* features in photoresists and tools showed strong correlation, and resulting mean values of 41.99 ± 2.39 μm and 16.19 ± 1.80 μm respectively. Therefore, the seamless cyldindrical μCP stamp accurately replicated the AZ 9260 photoresist mold.

6.2.3 Patterning Layer Repeatability

Photographs of the 16 representative A, B, C, and D, and all of the A*, B*,C*, and D* locations showed little to no degredation from after casting and removing tool S1, to after casting and removing tool S3. The only visible changes, albiet very slight, was perhaps the enlarging of gas pocket defects near D features. Root width edge roughness on all feature types remaining constant throughout all imaging steps was a promising indicatation of mold repeatability. The data used to assess PDMS replication of A* and B* further supports the stability of the photoresist between tool castings.

However, locations A1, B1, and C1 showed reshaping of the photoresist between develop-

ment and tool S1. While PDMS does accurately replicate the AZ 9260, and the photoresist remains unchanged between tools, there must exist some mechanism(s) by which the resist can be reshaped post development by the casting process. Referencing Figure 5-10c to interpret Figures 5-15a, 5-19a, and 5-38a, the features in A1, B1, and C1 appear to have very steep, or vertical, sidewalls immediately after development. However, much more tapered or curved sidewalls are present following tool casting S1. One could speculate that ideal focus was achieved in these regions. A1, B1, and C1 are circumferentially adjacent and drum eccentricity could have brought the laser out of focus in other regions. The subsequent pressure and temperatures involved in PDMS casting could have caused the photoresist to flow and reshape. These results could explain why no features with vertical sidewalls were spotted during focus experiments.

6.2.4 PDMS Stamp Repeatability

As just discussed, measurements of root width and top with of A* and B* features in the photoresist and PDMS for tools S1 and S3 were well correlated. Therefore, the PDMS stamps are repeatable over the studied casting range. Changing the casting parameters, and or altering the number of castings would be expected to alter the result.

6.2.5 Contact Replication of Pattern Geometry

Contact analysis of A* and B* features indicated a clear linear trend behind the contact (or print) force and the contact width. The steeper widening of B* features with force was in agreement with the stiffness models. Most importantly, evaluating the linear trend equatinos for contact at 0 N of force yielded values agreeing with measured feature top widths from PDMS and photoresist. This important evaluation suggest that at 0^+ N of force, only PDMS feature top widths would make contact with the substrate in printing. At nonzero print forces, more PDMS is displaced into contact (Figure 6-1). Lastly, Contact visualization of C and D features at the nominal print force of 4.9 N demonstrated the ability to change the contact region geometries relative to A* and B*. Therefore, tools in contact reflect the general PDMS top surface geometry and in the limit of zero applied force, contact geometry

approaches the geometry of the tool.

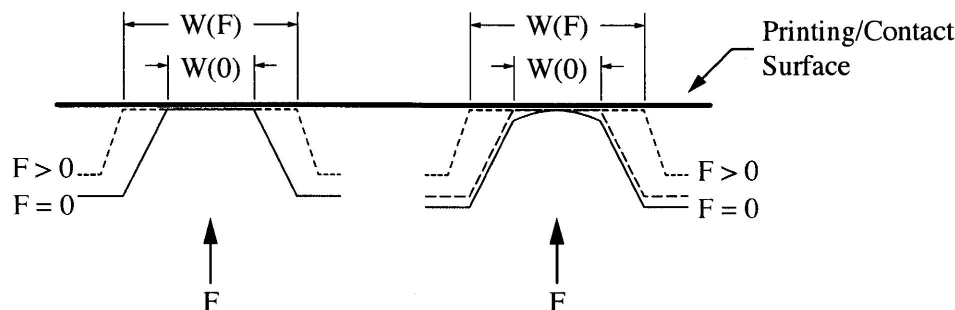

Figure 6-1: Expected feature geometry from contact analysis. Left: For a perfectly flat top feature, initially only the top width comes into conctact (blue, W(0)) at 0 N of force. As F increases, PDMS is displaced into the surface and the feature effectively widens to W(F) as it compresses (red). Right: For an approximately flat top feature, only a small portion of the approximate top width is in contact at F = 0 (blue). After applying a small force dF, or through adhesion, the PDMS conforms and the top width is achieved (green, W(0)). As F is increased again, the feature widens to W(F) (red).

6.2.6 Printing Replicaiton of Contact Geometry

Contact visualization of A, B, C, and D features all qualitatively demonstrate the same feature shape when printed in HDT on gold. Line width measurements of A* of tool S4 in printing and contact presented a quantitative correlation. Contact of the A* exhibited a mean line width of 32.98 $\pm$ 4.92 μm, while prints showed a scaling and shifting of the distribution to a mean line widht of 38.45 $\pm$ 2.67 μm. Therefore, an adjustment is presented, but the repeatability of the distribution suggests the change is deterministic.

6.3 Future Work

The conducted experimentation brings forth a few areas of tool making that still need to be studied. Pertaining to seamless cylindrical tooling in general, application specific patterns need to be manufactured. While this body of work presents attempts at creating diverse feature sets, a tool designed specific to a printing application will be necessary. Only then can it be claimed that the current setup can create useful patterns. The tool fabrication

process may also require further optimization to create specific feature types required by industry.

More significantly, a number of lithography limitations and problems were brought forth. If AZ 9260 (or another positive tone photoresist) is to continued to be used as the patterning layer, more extensive research on direct-write lithography and a much more advanced setup will be required. As discussed in Chapter 4 there are multiple, unknowns, noise sources, and precision machine errors that pose challenges to repeatedly fabricating the patterned mold. The process, casting machine, and simulation require refinement for accuracy in creating the desired feature shape, and repeatability in patterning the master mold. One must be able to fabricate the exact desired feature shape with relative ease.

Lastly, the link between contact geometry and printed geometry requires further investigation. PDMS accurately replicated the AZ 9260 mold, and contact widths were shown to be linearly adjusted from the top width as a function of the applied force. However, there was an observed adjustment between print and contact widths of A* features could be caused by many different mechanisms. Stamp swelling from inking, thermal expansion and contraction of the PDMS stamp, steady state dynamics of force control in printing, and registration could all be possible sources of error. For scalable, continuous, roll-to-roll μCP to be fully realized, there must be a predictable and understood relationship between measured contact geometry and the resulting print geometry.

Chapter 7

Conclusion

7.1 Thesis Contributions

This thesis sought to manufacture arbitrarily patterned seamless tools for continuous, roll-to-roll μCP. To this end, five main tasks were undertaken. First, a direct-write raster scan protocol was implemented for creating the stamp mold (patterning layer) with laser-scribe lithography. Second, literature review, analytical simulation, and physical experimentation were performed to investigate feature shape as a function of exposure dose, focal plane position, and number of exposures. Third, non-destructive tool contact visualization and photoresist mold imaging metrology setups were developed. Fourth, experimentation was conducted to create four different feature shapes in a diverse pattern in one photoresist mold. Lastly, said patterning layer and associated tools were thoroughly analyzed to track the evolution of feature geometry from simulation results, to the photoresist relief pattern, to the PDMS stamp, to tool in contact, and finally to the resulting print.

The results demonstrated the ability to control exposure over the entire stamp area, create a variety of feature shapes, and defined a narrow process window for laser-scribe, maskless lithography of AZ 9260 in the centrifugal caster setup. Four different feature geometries were fabricated, each with different tool cross section profiles, contact regions and behavior, and print geometries. The analysis of feature evolution of standard circumferential line features established a significant progress step in programming the tool geometry for a desired print result. First, trapezoidal feature shapes were fabricated using exposure settings developed

from simulation resulting in a similar profile. Second, PDMS stamps and the patterning layer were shown to be repeatable, with the stamp accurately replicating the mold. Third, a linear contact trend was recorded, showing the actuation of contact line width as a function of applied force. And finally, print line widths were shown to be of the same statistical distribution as the contact data set for the same force. Consequently, the deterministic fabrication of seamless cylindrical PDMS tools for continuous roll-to-roll μCP was validated.

7.2 Next Steps

While progress has been made toward demonstrating the fabrication of arbitrarily-patterned seamless cylindrical tooling, multiple barriers still remain for proving full scalability and utility of tools for roll-to-roll μCP. First photoresist processing posed a significant challenge to overcome for this thesis. Further experimentation is required to determine the exact impact of each processing step. If baking, exposure, developing, or PDMS casting parameters vary somewhat from their current setpoints, what will be the resulting tool. For instance, some feature exhibit crisp flat tops, but not all, could this be caused by not quite crossing a procedural threshold? The current steps may yield a working state, but perhaps not the absolute optimum. Additional laser-optics setups can be tested too. A signifantly different incident radiation profile may require substantially different pre-processing of the photoresist. Subsequently the simulation scope would require expansion, first to compensate for current inaccuracies, second to reflect changes in resist properties as a function of baking, and lastly to model development to confirm final mold topology.

Non-lithographic methods of fabricating patterning layers should be investigated since the processing complexity of photoresists may not prove to be ideal mold solution at the desired scale. For example, micromachining of PMMA molds in a cylindrical setup may prove to be a simpler solution. Cutting mechanics are well studied, and molds for positive and negative featured stamps could easily be machined. A lithographic setup would require switching between positive and negative resists, requiring at least two different procedures and process optimizations.

Regardless of exact method of creating tool molds, a new higher quality caster is required,

one with enough precision to control accurate feature formation and ensure repeatable performance. Starting with a newly designed machine, with well-defined performance metrics is paramount. Using the lithographic example, a machine designed and measured to focusing within 10 μm of the intended focal plane position would be significantly more useful in accuracy, and the precision creates a tightly-bound and repeatable process window for experimentation.

The serial fabrication and measurement methods of the current caster makes experimentation a very slow process. A new machine with easily interchangable drums and separate fabrication and metrology stations would substantially increase research productivity.

Finally, application-specific stamp geometries must be identified, and corresponding tools fabricated. The scale-up of microcontact printing with industry-specific tool and print performance metrics will result in substantially more proven manufacturing method. Along those lines, the transition from simulated feature shape to resulting print geometries must be thoroughly analyzed to prove that a certain set of simulated features will deterministically form a client's print specifications. Only then, can it be shown that sufficiently diverse features on continuous tools can be fabricated and scaled.

THIS PAGE INTENTIONALLY LEFT BLANK

Appendix A

Planarizing Layer Casting Procedure

Outlined below is the procedure for casting the SU8 planarizing layer in a bare aluminum drum. Nitrile gloves, safety goggles, and a lab coat should be warn at all times. The caster should be contained in its ventialtion configuration in all steps except during exposure, when it should be set up in the laser safety configuration. All chemistry-related work that cannot be conducted inside of the caster's ventilation enclosure should be conducted in a fume hoood. SDS sheets of all chemicals should be read and any concerns be brought to the attention of EHS.

1. Initialize the Machine

   (a) Turn on the three power switches on the power distributor unit of the electrical tower associated with the centrifuge motor, thermal system (heat gun), and electronics box.

   (b) Open centrifuge-pascoli2.lvproj in LabVIEW. Start the FPGA VI (FPGA_VI_raster_17.vi) then start the Host VI (raster_dots_pascoli_V4_7). Note that the FPGA VI will set the stage's position to 0 wherever it is on startup. As such, the stage should be tared against the reverse hardstop prior to starting the FPGA VI (simply open the Host VI and home the stage).

   (c) Spin the drum manually by hand at least one revolution so the rotary encoder will appriopriately zero itself its index.

2. Clean the Interior Aluminum Surface
    (a) Remove the the optics kinematic coupling plate from the linear stage.
    (b) Place a collection bin under the centrifuge to catch leaks and to directly drain into.
    (c) Squirt a small amount of Acetone into the drum while spinning at 75 rad/s.
    (d) Let the Acetone evaporate naturally or use a lint free cloth (ie beta-cloth) to absorb Acetone.
    (e) Set angular velocity to 0 rad/s when cleaning of the surface is complete.
3. Mix the SU8 2015 photoresist and Cyclopentanone solvent
    (a) Procure a 10 mL beaker and tare the scale to its weight.
    (b) Using a 5 mL pipet, deposit 2.5 mL of SU8 2015 into the beaker.
    (c) Place the beaker on the scale (if not there already) to obtain the mass of SU8 2015. Record this value. Retare the scale.
    (d) Using a 5 ML pipet and multiple draws, pipet 5.5[1] mL of SU8 2000 Thinner (Cyclopentanone) into the beaker.
    (e) Place the beaker on the scale again (if not there already) to obtain the mass of thinner used. Record this value.
    (f) Slowly mix the contents of the beaker with a stirring rod. Take care to not introduce bubbles into the solution while stirring.
4. Deposit SU8 mixture into the drum
    (a) Transfer beaker contents via 5 mL pipet into 10 mL syringe.
    (b) Spin the drum at 50 rad/s.
    (c) While moving the syringe outlet from one end of the drum to the other, dispense the mixture onto the internal spinning surface. I recommend traversing back and forth at least twice.

[1]The total solution volume to obtain is 8mL, regardless of exactly how much thinner volume that requires.

(d) Set the drum speed to 300 rad/s.

5. Evaporate solvent for 60 minutes at 95°C

   (a) Keep the drum spinning at 300 rad/s.

   (b) Turn on the heater fan, cooling fan, heater, set temperature to 95°C, set the timer for 60 minutes and start the thermal timer. This heat the drum to 95C and keep it there for 60 minutes before shutting down the thermal systems and conventively cooling down to room temperature while still spinning.

   (c) Briefly set drum speed to 0 rad/s while preparing for expsoure for handling safety.

6. Exposure Preperation

   (a) Remove the enclosure hardware specific to local ventialtion in preparation for installing the OD 5 viewing windows to the machine enclosure.

   (b) Place the UV LED arm (three 20 mW 405 nm LEDs) kinematic coupling plate on the linear stage. Connect the wires to power and ground of a power supply at 10V. Turn on the power supply.

   (c) Fasten the OD 5 laser safety panels.

7. Exposure

   (a) Set the drum speed to 300 rad/s.

   (b) Set linear stage speed to 5 μm/s (measured emperically). The stage has poor performance at such low speeds, I found that setting a speed of 16 μm/s led to a measured average speed of the desired 5 μm/s. Traverse from front end to back end of drum to expose the entire length of the casting area.

8. Disconnect LEDs and remove UV protection

   (a) Briefly set drum speed to 0 rad/s while prepping for handling safety.

   (b) Remove laser safety panels.

   (c) Power off the exposure arm, and remove it from the linear stage.

(d) Reinstall enclosure hardware specific to local ventilation.

9. Crosslink

   (a) Repeat the solvent evaporation step. This time the thermal process will crosslink the resist rather than evaporate solvent. However, do not let the drum cool to room temperature, immediately proceeed to the next step after 1 hour of crosslinking.

10. Post Bake

   (a) Keep the drum spinning at 300 rad/s.

   (b) Bake the photoresist for 1 hour at 1500°C.This will require at least one additional heat gun. Prior testing should be done to figure out the exact number and setup to appropriatly raise drum temperature since the normal thermal system cannot heat the drum to such high temperatures. Note that the full ventilation enclosure may need to be removed, but the snorkel should still be used to capture as many volatiles as possible.

   (c) After 1 hour shut off the thermal a system and extra heat guns and let the drum cool down while spinning.

   (d) Once the drum has returned to ambient temerpature set the centrifuge speed to 0 rad/s.

11. Power Down

   (a) Home the linear stage (will automatically shut down the Host VI)

   (b) Stop the FPGA VI and close LabVIEW.

   (c) Turn off the centrifuge motor, thermal system, and electric box power switches.

Appendix B

Patterning Layer Procedure

Outlined below is the procedure for casting the AZ 9260 photoresist patterning layer. Note that in the event of discrepancies between the provided text and the associated video[1], follow the procedure written here. The chemicals used in this process are respiratory and skin irritants. Nitrile gloves, safety goggles, and a lab coat should be warn at all times. The caster should be contained in its ventilation configuration in all steps except during writing/exposure, when it should be set up in the laser safety configuration. All chemistry-related work that cannot be conducted inside of the caster's ventilation enclosure should be conducted in a fume hood. SDS sheets of all chemicals should be read and any concerns be brought to the attention of EHS.

1. Initialize the Machine

   (a) Turn on the three power switches on the power distributor unit of the electrical tower associated with the centrifuge motor, thermal system (heat gun), and electronics box.

   (b) Open centrifuge-pascoli2.lvproj in LabVIEW. Start the FPGA VI (FPGA_VI_raster_17.vi) then start the Host VI (raster_dots_pascoli_V4_7). Note that the FPGA VI will set the stage's position to 0 wherever it is on startup. As such, the stage should be tared against the reverse hardstop prior to starting the FPGA VI (simply open the Host VI and home the stage).

[1] https://www.dropbox.com/s/ra970lc9403a5ep/stamp_procedure.mov?dl=0

(c) Spin the drum manually by hand at least one revolution so the rotary encoder will appriopriately zero itself its index.

2. Clean the SU8 surface by dissolving the existing AZ 9260 patterning layer in Acetone.

    (a) Remove the optics from the linear stage.

    (b) Place a collection bin under the centrifuge opening to catch leaks and to directly drain into.

    (c) Squirt a small amount (dispense time of about 5 seconds) of Acetone into the drum while spinning (75 rad/s). Stop the drum after 10 seconds, and drain liquid into bin by tipping centrifuge assembly. Repeat until the SU8 layer looks clear of AZ 9260.

    (d) Dampen a beta-cloth (or other lint free cloth/towel) with Acetone and gently wipe the SU8 surface while spinnning manually or slowly (10 rad/s). Repeat until the the cloth no longer becomes stained red, pink, or purple with the AZ 9260.

    (e) Dampen a standard paper towel with Acetone and gently wipe the ouside of the drum while spinnning manually or slowly (10 rad/s). This removes chemical residue on the external surface that can lead incorrect drum temperature measurements. Repeat until the towel no longer becomes stained red, pink, or purple.

3. Mix the AZ 9260 photoresist and PGMEA solvent.

    (a) For 15 μm stamp thickness: 0.38 mL of AZ 9260 and 5 mL of PGMEA (also known as AZ EBR or SU8 Developer).

    (b) Procure a 10 mL beaker and tare the scale to its weight.

    (c) Using the 1 mL pipet, add AZ 9260 into beaker. The photoresist has a high viscosity, so draw very slowly and dispense similarly slowly. Full deposition will likely require at least 2 or 3 releases of the button. Relevant video 0:00 to 0:55.

    (d) Place the beaker on the scale (if not there already) to obtain the mass of the AZ 9260. Tare the scale again.

(e) Using the 5 mL pipet, add the PGMEA into the beaker. Relevant video 0:55 to 1:21.

(f) Place the beaker on the scale (if not there already) to obtain the mass of the PGMEA.

(g) Mix the contents of the beaker for at least 10 seconds with a stirring rod until the AZ 9260 appears dissolved in the solvent and the mixture is visually homogenous. Relevant video 1:21 to 1:41.

4. Deposit the AZ 9260 and PGMEA mixture into the drum. Relevant video 1:48 to 2:25.

   (a) Spin the drum at 75 rad/s.

   (b) Draw 2 mL of mixture into the 5 mL pipet (larger volumes may contaminate the pipet due to the tilt angle necessary to dispense the mixture into the spinning centrifuge drum).

   (c) While moving the pipet tip from one end of the drum to to the other, dispense the mixture onto the internal spinning surface. I recommend traversing back and forth at least twice per 2 mL dispensed.

   (d) Repeat the above two steps as many times as needed to transfer all liquid into the centrifuge.

5. Post Apply Bake

   (a) Set the drum speed to 300 rad/s.

   (b) Turn on the heater fan, cooling fan, and enter the temperature set point of 60°C.

   (c) Once the measured temperature has reached the set point, wait 30 minutes.[2]

6. Soft Bake

   (a) Keep the centrifuge spinning at 300 rad/s

[2]The Post Apply Bake and subsequent Soft Bake can be automated, and should be implemented as such. Set the desired Post Apply Bake time (30 minutes) in the Thermal Process Timer. Set the Soft Bake temperature set point (110°C), time (3 minutes and 20 second) in Thermal Process Timer 2. Turn on Thermal Process Timer 2, followed by turning on Thermal Timer.

(b) Raise the temperature set point to 110°C.

(c) Once the temperature setpoint has been reached wait 200 seconds.

7. Cool Down

(a) Turn off the heating fan, cooling fan and enter a temperature set point of 0°C. The thermal process automation will do this automatically.

(b) Keep the centrifuge spinning at 300 rad/s until the drum temperature decreases to room temperature (25°C).

(c) Set centrifuge speed to 0 rad/s by gradually decreasing the speed from 300 to 200 to 100 to 50 to 25 to 10 to 5 to 1 to 0.

8. Resist Rehydration

(a) Wait 1 hour at to allow the resist to rehydrate via diffusion from the humidity in the room. Record the relative humidity and temperature.

9. Exposure Preperation

(a) Remove the ventilation-specific enclosure components and retrieve the OD 5 laser safety panels.

(b) Place the optics on the linear stage if not installed already.

(c) Put on laser safety goggles of at least OD 2 for 405 nm as a precaution.

(d) Connect the laser power cord.

(e) Fasten on the OD 5 viewing windows. If they cannot be installed for whatever reason, wear safety goggles and warn others in the lab space.

(f) Turn on the flashing laser sign.

(g) Remove laser safety goggles if the viewing windows successfully were installed.

10. Exposure

(a) Enter the appropriate exposure settings in LabVIEW via the Front Panel controls or by inserting an appropriate MATLAB script in the mathscript node in the Block Diagram.

(b) Press the Generate Arrays button to create the vectors and matrices LabVIEW will access for writing.

(c) Press the Write/Raster buttom to begin the exposure.

(d) When exposure is complete the laser will power off and the drum will come to rest automatically.

11. Disconnect Laser and Remove Laser Protection

    (a) Put on laser safety goggles as a precaution.

    (b) Remove the laser safety viewing panels from the machine enclosure.

    (c) Disconnect the laser power cord.

    (d) Turn off the flashing laser sign.

    (e) Remove the laser safety googles.

    (f) Reinstall the ventilation specific enclosure hardware.

12. Development with AZ 400K 1:4 Developer. Relevant video 2:25 to 3:14.

    (a) Place a collection bin under drum opening for draining and leaks.

    (b) Squirt developer into the drum spinning at 75 rad/s

    (c) Dispense a total of 8 mL of AZ 400K Developer 1:4 into the spinning drum in 2 mL increments with the 5 mL pipet per the procedure described before. Wait 220 seconds starting after the first deposition.

    (d) Gradually decrease the drum speed to 0 rad/s. Tip the drum to drain as much developer as possible into the collection bin.

    (e) Reset the centrifuge speed to 75 rad/s.

    (f) Squirt in DI water into drum (agitation in DI H_2O).

(g) Use squirt bottle to deposit DI water into drum. Spray for 10 seconds while moving the nozzle back and forth / in and out of the drum. Relevant video 3:04 to 3:14.

(h) Wait 60 seconds after starting to dispense the DI water.

(i) Gradually decrease the centrifuge speed to 0 rad/s. Tip the drum to drain as much water as possible into the collection bin

(j) Spin the drum for 5 minutes at 300 rad/s to air assist drying the photoresist post development since some liquid will be left over. You may notice a small droplet or two of liquid still on the resist after this, I recommend gently soaking up the liquid with a cotton swab if it is not directly on top of a feature.

13. Resist Outgas

(a) Wait 60 minutes to let some of the N_2 generated in exposure naturally outgas from the AZ photoresist

(b) Do not post-exposure bake the resist, as is common in many lithography applications.

Appendix C

Single Layer PDMS Stamp Casting Procedure

Outlined below is the procedure for casting the a single layer PDMS tool. Note that in the event of discrepancies between the provided text and the associated video[1], follow the procedure written here. The chemicals used in this process are respiratory and skin irritants. Nitrile gloves, safety goggles, and a lab coat should be warn at all times. The caster should be contained in its ventilation configuration in all steps except during writing/exposure, when it should be set up in the laser safety configuration. All chemistry-related work that cannot be conducted inside of the caster's ventilation enclosure should be conducted in a fume hood. SDS sheets of all chemicals should be read and any concerns be brought to the attention of EHS.

Note that the volume of the centrifuge is 10 mL, and stamp thickness is roughly linear with PDMS volume. For stamp with a 1 mm thickness (what is required to mount on the print roll), 10 mL of PDMS will be required (10 mL of the elastomer base, and 0.1 mL of the elastomer curing agent). Similarly for a stamp with a 0.6 mm thickness, 6 mL of PDMS is required (10 mL of the elastomer base, and 0.1 mL of the elastomer curing agent). The procedure remains the same regardless of PDMS volume, the text below is outlined for a stamp 0.6 mm thick.

[1] https://www.dropbox.com/s/ra970lc9403a5ep/stamp_procedure.mov?dl=0

1. Create PDMS Mixture (10:1 Base to Curing Agent)

   (a) Prepare syringe setup. Relevant video 3:15 to 3:25.

      i. Procure a 10 mL syringe and appopriately sized outlet cap. Tighten on the cap. Remove syring plunger, but save it for later.

      ii. Place the syringe (open side up) into a 150 mL beaker with a paper towel stuffed inside to help stabilize the syringe.

      iii. Place the beaker and contents on the scale and tare it.

   (b) Pour 6 grams of Syligard 184 Elastomer Base (very viscous, pour slowly) into the syringe and record its mass. Tare the scale. Note that hitting 6 grams exactly is not necessary - of concern is the 10:1 ratio. Relevant video 3:25 to 3:49.

   (c) Pour 10% of the elastomer base weight (0.6 grams if exactly 6 grams was hit) of Syligard 184 Elastomer Curing Agent into the syringe and record its mass. Variations in the 10:1 ratio impact the PDMS stiffness so hit the ratio as close as possible, though keep in mind that 0.7 grams on 6 grams (10:1.17) has currently negligble impact on stamp performance for our printing purposes. Relevant video 3:49 to 4:16.

   (d) Remove the 10 mL syringe from the beaker and vigorously mix contents with a stirring rod. Small macroscopic bubbles will form, giving the previously clear mixture a cloudy white/gray color. Relevant video 4:16-4:31. item

2. Degas the PDMS mixture. Relevant video 4:31 to 7:14.

   (a) Insert 10 mL syringe into the capped 60 mL syringe for the degasing setup. Place the 60 mL syring in the degasing setup.

   (b) Turn on vacuum pump and vacuum regulator.

   (c) Start a timer for 15 minutes.

   (d) Continuously hit the degasing syringe at roughly a 2 Hz frequency with a metal stirring rod or spatula to agitate the mixture. Also increase the magnitude of vacuum pulled on the syring to expand degas the mixture bubbles. Take care into

slowly increase the vacuum such that the PDMS mixture does not overflow from the 10 mL syringe containing the PDMS.[2]

3. Insert the PDMS. Relevant video 7:14 to 8:32.
   (a) Power off the vacuum pump and vacuum regulator.
   (b) Remove the 10 mL syringe containing the degased PDMS mixture from the degassing setup. Use a pair of pliers to pull the 10 mL syringe out of the 60 mL syringe.
   (c) Insert the 10 mL syringe plunger, invert, remove the syringe cap, and push out excess gas until PDMS mixture is at the tip of the syringe outlet
   (d) Inject PDMS onto the resist.
      i. Set centrifuge speed to 10 rad/s.
      ii. Place a chemical collection bin beneath drum opening in case of spill over.
      iii. Deposit PDMS into spinning drum drum while traversing the drum length just as in the photoresist deposition step.
4. Cure the PDMS
   (a) Increase the centrifuge speed from 10 rad/s to 300 rad/s in one step and wait 5 minutes.
   (b) Decrease the centrifuge speed to 200 rad/s, set the temeprature to 60°C, turn on the heater fan and turn on the cooling fan.
   (c) Wait 120 minutes once the set point is reached. Once again this heating can be automated.
   (d) Set temperature to 0°C, turn off the cooling fan, and turn off the heating fan.
   (e) Once the drum reads room temperature (25°C) gradually decrease the centrifuge speed to 0 rad/s.

[2]Agitation and continuous increase in the vacuum pulled (associated lever moved from the position of weakest vacuum to the opposite hardstop of maximum vacuum) should be completed in 5-10 minutes. In the remaining time a small number of bubbles may still be pulled by the vacuum but cannot be easily induced or subseqently outgased via mechanical agitation. Though continue to mechanically agitate the setup throughout the 15 minutes.

5. Remove the Stamp. Relevant video 8:32 to 9:23.

    (a) Use the green, Teflon-coated spatula to free the PDMS stamp edge at the open end of the centrifuge drum.

    (b) While wearing gloves, grip a portion of the free edge pried free of the photoresist with the spatula, and peel to remove the stamp. DO NOT shove the spatula under the entire stamp during removal, as this will damage the photoresist pattern.

6. Power Down

    (a) Home the linear stage.

    (b) Stop the Host VI (will happen automatically from zeroing the linear stage), then the FPGA VI, and then close LabView.

    (c) Turn off the centrifuge motor, thermal system, and electrical box power switches.

Appendix D

Dual Layer PDMS Stamp Casting Procedure

Outlined below is the procedure for casting the a dual layer PDMS tool. Note that in the event of discrepancies between the provided text and the associated video[1], follow the procedure written here. The chemicals used in this process are respiratory and skin irritants. Nitrile gloves, safety goggles, and a lab coat should be warn at all times. The caster should be contained in its ventilation configuration in all steps except during writing/exposure, when it should be set up in the laser safety configuration. All chemistry-related work that cannot be conducted inside of the caster's ventilation enclosure should be conducted in a fume hood. SDS sheets of all chemicals should be read and any concerns be brought to the attention of EHS.

Note that the volume of the centrifuge is 10 mL, and stamp thickness is roughly linear with PDMS volume. For stamp with a 1 mm thickness (what is required to mount on the print roll), 10 mL of PDMS will be required (10 mL of the elastomer base, and 0.1 mL of the elastomer curing agent). The procedure detailed here is for a 0.7 mm thick clear layer (7 mL PDMS volume), backed with a 0.3 mm thick black layer (3 mL). Other ratios of layer thicknesses are certainly possible, however only this procedure was validated through use.

1. Create Clear Layer PDMS Mixture (10:1 Base to Curing Agent)

[1] https://www.dropbox.com/s/ra970lc9403a5ep/stamp_procedure.mov?dl=0

(a) Prepare syringe setup. Relevant video 3:15 to 3:25.

i. Procure a 10 mL syringe and appopriately sized outlet cap. Tighten on the cap. Remove syring plunger, but save it for later.

ii. Place the syringe (open side up) into a 150 mL beaker with a paper towel stuffed inside to help stabilize the syringe.

iii. Place the beaker and contents on the scale and tare it.

(b) Pour 7 grams of Syligard 184 Elastomer Base (very viscous, pour slowly) into the syringe and record its mass. Tare the scale. Note that hitting 7 grams exactly is not necessary - of concern is the 10:1 ratio. Relevant video 3:25 to 3:49.

(c) Pour 10% of the elastomer base weight (0.7 grams if exactly 7 grams was hit) of Syligard 184 Elastomer Curing Agent into the syringe and record its mass. Variations in the 10:1 ratio impact the PDMS stiffness so hit the ratio as close as possible. Relevant video 3:49 to 4:16.

(d) Remove the 10 mL syringe from the beaker and vigorously mix contents with a stirring rod. Small macroscopic bubbles will form, giving the previously clear mixture a cloudy white/gray color. Relevant video 4:16-4:31. item

2. Degas the Clear Layer PDMS mixture. Relevant video 4:31 to 7:14.

(a) Insert 10 mL syringe into the capped 60 mL syringe for the degasing setup. Place the 60 mL syring in the degasing setup.

(b) Turn on vacuum pump and vacuum regulator.

(c) Start a timer for 15 minutes.

(d) Continuously hit the degasing syringe at roughly a 2 Hz frequency with a metal stirring rod or spatula to agitate the mixture. Also increase the magnitude of vacuum pulled on the syring to expand degas the mixture bubbles. Take care into slowly increase the vacuum such that the PDMS mixture does not overflow from the 10 mL syringe containing the PDMS.[2]

[2]Agitation and continuous increase in the vacuum pulled (associated lever moved from the position of weakest vacuum to the opposite hardstop of maximum vacuum) should be completed in 5-10 minutes. In

3. Insert the Clear Layer PDMS. Relevant video 7:14 to 8:32.

   (a) Power off the vacuum pump and vacuum regulator.

   (b) Remove the 10 mL syringe containing the degased PDMS mixture from the degassing setup. Use a pair of pliers to pull the 10 mL syringe out of the 60 mL syringe.

   (c) Insert the 10 mL syringe plunger, invert, remove the syringe cap, and push out excess gas until PDMS mixture is at the tip of the syringe outlet

   (d) Inject PDMS onto the resist.

      i. Set centrifuge speed to 10 rad/s.

      ii. Place a chemical collection bin beneath drum opening in case of spill over.

      iii. Deposit PDMS into spinning drum drum while traversing the drum length just as in the photoresist deposition step.

4. Cure the Clear Layer PDMS

   (a) Increase the centrifuge speed from 10 rad/s to 300 rad/s in one step and wait 5 minutes.

   (b) Decrease the centrifuge speed to 200 rad/s, set the temeprature to 60°C, turn on the heater fan and turn on the cooling fan.

   (c) Wait 120 minutes once the set point is reached. Once again this heating can be automated.

   (d) Set temperature to 0°C, turn off the cooling fan, and turn off the heating fan.

   (e) Once the drum reads room temperature (25°C) gradually decrease the centrifuge speed to 10 rad/s. The drum will take about 20 minutes to cool to room temperature, just enough time to create the black layer and have it ready for deposition once ambient temperature is achieved.

---

the remaining time a small number of bubbles may still be pulled by the vacuum but cannot be easily induced or subseqently outgased via mechanical agitation. Though continue to mechanically agitate the setup throughout the 15 minutes.

5. Create Black Layer PDMS Mixture (10:1 Base to Curing Agent)

    (a) Prepare syringe setup. Relevant video 3:15 to 3:25.

        i. Procure a 10 mL syringe and appopriately sized outlet cap. Tighten on the cap. Remove syring plunger, but save it for later.

        ii. Place the syringe (open side up) into a 150 mL beaker with a paper towel stuffed inside to help stabilize the syringe.

        iii. Place the beaker and contents on the scale and tare it.

    (b) Pour 3 grams of Syligard 184 Elastomer Base (very viscous, pour slowly) into the syringe and record its mass. Tare the scale. Note that hitting 3 grams exactly is not necessary - of concern is the 10:1 ratio. Relevant video 3:25 to 3:49.

    (c) Pour 10% of the elastomer base weight (0.3 grams if exactly 3 grams was hit) of Syligard 184 Elastomer Curing Agent into the syringe and record its mass. Variations in the 10:1 ratio impact the PDMS stiffness so hit the ratio as close as possible. Relevant video 3:49 to 4:16.

    (d) Pour 200 grams of PMS Black Silc Pig silicone rubber paint by Smooth-On into the syringe. The paint is difficult to pick up with a spatula and accurately dispense. Reasonable variations to the 200 gram marker have shown negligible impact to layer quality.

    (e) Remove the 10 mL syringe from the beaker and vigorously mix contents with a stirring rod. item

6. Degas the Black Layer PDMS mixture. Relevant video 4:31 to 7:14.

    (a) Insert 10 mL syringe into the capped 60 mL syringe for the degasing setup. Place the 60 mL syring in the degasing setup.

    (b) Turn on vacuum pump and vacuum regulator.

    (c) Start a timer for 15 minutes.

    (d) Continuously hit the degasing syringe at roughly a 2 Hz frequency with a metal stirring rod or spatula to agitate the mixture. Also increase the magnitude of

vacuum pulled on the syring to expand degas the mixture bubbles. Take care into slowly increase the vacuum such that the PDMS mixture does not overflow from the 10 mL syringe containing the PDMS.[3]

7. Insert the Black Layer PDMS mixture. Relevant video 7:14 to 8:32.

   (a) Power off the vacuum pump and vacuum regulator.

   (b) Remove the 10 mL syringe containing the degased PDMS mixture from the degassing setup. Use a pair of pliers to pull the 10 mL syringe out of the 60 mL syringe.

   (c) Insert the 10 mL syringe plunger, invert, remove the syringe cap, and push out excess gas until PDMS mixture is at the tip of the syringe outlet

   (d) Inject PDMS onto the exisitng cured layer of clear PDMS.

      i. Set centrifuge speed to 10 rad/s.

      ii. Place a chemical collection bin beneath drum opening in case of spill over.

      iii. Deposit PDMS into spinning drum drum while traversing the drum length just as in the photoresist deposition step. Note that the drum should only be filled to the 10mL volume. If for example 7.2 mL of PDMS was used for the clear layer, 2.8 mL of the black PDMS should be deposited, even if 3.2 mL was created.

8. Cure the Black Layer PDMS

   (a) Increase the centrifuge speed from 10 rad/s to 300 rad/s in one step and wait 5 minutes.

   (b) Decrease the centrifuge speed to 200 rad/s, set the temeprature to 60°C, turn on the heater fan and turn on the cooling fan.

[3]Agitation and continuous increase in the vacuum pulled (associated lever moved from the position of weakest vacuum to the opposite hardstop of maximum vacuum) should be completed in 5-10 minutes. In the remaining time a small number of bubbles may still be pulled by the vacuum but cannot be easily induced or subseqently outgased via mechanical agitation. Though continue to mechanically agitate the setup throughout the 15 minutes.

(c) Wait 120 minutes once the set point is reached. Once again this heating can be automated.

(d) Set temperature to 0°C, turn off the cooling fan, and turn off the heating fan.

(e) Once the drum reads room temperature (25°C) gradually decrease the centrifuge speed to 0 rad/s.

9. Remove the Stamp. Relevant video 8:32 to 9:23.

   (a) Use the green, Teflon-coated spatula to free the PDMS stamp edge at the open end of the centrifuge drum.

   (b) While wearing gloves, grip a portion of the free edge pried free of the photoresist with the spatula, and peel to remove the stamp. DO NOT shove the spatula under the entire stamp during removal, as this will damage the photoresist pattern.

10. Power Down

    (a) Home the linear stage.

    (b) Stop the Host VI (will happen automatically from zeroing the linear stage), then the FPGA VI, and then close LabView.

    (c) Turn off the centrifuge motor, thermal system, and electrical box power switches.

Appendix E

MATLAB Code Photoresist Pattern

This code is read in by the LabVIEW Host VI to expose the photoresist pattern used in Chapter 5.

```
1 clear all; close all; clc;
2
3 % Peter Ascoli
4 % M26 Standard Lines
5 % Created March 22 2017
6 % Last Updated March 22 2017
7
8 %% Input: Lines, Circ Overlap, or Ax Overlap
9
10 % TO WRITE EXPOSURE 1, STANDARD LINES, INPUT == 1
11 % TO WRITE EXPOSURE 2, CIRC OVERLAP, INPUT == 2
12 % TO WRITE EXPOSURE 3, AXIAL OVERLAP, INPUT == 3
13
14 input = 3;
15
16 %% Fixed values
17
18 Res = 8000; % [ticks] rotatary encoder resolution
19 P = 255; % [U8] nominal laser power
20 omega = 6.28; % [rad/s] nominal writing speed
```

```
21
22 %% Pattern Scenario values
23
24 % EXPOSURE 1
25 if input == 1
26     % line pitch
27     rho1 = 100; % [um] line pitch number 1
28     rho2 = rho1*2; % [um] line pitch number 2 (makes math easy)
29     rho = gcd(rho1,rho2); % [um] greatest common divisor for ...
           constructing matrix
30     % number of lines
31     n = 100; % writing on 1 cm axial length where focus is best
32 end
33
34 % EXPOSURE 2
35 if input == 2
36     n = 50; % only 50 lines were written at 200 um pitch in exp 1
37 end
38
39 % EXPOSURE 3
40 if input == 3
41     n_traverse = 10; % only 10 lines were written at 1mm pitch in exp 1
42     n = 100; % only 50 lines were written at 200 um pitch in exp 1
43 end
44
45 %% Construct Axial Matrix
46
47 x_start = 125; % [mm] staring position
48
49 % vector pitchs for axial array of each exposure group
50 pitch_A = 1;
51 pitch_B = 2;
52 pitch_C = pitch_B;
53 pitch_D = 10;
54
55 % EXPOSURE 1
```

```
56 if input == 1
57     x(1) = x_start; % [mm] starting position
58     for i = 2:pitch_A:n
59         x(i)=x(i-1)-0.1; % [mm] axial array
60     end
61 end
62
63 % EXPOSURE 2
64 if input == 2
65     offset = [5 5 10 10 15 15 20 20 25 25]./1000; % [mm] overlap offset ...
           amount
66     % reconstruct axial array from Exposure 1
67     x(1) = x_start; % [mm] starting position
68     for i = 2:pitch_A:100
69         x(i)=x(i-1)-0.1; % [mm] axial array
70     end
71     x = x(1:pitch_C:end); % axial array pertaining to Exposure 2
72     for i = 1:length(offset)
73         % offset each susbequent set of 5 lines by desired overlap offset
74         % amount
75         x(5*(i-1)+1:5*i) = x(5*(i-1)+1:5*i) - ...
               offset(i).*ones(size(x(5*(i-1)+1:5*i)));
76     end
77 end
78
79 % EXPOSURE 3
80 if input == 3
81     offset = [5 5 10 10 15 15 20 20 25 25]./1000; % [mm] overlap offset ...
           amount
82     % reconstruct axial array from Exposure 1
83     x(1) = x_start; % [mm] starting position
84     for i = 2:pitch_A:100
85         x(i)=x(i-1)-0.1; % [mm] axial array
86     end
87     x_base = x(1:10:end); % axial array pertaining to Exposure 3
88     x_offset = x_base - offset;
```

```
89      x = x_offset; % create first line of x array
90      for i = 2:10
91          % offset each line by offset(i) 10 times
92          x = [x x(end-10+1:end)-offset]; % [mm] axial array
93      end
94  end
95
96  %% Construct Speed Matrix
97
98  % this is the same regardless of which exposure is written
99  w = omega.*ones(size(x)); % [rad/s]
100
101 %% Construct Laser Power Matrix
102
103 % create appropriately sized matrix
104 LP = zeros(n,Res);
105 % section information (A,B,C,D)
106 A = [1:1:500,2001:1:2500,4001:1:4500,6001:1:6500]; % A writable area
107 B = [501:1:1000,2501:1:3000,4501:1:5000,6501:1:7000]; % B writable area
108 C = [1001:1:1500,3001:1:3500,5001:1:5500,7001:1:7500]; % C writable area
109 D_start = [1500+24 3500+24 5500+24 7500+24]; % D strarting markers
110 D_ticks = [1:5 11:20 31:45 61:80 101:125 151:180 211:245 286:325 366:410];
111 D = [];
112
113 % schematic for future plotting
114 schematic_A = ...
        [1+48:500-36,2001+24:2500-24,4001+24:4500-24,6001+24:6500-24];
115 schematic_B = [501+36:1000-24 2501+24:3000-24 4501+24:5000-24 ...
        6501+24:7000-24];
116 schematic_C = [1001+24:1500-24 3001+24:3500-24 5001+24:5500-24 ...
        7001+24:7500-24];
117 schematic_D = [1501+24:2000-24 3501+24:4000-24 5501+24:6000-24 ...
        7501+24:Res-48];
118
119 for i = 1:length(D_start)
120     D = [D D_start(i).*ones(size(D_ticks))+D_ticks];
```

```
121 end
122
123 if input == 1
124     % create A pattern
125     LP(1:pitch_A:end,A) = P;
126     % create B pattern
127     LP(1:pitch_B:end,B) = P;
128     % create C pattern base
129     LP(1:pitch_C:end,C) = P;
130     % create D pattern base
131     LP(1:pitch_D:end,D) = P;
132 end
133
134 if input == 2
135     % create C pattern
136     LP(:,C) = P;
137 end
138
139 if input == 3
140     % create D pattern
141     LP(:,D) = P;
142 end
143
144 %axial markers
145 ax_markers = [1:1:1+48,... % 2mm
146     500-36:1:500+36,... % 1.5mm
147     1000-24:1:1000+24,... % 1mm
148     1500-24:1:1500+24,... % 1mm gap forever now, easy to see wiritng ...
        direction on cast tool
149     2000-24:1:2000+24,...
150     2500-24:1:2500+24,...
151     3000-24:1:3000+24,...
152     3500-24:1:3500+24,...
153     4000-24:1:4000+24,...
154     4500-24:1:4500+24,...
155     5000-24:1:5000+24,...
```

```
156     5500-24:1:5500+24,...
157     6000-24:1:6000+24,...
158     6500-24:1:6500+24,...
159     7000-24:1:7000+24,...
160     7500-24:1:7500+24,...
161     Res-48:1:Res];
162 % create zeros for axial markers (for all sub-patterns)
163 LP(:,ax_markers)=0;
164 % 48.3 rotary counts is 1 mm
165 
166 %% Outputs for LabVIEW
167 
168 x_array = x; % [mm] stage axial position array
169 w_array = w; % [rad/s] centrifuge speed array
170 p_matrix = LP; % [u8] laser power 2D array
171 p_array = max(transpose(LP)); % [u8] constant laser power for each row ...
        1D array
172 
173 %% Outputs for Figures
174 
175 % 3D matrix u8, x pos, theta pos, drum speed (manually derive section
176 % number in plots)
177 
178 stamp(:,:,1) = p_matrix; % [U8] power at every position
179 
180 for i = 1:Res
181     stamp(:,i,2) = transpose(x_array); % [mm] axial location at every ...
            position
182 end
183 
184 for i = 1:n
185     stamp(i,:,3) = 1:1:8000; % [tick] rotary encoder position
186 end
187 
188 for i = 1:n
189     stamp(:,i,4) = transpose(w_array); % [rad/s] centrifuge speed ...
```

```
        location at every position
190 end
191
192 % assign sections (x,theta,layer) = section#
193 stamp(:,:,5) = 0; % nominal
194
195 if input == 1
196     stamp(:,[schematic_A schematic_B schematic_C schematic_D],5) = 1; % ...
        written area
197 end
198
199 if input == 2
200     stamp(:,schematic_C,5) = 1; % written area
201 end
202
203 if input == 3 % for plotting
204     stamp = p_matrix(1:pitch_D,:); % [U8] power at every position
205
206     for i = 1:Res
207         stamp(1:pitch_D,i,2) = transpose(x_array(1:pitch_D)); % [mm] ...
            axial location at every position
208     end
209
210     for i = 1:pitch_D
211         stamp(i,:,3) = 1:1:8000; % [tick] rotary encoder position
212     end
213
214     for i = 1:pitch_D
215         stamp(:,i,4) = transpose(w_array(1:pitch_D)); % [rad/s] ...
            centrifuge speed location at every position
216     end
217
218     stamp(:,schematic_D,5) = 1; % written area
219 end
220
221 %% Save Outputs for Plotting Double Checks and Figures
```

```
222
223 save('x.mat','x_array');
224 save('w.mat','w_array');
225 save('LP.mat','p_matrix');
226 save('p.mat','p_array');
227 save('stamp.mat','stamp');
```

Appendix F

MATLAB Code for Analyzing Print and Contact Images

This script is run first to analyze images taken with the contact system on the roll-to-roll machine or microscoping images taken of prints. The script loads in the images, and processes them to binary images representing the tool in contact with the impression roll, or the inked portion of the printing substrate. This data is exported for plotting.

```
1  %% Info
2
3  % Imports and processes images for contact/printing width statistics
4  % Data saved for plotting in PlotData.mat, DataIndices.mat, and in
5  % PrintContact.mat
6  % Plots of processed images with labeled lines are shown
7  % Last Updated April 2, 2017
8
9  %% Reset
10
11 clear all; close all; clc;
12
13 %% Figures to plot
14
15 plot_orig = 1; % if 1, create figure of original image
```

```
16 % ^ will not work if plot has only 1 line
17 plot_proc = 1; % if 1, create figure of processed image
18 % ^ will not work if plot has only 1 line
19
20 tic
21 %% Load Files
22
23 % magnification number of 18 denotes contact, else, print imaging algorithm
24 % will be run, at 4,10,and 40 scales determined by Chris
25
26 % test contact image #1
27 FileNamesRes1 = {... %{File Names, Magnification number,force}
28     '6N.png',18,6};
29 LineWidth1 = 50; % [um] expected feature width (max)
30 LinePitch1 = 100; % [um] expected feature pitch
31
32 % test print image #1
33 FileNamesRes2 = {... %{File Names, Magnification number,force}
34     '24N-p2.png',10,24};
35 LineWidth2 = 50; % [um] expected feature width (max)
36 LinePitch2 = 100; % [um] expected feature pitch
37 % Chris' orginal parameters were 30 and 100 (w,p) may need to adjust for
38 % new tool and associated line width size
39
40 % Aprime trend
41 FileNamesRes3 = {... %{File Names, Magnification number,force}
42     'Aprime-1.png',18,1.60;...
43     'Aprime-2.png',18,2.38;...
44     'Aprime-3.png',18,3.08;...
45     'Aprime-4.png',18,3.82;...
46     'Aprime-5.png',18,4.43;...
47     'Aprime-6.png',18,5.24;...
48     'Aprime-7.png',18,6.06;...
49     'Aprime-8.png',18,6.95;...
50     'Aprime-9.png',18,7.76;...
51     'Aprime-10.png',18,8.61;...
```

```
52      'Aprime-11.png',18,9.46;...
53      'Aprime-12.png',18,10.34;...
54      'Aprime-13.png',18,11.18;...
55      'Aprime-14.png',18,12.06;...
56      'Aprime-15.png',18,12.91;...
57      'Aprime-16.png',18,13.76;...
58      'Aprime-17.png',18,14.55;...
59      'Aprime-18.png',18,15.33;...
60      'Aprime-19.png',18,16.12;...
61      'Aprime-20.png',18,16.81;...
62      };
63  LineWidth3 = 50; % [um] expected feature width (max)
64  LinePitch3 = 100; % [um] expected feature pitch
65
66  % Bprime trend
67  FileNamesRes4 = {... %{File Names, Magnification number,force}
68      'Bprime-1.png',18,1.40;...
69      'Bprime-2.png',18,2.16;...
70      'Bprime-3.png',18,2.88;...
71      'Bprime-4.png',18,3.69;...
72      'Bprime-5.png',18,4.31;...
73      'Bprime-6.png',18,5.05;...
74      'Bprime-7.png',18,5.89;...
75      'Bprime-8.png',18,6.72;...
76      'Bprime-9.png',18,7.55;...
77      'Bprime-10.png',18,8.38;...
78      'Bprime-11.png',18,9.23;...
79      'Bprime-12.png',18,10.07;...
80      };
81  LineWidth4 = 50; % [um] expected feature width (max)
82  LinePitch4 = 200; % [um] expected feature pitch
83
84  % Cprime Visualization
85  FileNamesRes5 = {... %{File Names, Magnification number,force}
86      'Cprime-6.png',18,5.21;...
87      };
```

```
88 LineWidth5 = 50; % [um] expected feature width (max)
89 LinePitch5 = 200; % [um] expected feature pitch
90
91 % Aprime2 trend
92 FileNamesRes6 = {... %{File Names, Magnification number,force}
93     'Aprime2-1.png',18,1.42;...
94     'Aprime2-2.png',18,2.17;...
95     'Aprime2-3.png',18,3.04;...
96     'Aprime2-4.png',18,3.63;...
97     'Aprime2-5.png',18,4.41;...
98     'Aprime2-6.png',18,5.24;...
99     'Aprime2-7.png',18,6.07;...
100    'Aprime2-8.png',18,6.89;...
101    'Aprime2-9.png',18,7.72;...
102    'Aprime2-10.png',18,8.54;...
103    'Aprime2-11.png',18,9.35;...
104    'Aprime2-12.png',18,10.22;...
105    'Aprime2-13.png',18,11.08;...
106    'Aprime2-14.png',18,11.94;...
107    'Aprime2-15.png',18,12.77;...
108    'Aprime2-16.png',18,13.56;...
109    'Aprime2-17.png',18,14.37;...
110    'Aprime2-18.png',18,15.09;...
111    'Aprime2-19.png',18,15.88;...
112    'Aprime2-20.png',18,16.69;...
113    };
114 LineWidth6 = 50; % [um] expected feature width (max)
115 LinePitch6 = 100; % [um] expected feature pitch
116
117 % Bprime2 trend
118 FileNamesRes7 = {... %{File Names, Magnification number,force}
119    'Bprime2-0.2.png',18,0.73;...
120    'Bprime2-0.4.png',18,0.9;...
121    'Bprime2-0.6.png',18,1.06;...
122    'Bprime2-0.8.png',18,1.20;...
123    'Bprime2-1.png',18,1.33;...
```

```
124      'Bprime2-1.2.png',18,1.47;...
125      'Bprime2-1.6.png',18,1.74;...
126      'Bprime2-1.8.png',18,1.9;...
127      'Bprime2-2.png',18,2.09;...
128      'Bprime2-3.png',18,2.96;...
129      'Bprime2-4.png',18,3.57;...
130      };
131  LineWidth7 = 50; % [um] expected feature width (max)
132  LinePitch7 = 200; % [um] expected feature pitch
133
134  % Aprime3 trend
135  FileNamesRes8 = {... %{File Names, Magnification number,force}
136      'Aprime3-1.png',18,1.23;...
137      'Aprime3-2.png',18,1.92;...
138      'Aprime3-3.png',18,2.66;...
139      'Aprime3-4.png',18,3.28;...
140      'Aprime3-5.png',18,4.08;...
141      'Aprime3-6.png',18,4.91;...
142      'Aprime3-7.png',18,5.73;...
143      'Aprime3-8.png',18,6.56;...
144      'Aprime3-9.png',18,7.45;...
145      'Aprime3-10.png',18,8.27;...
146      'Aprime3-11.png',18,9.06;...
147      'Aprime3-12.png',18,9.85;...
148      'Aprime3-13.png',18,10.63;...
149      'Aprime3-14.png',18,11.44;...
150      'Aprime3-15.png',18,12.23;...
151      'Aprime3-16.png',18,13.02;...
152      'Aprime3-17.png',18,13.81;...
153      'Aprime3-18.png',18,14.61;...
154      'Aprime3-19.png',18,15.48;...
155      'Aprime3-20.png',18,16.28;...
156      'Aprime3-21.png',18,17.04;...
157      'Aprime3-22.png',18,17.83;...
158      'Aprime3-23.png',18,18.66;...
159      'Aprime3-24.png',18,19.29;...
```

```
160     'Aprime3-25.png',18,20.03;...
161     'Aprime3-26.png',18,20.74;...
162     'Aprime3-27.png',18,21.37;...
163     'Aprime3-28.png',18,22.15;...
164     'Aprime3-29.png',18,22.93;...
165     'Aprime3-30.png',18,23.72;...
166     'Aprime3-31.png',18,24.47;...
167     'Aprime3-32.png',18,25.23;...
168     'Aprime3-33.png',18,26.03;...
169     'Aprime3-34.png',18,26.79;...
170     'Aprime3-35.png',18,27.48;...
171     'Aprime3-36.png',18,28.16;...
172     'Aprime3-37.png',18,29.28;...
173     };
174 LineWidth8 = 50; % [um] expected feature width (max)
175 LinePitch8 = 100; % [um] expected feature pitch
176 
177 % Bprime3 trend
178 FileNamesRes9 = {... %{File Names, Magnification number,force}
179     'Bprime3-1.png',18,1.04;...
180     'Bprime3-2.png',18,1.92;...
181     'Bprime3-3.png',18,2.75;...
182     'Bprime3-4.png',18,3.51;...
183     'Bprime3-5.png',18,4.05;...
184     'Bprime3-6.png',18,4.84;...
185     'Bprime3-7.png',18,5.65;...
186     'Bprime3-8.png',18,6.42;...
187     'Bprime3-9.png',18,7.20;...
188     'Bprime3-10.png',18,7.99;...
189     'Bprime3-11.png',18,8.80;...
190     'Bprime3-12.png',18,9.59;...
191     %'Bprime3-13.png',18,10.41;...
192     'Bprime3-14.png',18,11.19;...
193     'Bprime3-15.png',18,11.95;...
194     'Bprime3-16.png',18,12.73;...
195     'Bprime3-17.png',18,13.50;...
```

```
196        'Bprime3-18.png',18,14.28;...
197        'Bprime3-19.png',18,15.07;...
198        'Bprime3-20.png',18,15.86;...
199        'Bprime3-21.png',18,16.64;...
200        'Bprime3-22.png',18,17.44;...
201        'Bprime3-23.png',18,18.23;...
202        'Bprime3-24.png',18,19.01;...
203        'Bprime3-25.png',18,19.79;...
204        'Bprime3-26.png',18,20.57;...
205        'Bprime3-27.png',18,21.33;...
206        'Bprime3-28.png',18,22.10;...
207        'Bprime3-29.png',18,22.85;...
208        'Bprime3-30.png',18,23.63;...
209        'Bprime3-31.png',18,24.39;...
210        'Bprime3-32.png',18,25.16;...
211        'Bprime3-33.png',18,25.90;...
212        'Bprime3-34.png',18,26.67;...
213        'Bprime3-35.png',18,27.43;...
214        'Bprime3-36.png',18,28.19;...
215        'Bprime3-37.png',18,28.96;...
216        };
217    LineWidth9 = 50; % [um] expected feature width (max)
218    LinePitch9 = 200; % [um] expected feature pitch
219
220    % Aprime and Bprime calibration
221    FileNamesRes10 = {... %{File Names, Magnification number,force}
222        %'Aprime3-6.png',18,4.91;...
223        'Bprime3-6.png',18,4.84;...
224        };
225    LineWidth10 = 50; % [um] expected feature width (max)
226    LinePitch10 = 200; % [um] expected feature pitch
227
228    % Cprime3 comparison
229    FileNamesRes11 = {... %{File Names, Magnification number,force}
230        'Cprime3-6.png',18,4.91;...
231        };
```

```
232 LineWidth11 = 100; % [um] expected feature width (max)
233 LinePitch11 = 200; % [um] expected feature pitch
234
235 % Select an Image for Thesis Figures
236 FileNamesRes12 = {... %{File Names, Magnification number,force}
237     'Aprime3-6.png',18,4.91;...
238     };
239 LineWidth12 = 50; % [um] expected feature width (max)
240 LinePitch12 = 200; % [um] expected feature pitch
241
242 % SELECT WHICH IMAGES TO CALL AND THEIR PARAMETERS
243 FileNamesRes = FileNamesRes11;
244 LineWidth = LineWidth11;
245 LinePitch = LinePitch11;
246
247 N = size(FileNamesRes,1);
248 Images = cell(N,2); % {Picture, Magnification number}
249
250 for i = 1:N
251     Images{i,1} = imread(FileNamesRes{i,1});
252     Images{i,2} = FileNamesRes{i,2};
253 end
254
255 %% Pre-processing
256
257 ims_2_process = N % print number of images
258
259 Images2 = cell(N,1); % processed images
260 Images3 = cell(N,1); % original images cropped and rotated accordingly
261
262 for i = 1:N
263
264     if Images{i,2} == 18 % process image for contact width nalysis
265         [Images2{i,1},Images3{i,1}] = ImProcessContact(Images{i,1});
266     else % process image for print width nalysis
267         [Images2{i,1},Images3{i,1}] = ImProcessPrint(Images{i,1});
```

```
268     end
269
270
271     improcess1_process = i % print progress
272 end
273
274 %% Length Processing
275
276 % add method to reject bad lines! (can still be in image, no nead to
277 % recrop) but remove from analysis if ananlysis range limited by top or
278 % bottom edge of image (buffer)
279
280 Scales = [18 4 10 40;... % [ImageResolution(MP) Magnification ...
        Magnification Magnification]
281     3336318.68 980131, 2460052, 9642130]; %px/m
282 Scales(3,:) = 1./Scales(2,:) * 10^6; %micron/pixel
283
284 [Widths,Defects] = deal(cell(N,1)); %[Mean Std]
285
286 for j = 1:N
287     Scale = Scales(3,Scales(1,:) == Images{j,2}); % should be and is ...
            1.6162!
288     [Widths{j},Defects{j},Centers{j},Widths2{j}] =...
289         ImProcessWidth(Images2{j,1},Scale,LineWidth,LinePitch); % max ...
                width as we approach roof collapse is ¬ 50um
290
291     PlotWidths = cat(1,Widths{j}); %PlotWidths = cell2mat(PlotWidths);
292     PlotDefects = cat(1,Defects{j}); %PlotDefects = cell2mat(PlotDefects);
293     R = size(PlotWidths,1); % must remain constant to work
294
295     PlotData1 = [PlotDefects PlotWidths...
296         FileNamesRes{j,3}*ones(size(PlotDefects))]; % place into master ...
                matrix
297     % [Defects ; Width Mean ; Width STDEV ; Force]
298     if j == 1
299         PlotData = PlotData1;
```

```
300     else
301         PlotData = [PlotData(:,:) ; PlotData1]; % concatonate
302     end
303
304     Rvec(j) = R; % count number of rows for each image group in PlotData
305
306     if Images{j,2} == 18
307         PoC(j) = 1; % 1 if contact
308     else
309         PoC(j) = 0; % 0 if print
310     end
311
312     improcess3_process = j % print progress
313 end
314
315 %% Show processed figures with line labels
316
317 if plot_proc == 1
318
319     for i = 1:N
320
321         loc = cell2mat(Centers(i)); % line locations in each image
322
323         f_proc = figure
324         hold on
325         warning off
326         imshow(Images2{i,1})
327
328         if Images{i,2} == 18
329             str_title = 'Processed Contact Image: Force of '; % image title
330             sdf_proc = 'proc_v1'; % export scenario
331         else
332             str_title = 'Processed Print Image: Force of '; % image title
333             sdf_proc = 'proc_v1'; % export scenario
334         end
335
```

```
336            %set(gca,'fontsize',18,'Interpreter','latex')
337            title([str_title,num2str(FileNamesRes{i,3}),'N'])
338            for j = 1:Rvec(i)
339                % label each line
340                textshift(j,i) = 0;%0.25*widths((i-1)*R+j);
341                str = ['Contact Line ',num2str(j)];
342                text(10,loc(j)+textshift(j),str,...
343                    'HorizontalAlignment','left','Color','red','FontSize',10);
344            end
345            hold off
346
347            sdf(f_proc,sdf_proc)
348
349        end
350
351    end
352
353    %% Show original figures with line labels
354
355    if plot_orig == 1
356
357        for i = 1:N
358
359            loc = cell2mat(Centers(i)); % line locations in each image
360
361            f_orig = figure;
362            hold on
363            warning off
364            imshow(Images3{i,1})
365
366            if Images{i,2} == 18
367                str_title = 'Original Contact Image: Force of '; % image title
368                sdf_proc = 'proc_v1'; % export scenario
369            else
370                str_title = 'Original Print Image: Force of ';
371                sdf_proc = 'proc_v1'; % export scenario
```

```
372         end
373
374         %set(gca,'fontsize',18,'Interpreter','latex')
375         title([str_title,num2str(FileNamesRes{i,3}),'N'])
376         for j = 1:Rvec(i)
377             % label each line
378             textshift(j,i) = 0;%0.25*widths((i-1)*R+j);
379             str = ['Contact Line ',num2str(j)];
380             text(10,loc(j)+textshift(j),str,...
381                 'HorizontalAlignment','left','Color','red','FontSize',10);
382         end
383         hold off
384
385         sdf(f_orig,sdf_proc)
386
387     end
388
389 end
390
391 %% Save Data
392
393 save('PlotData.mat','PlotData'); % save width data
394 save('DataIndices.mat','Rvec'); % save number of lines per image data
395 save('PrintContact.mat','PoC'); % save print or image data
396
397 toc
```

Appendix G

MATLAB Code for Contact Image Binarization

This fucntion is called in the analysis script. It processes the image from the contact system to a binary image of contact. Image processing parameters in this function were found emperically by taring the processed contact data against the unprocessed image measured manually in Adobe Photoshop CS6.

```
1  function [ImOut,Im_orig] = ImProcessContact(Im)
2  %% ImProcessContact performs basic pre-processing on line images
3  % Last Updated 03/30/2017
4
5  % Im in the input image file (uint8)
6  %% Convert to grayscale
7
8  %ImG = rgb2gray(Im);
9  ImG = Im;
10 ImG = imrotate(ImG,90);
11 % figure
12 % warning off
13 % imshow(ImG)
14
15 % original image cropped and rotated accordingly
```

```
16 Im_1 = ImG; % rename orignal image
17
18 %% Invert image
19 ImGI = imcomplement(ImG);
20
21 %% Background Creation
22 %ImBackground = imopen(ImGI,strel('disk',80,4));
23 % 60 4, 80 was good for 6N calibration
24 ImBackground = imopen(ImGI,strel('disk',60,8));
25 % Values are currently arbitrary and need to be double checked. I'm not
26 % sure I'm using the strel command correctly
27
28 % figure
29 % warning off
30 % imshow(ImBackground)
31 % title('background')
32
33 % % % figure
34 % % % imshow(ImGI)
35 % % % title('inverted image')
36 %% Background Subtraction
37 ImGI2 = ImGI - ImBackground;
38
39 % figure
40 % imshow(ImGI2)
41 % title('background subtracted')
42
43 %% Crop Image
44 % To deal with non-uniform lighting, cutting off edges
45 Dim = size(ImGI2);
46 HCrop = round(Dim(2)*[0 1]); % Horizontal crop points, set to none
47 VCrop =  round(Dim(1)*[0 1]); % Vertical crop points, set to none
48
49 ImGI2C = imcrop(ImGI2,[HCrop(1),VCrop(1),...
50     HCrop(2)-HCrop(1),VCrop(2)-VCrop(1)]);
51 % figure
```

```
52 % imshow(ImGI2C)
53
54 % original image cropped and rotated accordingly
55 Im_2 = imcrop(Im_1,[HCrop(1),VCrop(1),...
56     HCrop(2)-HCrop(1),VCrop(2)-VCrop(1)]); % crop 1
57 %% Contrast adjust
58
59 % chris' contrast (global)
60 % ImGI3 = imadjust(ImGI2C);
61 % figure
62 % imshow(ImGI3)
63 % title('contrast adjusted image')
64
65 % local adaptive contrast adjustment
66 ImGI3 = adapthisteq(ImGI2C,'Distribution','uniform','NumTiles',[4,2]); ...
       % exp dist is better but worsens hough transform
67 % figure
68 % imshow(ImGI3)
69 % title('adaptive histeq image')
70
71 % try no contrast adjustment
72 % ImGI3 = ImGI2C;
73
74 % could histogram adjustment improve?
75 % ImG13 = histeq(imGI3,5);
76 % figure
77 % imshow(ImGI3)
78
79 %% Thresholding
80 %thresh = graythresh(ImGI3);
81 % figure
82 % imshow(thresh)
83 % this thresholding does not seem ideal
84
85 % try adaptive thresholding
86 %thresh = adaptthresh(ImGI3); % assumes consistent exposure across images
```

```
87
88
89 %% Create BW Image
90
91 % for 2015 Matlab
92 %ImBW = im2bw(ImGI3,thresh);
93 % Image is color inverted from original
94 % figure
95 % imshow(ImBW)
96
97 % for 2016 Matlab
98 %ImBW = imbinarize(ImGI3,'adaptive');
99 %ImBW = imbinarize(ImGI3,'adaptive',...
100 %'ForegroundPolarity','dark','Sensitivity',0.5);
101 % is this now looking for the 'largest contrast' (=1) in a local setting?
102
103 ImBW = imbinarize(ImGI3,...
104      'adaptive','ForegroundPolarity','dark','Sensitivity',0.75);
105 % 0.75 was a little too intense
106
107 % figure
108 % imshow(ImBW)
109 % title('imbinarize result')
110
111 % clean up large spots - Peter 10/25/2016
112 % was 100000
113 ImBW = bwareaopen(ImBW,50000); % 100,000 ideal for 18MP camera (order ...
        of magnitude higher will remove lines)
114 % this is a pixel square of 20 by 20 (anything this size or smaller is
115 % removed (ie anything smaller than 1 nominal line width in any dimension)
116 % trial and error made this seem good (40-2000 -> mu_6N = 30.05N)
117 % figure
118 % imshow(ImBW)
119 % title('bwareopen result')
120
121 % smooth border
```

```
122 seD = strel('diamond',4); %4 gets mean adequate (STDEV still large...)
123 seD = strel('disk',4,8); % new..
124 ImBW = imerode(ImBW,seD); ImBW = imerode(ImBW,seD); %ImBW = ...
        imerode(ImBW,strel('square',5)); % erode twice
125
126 % figure
127 % imshow(ImBW)
128 % title('imerode')
129
130 % ImBWoutline = bwperim(ImBW);
131 % Segout = I;
132 % Segout(ImBWoutline) = 255;
133 %
134 % figure
135 % imshow(Segout)
136 % title('perimeter')
137
138 % fill openings
139 ImBW = imfill(ImBW,'holes');
140 % % % figure
141 % % % imshow(ImBW)
142 % % % title('hole fill')
143
144
145 % remove open again
146 % was 25k
147 ImBW = bwareaopen(ImBW,10000); % 400000 and above lost lines
148 % figure
149 % imshow(ImBW)
150 % title('bwareaopen again')
151
152 %% Create edge detection image for Hough Transform
153 % Performs edge detection and rotates image to vertical
154 ImERot = imrotate(edge(ImGI3,'Sobel',0.05,'horizontal'),90);
155
156 %% Hough transform to find image orientation and horizontally align
```

```
157 AngleRes = 0.1; % Resolution of Hough Transform
158 AngleLimit = 1; %2;
159 AngleRange = -AngleLimit:AngleRes:AngleLimit-AngleRes; %Array of angles ...
        checked in Hough Transform
160 [H,T,R] = hough(ImERot,'Theta',AngleRange);
161
162 % figure
163 % imshow(imadjust(mat2gray(H)),'XData',T,'YData',R,...
164 %     'InitialMagnification','fit');
165 % xlabel('\theta'), ylabel('\rho');
166 % axis on, axis normal;
167 % colormap(hot)
168
169 peaks = houghpeaks(H,5);
170
171 % figure
172 % P  = peaks;
173 % imshow(H,[],'XData',T,'YData',R,'InitialMagnification','fit');
174 % xlabel('\theta'), ylabel('\rho');
175 % axis on, axis normal, hold on;
176 % plot(T(P(:,2)),R(P(:,1)),'s','color','white');
177
178 % lines = houghlines(ImERot,T,R,peaks,'FillGap',5,'MinLength',7);
179
180 % figure, imshow(ImERot), hold on
181 %
182 % for k = 1:length(lines)
183 %     xy = [lines(k).point1; lines(k).point2];
184 %     plot(xy(:,1),xy(:,2),'LineWidth',2,'Color','green');
185 %
186 %     % Plot beginnings and ends of lines
187 %     plot(xy(1,1),xy(1,2),'x','LineWidth',2,'Color','yellow');
188 %     plot(xy(2,1),xy(2,2),'x','LineWidth',2,'Color','red');
189 % end
190
191 angle = mean(AngleRange(peaks(:,2))); % works now that image oriented ...
```

```
    properly
192 %angle = -1; % force angle change per photoshop
193 % Looks right, should triple check
194 ImBW = imrotate(ImBW,angle,'crop'); %ImOut = imrotate(ImBW,angle,'crop');
195
196 % original image cropped and rotated accordingly
197 Im_3 = imrotate(Im_2,angle,'crop'); % hough transform rotation
198 %% Recrop rotated image since above doesn't seem to cut it
199 Dim = size(ImBW);
200 HCrop2 = round(Dim(2)*[.1 .9]); %Horizontal crop points
201 VCrop2 =  round(Dim(1)*[.1 .9]); %Vertical crop points
202
203 ImOut = imcrop(ImBW,[HCrop2(1),VCrop2(1),...
204     HCrop2(2)-HCrop2(1),VCrop2(2)-VCrop2(1)]);
205 % figure
206 % imshow(ImOut)
207
208 % original image cropped and rotated accordingly
209 Im_4 = imcrop(Im_3,[HCrop2(1),VCrop2(1),...
210     HCrop2(2)-HCrop2(1),VCrop2(2)-VCrop2(1)]); % crop 2
211 Im_orig = Im_4;
212 % figure
213 % imshow(Im_4)
214
215 end
```

THIS PAGE INTENTIONALLY LEFT BLANK

Appendix H

MATLAB Code for Print Image Binarization

This function is called in the first script. It processes microscoping images of prints according to the process developed by Merian [reference!!!].

```
1  function [ImOut,Im_orig] = ImProcessPrint(Im)
2  %% ImProcessPrint performs basic pre-processing on line images
3  % Last Updated 03/23/2017
4
5  % Im in the input image file (uint8)
6  %% Convert to grayscale
7  ImG = rgb2gray(Im);
8  % figure
9  % warning off
10 % imshow(ImG)
11
12 %% Invert image
13 ImGI = imcomplement(ImG);
14
15 %% Background Creation
16 ImBackground = imopen(ImGI,strel('disk',60,4));
17 % Values are currently arbitrary and need to be double checked. I'm not
```

```
18 % sure I'm using the strel command correctly
19 % figure
20 % warning off
21 % imshow(ImBackground)
22 %% Background Subtraction
23 ImGI2 = ImGI - ImBackground;
24
25 %% Crop Image
26 % To deal with non-uniform lighting, cutting off edges
27 Dim = size(ImGI2);
28 HCrop = round(Dim(2)*[.1 .9]); %Horizontal crop points
29 VCrop =  round(Dim(1)*[.1 .9]); %Vertical crop points
30
31 ImGI2C = imcrop(ImGI2,[HCrop(1),VCrop(1),...
32     HCrop(2)-HCrop(1),VCrop(2)-VCrop(1)]);
33 %% Contrast adjust
34 ImGI3 = imadjust(ImGI2C);
35
36 %% Thresholding
37 thresh = graythresh(ImGI3);
38
39 %% Create BW Image
40 ImBW = im2bw(ImGI3,thresh);
41 % Image is color inverted from original
42
43 %% Create edge detection image for Hough Transform
44 % Performs edge detection and rotates image to vertical
45 ImERot = imrotate(edge(ImGI3,'Sobel',0.05,'horizontal'),90);
46 %% Hough transform to find image orientation and horizontally align
47 AngleRes = 0.1; % Resolution of Hough Transform
48 AngleLimit = 2;
49 AngleRange = -AngleLimit:AngleRes:AngleLimit-AngleRes; %Array of angles ...
       checked in Hough Transform
50 [H,T,R] = hough(ImERot,'Theta',AngleRange);
51
52 % figure
```

```
53 % imshow(imadjust(mat2gray(H)),'XData',T,'YData',R,...
54 %     'InitialMagnification','fit');
55 % xlabel('\theta'), ylabel('\rho');
56 % axis on, axis normal;
57 % colormap(hot)
58
59 peaks = houghpeaks(H,5);
60
61 % figure
62 % P  = peaks;
63 % imshow(H,[],'XData',T,'YData',R,'InitialMagnification','fit');
64 % xlabel('\theta'), ylabel('\rho');
65 % axis on, axis normal, hold on;
66 % plot(T(P(:,2)),R(P(:,1)),'s','color','white');
67
68 % lines = houghlines(ImERot,T,R,peaks,'FillGap',5,'MinLength',7);
69
70 % figure, imshow(ImERot), hold on
71 %
72 % for k = 1:length(lines)
73 %     xy = [lines(k).point1; lines(k).point2];
74 %     plot(xy(:,1),xy(:,2),'LineWidth',2,'Color','green');
75 %
76 %     % Plot beginnings and ends of lines
77 %     plot(xy(1,1),xy(1,2),'x','LineWidth',2,'Color','yellow');
78 %     plot(xy(2,1),xy(2,2),'x','LineWidth',2,'Color','red');
79 % end
80
81 angle = mean(AngleRange(peaks(:,2)));
82 % Looks right, should triple check
83 ImOut = imrotate(ImBW,angle,'Crop');
84
85 % original image cropped and rotated accordingly
86 Im_orig = imrotate(imcrop(ImG,[HCrop(1),VCrop(1),...
87     HCrop(2)-HCrop(1),VCrop(2)-VCrop(1)]),angle,'Crop');
88 end
```

THIS PAGE INTENTIONALLY LEFT BLANK

Appendix I

MATLAB Code for Line Width Analysis

This function is called by the first script to analyze the binarize contact or print image and measure the width(s) of each feature.

```
1  function [WidthsOut,DefectsOut,Centers1,Widths2] = ...
       ImProcessWidth(ImBW,Scale,LineWidth,LinePitch)
2  %% ImProcess3 performs line width analysis on pre-processed images
3  % last updated 03/23/2017
4  
5  % Attemping to add defect detection over ImProcess2
6  
7  % ImBW in the input image file from ImProcess1 (logical)
8  % Scale is the image scale in micron/pixel
9  % LineWidth is the expected line width in microns
10 % LinePitch is the period of the print in microns
11 
12 % WidthsOut is a list of line width [Mean Std]
13 % DefectsOut is a list of percentage of line which is defective
14 %% Get image dimensions
15 Dim = size(ImBW);
16 %% Average picture along edge
17 Mean1 = mean(ImBW,2);
18 
19 %% Peak Detection
```

```
20 MinSep = (LinePitch-LineWidth)/Scale; % Expected line separation in pixels
21 MinSep = MinSep*0.8; % Fudge factor to give some margin on line separation
22
23 [Peak1,Loc1] = ...
       findpeaks(Mean1,'MinPeakHeight',.5,'MinPeakDistance',MinSep);
24 % Height of .5 is pretty reasonable
25 % Distance is based on resolution and expected print parameters
26
27 %% Basic width measurement
28 N = length(Peak1); % Number of peaks detected => Number of lines
29 WidthRange = ceil((LineWidth/Scale)*1.4); % Number of pixels around ...
       peak that will be checked for line
30 % Fudge factor of 40% to detect everything
31
32 % WidthRange must be even
33 if mod(WidthRange,2) ≠ 0
34      WidthRange = WidthRange + 1;
35 end
36
37 HeightThresh = 0.1; % Min height to be included in measurement
38 % Do I even need this on a black and white image?
39
40 %% Find centerlines
41 [Widths1,Centers1] = deal(zeros(N,1));
42
43 % Peter's method below to reject incomplete contact lines at edges of ...
       images
44
45 InValidIndex = zeros(1,N); % preallocate as all valid regions
46 for i = 1:N
47      Region = Loc1(i)+ [-WidthRange/2:WidthRange/2]; % Region of pixels ...
            to check
48      RegionStart_limits = [max(Region) min(Region)]; % starting region ...
            limits
49      Region(Region ≤ 0) = []; %reject region if portion out of picture
50      Region(Region > Dim(1)) = []; %reject region if portion out of picture
```

```
51      Region_limits = [max(Region) min(Region)]; % sanity check
52      ValidRegion = Region(Mean1(Region)>HeightThresh); % Pulls all ...
            values in region above height threshold
53      Widths1(i) = length(ValidRegion); % Calculates valid region width not
54      Centers1(i) =  ValidRegion(round(length(ValidRegion)/2)); %Midpoint ...
            of valid region
55
56      % reject regions intersecting border
57      if RegionStart_limits(1) ≠ Region_limits(1) | RegionStart_limits(2) ...
            ≠ Region_limits(2)
58          InValidIndex(i) = 1; % region to ignore analysis
59          here = 1; % sanity check
60      end
61  end
62
63  InValidIndex; % sanity check
64  c = InValidIndex == 1; % indices to remove
65  Centers1(c) = []; % remove non valid lines
66  CentersValid = Centers1; % sanity check
67  N = length(CentersValid); % set new vector length
68
69
70  % for i = 1:N
71  %     Region = Loc1(i)+ [-WidthRange/2:WidthRange/2]; % Region of ...
        pixels to check
72  %     acomp = zeros(1,0); bcomp = zeros(1,0); % reset region markers
73  %     a = find(Region ≤ 0) % is region on border? empty if ok!
74  %     b = find(Region > Dim(1)) % is region on border? empty if ok!
75  %     % reject region if on border
76  %     %     Region(Region ≤ 0) = []; %reject region if portion out of ...
        picture
77  %     %     Region(Region > Dim(1)) = []; %reject region if portion out ...
        of picture
78  %     ValidRegion = Region(Mean1(Region)>HeightThresh); % Pulls all ...
        values in region above height threshold
79  %     Widths1(i) = length(ValidRegion); % Calculates valid region width not
```

```
80  %     Centers1(i) =  ValidRegion(round(length(ValidRegion)/2)) ...
    %Midpoint of valid region
81  %     InValidIndex = ones(1,N); % preallocate invalid regions
82  %     if a == acomp
83  %         if b == bcomp % if region is not on edge of image!
84  %             InValidIndex(i) = 0; % region to ignore analysis
85  %             here = 1 % sanity check
86  %         end
87  %     end
88  % end
89  % c = InValidIndex == 1 % indices to remove
90  % Centers1(c) = []; % remove non valid lines
91  % CentersValid = Centers1 % sanity check
92
93  % attempt 1
94  % for i = 1:N
95  %     Region = Loc1(i)+ [-WidthRange/2:WidthRange/2]; % Region of ...
    pixels to check
96  %     Region(Region ≤ 0) = []; %Remove region out of picture
97  %     Region(Region > Dim(1)) = []; %Remove region out of picture
98  %     if abs(Region(1)-Region(end)) == WidthRange/2
99  %         % only allocates centering scheme if analysis over full width is
100 %         % possible (ie, don't check regions if at edge top or bottom edge
101 %         % of the image processed for analysis
102 %         ValidRegion = Region(Mean1(Region)>HeightThresh); % Pulls all ...
    values in region above height threshold
103 %         Widths1(i) = length(ValidRegion); % Calculates valid region width
104 %         Centers1(i) =  ValidRegion(round(length(ValidRegion)/2)); ...
    %Midpoint of valid region
105 %     end
106 % end
107
108 % Chris's method below.
109 % for i = 1:N
110 %     Region = Loc1(i)+ [-WidthRange/2:WidthRange/2]; % Region of ...
    pixels to check
```

```
111 %     Region(Region ≤ 0) = []; %Remove region out of picture
112 %     Region(Region > Dim(1)) = [];
113 %     ValidRegion = Region(Mean1(Region)>HeightThresh); % Pulls all ...
        values in region above height threshold
114 %     Widths1(i) = length(ValidRegion); % Calculates valid region width
115 %     Centers1(i) =  ValidRegion(round(length(ValidRegion)/2)); ...
        %Midpoint of valid region
116 % end
117
118
119 %% Pre-allocate
120 [Widths2,Defects] = deal(zeros(N,Dim(2)));
121 [WidthsOut,NonDefectRange] = deal(zeros(N,2));
122 [DefectsOut, NormalCheck] = deal(zeros(N,1));
123 %% Process at each image column
124
125 % these parameters seem to alter the number of defects (at least when width
126 % was fixed at 20) perhaps how they will also alter stdev...get mean 6N
127 % calibrated first then play with these and see how it changes the data
128 % error
129
130 % Number of standard devitations from the mean a width must be to count ...
        as a defect
131 DefectThresh = 1; % ARBITRARY - chris had 1
132
133 % Percentage from mean a width must be to count as a defect
134 DefectPercent = 0.2; % chris had at 0.2
135
136 for k = 1:N; %For each centerline
137     Region2 = Centers1(k) + [-WidthRange/2:WidthRange/2]; %Region to ...
            check around the centerline
138     Region2(Region2 ≤ 0) = []; %Remove region that is out of picture
139     Region2(Region2 > Dim(1)) = [];
140
141     for j = 1:Dim(2); %Along each column
142         Widths2(k,j) = sum(ImBW(Region2,j))*Scale; %Sum along line and ...
```

```
            Convert to microns
143         %         Defects2(k,j) = std(ImBW(Region2,j))*Scale;
144     end
145
146     %         Plot along line
147     %         figure
148     %         plot(Widths2(k,:))
149
150     %% Create stats
151     WidthsOut(k,1) = mean(Widths2(k,:)); %Mean
152     WidthsOut(k,2) = std(Widths2(k,:)); %Std Dev
153     NormalCheck(k) = ztest(Widths2(k,:),WidthsOut(k,1),WidthsOut(k,2)); ...
            %Is the data normally distributed
154
155     %% Calculate Defects
156     % Range of line widths for line that defines not defective
157     %     NonDefectRange(k,:) = ...
            [WidthsOut(k,1)-DefectThresh*WidthsOut(k,2) ...
            WidthsOut(k,1)+DefectThresh*WidthsOut(k,2)];
158
159     NonDefectRange(k,:) = [1-DefectPercent ...
            1+DefectPercent].*WidthsOut(k,1);
160
161     % Calculate defective pixels
162     Defects(k,:) =  (Widths2(k,:)<NonDefectRange(k,1)) + ...
            (Widths2(k,:)>NonDefectRange(k,2));
163     DefectsOut(k) = sum(Defects(k,:))/Dim(2) * 100; %Sum defects. ...
            Convert to percentage
164 end
165 end
```

Appendix J

MATLAB Code for Plotting Contact and Print Data

This script is run second (last) to plot contact and print data extracted from images in the first script.

```
1  %% Info
2  % Creates individual and comparison contact line width statistics plots
3  % Last Updated 03/23/2017
4  %% Reset
5
6  %clear;
7  %close all;
8  clc;
9
10 %% Figures to plot
11
12 plot_ind = 0; % if 1, create figure data for individual contact image
13 % ^ will not work if plot has only 1 line
14 plot_ind_seq = 0; % if 1, create additional figure data for individual ...
       contact image
15 % ^will not work if plot has only 1 line, only works with one image laoded
16 % :(
```

```
17 plot_cmp = 1; % if 1, create comparative figure (trendline)
18 plot_conv = 0; % if 1, create comparative figure of all constant force
19
20 tic
21 %% Load Files
22
23 Data2Plot = cell2mat(struct2cell(load('PlotData.mat'))); % load data
24 Rvec = cell2mat(struct2cell(load('DataIndices.mat'))); % load number of ...
       lines
25 PC = cell2mat(struct2cell(load('PrintContact.mat'))); % load print or ...
       contact flag, 1 = Contact, 0 = Print
26 N = length(Rvec); % number of images
27
28 %% Create Identifying Indices for Each Data Set
29
30 Rsum = cumsum(Rvec); % # of data points / rows in each image
31 for i = 1:length(Rsum)
32     if i == 1
33         R_start(i) = 1;
34     else
35         R_start(i) = Rsum(i-1) + 1;
36     end
37     R_end(i) = Rsum(i);
38     %R_start = Rsum - Rsum(1).*ones(size(Rsum)) + ones(size(Rsum));
39     %starting indicies for each group of data
40     %R_end = Rsum; % ending indicies for each group of data
41 end
42
43 Rmat = [ transpose(Rvec) transpose(R_start) transpose(R_end) ]; % ...
       number of data , starting index , ending index (for given image)
44
45 %% Create Individual Plots
46
47 if plot_ind == 1
48     N = length(Rvec); % number of data sets (ie, processed images)
49
```

```
50
51      for i=1:N
52
53          R = Rmat(i,1); % number of data
54          Rs = Rmat(i,2); % data starting index
55          Re = Rmat(i,3); % data ending index
56
57          if PC(i) == 1
58              str_title = ['Contact Statistics: Force of ',...
59                  num2str(Data2Plot(Rs,4)),'N'];
60          else
61              str_title = ['Print Statistics: Force of ',...
62                  num2str(Data2Plot(Rs,4)),'N'];
63          end
64
65          f1 = figure;
66          hold on
67          scatter(Data2Plot(Rs:Re,2),Data2Plot(Rs:Re,3),[],...
68              Data2Plot(Rs:Re,1),'filled','MarkerEdgeColor','k')
69          c = colorbar;
70          hLegend = ylabel(c,'Defect Percentage');
71          title(str_title)%[num2str(Data2Plot(Rs,4)),'N  - Contact Line ...
               Width Statistics'])
72          xlabel('Mean Line Width [microns]')
73          ylabel('Standard Deviation [microns]')
74          grid on
75          set(gca,'fontsize',18)
76          %axis([20,30,0.5,3])
77
78          locx = Data2Plot(Rs:Re,2); %locx = reshape(locx,[R,N]);
79          locy = Data2Plot(Rs:Re,3); %locy = reshape(locy,[R,N]);
80
81          % label each line
82          for j = 1:R
83              label = [' CL ',num2str(j)];
84              text([locx(j)],[locy(j)],label,'HorizontalAlignment',...
```

```
85                  'left','Color','k','FontSize',18);
86          end
87          hold off
88
89          sdf(f1,'contact_spread_v1')
90
91      end
92
93  end
94
95
96  %% Create Individual Sequential Plots
97
98  if plot_ind_seq == 1
99
100     figure
101     colormap(jet)
102     for i = 1:Rvec(1)
103
104         R = Rmat(1); % number of data
105         Rs = Rmat(2); % data starting index
106
107         hold on
108         scatter(i,Data2Plot(Rs+(i-1),2),[],Data2Plot(Rs+(i-1),1),...
109             'filled','MarkerEdgeColor','k','SizeData',100); % force/# , ...
                width, defect
110         errorbar(i,Data2Plot(Rs+(i-1),2),Data2Plot(Rs+(i-1),3),'.k') % ...
               force, width, stdev
111         %axis([0.8,7.2,20,35])
112         %colormap(jet)
113         c = colorbar;
114         hLegend = ylabel(c,'Defect Percentage');
115         title([num2str(Data2Plot(Rs,4)),...
116             'N  - Contact Line Width Statistics'])
117         xlabel('Contact Line [#]')
118         ylabel('Mean Contact Line Width [microns]')
```

```
119            set(gca,'fontsize',18)
120            grid on
121        end
122
123    end
124
125    %% Comparison Plot
126
127    if plot_cmp == 1;
128
129        f3 = figure;
130        colormap(jet)
131        for i = 1:N
132
133            R = Rmat(i,1); % number of data
134            Rs = Rmat(i,2); % data starting index
135            Re = Rmat(i,3); % data ending index
136
137            if PC(i) == 1
138                str_title = ['Contact Trend: Variable Force'];
139            else
140                str_title = ['Print Trend: Variable Force'];
141            end
142
143            hold on
144            scatter(Data2Plot(Rs,4),mean(Data2Plot(Rs:Re,2)),...
145                [],mean(Data2Plot(Rs:Re,1)),...
146                'filled','MarkerEdgeColor','k','SizeData',100); % force, ...
                      width, defect
147            errorbar(Data2Plot(Rs,4),mean(Data2Plot(Rs:Re,2)),...
148                std(Data2Plot(Rs:Re,2)),'.k') % force, width, stdev
149            %axis([0.8,7.2,20,35])
150            %colormap(jet)
151            c = colorbar;
152            %caxis([0 8])
153            hLegend = ylabel(c,'Defect Percentage');
```

```
154         title(str_title)
155         xlabel('Applied Force [N]') % net force applied by BothBias
156         ylabel('Mean Line Width [microns]')
157         axis([0 30 17 30])
158         set(gca,'fontsize',18)
159         grid on
160
161
162     end
163
164     sdf(f3,'contact_spread_v1')
165
166 end
167
168 %% Constat Force Comparison Plot
169
170 if plot_conv == 1;
171
172     f4 = figure;
173     colormap(jet)
174     for i = 1:N
175
176         R = Rmat(i,1); % number of data
177         Rs = Rmat(i,2); % data starting index
178         Re = Rmat(i,3); % data ending index
179
180         if PC(i) == 1
181             str_title = ['Contact Variation: Constant Force of ',...
182                 num2str(Data2Plot(Rs,4)),'N'];
183         else
184             str_title = ['Print Variation: Variable Force of ',...
185                 num2str(Data2Plot(Rs,4)),'N'];
186         end
187
188         hold on
189         scatter(i,mean(Data2Plot(Rs:Re,2)),...
```

```
190             [],mean(Data2Plot(Rs:Re,1)),...
191             'filled','MarkerEdgeColor','k','SizeData',100); % force/# , ...
                    width, defect
192         errorbar(i,mean(Data2Plot(Rs:Re,2)),...
193             mean(Data2Plot(Rs:Re,3)),'.k') % force, width, stdev
194         %axis([0.8,7.2,20,35])
195         %colormap(jet)
196         c = colorbar;
197         hLegend = ylabel(c,'Defect Percentage');
198         title(str_title)
199         xlabel('Stamp Sample [#]')
200         ylabel('Mean Line Width [microns]')
201         set(gca,'fontsize',18)
202         grid on
203     end
204
205     sdf(f4,'contact_spread_v1')
206
207 end
208
209 toc
```

THIS PAGE INTENTIONALLY LEFT BLANK

Appendix K

MATLAB Code for Lithography Simulation

This simulation is run first. All simulations in this thesis were run at a spatial step size of 0.25 microns, temporal step size of 0.5 ms, resist thickness of 15 microns, and a U8 of 255. Focus, angular misalignment, and exposure time were varied as needed.

```
1  % Peter Ascoli
2  % Last updated 02/23/2017
3
4  % DESCRIPTION:
5  % Simulations of Feature Geometry in AZ 9260
6  % Set parameters in the 'INPUTS' section
7  % Graphs can easily be regenerated by adjusting input parameters and then
8  % re-running the related plot section
9  % General graph parameters can be adjusted in the appropriate section
10
11 % PREPARE TO RUN
12 clear all; close all; clc;
13
14 %% INPUTS [Only change values in this section. Do not touch other code.]
15
16 % ========================================================================
```

```
17 % Inputs to run the simulation
18 % ===========================================================================
19
20 % PHOTORESIST WIDTH
21 totWidth = 30; % [ţm] width mesh points array
22
23 % PHOTORESIST DEPTH
24 totDepth = 15; % [ţm] depth mesh points
25
26 % EXPOSURE TIMES
27 t100 = 26; % [ms] exposure time for nominal dose at 9.42 rad/s and 80 mW
28 numTimes = 2*t100; % [ms] amount of exposure time analyzed
29
30 % XY MESH SIZE
31 stepSize = 0.25; % [ţm] mesh grid size
32
33 % TIME MESH SIZE
34 timestep = 0.5; % [ms] time step size
35
36 % LASER INTENSITY
37 U8 = 255; % 0 (0%) < U8 < 255 (100%) integer in LABVIEW corresponding ...
       to laser intensity
38
39 % ANGULAR MISALIGNMENT
40 thetad = 10; % [deg] deviation from orthogonality
41
42 % FOCUS
43 focus = -30; %  [ţm] focus depth (0 = top of resist, negative is into ...
       resist, -totDepth = bottom of resist). Measurement along laser axis.
44
45 % ===========================================================================
46 % Inputs to which simulation is run
47 % ===========================================================================
48
49 % SIMULATION 1 - INTENSITY IN THE RESIST
50 sim1 = 0; % Runs intensity simulation if true [1]. Skips if false [0].
```

```
51
52 % SIMULATION 2 - FEATURE GEOMETRY / EXPOSURE
53 sim2 = 1; % Runs exposure simulation if true [1]. Skips if false [0].
54
55 % ============================================================================
56 % Inputs to control output plots
57 % ============================================================================
58
59 % FIGURE 1 - LASER INTENSITY PLOT
60 plot1 = 0; % Generates figure if true [1]. Does nothing if false [0].
61
62 % FIGURE 2 - FEATURE GEOMETRY AT FOUR DIFFERENT EXPOSURE TIMES
63 plot2 = 0; % Generates figure if true [1]. Does nothing if false [0].
64 timesample1 = 0.5*t100; % [ms] sample at this time
65 timesample2 = 0.75*t100; % [ms] sample at this time
66 timesample3 = t100; % [ms] sample at this time
67 timesample4 = 1.5*t100; % [ms] sample at this time
68
69 % FIGURE 3 - FEATURE GEOMETRY ZOOM BOX AT ONE EXPOSURE TIME
70 plot3 = 0; % Generates figure if true [1]. Does nothing if false [0].
71 timesample = timesample4; % [ms] sample at this time
72 xwindow = [6 12]; % [ţm], x boundaries of 'zoom' window
73 ywindow = [10 15]; % [ţm], y boundaries of 'zoom' window
74
75 % ============================================================================
76 % Inputs to save figures
77 % ============================================================================
78
79 savefiles = 0; % saves figures if true [1]. Does nothing if false [0].
80
81 % ============================================================================
82 %% BEGIN SIMULATION CLOCK
83 % ============================================================================
84
85 tic % start simulation timer
86
```

```
87  % ========================================================================
88  %% Absorbtion Coefficients for AZ P9260 Thick Film Resist
89  % ========================================================================
90
91  % PHOTORESIST PROPERTIES
92  A = 0.36; % [ţm^-1] (absorbtion coefficient of unexposed resist - B) ...
        [function of transmittance]
93  B = 0.01; % [ţm^-1] absorbtion coeffcient of exposed resist [function ...
        of transmitance]
94  C = 0.005; % [cm^2/m] coefficient of composition change upon exposure
95
96  % FOR SPR 220 JUST IN CASE:
97  %A = 0.71 ; B = 0.02 ; C = 0.017 ;
98
99  % ========================================================================
100 %% Define Mesh Parameters
101 % ========================================================================
102
103 % SPATIAL AND TEMPORAL DISCRETIZATION
104 stepSize = 1 .* stepSize; % [ţm] mesh grid size
105 timestep = 1 .* timestep; % [ms] time step size
106
107 % SPATIAL AND TEMPORAL BOUNDS
108 totWidth = 1 .* totWidth; % [ţm] width mesh points array
109 totDepth = 1 .* totDepth; % [ţm] depth mesh points
110 numTimes = 1 * numTimes; % [ms] amount of exposure time analyzed
111
112 % GENERATE MESH
113 width = (0:stepSize:totWidth); % mesh width [ţm]
114 depth = (0:stepSize:totDepth); % mesh depth [ţm]
115 times = (0:timestep:numTimes); % define time step [ms]
116
117 % SIZES OF 3D MESH DIMENSIONS FOR SIMULATION
118 dims = [size(width,2) size(depth,2) size(times,2)]; % dimension ...
        collector [width, depth, times]
119
```

```
120 % ========================================================================
121 %% Laser Properties
122 % ========================================================================
123 
124 % LABVIEW CONTROLLED LASER POWER PARAMETER
125 U8 = 1 .* U8; % 0 (0%) < U8 < 255 (100%) integer in lab view ...
        corresponding to laser intensity
126 
127 % LASER INTENSITY, POWER, WAIST, WAVELENGTH
128 I0_max = 103e3; % maximum possible peak laser intensity [W/cm^2]
129 I0 = I0_max * (U8/255); %applied laser intensity [W/cm^2]
130 P = (U8/255) * 80; % [mW] applied laser power
131 omega0 = 5; % beam waist [ţm]
132 l = 0.405; % beam wavelength [ţm]
133 Zr = (pi*omega0^2)/l; % raleigh length [ţm] (w = 2*w0 = 194). in ...
        photography terms, hyperfocal dist = 2*Zr
134 
135 % FOCAL PLANE OF LASER
136 focus = 1 .* focus; % [ţm] focus depth (0 = top of resist, negative is ...
        into resist). Measurement along laser axis.
137 
138 % ANGLE OF INCEDENCE OF LASER WITH RESIST
139 thetad = 1 .* thetad; % [deg] deviation from orthogonality
140 thetar = thetad * pi/180; % [rad] deviation from orthogonality
141 
142 % ========================================================================
143 %% Normalized Laser Beam Intensity at (x,y) as Function of theta & focus
144 % ========================================================================
145 
146 thetar = - thetar; % so that beam angle plots the same in all figures
147 
148 if sim1 == 1
149 
150     % DEFINE INTENSITY FUNCTION
151     I_tilt_func = @(a,b) (omega0/(omega0*sqrt(1+(l*(abs(focus-...
152         (a*sin(thetar)-b*cos(thetar))))/(pi*omega0^2))^2)))^2 *...
```

```
153         (exp((-2*(abs(a*cos(thetar)+b*sin(thetar)))^2)/...
154         (omega0*sqrt(1+(l*(abs(focus-(a*sin(thetar)-b*cos(thetar))))/...
155         (pi*omega0^2))^2))^2));
156     % ^ intensity function (x position, y position) at x=0 r=0. Theta ...
        rotation about origin x=y=0
157
158     % ITERATE AND SOLVE FOR I(X,Y)
159     for i = 1:dims(1) % loop width [-totWidth/2 ţm < x < totWidth/2 ţm]
160         x_func(i) = width(i) - stepSize * ((dims(1)-1)/2); % x grid [ţm]
161         for j = 1:dims(2) % loop depth [ 0 ţm < x < totDepth ţm]
162             y_func(j) = depth(j); % y grid [ţm]
163             I_tilt(i,j) = I_tilt_func(x_func(i),y_func(j)); % calculate ...
                    intensity at location x,y
164         end
165         sim1_percent_complete = i/dims(1)*100 % [%] display progress
166     end
167
168     % FIND LOCATION (X,Y) OF PEAK INTENSITY
169     [maxI_tilt,ind] = max(I_tilt(:)); % find max value and index
170     [xp_ind,yp_ind] = ind2sub(size(I_tilt),ind); % conevert index into  ...
        ij matrix position
171     I_p = I_tilt(xp_ind,yp_ind); % calculate intensity at matrix ...
        position ij
172     %xp = width(xp_ind) - stepSize * ((dims(1)-1)/2); % find x(i) [ţm]
173     %yp = depth(yp_ind); % find y(i) [ţm]
174
175 else
176
177     plot1 = 0; % set to false in case value is true above
178
179 end
180
181 thetar = - thetar; % so that beam angle plots the same in all figures
182
183 clc % clear sim1_percent_complete from command window
184
```

```
185 % ==========================================================================
186 %% Simulation Initial Conditions
187 % ==========================================================================
188 
189 % INITIALIZE MATRICES FOR SIMULATION
190 I = zeros(dims); % 3D of intensities in time
191 intensity = zeros(dims(1:2));% 2D of intensities in time
192 M = ones(dims); % 3D matrix of remaining photoresist (1=100%, 0 = 0% in ...
        element)
193 
194 % ==========================================================================
195 %% Exposure Simulation
196 % ==========================================================================
197 
198 if sim2 == 1
199 
200     % DEFINE INTENSITY FUNCTION
201     I_t = @(a,b,c) I0 * (omega0/(omega0*sqrt(1+(l*(abs(focus-...
202         (a*sin(thetar)-b*cos(thetar))))/(pi*omega0^2))^2)))^2 *...
203         (exp((-2*(abs(a*cos(thetar)+b*sin(thetar)))^2)/...
204         (omega0*sqrt(1+(l*(abs(focus-(a*sin(thetar)-b*cos(thetar))))/...
205         (pi*omega0^2))^2))^2)) * (exp(-(A*c*stepSize+B)*...
206         abs(focus-(a*sin(thetar)-b*cos(thetar)))));
207     %^ intensity function (x position, y position, mDev) at x=0 r=0. ...
            Theta rotation about origin x=y=0
208 
209     % ITERATE AND SOLVE FOR M(X,Y)
210     for i = 1:dims(1) % loop width [-15 ţm < x < 15 ţm]
211         x(i) = width(i) - stepSize * ((dims(1)-1)/2); % x grid [ţm]
212 
213         for t = 1:dims(3) % loop time [ 0 ms < t < 30 ms]
214             time(t) = timestep*times(t); %ms
215 
216             for j = 1:dims(2) % loop depth [ 0 ţm < x < 15 ţm]
217                 y(j) = depth(j); % y grid [ţm]
218 
```

```
219                 if t == 1
220                     mDev(i,j,t) = depth(j);
221                 else
222                     bubble = cumsum(M,2); % every entry plus all depth ...
                            values 'above'
223                     mDev(i,j,t) = bubble(i,j,t-1);
224                 end
225                 I(i,j,t) = I_t(x(i),y(j),mDev(i,j,t)); % calculate ...
                        intensity
226                 M(i,j,t)= exp(-I(i,j,t)*C); % calculate point concentration
227             end
228         end
229         sim2_percent_complete = i/dims(1)*100 % [%] display progress
230     end
231 
232 else
233 
234     plot2 = 0; plot3 = 0; % set to false in case values are true above
235 
236 end
237 
238 clc % clear sim2_percent_complete from command window
239 
240 % ========================================================================
241 %% END SIMULATION CLOCK
242 % ========================================================================
243 
244 toc % stop simulation timer
245 
246 % ========================================================================
247 %% Plot Laser Intensity Results
248 % ========================================================================
249 
250 if plot1 == 1
251 
252     f1 = figure
```

```
253     contourf(x_func,y_func,rot90(I_tilt(:,:)))
254     caxis([0, 1])
255     colorbar('location','eastoutside')
256     title(['Laser Beam Intensity: U8 = ',num2str(U8),...
257         ' [0:1:255 of 80mW] (Power=',num2str(P),'[mW]) ; Theta = ',...
258         num2str(thetad),' [deg] ; Focus = ',num2str(focus),...
259         ' [ţm] ; XY Step = ',num2str(stepSize),...
260         ' [ţm] ; Simulation Time = ',num2str(toc),' [s]'])
261     xlabel('width [ţm]')
262     ylabel('depth [ţm]')
263     %pbaspect([size(x_func,2) size(y_func,2) 1])
264     grid on
265     set(gca,'xtick',[x_func(1):1:x_func(end)])
266     set(gca,'ytick',[y_func(1):1:y_func(end)])
267     hold on
268     %plot(xp, yp ,'.r', 'markersize', 30);
269     plot(x_func(xp_ind), totDepth-y_func(yp_ind) ,'.r', 'markersize', 30);
270     hold off
271     legend('Int.',['Peak Int. = ',num2str(I_p),''],'location','northeast')
272 
273     disp(['Figure 1 Generated'])
274 
275 else
276 
277     disp(['Figure 1 Not Generated'])
278 
279 end
280 
281 % ============================================================================
282 %% Plot Simulation [Feature Geometry] Results
283 % ============================================================================
284 
285 if plot2 == 1
286 
287     f2 = figure
288 
```

```
289    subplot(2,2,1);
290    timesample1 = 1 .* timesample1; % [ms] sample at this time
291    ts = timesample1/timestep; % time vector index according to step size
292    contourf(x,y,rot90(rot90(M(:,:,ts)')));
293    caxis([0, 1])
294    pbaspect([dims(1) dims(2) 1])
295    title(['Remaining PAC (time[ms]*dose = ',num2str(timesample1),'*I_0)'])
296    xlabel('width [ţm]')
297    ylabel('depth [ţm]')
298    colorbar('location','eastoutside')
299    grid on
300    set(gca,'xtick',[x(1):1:x(end)])
301    set(gca,'ytick',[y(1):1:y(end)])
302
303    subplot(2,2,2);
304    timesample2 = 1 .* timesample2; % [ms] sample at this time
305    ts = timesample2/timestep; % time vector index according to step size
306    contourf(x,y,rot90(rot90(M(:,:,ts)')));
307    caxis([0, 1])
308    pbaspect([dims(1) dims(2) 1])
309    title(['Remaining PAC (time[ms]*dose = ',num2str(timesample2),'*I_0)'])
310    xlabel('width [ţm]')
311    ylabel('depth [ţm]')
312    colorbar('location','eastoutside')
313    grid on
314    set(gca,'xtick',[x(1):1:x(end)])
315    set(gca,'ytick',[y(1):1:y(end)])
316
317    subplot(2,2,3);
318    timesample3 = 1 .* timesample3; % [ms] sample at this time
319    ts = timesample3/timestep; % time vector index according to step size
320    contourf(x,y,rot90(rot90(M(:,:,ts)')));
321    caxis([0, 1])
322    pbaspect([dims(1) dims(2) 1])
323    title(['Remaining PAC (time[ms]*dose = ',num2str(timesample3),'*I_0)'])
324    xlabel('width [ţm]')
```

```
325     ylabel('depth [ţm]')
326     colorbar('location','eastoutside')
327     grid on
328     set(gca,'xtick',[x(1):1:x(end)])
329     set(gca,'ytick',[y(1):1:y(end)])
330
331     subplot(2,2,4);
332     timesample4 = 1 .* timesample4; % [ms] sample at this time
333     ts = timesample4/timestep; % time vector index according to step size
334     contourf(x,y,rot90(rot90(M(:,:,ts)')));
335     caxis([0, 1])
336     pbaspect([dims(1) dims(2) 1])
337     title(['Remaining PAC (time[ms]*dose = ',num2str(timesample4),'*I_0)'])
338     xlabel('width [ţm]')
339     ylabel('depth [ţm]')
340     colorbar('location','eastoutside')
341     grid on
342     set(gca,'xtick',[x(1):1:x(end)])
343     set(gca,'ytick',[y(1):1:y(end)])
344
345     % set master title - input xy step size, and time step size and ...
            degree of beam
346     test = num2str(thetad);
347     test2 = num2str(stepSize);
348     test3 = num2str(timestep);
349     mtit(['AZ 9260 PHOTORESIST: U8 = ',num2str(U8),...
350         ' [0:1:255 of 80mW] (Power=',num2str(P),'[mW]) ; Theta = ',...
351         num2str(thetad),' [deg] ; Focus = ',num2str(focus),...
352         ' [ţm] ; XY Step = ',num2str(stepSize),' [ţm] ; Time Step = ',...
353         num2str(timestep),' [ms] ; Simulation Time = ',...
354         num2str(toc),' [s]'])
355
356     disp(['Figure 2 Generated'])
357
358 else
359
```

```
360     disp(['Figure 2 Not Generated'])
361
362 end
363
364 % ============================================================================
365 %% Plot Window of Interest
366 % ============================================================================
367
368 if plot3 == 1
369
370     f3 = figure
371     timesample = 1 .* timesample; % [ms] sample at this time
372     ts = timesample4/timestep; % time vector index according to step size
373     contourf(x,y,rot90(rot90(M(:,:,ts)')));
374     axis([ xwindow(1), xwindow(2), ywindow(1), ywindow(2)])
375     caxis([0, 1])
376     pbaspect([(abs(xwindow(2)-xwindow(1))) (abs(ywindow(2)-ywindow(1))) 1])
377     title({['Remaining PAC (time[ms]*dose = ',...
378         num2str(timesample),'*I_0)'];['AZ 9260 CORNER UNDERCUT: U8 = ',...
379         num2str(U8),' [0:1:255 of 80mW] (Power=',num2str(P),...
380         '[mW]) ; Theta = ',num2str(thetad),' [deg] ; Focus = ',...
381         num2str(focus),' [ţm] ; XY Step = ',num2str(stepSize),...
382         ' [ţm] ; Time Step = ',num2str(timestep),...
383         ' [ms] ; Simulation Time = ',num2str(toc),' [s]']})
384     xlabel('width [ţm]')
385     ylabel('depth [ţm]')
386     colorbar('location','eastoutside')
387     grid on
388     set(gca,'xtick',[x(1):1:x(end)])
389     set(gca,'ytick',[y(1):1:y(end)])
390
391     disp(['Figure 3 Generated'])
392
393 else
394
395     disp(['Figure 3 Not Generated'])
```

```
396
397 end
398
399 % ===========================================================================
400 %% Display Simulation Outcomes
401 % ===========================================================================
402
403 if sim1 == 1
404     disp(['Sim1 Completed'])
405 else
406     disp(['Sim1 Skipped'])
407 end
408
409 if sim2 == 1
410     disp(['Sim2 Completed'])
411 else
412     disp(['Sim2 Skipped'])
413 end
414
415 %% Save Figures
416
417 if savefiles == 1;
418
419     % EXPORT FIGURE 1
420     if plot1 == 1 % export only if figure was created
421         savefig(f1,'test1')
422     end
423
424     % EXPORT FIGURE 2
425     if plot2 == 1 % export only if figure was created
426         savefig(f2,'test2')
427     end
428
429     % EXPORT FIGURE 3
430     if plot3 == 1 % export only if figure was created
431         savefig(f3,'test3')
```

```
432     end
433
434     disp(['Figures Saved'])
435
436 else
437
438     disp(['Figures Not Saved'])
439
440 end
441
442 % ========================================================================
443 %% Export Data
444 % ========================================================================
445
446 save(['x_focus_',num2str(focus),'.mat'],'x');
447 save(['y_focus_',num2str(focus),'.mat'],'y');
448 save(['t_focus_',num2str(focus),'.mat'],'times');
449 save(['M_focus_',num2str(focus),'.mat'],'M');
450
451 % if tilted, theta =/= 0
452 %save(['x_focus_',num2str(focus),'_tilt_',num2str(thetad),'.mat'],'x');
453 %save(['y_focus_',num2str(focus),'_tilt_',num2str(thetad),'.mat'],'y');
454 %save(['t_focus_',num2str(focus),'_tilt_',num2str(thetad),'.mat'],'times');
455 %save(['M_focus_',num2str(focus),'_tilt_',num2str(thetad),'.mat'],'M');
456
457
458 disp(['Matrices Saved'])
```

Appendix L

MATLAB Code for Creating Stamp Feature Shape

This script is run second, reads in the matrices exported in the first simulation, and plots the tool feature shape. One can select the exposure time, overlap amount (if a double exposure is of interest), and photoactive compound (PAC) concentration threshold.

```
% Peter Ascoli
% Lithography Simulation Plots
% Created 02/20/2017
% Last Updated 02/23/2017
clear all; close all; clc;

tic

% ========================================================================
%% Process Window Parameters
% ========================================================================

resist = [15 10 5]; % [um] resist thickness !
beamfocus = -50:5:50; % [um] focus position !
exposure = ceil([0.25 0.5 0.75 1 1.25 1.5 1.75 2] .* 26); % [ms] exp time
dblexp = 0;%0:1:20; % [um] offset between overlapping exposures
```

```
17
18 plotfigures = 1; % 1 if yes, else no
19 override = 1; % override looping if true for specific desired figure
20
21 if override == 1
22     plotfigures = 1;
23     resist = 15; % [um] resist thickness !
24     beamfocus = -30; % [um] focus position !
25     exposure = 26; % [ms] exposure time
26     dblexp = 6; % [um] offset between overlapping exposures
27 end
28
29 % ============================================================================
30 %% Import Data
31 % ============================================================================
32
33 for i = 1:length(beamfocus)
34     for j = 1:length(resist)
35         for k = 1:length(exposure)
36             for l = 1:length(dblexp)
37
38                 str = ['_focus_',num2str(beamfocus(i))];
39                 x = cell2mat(struct2cell(load(['x',str])));
40                 y = cell2mat(struct2cell(load(['y',str])));
41                 t = cell2mat(struct2cell(load(['t',str])));
42                 M = cell2mat(struct2cell(load(['M',str])));
43
44                 % override for tilted feature
45 %                 x = cell2mat(struct2cell(load(['x',str,'_tilt_10'])));
46 %                 y = cell2mat(struct2cell(load(['y',str,'_tilt_10'])));
47 %                 t = cell2mat(struct2cell(load(['t',str,'_tilt_10'])));
48 %                 M = cell2mat(struct2cell(load(['M',str,'_tilt_10'])));
49
50                 % ==========================================================
51                 %% Specify Plotting Parameters
52                 % ==========================================================
```

```
53
54                      time = exposure(k); % [ms] exposure time to plot
55                      thresh = 0.01; % [%/100]  PAC ≤ thresh is assumed removed
56                      height = resist(j); % [um] feature height
57                      offset = dblexp(l); % [um] offset of overlapping exposures
58
59                      % =========================================================
60                      %% Find Index of t Closest to Desired Value
61                      % =========================================================
62
63                      % bound input value
64                      if time < t(1)
65                          time = t(1); % set time to t(1) if value too small
66                          disp(['MESSAGE: Requested Time Too Short'])
67                      end
68                      if time > t(end);
69                          time = t(end); % set time to t(end) if value too large
70                          disp(['MESSAGE: Requested Time Too Long'])
71                      end
72
73                      % index for values equal to, less than, and greater than
74                      a = find(t==time);
75                      b = find(t>time);
76                      c = find(t<time);
77
78                      % select index of t closest to desired time
79                      if size(a) == [1 1]
80                          t_plot = t(a); % [ms] time to plot is index a of ...
                                vec t
81                          disp(['MESSAGE: "Time" Not Rounded'])
82                      else
83                          t_upper = t(min(b)); % value to round up to
84                          t_lower = t(max(c)); % value to round down to
85                          dist_upper = sqrt(abs(t_upper-time)); % difference
86                          %with upper value
87                          dist_lower = sqrt(abs(t_lower-time)); % difference
```

```
88                  %with lower value
89                  if dist_upper < dist_lower
90                      t_plot = t_upper; % [ms] time to plot is ...
                            t_upper if
91                      %it is closer to "time"
92                      disp(['MESSAGE: "Time" Rounded Up'])
93                  else
94                      t_plot = t_lower; % [ms] time to plot is t_lower
95                      %if it is closer to "time"
96                      disp(['MESSAGE: "Time" Rounded Down'])
97                  end
98              end
99
100             % =========================================================
101             %% Manipulate Matrices for Plotting
102             % =========================================================
103
104             % isolate M 2D matrix of interest
105             M_time = rot90(rot90(M(:,:,t_plot)')); % M to plot (2D ...
                    matrix)
106
107             % construct overlapping exposure if requested
108             if offset > 0
109                 stepsize = x(end) - x(end-1); % step size of x mesh
110                 offset_elem = offset ./ stepsize; % [#indices] that ...
                        represent offset
111                 x_over = -0.5*(abs(max(x)-min(x))+offset):stepsize:...
112                     0.5*(abs(max(x)-min(x))+offset); % [um] new x
113                 x_over_elem = length(x) + offset_elem; % [#indices] ...
                        for total overlap
114                 M_time_left = ...
115                     [M_time ones(size(M_time,1),offset_elem)]; % ...
                            left exposure
116                 M_time_right = ...
117                     [ones(size(M_time,1),offset_elem) M_time]; % ...
                            right exposure
```

```
118             M_time_over = M_time_left .* M_time_right ...
119                 .* M_time_left;
120             M_time = M_time_over; x = x_over;
121             disp(['MESSAGE: Constructed Overlapping Exposure'])
122         end
123 
124         % binarize for easier feature shape
125         d = find(M_time < thresh); % indices less than thresh
126         e = find(M_time ≥ thresh); % indices ≥ than thresh
127         M_bin = M_time; % rename for binary image
128         M_bin(d) = 0; % set binary value
129         M_bin(e) = 1; % set binary value
130 
131         % clip y and M for feature height
132         if height > max(y);
133             height = max(y);
134             disp(['MESSAGE: Thickness Rounded to Max Y Value'])
135         end
136         f = find(y<(max(y)-height));
137         y(f) = [];
138         y = y - min(y);
139         M_time(f,:) = [];
140         M_bin(f,:) = [];
141 
142         % ============================================================
143         %% Plot Feature(s)
144         % ============================================================
145 
146         if plotfigures == 1
147 
148             figPAC = figure; % plot full spectrum PAC
149             [c,h] = contourf(x,y,M_time);
150             %set(h,'EdgeColor','none');
151             colormap(parula(1000));
152             caxis([0 1])
153             %c = colorbar;
```

```
154             %hlegend = ylabel(c,'Concentration [%/100]');
155             pbaspect([abs(max(x)-min(x)) abs(max(y)-min(y)) 1])
156             %title(['Remaining PAC (time[ms]*dose = ...
                    ',num2str(t_plot),'*I_0)'])
157             title(['PAC Concentration After ',num2str(t_plot),...
158                 ' ms Exposure'])
159             xlabel('width [ţm]')
160             ylabel('depth [ţm]')
161             colorbar('location','eastoutside')
162             grid on
163             set(gca,'xtick',[x(1):3:x(end)],'XTickLabel',...
164                 x(1):3:x(end))
165             set(gca,'ytick',[y(1):3:y(end)])
166
167             figBIN = figure; % plot binary feature geometry ...
                    based on thresh
168             [c,h] = contourf(x,y,M_bin,'-w','LineWidth',1e-10);
169             set(h,'EdgeColor','none');
170             colormap(gray(2));
171             caxis([0 1])
172             pbaspect([abs(max(x)-min(x)) abs(max(y)-min(y)) 1])
173             title(['Stamp Feature Cross Section After ',...
174                 num2str(t_plot),' ms Exposure'])
175             xlabel('width [ţm]')
176             ylabel('depth [ţm]')
177             %colorbar('location','eastoutside')
178             grid on
179             set(gca,'xtick',[x(1):3:x(end)],'XTickLabel',...
180                 x(1):3:x(end))
181             set(gca,'ytick',[y(1):3:y(end)])
182
183         end
184
185         % ==========================================================
186         %% Group Data and Export (comment / uncomment as needed)
187         % ==========================================================
```

```
188
189                 focus = beamfocus(i);
190                 data = {M_bin,x,y,time,focus,offset,height};
191                 save(['M-t',num2str(time),'-f',num2str(focus),...
192                     '-o',num2str(offset),'-h',num2str(height),'.mat'],...
193                     'data');
194                 disp(['MESSAGE: Data Saved and Exported'])
195
196                 disp(['M-t',num2str(time),'-f',num2str(focus),'-o',...
197                     num2str(offset),'-h',num2str(height),' COMPLETED'])
198
199             end
200         end
201     end
202 end
203
204 toc
205
206 %% Export Figures
207
208 sdf(figPAC, 'simulation_single_v1')
209 sdf(figBIN, 'simulation_single_v1')
```

THIS PAGE INTENTIONALLY LEFT BLANK

Appendix M

MATLAB Code for Single Exposure Simulation Trends

This script is run third. It loads in all focus and exposure time scenarios and creates single feature trend plots at the resist thickness specified. Feature root width, contact width, and height as a function of exposure time and focus are the resulting plots.

```
% Peter Ascoli
% Lithography Process Window Analysis for Single and Overlapping Features
% Created 02/23/2017
% Last Updated 02/24/2017

clear all; close all; clc;
% ========================================================================
%% Analysis Settings
% ========================================================================

% single features
s_analysis = 1; % 1 to analyze, else 0
s_plots = 1; % 1 to plot, else 0

% % overlapping features
% o_analysis = 0; % 1 to analyze, else 0
```

```
17 % o_plots = 0; % 1 to analyze, else 0
18
19 % ==========================================================================
20 %% Import Data for Single Features
21 % ==========================================================================
22
23 if s_analysis == 1
24
25     % import in form
26     % data = {M,x,y,t,f,o,d} M matrix, x vector, y vector, time, focus, ...
           offset
27     % note that M is binarized M
28
29     focus = -50:5:50; % [um] focus
30     time = ceil(26 .* [0.25 0.5 0.75 1 1.25 1.5 1.75 2 ] ); % [ms] exp time
31     height = [15 10 5]; % [um[ resist thickness
32     height = height(3); % CHANGE THIS VALUE FOR DIFFERENT RESIST THICKNESS
33
34     for i = 1:length(time)
35         for j = 1:length(focus)
36
37             data = struct2cell(load(['M-t',num2str(time(i)),'-f',...
38                 num2str(focus(j)),'-o0-h',num2str(height)]));...
39                 data = data{1};
40
41             % extract matrices from imported data
42             M = cell2mat(data(1));
43             x = cell2mat(data(2));
44             y = cell2mat(data(3));
45             t = cell2mat(data(4));
46             f = cell2mat(data(5));
47             o = cell2mat(data(6));
48             d = cell2mat(data(7));
49
50             % step size for analysis
51             stepsize = abs(x(end))-abs(x(end-1));
```

```
52
53
54             % ==============================================================
55             %% Analyze Single Feature Data
56             % ==============================================================
57
58             if o == 0
59
60                 % ROOT WIDTH
61                 RW(i,j) = 0;
62                 indRW = find(M(end,:)==0);
63                 RW(i,j) = x(max(indRW)) - x(min(indRW)); % [um] feature ...
                       root width
64
65                 % HEIGHT
66                 H(i,j) = 0;
67                 x0 = find(x==0);
68                 indH = find(M(:,x0)==0);
69                 H(i,j) = d-(y(min(indH))); % [um] feature height
70
71                 % CONTACT WIDTH
72                 CW(i,j) = 0;
73                 indCW = find(M(1,:)==0);
74                 wtf(i,j) = 0;
75                 if H(i,j) ≥ d
76                     CW(i,j) = x(max(indCW)) - x(min(indCW)); % [um] ...
                           feature contact width
77                     wtf(i,j) = 1;
78                 end
79
80                 dataplot(j+(i-1)*length(focus),:) = [f RW(i,j) H(i,j)...
81                     CW(i,j)];
82
83             end % for i (time)
84         end % for j (focus)
85     end % for overlap = 0
```

```
86  end % for single analysis
87
88  % ==========================================================================
89  %% Single Feature Plots
90  % ==========================================================================
91
92  % set line styles
93  co = [0 0.4470 0.7410; 0.8500 0.3250 0.0980; 0.9290 0.6940 0.1250;...
94      0.4940 0.1840 0.5560;
95      0.4660 0.6740 0.1880; 0.3010 0.7450 0.9330; 0.6350 0.0780 0.1840;...
96      0 0 0];
97  set(groot,'defaultAxesColorOrder',co);
98  style = {'o-','>--','d-.','+:','o-','>--','d-.','+:'};
99
100 % RW as a function of focus for 8 doses
101 figRW = figure;
102 hold on
103 for i = 1:length(time)
104     toplot = dataplot((1+(i-1)*length(focus)):...
105         (length(focus)+(i-1)*length(focus)),[1 2]);
106     plot(toplot(:,1),toplot(:,2),style{i})
107 end
108 hold off
109 xlabel('Focus Position [microns]')
110 ylabel('Root Width [microns]')
111 title(['Feature Root Width for ',num2str(d),' micron Resist Thickness'])
112 lgd = legend('7','13','20','26','33','39','46','52','Location',...
113     'southoutside','Orientation','horizontal');
114 title(lgd,'Exposure Time [ms]')
115 grid on
116 ymin = 14; ymax = 15.5; yinc = 0.25; % [um] y axis limits and steps
117 xmin = -50; xmax = 50; xinc = 5; % [um] x axis limits and steps
118 axis([xmin xmax ymin ymax])
119 set(gca,'YTick',ymin:yinc:ymax,'YTickLabel',ymin:yinc:ymax)
120 set(gca,'XTick',xmin:xinc:xmax,'XTickLabel',xmin:xinc:xmax)
121
```

```
122 % CW as a functtion of focus for 8 doses
123 figCW = figure;
124 hold on
125 for i = 1:length(time)
126     toplot = dataplot((1+(i-1)*length(focus)):...
127         (length(focus)+(i-1)*length(focus)),[1 4]);
128     plot(toplot(:,1),toplot(:,2),style{i})
129 end
130 hold off
131 xlabel('Focus Position [microns]')
132 ylabel('Contact Width [microns]')
133 title(['Feature Contact Width for ',num2str(d),' micron Resist Thickness'])
134 lgd = legend('7','13','20','26','33','39','46','52','Location',...
135     'southoutside','Orientation','horizontal');
136 title(lgd,'Exposure Time [ms]')
137 grid on
138 ymin = 0; ymax = 16; yinc = 2; % [um] y axis limits and steps
139 xmin = -50; xmax = 50; xinc = 5; % [um] x axis limits and steps
140 axis([xmin xmax ymin ymax])
141 set(gca,'YTick',ymin:yinc:ymax,'YTickLabel',ymin:yinc:ymax)
142 set(gca,'XTick',xmin:xinc:xmax,'XTickLabel',xmin:xinc:xmax)
143
144 % H as a function of focus for 8 doses
145 figH = figure;
146 hold on
147 for i = 1:length(time)
148     toplot = dataplot((1+(i-1)*length(focus)):...
149         (length(focus)+(i-1)*length(focus)),[1 3]);
150     plot(toplot(:,1),toplot(:,2),style{i})
151 end
152 hold off
153 xlabel('Focus Position [microns]')
154 ylabel('Height [microns]')
155 title(['Feature Height for ',num2str(d),' micron Resist Thickness'])
156 lgd = legend('7','13','20','26','33','39','46','52','Location',...
157     'southoutside','Orientation','horizontal');
```

```
158 title(lgd,'Exposure Time [ms]')
159 grid on
160 ymin = 0; ymax = d+1; yinc = d/10; % [um] y axis limits and steps
161 xmin = -50; xmax = 50; xinc = 5; % [um] x axis limits and steps
162 axis([xmin xmax ymin ymax])
163 set(gca,'YTick',ymin:yinc:ymax,'YTickLabel',ymin:yinc:ymax)
164 set(gca,'XTick',xmin:xinc:xmax,'XTickLabel',xmin:xinc:xmax)
165
166 %% Export Figures
167
168 sdf(figRW, 'feature_trends_v2')
169 sdf(figCW, 'feature_trends_v2')
170 sdf(figH, 'feature_trends_v2')
```

Appendix N

MATLAB Code for Overlapping Exposure Lithography Simulation

This script is run fourth (last). It loads in all focus and exposure time scenarios and creates overlapping feature trend plots at the resist thickness specified. Feature root width, contact width, and height as a function of exposure time, focus, and overlap amount are the resulting plots.

```
1  % Peter Ascoli
2  % Lithography Process Window Analysis for Single and Overlapping Features
3  % Created 02/23/2017
4  % Last Updated 02/27/2017
5
6  clear all; close all; clc;
7  tic
8  % ============================================================================
9  %% Analysis Settings
10 % ============================================================================
11
12 % single features
13 % s_analysis = 0; % 1 to analyze, else 0
14 % s_plots = 0; % 1 to plot, else 0
15
```

```
16 % overlapping features
17 o_analysis = 1; % 1 to analyze, else 0
18 o_plots = 1; % 1 to plot, else 0
19
20 % ===========================================================================
21 %% Import Data for Single Features
22 % ===========================================================================
23
24 if o_analysis == 1
25
26     % import in form
27     % data = {M,x,y,t,f,o,d} M matrix, x vector, y vector, time, focus, ...
           offset
28     % note that M is binarized M
29
30     focus = -50:5:50; % [um] focus
31     time = ceil(26 .* [0.25 0.5 0.75 1 1.25 1.5 1.75 2 ] ); % [ms] exp time
32     height = [15 10 5]; % [um[ resist thickness
33     height = height(3); % CHANGE THIS VALUE FOR DIFFERENT RESIST THICKNESS
34     overlap = 1:1:20; % [um] overlap vector error kicks in at 16 - no ...
           singleton RHS for H
35
36     for i = 1:length(time)
37         for j = 1:length(focus)
38             for k = 1:length(overlap)
39                 data = struct2cell(load(['M-t',num2str(time(i)),'-f',...
40                     num2str(focus(j)),'-o',num2str(overlap(k)),'-h',...
41                     num2str(height)])); data = data{1};
42
43                 % extract matrices from imported data
44                 M = cell2mat(data(1));
45                 x = cell2mat(data(2));
46                 y = cell2mat(data(3));
47                 t = cell2mat(data(4));
48                 f = cell2mat(data(5));
49                 o = cell2mat(data(6));
```

```
50              d = cell2mat(data(7));
51
52              % step size for analysis
53              stepsize = abs(x(end))-abs(x(end-1));
54
55
56              % ==========================================================
57              %% Analyze Single Feature Data
58              % ==========================================================
59
60              if o > 0
61
62                  % ROOT WIDTH
63                  RW(i,j,k) = 0;
64                  indRW = find(M(end,:)==0);
65                  RW(i,j,k) = x(max(indRW)) - x(min(indRW)); % [um] ...
                        feature root width
66
67                  % HEIGHT
68                  H(i,j,k) = 0;
69                  x0 = find(x==0-o./2);
70                  indH = find(M(:,x0)==0);
71                  H(i,j,k) = d-(y(min(indH))); % [um] feature height
72
73                  % CONTACT WIDTH
74                  CW(i,j,k) = 0;
75                  indCW = find(M(1,:)==0);
76                  wtf(i,j,k) = 0;
77                  if H(i,j,k) ≥ d
78                      CW(i,j,k) = x(max(indCW)) - x(min(indCW)); % ...
                            [um] feature contact width
79                      wtf(i,j,k) = 1;
80                  end
81
82                  xyz(i,j,k) = {[time(i) focus(j) overlap(k)]'};
83                  %dataplot(j+(i-1)*length(focus),:) = [f RW(i,j,k) ...
```

```
                       H(i,j,k) CW(i,j,k)];
84
85                 end % for i (time)
86             end % for j (focus)
87         end % for k (overlap)
88     end % for overlap = 0
89 end % for single analysis
90
91 % reshape matrices for plotting
92 xyz_reshape = cell2mat(reshape(xyz,[1 length(time)*length(focus)*...
93     length(overlap)]));
94 RW_reshape = reshape(RW,[1 length(time)*length(focus)*length(overlap)]);
95 CW_reshape = reshape(CW,[1 length(time)*length(focus)*length(overlap)]);
96 H_reshape = reshape(H,[1 length(time)*length(focus)*length(overlap)]);
97
98 toc
99 % ==========================================================================
100 %% Overlap Feature Plots
101 % ==========================================================================
102
103 if o_plots > 0
104
105     % RW as a function of focus for 8 doses
106     figRW = figure;
107     scatter3(xyz_reshape(1,:),xyz_reshape(2,:),xyz_reshape(3,:),10,...
108         RW_reshape,'filled')
109     colorbar
110     colormap(jet)
111     c = colorbar;
112     hlegend = ylabel(c,'Root Width [microns]');
113     xlabel('Individual Exposure Time [ms]')
114     ylabel('Focus Position [microns]')
115     zlabel('Axial Offset of Exposures [microns]')
116     title(['Feature Root Width for ',num2str(d),...
117         ' micron Resist Thickness'])
118     grid on
```

```
119     zmin = 0; zmax = 20; zinc = 2; % [um] z axis limits and steps, overlap
120     ymin = -50; ymax = 50; yinc = 10; % [um] y axis limits and steps, focus
121     xmmi = time; % [ms] x axis limits and steps, time
122     axis([min(xmmi) max(xmmi) ymin ymax zmin zmax])
123     set(gca,'ZTick',zmin:zinc:zmax,'ZTickLabel',zmin:zinc:zmax)
124     set(gca,'YTick',ymin:yinc:ymax,'YTickLabel',ymin:yinc:ymax)
125     set(gca,'XTick',xmmi,'XTickLabel',xmmi)
126     view(-38,45)
127
128     % CW as a functtion of focus for 8 doses
129     figCW = figure;
130     scatter3(xyz_reshape(1,:),xyz_reshape(2,:),xyz_reshape(3,:),10,...
131         CW_reshape,'filled')
132     colorbar
133     colormap(jet)
134     c = colorbar;
135     hlegend = ylabel(c,'Contact Width [microns]');
136     xlabel('Individual Exposure Time [ms]')
137     ylabel('Focus Position [microns]')
138     zlabel('Axial Offset of Exposures [microns]')
139     title(['Feature Contact Width for ',num2str(d),...
140         ' micron Resist Thickness'])
141     grid on
142     zmin = 0; zmax = 20; zinc = 2; % [um] z axis limits and steps, overlap
143     ymin = -50; ymax = 50; yinc = 10; % [um] y axis limits and steps, focus
144     xmmi = time; % [ms] x axis limits and steps, time
145     axis([min(xmmi) max(xmmi) ymin ymax zmin zmax])
146     set(gca,'ZTick',zmin:zinc:zmax,'ZTickLabel',zmin:zinc:zmax)
147     set(gca,'YTick',ymin:yinc:ymax,'YTickLabel',ymin:yinc:ymax)
148     set(gca,'XTick',xmmi,'XTickLabel',xmmi)
149     view(-38,45)
150
151     % H as a function of focus for 8 doses
152     figH = figure;
153     scatter3(xyz_reshape(1,:),xyz_reshape(2,:),xyz_reshape(3,:),10,...
154         H_reshape,'filled')
```

```
155     colorbar('Ticks',0:d/10:d,'TickLabels',0:d/10:d)
156     colormap(jet)
157     c = colorbar;
158     %colobar('Ticks',0:d/10:d,'TickLabels',0:d/10:d)
159     hlegend = ylabel(c,'Height [microns]');
160     xlabel('Individual Exposure Time [ms]')
161     ylabel('Focus Position [microns]')
162     zlabel('Axial Offset of Exposures [microns]')
163     title(['Feature Height for ',num2str(d),' micron Resist Thickness'])
164     grid on
165     zmin = 0; zmax = 20; zinc = 2; % [um] z axis limits and steps, overlap
166     ymin = -50; ymax = 50; yinc = 10; % [um] y axis limits and steps, focus
167     xmmi = time; % [ms] x axis limits and steps, time
168     axis([min(xmmi) max(xmmi) ymin ymax zmin zmax])
169     set(gca,'ZTick',zmin:zinc:zmax,'ZTickLabel',zmin:zinc:zmax)
170     set(gca,'YTick',ymin:yinc:ymax,'YTickLabel',ymin:yinc:ymax)
171     set(gca,'XTick',xmmi,'XTickLabel',xmmi)
172     view(-38,45)
173
174 end
175
176 %% export figures
177
178 sdf(figRW,'overlap_trends_v1')
179 sdf(figCW,'overlap_trends_v1')
180 sdf(figH,'overlap_trends_v1')
```

Bibliography

[1] Younan Xia and George M. Whitesides. Soft lithography. pages 28(12):153–184. Annual Review in Material Sciecne, 1998.

[2] Daniel B. Wolfe, J. Christopher Love, and George M. Whitesides. *Nanostructures Replicated by Polymer Molding.* CRC Press, Florida, March 2004.

[3] Arjan P. Quist, Elisabeth Pavlovic, and Sven Oscarsson. Recent advances in microcontact printing. *Analytical and Bioanalytical Chemistry*, 381(3):591–600, 2005.

[4] J. Christopher Love, Lara A. Estroff, Jennah K. Kriebel, Ralph G. Nuzzo, and George M. Whitesides. Self-assembled monolayers of thiolates on metals as a form of nanotechnology. *Chemical Reviews*, 105(4):1103–1170, 2005. PMID: 15826011.

[5] Adam Stagnaro. Design and development of a roll-to-roll machine for continuous high-speed microcontact printing. Master's thesis, Massachusetts Insitute of Technology, 2008.

[6] Christopher A. Merian. Development of an inking system for continuous roll-to-roll microcontact printing of hexadecanethiol (hdt) on gold-cated pet substrate. Master's thesis, Massachusetts Insitute of Technology, 2016.

[7] S. Khan, L. Lorenzelli, and R. S. Dahiya. Technologies for printing sensors and electronics over large flexible substrates: A review. *IEEE Sensors Journal*, 15(6):3164–3185, June 2015.

[8] Arash Sayyah, Mark N. Horenstein, and Malay K. Mazumder. Energy yield loss caused by dust deposition on photovoltaic panels. *Solar Energy*, 107:576 – 604, 2014.

[9] M. Mazumder, M. N. Horenstein, J. W. Stark, P. Girouard, R. Sumner, B. Henderson, O. Sadder, I. Hidetaka, A. S. Biris, and R. Sharma. Characterization of electrodynamic screen performance for dust removal from solar panels and solar hydrogen generators. *IEEE Transactions on Industry Applications*, 49(4):1793–1800, July 2013.

[10] Joseaph Edward Petrzelka. *Contact region fidelity, sensitivity, and control in roll-based soft lithography.* PhD thesis, Massachusetts Insitute of Technology, 2012.

[11] Larissa F. Nietner. A direct-write thick-film lithography process for multi-parameter control of tooling in continuous roll-to-roll microcontact printing. Master's thesis, Massachusetts Insitute of Technology, 2014.

[12] Adam M. Libert. Precision control of cylindrical stamp contact in a continuous roll-to-roll microcontact printing machine. Master's thesis, Massachusetts Insitute of Technology, 2014.

[13] Scott T. Nill. Integrated hardware, software, and sensor design for control of scalable, continuous roll-to-roll microcontact printing process. Master's thesis, Massachusetts Insitute of Technology, 2014.

[14] Maia R. Bageant and David E. Hardt. The force control problem in precision microcontact printing. Cambridge, MA, 2016. ASPE.

[15] Chris Merian, Xian Du, David Hardt, and Hussain AlQahtani. Roll-to-roll microcontact printing of flexible aluminum substrates using octadecylphosphonic acid (odpa). International Mechanical Engineering Congress and Exposition, Houston, TX, 2015. ASME.

[16] Larissa F. Neitner and David E. Hardt. Direct-write photolithography for cylindrical tooling fabrication in roll-to-roll microcontact printing. *ASME Journal of Micro and Nano-Manufacturing*, 2015.

[17] H. A. Biebuyck, N. B. Larsen, E. Delamarche, and B. Michel. Lithography beyond light: Microcontact printing with monolayer resists. *IBM Journal of Research and Development*, 41(1.2):159–170, Jan 1997.

[18] Jo A. Helmuth, Heinz Schmid, Richard Stutz, Andreas Stemmer, and Heiko Wolf. High-speed microcontact printing. *Journal of the American Chemical Society*, 128(29):9296–9297, 2006. PMID: 16848441.

[19] Tobias E. Balmer, Heinz Schmid, Richard Stutz, Emmanuel Delamarche, Bruno Michel, Nicholas D. Spencer, and Heiko Wolf. Diffusion of alkanethiols in pdms and its implications on microcontact printing (Îijcp). *Langmuir*, 21(2):622–632, 2005. PMID: 15641832.

[20] Melinda Hale. *Manufacturing conductive patterns on polymeric substrates: development of a microcontact printing process*. PhD thesis, Massachusetts Insitute of Technology, 2013.

[21] Jessamine Ng Lee, Cheomlin Park, and George M. Whitesides. Solvent compatibility of poly(dimethylsiloxane)-based microfluidic devices. *Analytical Chemistry*, 75:6544–6554, 2003.

[22] Younan Xia, Dong Qin, and George M. Whitesides. Microcontact printing with a cylindrical rolling stamp: A practical step toward automatic manufacturing of patterns with submicrometer-sized features. *Advanced Materials*, 8(12):1015–1017, 1996.

[23] *Laser direct write system for fabricating seamless roll-to-roll lithography tools*, volume 8612, 2013.

[24] Jongho Park and Beomjoon Kim. 3d micro patterning on a concave substrate for creating the replica of a cylindrical {PDMS} stamp. *Microelectronic Engineering*, 98:540 – 543, 2012. Special issue {MNE} 2011 - Part {II}.

[25] Younan Xia, Joe Tien, Dong Qin, and George M Whitesides. Non-photolithographic methods for fabrication of elastomeric stamps for use in microcontact printing. *Langmuir*, 12(16):4033–4038, 1996.

[26] Rebecca J. Jackman, James L. Wilbur, and George M. Whitesides. Fabrication of submicrometer features on curved substrates by microcontact printing. *Science*, 269(5224):664, Aug 04 1995. Copyright - Copyright American Association for the Advancement of Science Aug 4, 1995; Last updated - 2010-06-08; CODEN - SCIEAS.

[27] Joseph E. Petrzelka and David E. Hardt. Limitations on roll based microcontact printing imposed by variations in macro scale stamp dimensions. *MRS Proceedings*, 1401, 2012.

[28] Joseph E. Petrzelka and David E. Hardt. Static load-displacement behavior of pdms microfeatures for soft lithography. *Journal of Micromechanics and Microengineering*, 2012.

[29] Andres Salgado-Bierman. In-process measurement of micro-contact printing, 2016. Massachusetts Institute of Technology. Bachelor's Thesis.

[30] F. H. Dill, W. P. Hornberger, P. S. Hauge, and J. M. Shaw. Characterization of positive photoresist. *IEEE Transactions on Electron Devices*, 22(7):445–452, Jul 1975.

[31] MicroChemicals. Az 9200 photoresist: High-resolution thick resist. `http://www.microchemicals.com/micro/az_9200.pdf`. [Online; Last Revised N/A].

[32] Chris Mack. *Fundamental Principles of Optical Lithography: The Science of Microfabrication.* Wiley, Hoboken, New Jersey, 2007.

[33] Haiyin Sun. *Laser Diode Beam Basics, Manipulations and Characterizations.* Springer, 2012.

[34] Andreas Schilling, Hans Peter Herzig, Laurent Stauffer, Urs Vokinger, and Markus Rossi. Efficient beam shaping of linear, high-power diode lasers by use ofmicro-optics. *Appl. Opt.*, 40(32):5852–5859, Nov 2001.

[35] D. F. Swinehart. The beer-lambert law. *Journal of Chemical Education*, 39(7):333, 1962.

[36] Ron Eakin. [Phone Conversation with Integrated Micro Materials Representative; August 30, 2016].

[37] MicroChemicals. Exposure of photoresists. `http://www.microchemicals.com/downloads/application_notes.html`. [Online; Last Revised 2013-11-07].

[38] Chris A. Mack. Understanding focus effects in submicrometer optical lithography: a review. *Optical Engineering*, 32(10):2350–2362, 1993.

[39] Dennis Ward. [Personal Conversation with MIT MTL; September 20, 2016].

[40] MicroChemicals. Hardbake of photoresist structures. http://www.microchemicals.com/downloads/application_notes.html. [Online; Last Revised 2013-11-07].

[41] MicroChemicals. Reflow of photoresist. http://www.microchemicals.com/downloads/application_notes.html. [Online; Last Revised 2013-11-07].

[42] MicroChemicals. Softbake of photoresist films. http://www.microchemicals.com/downloads/application_notes.html. [Online; Last Revised 2013-11-07].

[43] MicroChemicals. General properties of az / ti photoresists. http://www.microchemicals.com/downloads/application_notes.html. [Online; Last Revised 2013-11-07].

[44] MicroChemicals. Solvents: Theory and application. http://www.microchemicals.com/downloads/application_notes.html. [Online; Last Revised 2013-11-07].

[45] MicroChemicals. Storage, ageing, refilling, and dilution of photoresists. http://www.microchemicals.com/downloads/application_notes.html. [Online; Last Revised 2013-11-07].

[46] MicroChemicals. Thick resist processing. http://www.microchemicals.com/downloads/application_notes.html. [Online; Last Revised 2013-11-07].

[47] MicroChemicals. Rehydration of photoresists. http://www.microchemicals.com/downloads/application_notes.html. [Online; Last Revised 2007-02-26].

[48] MicroChemicals. High-resolution photoresist processing. http://www.microchemicals.com/downloads/application_notes.html. [Online; Last Revised 2013-11-07].

[49] MicroChemicals. Development of photoresists. http://www.microchemicals.com/downloads/application_notes.html. [Online; Last Revised 2013-11-07].

[50] MicroChemicals. Baking steps in photoresists processing. http://www.microchemicals.com/downloads/application_notes.html. [Online; Last Revised 2013-11-07].

[51] MicroChemicals. Photoresist removal. http://www.microchemicals.com/downloads/application_notes.html. [Online; Last Revised 2013-11-07].

[52] MicroChemicals. Laser-exposure of photoresists. http://www.microchemicals.com/downloads/application_notes.html. [Online; Last Revised 2013-11-07].

[53] MicroChemicals. Lithography trouble shooter: Questions and answers around the most common problems in micro-structuring. http://www.microchemicals.com/downloads/application_notes.html. [Online; Last Revised 2012].